The role of vorticity, turbulence and three-dimensional flow structure on the development of scour

Elizabeth Clare Jamieson

Thesis submitted to the
Faculty of Graduate and Postdoctoral Studies
In partial fulfillment of the requirements
For the PhD degree in Civil Engineering (Water Resources)

Department of Civil Engineering
Faculty of Engineering
University of Ottawa

Abstract

Fundamental to the understanding of how rivers transform and shape our environment is the role of turbulence and complex, three-dimensional flow, such as vorticity, in sediment transport and erosion. However, classical sediment transport models (or formulae) are based, for the most part, on boundary shear stress and do not incorporate these natural phenomena. This is understandable given that the relationship between turbulence generation, intensity and form; the influence of turbulence on mobile sediment; and the magnitude and patterns of deposition and erosion are complex and difficult to quantify. Nevertheless, the failure to incorporate turbulence and complex, three-dimensional flow into existing models means that our understanding of sediment transport remains incomplete.

The central hypothesis of this thesis is that vortical motion is the main factor in the development of local scour. To examine this, a comprehensive experimental approach was taken. This approach involved detailed measurements of the unique three-dimensional patterns of velocity, turbulence and bed morphology associated with flow in an open channel with and without the presence of submerged groyne-like structures (stream barbs and wing dikes) at both the laboratory and field scales. Using densely spaced velocity data and new techniques for processing and analyzing these data, it was possible to identify complex features of the flow field at both scales, such as the presence of vortex cores, and correlate these with changes in bed levels. These data provide a unique perspective of the spatial variability of velocity, turbulence and bed morphology in open channels (and in particular in channel bends, where flow is highly three-dimensional). In particular, it was found that, of the flow parameters analyzed, turbulent stresses were most correlated to scour in channel bends without the presence of structures. In contrast, vorticity was found to be the dominant factor in local scour hole development in the vicinity of submerged structures at both the laboratory and field scale. Such data are rare (if non-existent) in existing experimental research, particularly at the scale of a large natural river.

This research also examines stream barb design and performance. Stream barbs (also known as submerged groynes or spur dikes) are a relatively novel approach to stream bank protection and are not common in Canada. The design and installation of stream barbs in a creek in Ottawa (Sawmill Creek) was undertaken to serve as a demonstration project for the use of these structures in a semi-alluvial channel, for which no such case studies exist. Three years of monitoring the site and the performance of these structures to reduce bank erosion and improve aquatic habitat have been carried out. Laboratory testing of stream barb performance was also undertaken and showed that with improper design, the outer bank in a channel bend may be more susceptible to erosion due to excessive local scour downstream of the barb. In particular, to avoid bank erosion downstream of the barb, barbs should be small, such that they create minimum flow obstruction, and include a bank key that is wider than the barb itself and extends in the downstream direction.

Acknowledgements

I would like to thank my two thesis supervisors Dr. Colin Rennie and Dr. Ronald Townsend, who have provided valuable and continuous support and guidance throughout my PhD studies. In particular I would like to recognize Colin's generous time and commitment to field work and data analysis at various stages during this research. His availability, enthusiasm and valuable feedback, continued to inspire and motivate me to produce useful, timely and interesting research.

I would like to thank all the technical staff at the University of Ottawa, and in particular Mark Lapointe and Léo Denner, who have helped me at various stages to solve problems, collect data and fix equipment.

I would like to acknowledge Darlene Conway at the City of Ottawa Department of Planning, Transit and the Environment for her valuable comments and leadership throughout the design and implementation phase of the stream barb project at Sawmill Creek. As well, I would like to thank other City of Ottawa staff (Tara Redpath and Brian Bezaire) for their ongoing monitoring efforts at the site.

I would like to thank Dr. Robert Jacobson and his staff at the Columbia Environmental Research Center, U.S. Geological Survey, in Columbia, Missouri for providing me with the opportunity to experience field work on a large river. Their time, equipment and expertise allowed us to collect valuable and useful data.

I would like to thank the three French exchange students who visited during various summer internships (Stéphanie Renous, Geneviève Téphaine and Amélie Rondot) for their assistance in data collection at the field site and in the laboratory.

Last, but not least, I would like to thank my family (the Jamieson's and the Morris') for their continued support and interest in my research – even when they were not quite sure what I was actually up to! I would like to especially thank my husband Regan Morris for all his support, emotional and otherwise, without whom I could not have accomplished any of this work, and who ultimately helped to provide the final incentive to finish!

This work was supported in part by grants from the Green Municipal Fund (Canada), the City of Ottawa, the Natural Sciences and Engineering Research Council (Canada), the Canadian Foundation for Innovation, the Canadian Water Resources Association and the Ontario Government's Ontario Graduate Scholarship program.

Table of Contents

List of Figures

List of Tables

List of Symbols

A	cross sectional area
B	channel width
CI	confidence interval
CV	coefficient of variation
D	sediment size
d_{50}	mean sediment size
f	sampling frequency
$f_{Nyquist}$	Nyquist frequency, $f_{Nyquist} = f / 2$
g	acceleration due to gravity, $g = 9.81$ m/s^2
g_b	bed load transport rate
h	local water depth
L	channel length or time lag (Chapter 5.3)
L_x	integral length scale
n	number of matched points (Chapter 1.1) or spectral energy above the fitted -5/3 slope (Chapter 5.1)
N	noise
NR	noise ratio, $NR = N/\overline{\lvert u' \rvert}$
k_s	roughness parameter
Q	discharge
Q_E	percent daily flow exceedance
r^2, R^2	coefficient of determination, regression coefficient
r	lag distance
R	hydraulic radius
Re	Reynolds number
RMSE	root mean square error
R_x	correlation coefficient
S	water surface slope or channel bed slope
$\boldsymbol{S}$	rate-of-strain tensor, $\boldsymbol{S} = \frac{1}{2}\left[\nabla \upsilon + (\nabla \upsilon)^T\right]$
T_E	integral time scale
tke	turbulent kinetic energy

u, U, v_x	x component of velocity, streamwise velocity
$\overline{U}$	depth averaged velocity
U_*	shear velocity
$\mathbf{u}$	velocity vector, $\mathbf{u} = u\hat{\mathbf{i}} + v\hat{\mathbf{j}} + w\hat{\mathbf{k}}$
$\lvert\hat{u}\rvert$	relative turbulent intensity
u'	fluctuating streamwise velocity
v, V, v_y	y component of velocity, cross-stream velocity
v_b	apparent bed load velocity or bed velocity
v_{bE}	easting component of bed velocity
v_{bN}	northing component of bed velocity
v_{bt}	boat velocity measured with bottom tracking
v_e	easting component of velocity
v_n	northing component of velocity
v_{ref}	independent measure of boat velocity
v_ε	error velocity
v'	fluctuating cross-stream velocity
w, W, v_z	z component of velocity, vertical velocity
w'	fluctuating vertical velocity
WSE	water surface elevation
x	streamwise direction
y	cross-stream direction (positive towards left bank)
z	vertical direction (positive towards water surface)
Z	bed elevation
∇v	velocity gradient

Greek Symbols

γ	specific weight of water
Δv	velocity difference
ΔZ	bed level change
ε	estimation error
$\boldsymbol{\zeta}$	vorticity, $\boldsymbol{\zeta} = \nabla \times \mathbf{u}$ and $\boldsymbol{\zeta} = 2\boldsymbol{\omega}$

θ	bed velocity direction (Chapter 4.1) or side slope angle (Chapter 5)
θ_b	projection angle of structure to upstream bank
κ	von Kármán constant
$\lambda_2(\mathrm{A})$	intermediate eigenvalue of a symmetric tensor (A)
ρ	density of water
σ	standard deviation
τ_c	critical shear stress
τ_o, τ	bed shear stress
τ_{uv}	streamwise-cross stream Reynolds shear stress, $\tau_{uv} = -\rho\overline{u'v'}$
τ_{uw}	Principal Reynolds shear stress, $\tau_{uw} = -\rho\overline{u'w'}$
τ_{vw}	cross stream-vertical Reynolds shear stress, $\tau_{vw} = -\rho\overline{v'w'}$
τ^*	Shields coefficient
τ_c^*	critical Shields coefficient
$\boldsymbol{\omega}$	vorticity rotation vector, $\boldsymbol{\omega} = \omega_x\hat{\mathbf{i}} + \omega_y\hat{\mathbf{j}} + \omega_z\hat{\mathbf{k}}$
ω_x	vorticity/rotation about the x-axis
ω_y	vorticity/rotation about the y-axis
ω_z	vorticity/rotation about the z-axis
$\boldsymbol{\Omega}$	vorticity tensor, $\boldsymbol{\Omega} = \frac{1}{2}\left[\nabla v - (\nabla v)^T\right]$

Abbreviations

2-D	two-dimensional
3-D	three-dimensional
ADCP	acoustic Doppler current profiler
ADP	acoustic Doppler profiler
ADV	acoustic Doppler velocimeter
ADVP	acoustic Doppler velocity profiler
B	barb
Ens.	ADCP ensembles
GPS	global positioning system
LB	left bank

LES	large eddy simulation
MTM	Modified Transverse Mercator co-ordinate system
OSAP	Ontario Stream Assessment Protocol
RB	right bank
RS	Reynolds shear stress
RTK	real-time kinematic
SSIIM	Simulation in Intakes with Multiblock option
T	transect (Chapter 3.2) or transect spacing (Chapter 1.1)
TR	trapezoid run
USDA	United States Department of Agriculture
WEPP	City of Ottawa Water Environment Protection Program

1 Introduction

Complex flow, turbulence and sediment transport are fundamental to the understanding of rivers and environmental hydraulics and yet remain subjects that are not entirely understood. The overall objective of this research is to further our understanding of the interactions between turbulent flow structure, which is an inherent characteristic of flow in rivers, and sediment entrainment and transport, which itself is the primary mechanism by which rivers are formed and continue to evolve. Advances in understanding turbulence in open channel flows have provided the theoretical and physical framework for researchers to acknowledge the importance of turbulent velocity and boundary shear stress to sediment entrainment and transport (Bagnold, 1956; Sutherland, 1967; Grass, 1971; Leeder, 1983). Additional research in the last few decades has revealed organized vortical structures that exist within the turbulent boundary layer of open channel flows, which, for turbulent flows, control the dissipation of energy, the generation and magnitude of shear velocity and shear stress, and consequently the entrainment of sediment (Best, 1993). However, the relationship between turbulence generation, its intensity and form, and its influence on mobile sediment and the magnitude and patterns of deposition and erosion is complex and difficult to quantify. Despite the important role complex flow and turbulence play in how materials such as sediments (and pollutants and nutrients) are dispersed and deposited in the surrounding environment, our understanding of these properties in rivers and the extent to which they influence mass transport processes such as sediment entrainment and transport is incomplete.

The weakness of classical sediment transport models (and through extension, their formulae) is that they do not incorporate modern turbulence knowledge (Nezu and Nakagawa, 1993). Most models (which are typically stochastic or deterministic) are based on

mean flow conditions, with no consideration of the spatial and temporal variability of the flow field and bed resistance, and therefore are incapable of incorporating the effects of turbulence (with the exception of some new models, such as those of Schmeeckle and Nelson (2003) and Diplas *et al.* (2008)). In this thesis, the complex interactions between turbulent flow structures and sediment erosion (scour) have been investigated in detail through a comprehensive experimental approach. This experimental approach involved detailed measurements of the unique three-dimensional (3-D) patterns of velocity, turbulence and bed morphology associated with flow in a channel bend with and without the presence of a series of stream barbs (or barbs) at both the field and laboratory scale. Stream barbs (also known as submerged groynes or spur dikes) are low-profile linear rock structures that prevent the erosion of stream banks by redirecting high velocity currents away from the bank. These structures are an important method for stream bank protection as they can be built at a relatively low cost and provide notable ecological benefit. The submerged nature of these structures and the fact that they are typically placed in channel bends (where helicoidal flow dominates) creates a unique combination of vertical flow separation and overtopping (plunging) flow conditions, causing large and small scale 3-D eddies to form. Quantifying the influence of these 3-D turbulent eddies on a mobile bed will improve predictions of sediment transport. In turn, this will allow for better estimates of scour and bank erosion, which ultimately will lead to a better understanding of river morphology in general.

The central hypothesis of this thesis is that vortical motion, with a predictable recurrence, magnitude and form, dominates the development of local scour. By better quantifying the role of vorticity on local scour, this will enable better scour predictions (and by extension sediment transport in general). While analysing numerical model results from an earlier University of Ottawa study of flow in a channel bend containing a series of barbs (Minor *et*

al. 2007b), we found a noticeable relationship between the location of maximum scour and the calculated vorticity field (Minor *et al.,* 2007a). Specifically, the patterns of maximum scour, found at the barb tips, and which correlated well with previous laboratory experiments (Matsuura, 2004), corresponded with regions of maximum vertical vorticity. However, velocity measurements were never collected to verify these calculations and confirm the reliability and extent of the linkage between vorticity and scour.

To test this hypothesis, detailed measurements of the 3-D velocity field and corresponding changes in local bed topography have been taken at high spatial resolution in a mobile-bed laboratory channel bend, with and without stream barbs (Chapter 5: Experimental Channel Bend) and in the vicinity of submerged wing dikes (and corresponding scour holes) on the Missouri River, a large sand-bed river (Chapter 4: Missouri River). This experimental work complements a field-scale study of stream barb design, installation, and performance at Sawmill Creek (Chapter 3: Sawmill Creek) by providing a more detailed and systematic approach to capturing the unique flow field and corresponding patterns of scour for submerged structures in general, and for stream barbs in a channel bend in particular. Together, these data are used to characterize the scale and structure of coherent turbulent events, whether they are "small" vortices shed in the wake of an in-stream structure in the laboratory; or "large" vortex cores in the vicinity of a wing dike in a large sand-bed river, and to determine the influence of these structures on local scour development.

Complementary to the study of turbulence and sediment transport described above, this thesis will also provide an assessment of the suitability and performance of stream barbs for reducing stream bank erosion. Excessive stream bank erosion can damage infrastructure and degrade aquatic habitats by increasing fine sediments in the channel substrate and widening

streams (Espinosa *et al.,* 1997; Sekely *et al.,* 2003). Stream barbs are low-profile linear rock structures, typically anchored, in series, to the outside bank in stream bends and extend in an upstream direction away from the bank into the flow (USDA, 2005). This configuration redirects flow away from the outer stream bank and disrupts the velocity gradient close to the outer bank, encouraging sediment deposition adjacent to the barb, near the bank. Moreover, with time, barbs cause the thalweg in a channel bend to relocate away from the outside bank region (an undesirable and unstable location) to a new more stable location closer to the channel centreline. Unlike traditional measures of stream bank protection such as riprap, concrete paving or gabion walls, which impede the establishment of vegetated stream banks, hydraulic structures such as stream barbs are a more environmentally sustainable means of maintaining stream bank stability. As well as providing bank protection, these structures promote vegetated stream banks (Piper *et al.,* 2001), create resting pools and scour holes for fish habitat (Shields *et al.*, 1998) and increase bio-diversity for aquatic species (Shields *et al.*, 2000). Despite these benefits, because of their relative novelty as river training structures, stream barbs are not a common means of stream bank protection in Canada and are possibly non-existent for semi-alluvial or clay channels. Research is therefore needed to investigate the suitability and optimal design of stream barbs in rivers, particularly for the case of semi-alluvial channels where these structures are not typically used.

The design, construction and monitoring of a series of seven stream barbs installed at Sawmill Creek, an urban, meandering stream in Ottawa, Ontario, Canada (Chapter 3: Sawmill Creek) serves as a demonstration project for the use of these structures in a semi-alluvial channel. Field work at Sawmill Creek included: (i) the design and installation of barbs in two channel bends, (ii) detailed measurements of the velocity field in the vicinity of the submerged structures during periods of high and low flow (before and after installation of

the structures), and (iii) regular monitoring of flow rate, water level and bed and bank morphology for three years. The more detailed and systematic measurements of stream barb performance in the laboratory (Chapter 5: Experimental Channel Bend), provided valuable results on optimum barb geometry and layout in an open channel bend.

1.1 Research objectives and novel contribution

The contribution of turbulence to the development of scour is not completely understood (Roy *et al.,* 1999 and Thompson 2006). Recent research (MacVicar and Roy, 2007; Thompson and Wohl, 2009) has shown that a direct relationship between the level of turbulence in open channel flows, including the patterns and magnitude of coherent structures, and scour does exist; however this has yet to be fully quantified. This research seeks to explain the complex interactions between the 3-D turbulent flow field and the resulting patterns of sediment deposition and scour for both a natural and laboratory channel bend, where 3-D flow dominates, and in the vicinity of a submerged structure, where the resulting flow patterns become even more complex (i.e. highly 3-D and turbulent). Detailed measurements of velocity, turbulence and bed morphology in a channel bend with and without a series of submerged stream barbs, at both field and laboratory scale, provide novel and comprehensive experimental data and direct observation and measurement of these coupled and complex processes. This study also provides a systematic investigation (using both experimental and numerical methods) of the capabilities of stream barbs for stream bank stabilization and baseline results from which design guidelines will be developed, which currently are non-existent in Canada and absent for semi-alluvial systems in the United States.

The most recent studies of fluid and sediment dynamics around barbs (or equivalent, i.e. spur dikes) have considered straight laboratory channels (Fox *et al.,* 2005a and 2005b; Kuhnle *et al.,* 2008) and non-simultaneous measurements of flow field and bed morphology (Bhuiyan *et al.,* 2009). The one exception is the recent study of thin bank-attached vanes by Bhuiyan *et al.* (2010). We are not aware of any laboratory or field studies that have investigated the spatial variation in three-dimensional (3-D) turbulent flow structure and associated patterns of scour and deposition around a series of upstream-angled rock stream barbs in a channel bend, where in practice these structures are most typically deployed. The systematic study of the effects of in-stream structures on local flow and sediment transport processes under controlled conditions in a large-scale laboratory flume are rare. Such investigations are critical if we are to understand these complex processes and provide the necessary data for validating numerical models. This is especially true for mobile bed conditions, where data are most lacking, despite being vital for linking the influence of flow patterns and turbulence to sediment transport processes. As well, of the relevant laboratory-scale mobile bed studies that have been performed, none have studied bank erosion. The initial conditions of all previous mobile bed experiments was a horizontal (flat) bed with rigid vertical side walls. In this thesis, a sand bed with a trapezoidal-shaped cross-section was used, where both the bed and banks of the channel were subject to scour.

These laboratory and field experimental studies cover a range of sediment types, from non-cohesive sediments (sand and gravel) to cohesive sediments (clay). The transport characteristics of cohesive sediments are significantly different from those of non-cohesive sediment and at present are not well defined. The mechanisms of transport and erosion are more complex, due to the complex physio-chemical properties of clay particles, and are typically site specific (Gaskin *et al.,* 2003). The chosen field test site in Ottawa (Sawmill

Creek), like many other water courses in the National Capital Region, has the added complexity of being a predominately clay bed and banks channel. A number of case studies of the use of stream barbs (or equivalent) are available for the West and Midwestern United States, where alluvial (sand and gravel) rivers predominate. No such case studies are available for semi-alluvial streams, which highlights the absence of barbs (or equivalent) as a design option for bank protection in these types of rivers. The performance of these structures and their long term effects on morphology and habitat will largely depend on the local sediment transport characteristics, which are inherently different when cohesive sediments are present: there may no longer be a supply of alluvial sediment upstream and the mechanisms of soil erosion and transport are more complex. Moreover, available case studies all consider rural or semi-rural streams. The impact of urbanization (i.e. increased runoff and shorter time of concentration) on the functionality of stream barbs, where the estimation and behaviour of bankfull flow conditions is critical for successful barb design, appears to have been excluded from both previous field testing and monitoring, and design documentation. The installation of stream barbs at Sawmill Creek, Ottawa presents a unique opportunity to study the effects of these structures on a predominately clay bed and bank channel, in a heavily urbanized watershed. As well, using data collected from the field site, it may be possible to estimate the critical boundary shear stress for a natural semi-alluvial stream. This parameter is still not adequately defined in the current literature and yet it is critical for sediment transport and scour predictions.

This research is largely focused on an experimental approach to measuring, analysing and ultimately quantifying complex flow fields, turbulence and sediment transport. Incorporating the effects of turbulence into sediment transport relations is held back by the

difficulties of specifying and measuring meaningful parameters relating to both turbulent stresses and high frequency particle motions (Clifford and French, 1993). Consequently, research must be directed towards the search for a range of turbulence structures comparable to those elucidated through experimental measurement. One objective of this research is to investigate how interpolation techniques can be used for evaluating complex 3-D flow features and patterns of mean turbulence (i.e. vortex cores) from measured flow data. The most recent numerical modelling techniques have reached such a level of sophistication that they can provide very detailed and continuous (i.e. time dependant) results for a range of fluid phenomena, beyond that which can be captured through experimental measurement alone. For example, current large-eddy simulation (LES) models are capable of predicting instantaneous flow characteristics (velocity and turbulence) and resolving coherent structures with grids that are fine enough and time steps that are small enough to capture the important dynamics of these eddies (Koken and Constantinescu, 2008a and 2008b). However, due to their significant computational requirements, these particular models are limited to low Reynolds numbers ($Re < 20\ 000$) due to their significant computational requirements, which limit their ability to model adequately the highly turbulent flows characteristic of a natural river where typically $Re > 10^5$. To examine how well we can identify and quantify complex flow fields with experimental (measured) data, spatially dense 3-D velocity data were collected for highly 3-D flow at two different scales: (1) flow in a laboratory channel bend, with and without submerged stream barbs; and (2) flow in the vicinity of a submerged wing dike on a large sand-bed river (Missouri River).

The extent to which we can validate any numerical model is dependent on (or limited by) the experimental data available, which typically rely on time- and/or spatially-averaged point or profile measurements from discrete locations in the flow for characterizing patterns of

mean flow and turbulence. The direct measurement of the 3-D velocity field and corresponding turbulence parameters in a mobile bed channel bend will provide the necessary data for better validation of numerical simulations of turbulent flow and sediment transport. A fully resolved 3-D numerical solution for open channel flow problems which adequately incorporates the behaviour of turbulence and sediment transport has yet to be realized. Even the most recent attempts (Zeng *et al.,* 2008) have acknowledged the weaknesses of present numerical models for predicting flow, sediment transport and morphodynamics in alluvial bends, likely due to an incomplete characterization of turbulent stresses.

Finally, there is a dependence of aquatic habitat on bed topography and turbulence that is understood, but has yet to be fully measured. While it may be beyond the scope of this thesis to investigate this dependence closely, the results of on-going habitat monitoring and data collection at Sawmill Creek, which should provide an overall before and after picture of aquatic activity at the study site, could determine the important physical characteristics (i.e. small wake regions, velocity refuge, deep pool, etc.) necessary for various aquatic organisms (i.e. benthic invertebrates, fishes, etc.) at the local reach scale. More importantly, since the majority of previous studies have focused on rural or geographically remote streams (Jones and Tonn, 2004 and Shields and Rigby, 2005), we have the unique opportunity to monitor changes in aquatic activity in a highly urban environment. In an urban watershed, critical variables such as hydrology, water quality and temperature behave differently (for example, rapid and peaky rainfall-runoff events) and coupled with the addition of stream barbs, could possibly accelerate or enhance (or conversely diminish) the quantity and diversity of aquatic organisms and available habitat in an environment desperate for improved aquatic health.

In summary, the objectives of this thesis are as follows:

- To describe and quantify the role of vorticity on the development of scour.
- To describe (i) the distribution of the 3-D velocity field and turbulent stresses through a channel bend and (ii) the significance of these stresses on sediment transport and equilibrium scour.
- To develop new techniques for extracting 3-D flow features (including coherent flow structures) from experimental (discrete) data.
- To evaluate the performance of stream barbs on reducing bank erosion in an alluvial and semi-alluvial meander bend.
- To evaluate the impact of stream barbs on fish community and habitat in an urban stream.
- To provide substantial experimental data (collected at both field and laboratory scale) for numerical model validation.

1.2 Outline of thesis

This thesis takes the form of a series of manuscripts, prepared for publication (or in some cases already published or accepted) in a scholarly journal or conference proceeding. Additional chapters (1 Introduction, 2 Literature Review, 6 Additional Results and Discussion, and 7 Conclusions and Recommendations) are included, which integrate the material covered in each of the manuscripts and provide a global summary and discussion. The first chapter (Introduction) introduces the general topics that will be discussed in this thesis and provides context with respect to the current state of knowledge. The second chapter (Literature Review) discusses in detail the previous research relevant to this thesis and highlights where current research is lacking. The three middle chapters, Chapters 3 (Sawmill Creek), Chapter 4 (Missouri River) and Chapter 5 (Experimental Channel Bend) represent the core chapters of the thesis. Each core chapter is sub-divided according to

individual manuscripts or papers on each chapter topic, which have either been, published, accepted or submitted (as indicated at the beginning of each manuscript). The sixth chapter (Additional Results and Discussion) presents additional results and analysis that were not included in the three core chapters. These results are still considered preliminary and in some cases are taken from other sources. This chapter also provides a summary of the key results from each manuscript and discusses the relevance of each one with respect to the others. Finally, Chapter 7 (Conclusions and Recommendations) summarizes the important conclusions and provides detailed recommendations for continuing this research.

A manuscript based thesis was written as it presents a concise format for presenting the key findings of this research. This format is most suitable for timely sharing of these results in peer reviewed publications.

2 Literature Review

2.1 Turbulence and sediment transport

Current sediment transport theory maintains that the initiation or threshold of movement of a particle depends on local particle geometry and local fluid forcing (Raudkivi, 1998). Putting aside the effects of sediment properties and geometry, then the focus remains on the contribution of local fluid forcing to bed load entrainment. Local fluid forcing is a function of the bulk flow (mean bed shear stress) and turbulence (fluctuating turbulent stresses), both of which can vary (spatially and temporally) throughout a fluvial system. The discussion that follows will examine both factors of fluid forcing, shear stress and turbulence, which contribute to sediment transport and thus scour.

Despite the number of different formulae for predicting bed load sediment transport (see reviews by Gomez and Church, 1989; Habersack and Laronne, 2002), most of these contain the same general concept: that bed load transport rate is a function of excess shear stress, τ_o - τ_c, where τ_o is bed shear stress and τ_c is critical shear stress for particle entrainment. If the applied shear stress on the bed of an alluvial channel exceeds the threshold value of the bed material, it is set in motion (Raudkivi, 1998). Therefore, the magnitude and location of bed load transport will depend on the distribution of shear stress on the bed, which is affected by the distribution and pattern of fluid velocity. Dietrich and Whiting (1989) demonstrated that maximum bed load transport in a channel bend occurs where excess shear stress is greatest.

The weakness of classical sediment transport models (and through extension, their formulae) is that they do not incorporate modern turbulence knowledge (Nezu and Nakagawa 1993). Most models (which are typically stochastic or deterministic) are based on mean flow conditions, with no consideration of the spatial and temporal variability of the

flow field and bed resistance. Consequently, they are incapable of incorporating the effects of turbulence (with the exception of some new models, such as those by Schmeeckle and Nelson (2003) and Diplas *et al.* (2008)). Indeed, recent research by Bhuiyan *et al.* (2009) compared detailed measurements of bed load transport in a laboratory meander bend (with and without in-stream structures (vanes) for bank protection) with several deterministic and stochastic type bed load transport equations. They found that these predictive formulae, which are typically based on section-averaged parameters, generally underestimate transport rates.

Briefly, turbulence can affect entrainment in three ways: (1) a particle may be moved by the drag forces caused by a passing eddy; (2) the eddy may lower local pressure causing the particle to be ejected from the bed due to hydrostatic pressure (i.e. lift forces); (3) entrained particles may remain suspended rather than moved along the bed (Raudkivi, 1998). Turbulence contributes to sediment transport due to the generation of high instantaneous shear stresses near the bed that result from near-bed turbulent events, which lead to increased mobility of sediment particles. Research has shown that turbulence bursts near the bed impose a rapid and significant pressure fluctuation on the bed surface, which tends to lift particles, increasing sediment entrainment (Kline *et al.,* 1967; Grass, 1971; Drake *et al.*, 1988). Bursting eddies appear randomly in space and time near the bed; however, their behaviour is organized and coherent, due to the quasi-cyclic process of ejections and sweeps which comprise this process (Nezu and Nakagawa 1993). Most recently, a new approach to account for fluctuating forces due to turbulence in the sediment entrainment process is the role of impulse (Diplas *et al.,* 2008). Through laboratory experiments and analytical formulation, Diplas *et al.* (2008) were able to demonstrate that, in addition to the magnitude of the instantaneous turbulent forces applied to a grain of sediment, the duration of these

turbulent forces is also important in determining the grain's likelihood of entrainment. The authors propose that the product of turbulent force and duration (impulse) is better suited for specifying threshold conditions than the common method of time-averaged boundary shear stress.

Possibly the first research to examine the effect of turbulent flows on sediment entrainment and transport was that of Sutherland (1967). His hypothesis of sediment entrainment was based on the concept of turbulent eddies disrupting the viscous sublayer and impinging directly on particles on the surface of the bed, a concept we now describe as ejection and sweep motions. This concept of turbulent eddies disrupting the viscous sublayer can be considered synonymous with bursting motions, which incidentally was discovered by Kline *et al.* (1967) in the same year. Sutherland (1967) was not able to fully explain fluid-particle interactions; however, he did emphasize that particles could not be ejected from the bed without the presence of turbulent fluctuations.

In addition to the quasi-periodic bursts of small–scale turbulent motions generated near the bed, coherent vortical structures can form due to the presence of bed features (dunes and ripples) or structures placed in the flow (i.e. bridge abutments and groynes), all of which act to disrupt the mean flow pattern. For example, when flow passes the tip of a groyne, a shear (mixing) layer develops where the two streams of different velocity meet. This mixing can be characterized by vertically-oriented vortices that advect in the direction of the main downstream flow (also known as vortex shedding). Research has shown that near-bed fluctuations, like those found in regions with vortex shedding, create instantaneous forces greater than time-averaged values. This implies that sediment transport occurs at flows where the time-averaged conditions are below the critical entrainment threshold for sediments

(McLean et al, 1994; Roy *et al.*, 1999; Thompson, 2006) and a non-linear increase in transport as the amplitude of velocity fluctuations increases (Schmeeckle and Nelson, 2003).

In the context of large rivers, large-scale vortical motions consist of many kolk-boil vortices, a ubiquitous form of turbulence in rivers, which can have a variety of magnitudes and strengths, depending on the flow and bed form (Nezu and Nakagawa, 1993). Jackson (1976) hypothesized that the turbulent 'bursting' motions observed in turbulent boundary layers of large natural rivers (these kolk-boil vortices) plays a major role in how alluvial sediment is entrained and suspended in the flow. Strong upward flow in a burst provides the vertical anisotropy in the turbulence which is needed to suspend sediment. Bursting also promotes the entrainment of more and coarser sediment beyond that which can be accomplished by tractive forces alone (Jackson, 1976).

In attempts to confirm Jackson's (1976) hypothesis, Lapointe (1992) collected field data on a sandy section of the Fraser River in British Columbia to document the 'burst-like' turbulent motions and quantify their role to sediment suspension. While the record of fluctuating sediment concentrations revealed that the 'burst-like' motions were highly effective in vertically mixing suspended sediment, no discrete recurrence timescale for these bursting events was found. A continuous variation of return periods was observed. This evidence is contrary to Jackson's (1976) conceptual model of sediment transport due to predictably reoccurring burst events. However, it is possible that the generation of vortex shedding around a structure (such as a submerged wing dike or stream barb) helps to establish a certain degree of periodicity (or predictable recurrence) in the burst-like events.

Now, what about the modification of near-bed fluctuations by the introduction of a mobile sediment? The structure of turbulence can be modified by the presence of particles (or sediment grains) in natural flows and has been known to both dampen and enhance

turbulence in the presence of suspended sediment, depending on the distance from the bed (Best *et al.*, 1997; Nezu and Azuma, 2004), particle size (Nino and Garcia, 1998; Cao *et al.*, 2003) and particle mass loading (Kulick *et al.*, 1994). These studies and others (Yarin and Hetsroni, 1993; Muste and Patel, 1997; Muste *et al.*, 2009) demonstrate how research on particle-turbulence interactions has focused primarily on suspended sediments. With the exception of concentrated particle-fluid systems such as fluidized beds, where the influence of particle-particle interactions begins to dominate and possibly attenuate turbulence (Kulick *et al.*, 1994), bed load particle-turbulence interactions may be less important than those of suspended sediments. As turbulence influences particle motion (or the transport of solid particles) it will also influence grain-to-grain collisions near the bed. However, unlike the case for suspended sediments, these small-scale interactions are less likely to have a profound effect on the large-scale behaviour of the flow (Hanratty *et al.*, 2003).

2.1.1 Cohesive Sediments

Cohesive sediments are characterized as a mixture of predominantly clay, silt-sized fractions of clay-type minerals and a range of organic compounds, which together assume control of the properties of the soil (Krishnappan, 2007). The cohesive properties arise from the electro-chemical forces in the clay-water medium, which usually dominate and may be orders of magnitude larger than the weight force of individual particles (Raudkivi, 1998).

The mechanism of sediment transport (i.e. bed load versus suspended load) is usually determined by the relationship between flow conditions and the structure, density and size of the material, with the suspended load being composed of finer and/or less dense material. Non-cohesive sediments (i.e. sand and gravel) are transported by the flow as individual

particles, which have a defined size and density, and as a result, the mechanics of sediment transport relate almost exclusively to non-cohesive sediments. Fine-grained suspended load is predominately cohesive and therefore is not transported as individual discrete particles but rather as flocculated or aggregated particles (Droppo and Ongley, 1994; Droppo, 2001). The effective size and density of these aggregated particles (called flocs) change as a function of the flow field (van Leussen, 1988; Lau and Krishnappan, 1997 reported in Krishnappan, 2007), making the understanding and analysis of cohesive sediment transport in a complex three-dimensional flow field much more difficult. Review papers by Krishnappsn (2007) and De Boer *et al.* (2005) provide an overview of fine-grained and cohesive sediment transport processes, with a particular focus on research in Canada (De Boer *et al.*, 2005).

For rivers incising into clay, the channel geometry will be influenced by the erodability of the clay. The erosion of cohesive bank materials often occurs through entrainment of aggregates rather than single particles, making the quantification of entrainment process on the surface of these cohesive bank materials more complex (Debnath *et al.*, 2007). The complexity is further increased by the fact that the properties of the cohesive materials themselves are typically site specific (Gaskin *et al.,* 2003). The influence of turbulence and flow field on local sediment transport dynamics for cohesive materials is less understood since the influence of local fluid forcing can no longer be considered at the scale of an individual resting particle or entrained grain. Ottawa's surficial geology is dominated by glaciomarine clays that derive from the fine material that settled in the Champlain Sea after being eroded by glaciers. These sediments are consolidated and relatively difficult to entrain given their cohesive nature.

Cohesive sediment research is not only necessary for better estimates of soil erosion (for the protection of infrastructure, etc.), but also because a majority of highly toxic and

persistent chemicals entering a river system have a high affinity for fine particles and are transported mostly in association with cohesive sediments (Allen, 1986).

2.1.2 Definitions of Vorticity and Mean (Time-Averaged) Flow Field

Vorticity is a mathematical concept that is often used in fluid dynamics to describe the rotational characteristics of a fluid. Specifically, vorticity, ζ, is defined as the rate of rotation of a fluid and is related to the velocity field as the curl of the velocity vector $\boldsymbol{\zeta} = \nabla \times \mathbf{u}$, where $\mathbf{u} = u\hat{\mathbf{i}} + v\hat{\mathbf{j}} + w\hat{\mathbf{k}}$ is the velocity vector and u, v and w are the x, y and z components of velocity, respectively. Vorticity can also be defined as twice the local rate of rotation $\boldsymbol{\zeta} = 2\boldsymbol{\omega}$, where $\boldsymbol{\omega} = \omega_x\hat{\mathbf{i}} + \omega_y\hat{\mathbf{j}} + \omega_z\hat{\mathbf{k}}$ is the rotation vector and ω_x, ω_y and ω_z are the three components of rotation about the x, y and z-axis respectively. The rotation about each axis is defined as the average of the angular velocities perpendicular to the axis of rotation such that

$$\omega_x = \frac{1}{2}\left(\frac{\partial w}{\partial y} - \frac{\partial v}{\partial z}\right),\ \omega_y = \frac{1}{2}\left(\frac{\partial u}{\partial z} - \frac{\partial w}{\partial x}\right) \text{ and } \omega_z = \frac{1}{2}\left(\frac{\partial v}{\partial x} - \frac{\partial u}{\partial y}\right) \qquad \text{(2.1.1, 2.1.2 and 2.1.3)}$$

where $\partial v/\partial x$ and $\partial w/\partial x$ are angular velocities along the x-axis, $\partial u/\partial y$ and $\partial w/\partial y$ are angular velocities along the y-axis, and $\partial u/\partial z$ and $\partial v/\partial z$ are angular velocities along the z-axis (assuming the right hand rule for positive rotation about each axis). The units of vorticity are typically taken as s^{-1}.

Despite the apparent simplicity of the two mathematical definitions above, the physical meaning of vorticity is more difficult to describe. Fundamentally, vorticity corresponds to the local rotation of a fluid. More specifically, non-zero vorticity means that a volume element of fluid is changing its orientation in space (Sreenivasan, 1990). Vorticity is a function of the velocity gradient or more specifically, the change in local angular velocity of

a fluid. For a mean (or time-averaged) flow field, we assume that the velocity at a given point in space does not vary with time. Therefore, the calculated vorticity for a time-averaged flow field must also be constant.

It is necessary to distinguish between the properties of an instantaneous and a mean flow field when discussing the fluid phenomena responsible for turbulence and sediment transport in open channels (incompressible flows). In a time-averaged (mean) flow field it may be possible to identify statistically stationary large-scale flow patterns such as secondary currents. These circulating flow patterns are said to be stationary as they maintain the same position and orientation in space and time. Two examples of this flow behaviour are: the region of recirculating flow in a groyne field, and the secondary current that develops in a river bend. In both these examples, the large-scale pattern of circulation is described by the mean (time-averaged) flow field. Secondary currents can be produced by centrifugal forces in a curved channel (for either laminar or turbulent flow). For uniform flow in straight channels, secondary currents can only be generated by turbulence inhomogeneity and anisotropy. Secondary currents alter the distribution of shear stress acting on the bed, which in turn will alter the bed load transport.

Kuhnle *et al.* (2008) found that the downstream zone of local scour near a spur dike tip was correctly predicted by the distribution of bed shear stress. However, the local scour measured at the upstream corner of the structure was not predicted. After several attempts to predict this scour, the authors concluded that it is likely that variables calculated from time-averaged flow measurements do not contain sufficient information to allow a complete prediction of the initiation of local scour around an obstacle such as a spur dike. However, it is also possible that the method of measurement failed to adequately describe the stationary large-scale flow patterns which could play a role, but would go unseen without sufficient

spatial resolution of mean velocity and turbulence data. Despite the numerous studies on flow around hydraulic structures (which are typically for non-submerged conditions), the majority of these have considered steady, one-dimensional, time-averaged flow conditions, without considering the unsteady nature of turbulent flow and the non-uniform spatial characteristics. As a result, estimates of the bed shear stress around a structure are often poorly predicted (Kuhnle *et al.*, 2002 and 2008). Estimating the depth of local scour around a structure such as a barb remains complex given that reliable scour formulas are based on (i) an oversimplification of the flow field in the vicinity of the structure (uniform, one dimensional, steady flow conditions), and (ii) single maximum depths of scour without any information about the geometry and scale (i.e. shape) of the scour hole and how this geometry changes with time. Examples of such formulae include the methods developed by Laursen (1958, 1960, 1963), Liu *et al.* (1961) and Field (1971) for scour estimates at abutments (reported in Raudkivi, 1998).

In an instantaneous flow field, the fluid velocity will vary with time. Instantaneous measurements provide information on the frequency characteristics of traveling coherent structures, a good example of which is vortex shedding. Unlike large-scale circulation patterns that can be described by the time-averaged flow field, the motions of small-scale structures are more disorganized and random due to turbulence. Oweis and Ceccio (2005) examined the instantaneous and time-averaged flow fields in the region downstream of a rotor tip and found that vortical flow parameters that were identified in the average flow field were significantly different from properties identified instantaneously. The authors suggest that the process of averaging masks the presence of uncorrelated secondary vortices that remain distinct in the instantaneous flow realizations. Vortex wandering and the presence of multiple vortices can lead to the production of significant velocity fluctuations (Oweis and

Ceccio, 2005). Therefore, by definition and experiment, the description or characterization of vorticity will depend on the spatial and temporal scale of the flow field, owing in part, to the distinction between instantaneous and time-averaged flow. Clearly, each time scale has a role and discerning their relative importance is key to investigating the hypothesis on the role of vorticity in the development of scour. However, current techniques for quantifying turbulence (i.e. acoustic Doppler velocimeters) rely on time series measurements of velocity at a point, which in the case of open channel flows should be on the order of 60-90 seconds for reliable estimates of turbulence statistics (Buffin-Bélanger and Roy, 2005). (The required measurement durations may vary, depending on the turbulent time scales, which depend on the length scales of the channel dimensions). Consequently, in this thesis the evaluation of flow field characteristics (3-D velocity and turbulence) will be limited for the most part to mean (time-averaged) properties.

Turbulent motion is inherently random and irregular, and involves a wide range of scales, making the full description of turbulent flow (in space and time) altogether impossible. Therefore, it is necessary to use statistical methods to realize particular characteristics of such flows. A generally accepted method is Reynolds decomposition. In this approach, the fluctuating (instantaneous) value of a random process (for example, velocity, U) is decomposed into a mean or average value and its fluctuations, where the instantaneous value of U is equal to the sum of the mean and the fluctuations. Taking this one step further, vortices can be isolated using a triple decomposition theorem (introduced by Hussain and Reynolds, 1972), where an instantaneous velocity signal is decomposed into a mean velocity component and two fluctuating velocity components representing large- and small-scale vortices.

Fox *et al.* (2005b) developed an eddy taxonomy methodology (using triple decomposition theory) to classify the prominent coherent flow structures in the vicinity of a submerged barb. Their method adequately separated the small-scale eddies from large-scale, macroturbulent eddies and overall, provided a detailed and comprehensive assessment of turbulence in the vicinity of a submerged obstacle. However, these experiments were performed using a fixed bed and the effect of turbulence (and vorticity) on a mobile boundary (and the effect of an evolving mobile boundary on the production of turbulence) has yet to be investigated. As Roy *et al.* (1999) observed, in the presence of a shear layer, intense velocity fluctuations may play more of a role than mean streamwise velocities in high bed load transport rates. Therefore, a means of identifying and describing these "intense velocity fluctuations" is required if we are to understand their importance to sediment transport and local scour. As well, the temporal scale of a measured or calculated flow field may have an effect on calculated vorticity. As discussed earlier, Oweis and Ceccio (2005) found that uncorrelated secondary vortices that were distinct in the instantaneous flow realizations were no longer present when the flow field was averaged. The presence of local small-scale structures (and as such an understanding of their influence) may be lost in the statistical analysis of time series data and certainly so when averaging in a numerical computation.

Evaluating the relative importance of vorticity to local scour over other flow patterns and behaviour is challenging. In general, local scour is a complex process influcenced by a combination of factors (i.e. local flow conditions, water depth, bed material, etc.). It has been shown that time-averaged flow patterns, such as secondary currents, and instantaneous fluctuations, such as vortex shedding (i.e. Roy *et al.*, 1999; Thompson, 2006), can both have a significant impact on local scour. However, these relationships have yet to be fully

quantified. As well, as the geometry and size of the scour hole evolves, contributing factors such as turbulence and vorticity, and secondary flow features, may begin to dominate, and accelerate or continue scour beyond its theoretical maximum. Due to the complex dynamics of the scouring process, methods to predict local scour remain essentially empirical.

2.2 Channel bends

The earliest comprehensive studies of flow and sedimentary processes in channel bends began with Rozovskii (1957) and then grew in the 1970s and 80s with physical models by Engelund (1974) and Bridge (1977), and field measurements of natural river bends by Jackson (1976), Bathurst *et al.* (1977, 1979), Bridge and Jarvis (1977), Dietrich and Smith (1984) and Dietrich and Whiting (1989) (to name a few). Together, these studies provide a strong theoretical and experimental basis for the role of planform geometry and secondary currents on the distribution of velocity, boundary shear stress and bed load transport in a meander bend.

Flow in a channel bend can be characterized by the secondary (or helical) flow that develops as a result of the superelevation of the water surface and centrifugal forces imposed on the flow due to the bend geometry (Figure 2.2.1). While secondary flows are a natural feature in all channels (including straight channels) their magnitude and subsequent effects are most pronounced in channel bends. Secondary flow introduces a transverse shear that alters the distribution of shear stress (and turbulent stresses (Jamieson *et al.*, 2010; Chapter 5.1)) across a channel section and consequently influences the distribution of sediment. As the secondary flow interacts with the primary streamwise flow the result is maximum shear stress on the outside of the bank downstream of the channel bend, leading to increased erosion in the outer bank region. The distribution of shear stress, which is affected by the distribution and pattern of fluid velocity on the bed, will also affect the magnitude and location of bed load transport (Dietrich and Whiting, 1989) (Figure 2.2.2). In a sharp meader bend, superelevation is greatest where the primary flow collides with the outer bank, resulting in pronounced downwelling velocities that impinge on the bed and are more likely the main cause of bed scour (Blanckaert, 2010).

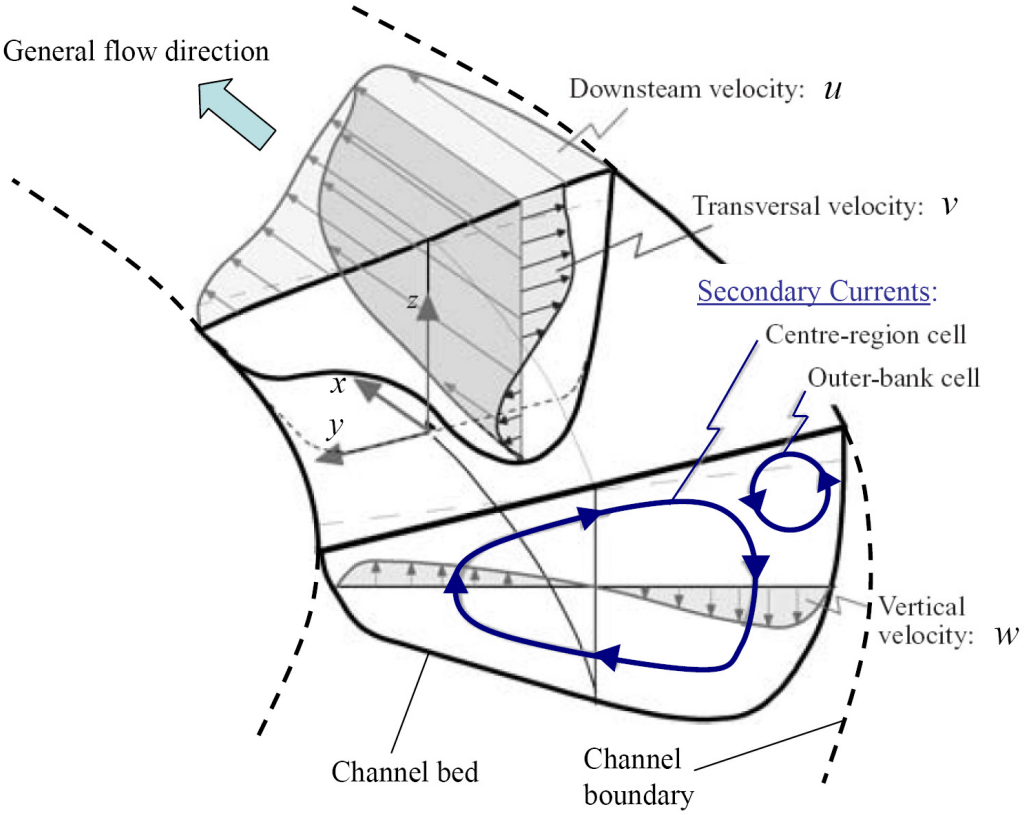

Figure 2.2.1. Definition sketch of flow in a meander bend. [Adapted from Blanckaert and de Vriend (2004)].

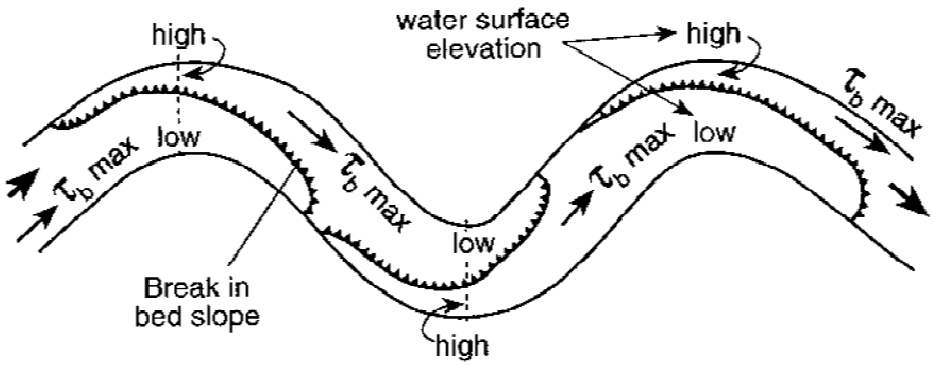

Figure 2.2.2. Distribution of boundary shear stress and water surface elevation in a meandering channel (Knighton, 1998).

A review of experimental research for flow in open channel bends by Blanckaert and Graf (2001) highlights the limited number of mobile-bed experiments, the limited spatial coverage of data collected in each study (typically, measurements were taken at only one cross section in the bend) and the lack of 3-D turbulence data (Dietrich and Smith, 1983 and Odgaard and Bergs, 1988). Experimental mobile-bed bend studies since 2001 include: Matsuura and Townsend (2004), Blanckaert *et al.* (2008), Shiono *et al.* (2008), Zeng *et al.* (2008), Bhuiyan *et al.* (2009 and 2010), Roca *et al.* (2009), Blanckaert (2009, 2010 and 2011), and Jamieson *et al.* (2010) (Chapter 5.1). Some of the latest experimental (Bhuiyan *et al.,* 2009) and numerical (Zeng *et al.*, 2008) investigations of flow and bathymetry throughout a meander bend do not discuss turbulence characteristics in great detail, if at all. Roca *et al.* (2009) provide experimental results of mean velocity and turbulence (turbulent kinetic energy and shear stress) at individual cross-sections through a sharp (186º) mobile-bed open channel bend, with and without an outer bank footing. The most recent studies by Blanckaert (2009, 2010 and 2011) are discussed below.

In their own experiment, which involved detailed acoustic Doppler velocity profiler (ADVP) measurements at one half of a single cross section (the apex of a 120º bend), Blanckaert and Graf (2001) found a reduction in turbulent activity at the outer bank, corresponding to a reduction in the bank shear stress. This result does not appear to conform to the general understanding of maximum shear stress and increased erosion at the outer bank (Figure 2.2.2). The authors also identified a second circulation cell near the outer bank (Bathurst *et al.*, 1977), which has an opposite sense of rotation than the principal secondary circulation cell in the center of the channel (Figure 2.2.1). It is thought that this cell stabilizes the region between the outer bank and the center region cell, thereby keeping the core of high velocity at some distance from the outer bank, thus providing an explanation for the reduced

outer bank shear stress. However, without details of the mean velocity and turbulent flow field at other cross sections, it is not possible to comment on the spatial extent (and therefore relative importance) of these features through the length of the bend. Even with more recent studies, results remain inconclusive (Blanckaert and de Vriend, 2004; Zeng *et al.*, 2008; Blanckeart, 2010), and there is likely more to the role of the counter-rotating cell than we understand. Indeed, Blanckaert (2011) most recently revealed that the magnitude of the outer bank cell shows amplification with increasing bend tightness. As a result, the outer bank cell may play a minor role in bank erosion in mildly curved channel bends but become relatively more important in very sharply curved bends (Blanckaert, 2011). As well, outer bank cells strengthen and widen considerably with increasing roughness (at least for straight channels (Blanckaert *et al.*, 2010)), indicating that the protective effect of this outer bank, counter-rotating cell may be more important in natural meander bends, which have irregular rough banks, than in laboratory experiments.

In Blanckaert's most recent laboratory investigations in a sharp (193º) meander bend (Blanckaert 2009, 2010 and 2011); a more complete picture of the role of secondary flow and turbulence in channel bend dynamics is presented. Blanckaert (2009) found that the curvature-induced secondary flow is the dominant mechanism responsible for altering the high velocity core and increasing turbulent stresses and turbulent kinetic energy through the bend. However, these features could not be related to changes in bed morphology as Blanckeart (2009) considered only a fixed, horiztonal bed. The subsequent experiments (Blanckaert 2010 and 2011) did consider mobile bed conditions and found that while secondary flow is significantly stronger over the deep pool zones (i.e. along the outer bank toe where erosion is greatest), turbulence is not a dominant mechanism with respect to the bed topography and flow redistribution. The maximum turbulence activity was not found

over the deepest parts of the cross sections. Instead, processes that increased turbulence activity were: the flow that collides with the outer bank (where channel curvature is most pronounced); the additional shear due to the secondary flow; and the additional horizontal shear due to the transverse flow gradients (Blanckaert, 2010).

With the exception of the most recently published work by Blanckaert (2010 and 2011), the current literature lacks a comprehensive experimental study of near-bed velocity and turbulent stresses for 3-D flow in a channel bend with a mobile bed. Most turbulence studies have focused on identifying and measuring the principal Reynolds shear stress, in part due to the difficulties of collecting high frequency 3-D turbulence data. Reynolds stresses, which are described by the frequency and magnitude of velocity fluctuations in the streamwise-vertical ($\overline{u'w'}$), streamwise-cross stream ($\overline{u'v'}$) and cross stream-vertical ($\overline{v'w'}$) directions, can be used to detect and characterize coherent turbulent structures in a highly 3-D flow field (Jamieson *et al.,* 2010; Chapter 5.1). Velocity fluctuations in the streamwise and vertical directions (u' and w' respectively) are typically responsible for most of the contribution to the Reynolds shear stress (Lu and Willmarth, 1973), and in the context of geophysical flows, these velocity fluctuations are understood to play an important role in sediment transport dynamics (Leeder, 1983; Best, 1993). The added complexity of secondary flow in a channel bend affects the magnitude and spatial distribution of 3-D turbulent shear stress, making the measurement of each component of Reynolds stress essential. With 3-D turbulence data it is possible to quantify the relative contributions of each Reynolds stress component and other turbulence parameters to describe better the overall characteristics of the 3-D turbulent flow field. Extending these results to analyse the corresponding changes in bed topography sheds new light on the role of turbulent stresses on sediment transport. Furthermore, the

comparison of two experiments, each with the same initial conditions but different durations, provides evidence of the temporal variation in bathymetry, mean flow field and turbulence activity before and at equilibrium scour (Jamieson *et al.,* 2010; Chapter 5.1).

2.3 Stream barbs

The overall goal of stream habitat restoration in incising channel systems should be to accelerate natural processes of channel equilibrium recovery, riparian re-vegetation, and stream-floodplain interaction (Shields *et al.*, 1998). Incorporating bioengineering alternatives (a combination of vegetation and engineered structures) such as stream barbs, instead of traditional bank protection measures, attempts to achieve these goals.

Stream barbs (or barbs) are low-profile linear rock structures that are primarily used to prevent the erosion of stream banks in channel bends. They are a variation of a groyne, similar to spur dikes and bendway weirs. Barbs are typically anchored, in series, to the outside bank in stream bends and they extend in an upstream direction away from the bank into the flow (Figure 2.3.1). This configuration redirects flow away from the outer stream bank and disrupts the velocity gradient close to the outer bank, encouraging sediment deposition adjacent to the barb. These interactions between the flow pattern and the sediment transport around the barb prevent erosion of the bank.

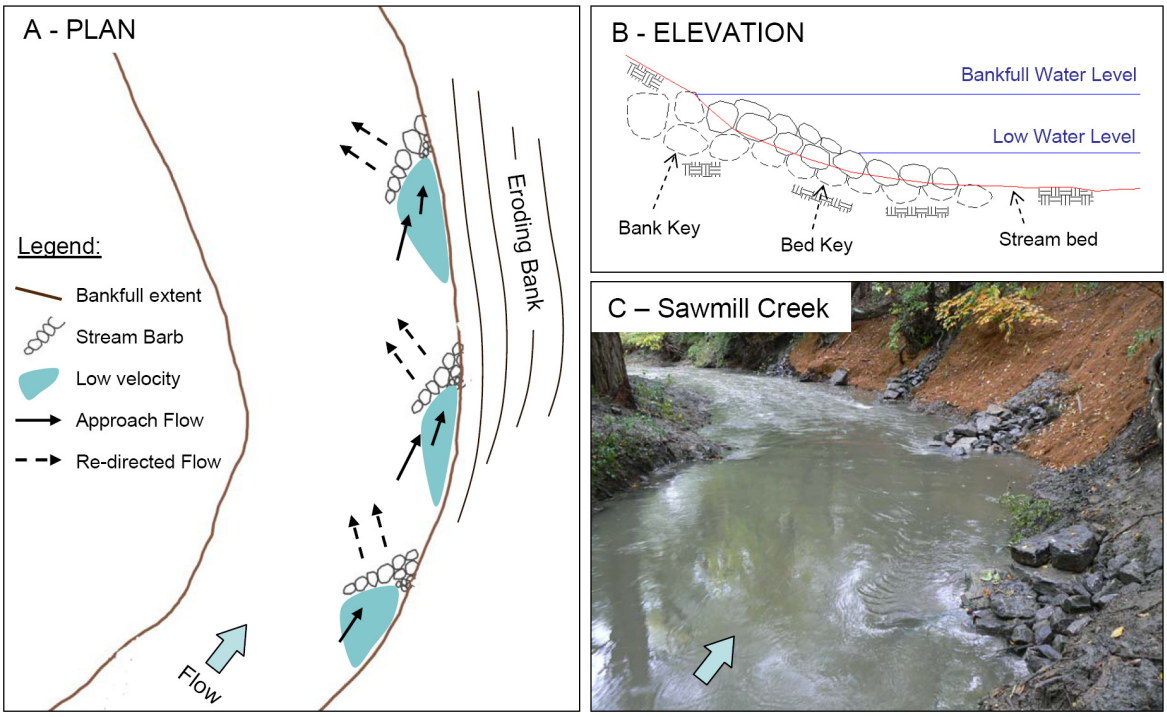

Figure 2.3.1. Typical arrangement of stream barbs in a meander bend. As flow overtops the structure at high flows (B), the structure acts as a weir and re-directs flow towards the center of the channel, away from the outside bank (A) and (C). Water level in (C) is at approximately 50% bankfull.

As well as providing bank protection, these structures promote vegetated stream banks, create resting pools and scour holes for fish habitat, and increase bio-diversity for aquatic species. Despite these benefits, because of their relative novelty as river training structures, stream barbs are not a common means of stream bank protection in Canada and possibly non-existent for semi-alluvial or clay channels.

2.3.1 Case Studies

This section highlights a few examples of the available stream barb (or equivalent) documentation and installation examples in the United States, where the use of these structures is becoming more common.

i. Natural Resources Conservation Service, Oregon

Stream barbs have been used by the Natural Resources Conservation Service (NRCS) in Oregon for river and stream bank protection since the late 1980s (USDA 2005). However, despite their frequent use, limited documentation on long-term performance and specific design criteria were available until the publication in 2000 of a Technical Note for the design of stream barbs by the US Department of Agriculture (USDA, 2000) and most recently the revised version (USDA, 2005). These technical notes are the most comprehensive design documents currently available and incorporate both the results of monitoring barb performance in the field and existing research on barbs and meander bend dynamics. The USDA (2005) technical note recommends that barbs are most appropriate for low gradient alluvial river systems (channel slope less than 2%), with a width to depth ratio greater than 12 and a cobble or gravel streambed substrate. However, this document also states that the use of barbs is not necessarily constrained by these criteria. The initial design of stream barbs at Sawmill Creek was primarily guided by the 2005 USDA technical note (USDA, 2005) and then refined using numerical modelling and analysis for optimizing barb geometry and configuration for the unique site conditions and naturally irregular channel planform.

ii. The Washington State Department of Transportation

The Washington State Department of Transportation (WSDOT) has employed barbs for bank protection in shallow gravel-bed streams along highways and river crossings and in some cases to also improve aquatic conditions (Papanicolaou *et al.,* 2004). Such examples include the Wenatchee River along state route (SR) 2 and SR 207; Newaukum River along SR 5 and SR 508 (South fork); Snoqualmie River along SR 202; and the North Fork of the Toutle River along SR 504 (Papanicolaou *et al.,* 2004). Based on their experience, the WSDOT recommend that barbs be used for mild-sloped, gravel-bed streams in the Pacific Northwest (Fox *et al.,* 2005b). However, the department has not tested the use of barbs in other soil or sediment types. In collaboration with the University of Iowa, the WSDOT have also carried out experimental investigations in the laboratory (i.e. Papanicolaou *et al.,* 2004 and Fox *et al.,* 2005a and 2005b) to investigate in detail (i) the local flow regime around a single submerged permeable barb (with and without a mobile bed); and (ii) the evolution of local scour around the barb under clear water scour conditions. These studies are discussed in more detail in Chapter 2.3.2.

iii. Carson River, Nevada

The Carson River in Nevada suffered considerable bank erosion and damage following a 100-year flood event in 1997. One meander bend in particular, which was cut back by approximately 4.5 m during this flood event, was treated with a number of different types of bioengineering methods, including the use of a series of stream barbs and re-vegetation (Piper *et al.,* 2001). [A number of different methods were implemented so that the site could serve as a demonstration project illustrating the different methods of bank protection available, for classroom instruction, workshops, etc.]. Five stream barbs were constructed,

with various planting and vegetation added between the barbs for additional protection. Examples of the vegetative treatments included; vertical bundles of willow cuttings, brush mattresses, and brush layering. Some results from the first two years of post construction monitoring at the site are available (Piper *et al.*, 2001) and the general conclusion was that the installation of stream barbs proved to be a very effective way to protect stream banks. The barbs deflected the flow away from the bank regardless of varying water levels, while creating pockets of calm water, sediment deposition and vegetative cover (from bioengineering treatments) between the barbs. The accumulation of sediment between the barbs and the movement of the thalweg away from the outer bank contributed to regaining land and habitat. Piper *et al.* (2001) recommend that for any such bioengineering projects, a monitoring program after installation should be conducted, for a minimum of 2 years or preferably until a substantial flood event occurs.

iv. Harland Creek, Mississippi

Similar to the Carson River study, three different bank protection measures (stone toe protection, willow posts and spur dikes) were added between 1991 and 1993 along a 4 km reach of Harland Creek in Mississippi to stabilize eroding banks and improve aquatic habitat (Derrick, 1997; Shields *et al.,* 2000). Harland Creek is a meandering sand- and gravel-bed stream where average bank migration rates were estimated to be 4.3 m per year (based on air photo comparisons) (Shields *et al.,* 2000). The stone spur dikes (angled 10º to 30º upstream) were added to three different sections along the 4 km reach and together with the other two types of bank protection, were studied over a 3-year period to monitor habitat and fish community response to the three different bank protection measures. Results indicated that while the reaches stabilized with spurs supported 1.6 to 2.1 times as much biomass per unit

channel length than the reaches with other treatments (and produced a greater volume of pool habitat); species diversity and fish abundance did not differ among treatments.

Summary

The large number of case studies that are available for the West and Midwestern United States, where alluvial (sand and gravel) rivers predominate, emphasizes the absence of stream barbs (or equivalent) as an option for bank protection measures in semi-alluvial streams. How well these structures perform and what their long term effects on morphology and habitat will be will largely depend on the local sediment transport characteristics, which are inherently different when cohesive sediments are present: we may no longer have the supply of alluvial sediment upstream and the mechanisms of soil erosion and transport are more complex. Further, these case studies all consider rural or semi-rural streams. The impact of urbanization (i.e. increased runoff and shorter time of concentration) on the functionality of stream barbs, where the estimation and behaviour of bankfull flow conditions is critical for successful barb design, appears to have been excluded from both previous field testing and monitoring, and design documentation. The installation of stream barbs at Sawmill Creek, Ottawa presents a unique opportunity to study the effects of these structures on a predominately clay bed and bank channel, in a heavily urbanized watershed.

2.3.2 Field and Laboratory Research

A number of different laboratory experiments on submerged structures (stream barbs, submerged groynes, spur dikes, bendway weirs, vanes, etc.) in open channel flows have been performed and the most important are summarized in Table 2.3.1. Similarly, a summary of field experiments on submerged structures in open channel flows is provided in Table 2.3.2.

The summaries provided in Table 2.3.1 and Table 2.3.2 highlight a few of the gaps in the current literature: (1) the limited number of studies considering a meandering or channel bend planform, where the use of these structures is most relevant; (2) the lack of detailed velocity and turbulence measurements; (3) the lack of coupled mobile-bed studies with comprehensive velocity and turbulence measurements. The experimental studies excluded from Table 2.3.1 include non-submerged (or emergent) groyne studies (Uijttewaal *et al.,* 2001; Weitbrecht *et al.,* 2002; Sukhodolov *et al.,* 2002); scour depth studies at abutments (Melville, 1992; Lim, 1997) and spur dikes (Garde *et al.*, 1961; Gill, 1972; Kuhnle *et al.*, 1999); those with a focus on numerical simulations (McCoy *et al.* 2008; Koken and Constantinescu, 2008a and 2008b) and finally those with a habitat objective (Biron *et al.*, 2004), where the prevention of stream bank erosion was not a principal objective and therefore was not investigated in detail.

Flume experiments by Kuhnle *et al.* (1999, 2002 and 2008) involved a single spur dike orientated perpendicular (Kuhnle *et al.,* 1999 and 2008) and angled (Kuhnle *et al.,* 2002) to the flow along a straight laboratory sand-bed channel. The earlier studies (1999 and 2002) characterized the volume of the scour hole at the tip of the spur dike, while the 2008 study measured the flow field in detail over a fixed, flat bed. Kuhnle *et al.* (2008) found that the 3-D flow separation at the spur dike yielded forces on the bed that were significantly different from non-submerged vertical obstructions that have been measured in other studies. The maximum bed shear stress adjacent to the dike was found to be approximately 2.7 times the approach flow value, which is substantially less than that found for emergent flat plates mounted perpendicular to the flow. Koken and Constantinescu (2008a) also found the largest bed shear stress values to be near the tip of the spur dike.

Table 2.3.1. Summary of laboratory research on submerged structures in open channel flows. Studies marked with an asterisk (*) included 3-D numerical modelling.

Literature	*Channel Planform*	*Structure Type/Name*	*No. of Structures*	Θ_b (º)	*Bed Material* d_{50} *(mm)*	*Mobile Bed?*	*Measuring Grid*	*Measurement Device*	*Flow and Turbulence Measurements*
Kuhnle *et al.* (1999)	Straight	Spur Dike	1	90	0.8	Yes	h/10 x B/1 x L/1	Pitot Tube	$\overline{U}$
Johnson *et al.* (2001)	Straight	Vane	2	20, 25, 35	1	Yes	(NA)	ADV meter	$\overline{U}$
Kuhnle *et al.* (2002)	Straight	Spur Dike	1	45, 90, 135	0.8	Yes	h/10 x B/1 x L/1	Pitot Tube	$\overline{U}$
Matsuura and Townsend (2004)	Single bend	Barb	3 and 4	20, 30, 40	0.78	Yes	(NA)	-	-
Fox. *et al.* (2005a)	Straight	Barb	1	50	Fixed rough bed[1]	No[1]	h/3 x B/24 x L/15	ADV	$u, v, w, \overline{\sqrt{u'_j{}^2}}, \overline{u'_j u'_k}$
Fox *et al.* (2005b)	Straight	Barb	1	50	Fixed rough bed	No	h/3 x B/24 x L/15	ADV	$u, v, w, \overline{\sqrt{u'_j{}^2}}, \overline{u'_j u'_k}, T_s$
Jia *et al.* (2005)*	Single bend	Submerged Weir[2]	1	70	0.43	No	h/3 x B/9 and B/16 x L/10	ADVP	u, v, w
Uijttewaal (2005)	Straight	Groynes[3]	2	90	Fixed bed	No	1.5 x 1.5 m (5 cm resolution)	PTV	u, v, w, u_j'
Kuhnle *et al.* (2008)*	Straight	Spur Dike	1	90	0.8	Yes	h/9 x B/12 x L/28	ADV	u, v, w, u_j'
Bhuiyan *et al.* (2009 and 2010)	Meandering	Vanes	1 and 4	20, 30, 60	1.5	Yes	Sections at 1/64 wavelength[4]	ADV	$u, \overline{U}/h, \overline{\sqrt{u'_j{}^2}}$

where θ_b is the projection angle of the structure to upstream bank; h is water depth and B and L are the width (cross-stream direction) and length (streamwise) of the measuring grid; $\overline{U}$ is depth averaged velocity; u, v, w are streamwise, cross-stream and vertical velocity respectively; $u'_j u'_k$ ($j, k = u, v, w$) are turbulent stresses; T_s is the moving-average timestep in eddy decomposition; NA stands for Not Applicable; ECM is an electro-magnetic current meter; ADV is an acoustic Doppler velocimeter; ADVP is an acoustic Doppler velocity profiler; PTV is particle tracking velocimetry.

[1] Mobile bed conditions were tested separately and without corresponding flow measurements. [2] Constructed out of 2 cm gravel. [3] Emerged and submerged conditions were tested.
[4] Velocity data are only presented in the 2010 paper.

Table 2.3.2. Summary of field research on submerged structures in open channel flows. (See Table 2.3.1 notes for symbol details).

Literature	*Channel Planform*	*Structure Type/Name*	*No. of Structures*	θ_b	*Bed Material* d_{50} *(mm)*	*Mobile Bed?*	*Measuring Grid*	*Measurement Device*	*Flow and Turbulence Measurements*
Shields *et al.* (1998)	Straight and meander	Stone Spur	11 (straight) 6 (meander)	90º	0.4-10	Yes	h/1 x B/25 x L/5	ECM	$\overline{U}$
Shields *et al.* (2006)	Meandering	Large Wood	72[1]	75º	0.2-0.3	(NA)	h/1 x B/2 x L/2	AD depth-velocity logger	$\overline{U}$
Carré *et al.* (2007)	Straight	Deflectors	2 pair sets	~ 90º	90	Yes	h/1 x (BxL)/65	ADV	u, v, w, u_j'
Abad *et al.* (2008)	Single bend	Bendway Weir	5	variable	unknown	No[2]	L/4 [3]	ADV	u, v, w, u_j'

[1] Constructed on concave eroding banks along a 2 km long study reach.
[2] Data collected for only low flow conditions.
[3] Details concerning measurement density are lacking.

Fox *et al.* (2005a and 2005b) also considered a single submerged groyne (in this case angled 50º with the upstream bank) along a straight laboratory channel, but separated their measurements of velocity and scour. First, detailed velocity measurements of the flow characteristics around the barb for a fixed bed were performed, to describe the redistribution of the flow in the vicinity of the structure. Next, a mobile gravel bed was employed to measure maximum scour depth and equilibrium bathymetry for the same flow conditions.

Most recently, Bhuiyan *et al.* (2010) present velocity and turbulence measurements in a meandering channel with and without a series of "bank-attached" vanes, constructed of 2 cm wide plywood, which slope from bankfull height at the outer bank down to the bed. Unlike previous laboratory studies, live bed scour conditions were simulated, which allowed testing of the functionality of installing the vanes after equilibrium scour in the meander bend was reached. Under live bed conditions, the performance of vanes to reduce scour along the outer bank through deposition in the vicinity of the vanes could be studied.

Fox *et al.* (2005b), Kuhnle *et al.* (2008) and Bhuiyan *et al.* (2010) present the most rigorous investigations of flow field dynamics around a submerged structure to date, with Fox *et al.* (2005b) developing an eddy taxonomy methodology to identify small- and large-scale eddies in the vicinity of an upstream-orientated barb. However, Fox *et al.* (2005b) found that while this method provided conclusive spatial and temporal scales of small- and large-scale eddies at locations where the barb had less impact on eddy generation (i.e. the approach flow and outer extent of the shear layer), the results were "more ambiguous" within the overtopping shear layer and downstream stagnant flow regions, which is where the barb presence dominates eddy generation. The combination of multiple eddy scales and strong secondary currents (generated in this case by the overtopping, plunging action) complicated

the analysis of the spatial and temporal eddy scales downstream of the barb obstacle, thereby increasing the uncertainty of the results.

Matsuura (2004) tested the effectiveness of different barb arrangements in series (or barb groups), in both 90º and 135º channel bends, with a mobile sand bed. For a range of hydraulic conditions, where several key parameters were varied (including, flow depth, maximum barb height, barb angle, and location of the first, upstream-most barb), the resulting bathymetries generated by the different barb groups were compared. This study provided useful results for understanding the effects of different barb parameters on the reduction of near-bank erosion and the location and magnitude of scour and deposition around the barbs. However, these experiments were unable to characterize the flow field due to a lack of velocity data. As well, the experimental barbs were constructed out of a fine mesh (approximate width < 2mm), essentially creating a two-dimensional, permeable structure. Preliminary tests showed that any increase in width or the use of a more trapezoidal cross section would result in severe local scouring beyond the available depth of sand in the channel (just as Kuhnle *et al.* (2008) predicted with their measurements of bed shear stress, and as we have found in our current experiments). This is also a limitation of Bhuiyan *et al.'s* 2009 and 2010 studies using thin, 2 cm-wide plywood vanes. The extent of local scour (depth and volume) adjacent to a submerged structure will depend on the geometry and size of the structure (in addition to local flow features) and every effort should be made to reproduce realistic scales of structure geometry in the laboratory. The barbs built for the current laboratory study were constructed of solid and slightly permeable material (loose stone), with a roughly cross-sectional trapezoidal shape, representing a realistic model of field-scale barbs (Figure 2.3.2). With this form of barb construction, each barb stone was free to move with respect to the others, thereby modeling the same conditions for riprap

stone adjustment in the field. While undermining of the structure may cause instability and lead to failure, the freedom of movement provided by the loose stone provides a protective measure from excessive undermining or scour. For example, as the local scour depth at the barb tip increases, rocks at the tip may fall into the scour hole, thereby armouring the scour hole from further erosion. To illustrate typical barb construction and performance, photos of the before and after conditions for individual barbs in two different experimental trapezoidal runs (TR5 and TR10) are shown in Figure 2.3.2. In the first case, TR5 barbs were larger and individual rocks experienced more shifting and movement into the neighbouring regions of scour than the smaller barbs in TR10.

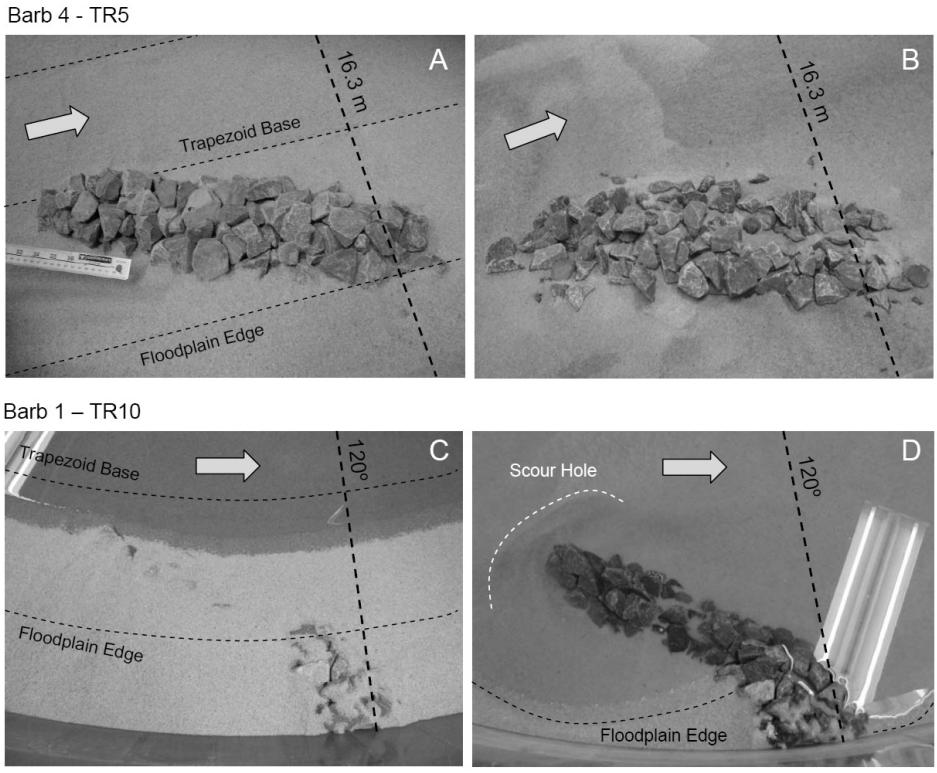

Figure 2.3.2. Photos of constructed stream barbs for Barb 4 in TR5 (A and B) and Barb 1 in TR10 (C and D). Photos were taken before (A and C) and after (B and D) equilibrium scour was reached. Water levels in C and D represent filling and draining conditions respectively. Flow is from left to right.

With the exception of Abad *et al.* (2008) and Bhuiyan *et al.* (2010), who present results for non-overtopping conditions (Abad *et al.*, 2008) or at only select cross-sections through the meander bend (Bhuiyan *et al.*, 2010), to date the most detailed flow measurements have been for a single structure only and one that was installed along a straight section (Fox *et al.*, 2005b and Kuhnle *et al.*, 2008). What is the interaction between consecutive barb structures in a channel and what are these effects to the local flow field? In typical applications, barbs are placed in series along the outside of a channel bend and their spacing, relative to channel dimensions and degree of channel curvature, is a critical parameter in their successful performance (USDA, 2005). Depending on the level of submergence and the amount of constriction caused by the barb (i.e. vertical flow separation), water levels upstream and downstream can be affected, thereby altering the local flow conditions between consecutive structures, not to mention the redistribution of flow around the first barb before it approaches the next. The helical (secondary) flow generated in a channel bend will alter the magnitude and direction of velocity as the flow approaches the barb and as a result the flow over and past the structure. In turn, this will play a role in local flow field characteristics and ultimately how the structure functions to disrupt velocity and shift the thalweg to the center of the channel, away from the outside bank.

Matsuura (2004) found that, although scouring in the 135º bend without barbs was significantly greater than in the 90º bend (tighter bends are known to increase water surface superelevation and secondary flow strength (Knighton, 1998)), barb groups in the 135º bend performed better. Maximum scour reduction in the 135º bend was 85.9% compared to 74.7% for the 90º case, for the same flow conditions and barb group arrangement. (Maximum scour reduction for the 90º bend was 79.6% for a different barb group that had a greater upstream barb angle). However, it should be noted that it is assumed here that “maximum scour

reduction" refers to total scour in the channel, since with rigid, vertical plexiglass walls it is not possible to evaluate the reduction in scour of the outer bank. This suggests that in this case, the percent reduction may not be a useful metric since some scour at the barb tip is desirable. In fact, of the relevant laboratory-scale mobile bed studies that have been performed (Table 2.3.1), none have studied bank erosion – the initial conditions of all mobile bed experiments was a horizontal (flat) bed with rigid vertical side walls. In this thesis, a sand-bed with a uniform trapezoidal-shaped cross-section was installed inside a flume having a rectangular cross-section. With this arrangement, both the bed and banks of the channel are composed of sand and subject to scour.

Minor (2006) and Minor *et al.* (2007b) used a 3-D numerical model (SSIIM) to examine the turbulent flow field and associated sediment transport for the same barb group arrangements as Matsuura (2004), by calibrating the numerical model's bed topography results to that measured by Matsuura (2004). As expected, maximum bed shear stresses were found to correspond to the observed regions of maximum scour and velocity. As well, velocity vectors over and around the submerged structures illustrated the plunging action of the flow over the structure and flow separation at the barb tip, which was observed in previous studies using dye (Fox *et al.,* 2005a). Select results were further analysed (Minor *et al.,* 2007a) to understand better the specific contributions of particular aspects of the flow field, such as vorticity and time-averaged stream traces, to changes in channel bathymetry. These results provided a comprehensive view of the 3-D characteristics of the flow for a series of barbs in a channel bend. This analysis demonstrated that the pattern and magnitude of erosion and deposition were dependent on the characteristics of the flow field, and perhaps most significantly, vorticity. The location of maximum vorticity magnitude (and in particular

z-vorticity), which was found at the barb tips, corresponded with the locations of maximum scour (Minor *et al.,* 2007a).

By definition, stream barbs are submerged structures that slope away from the bank along the channel bed, with their highest crest elevation nearest to the bank typically corresponding to the bankfull water level. With this arrangement, at high (channel forming) flows the structure is continuously overtopped, which results in a plunging flow over the structure. Bhuiyan *et al.* (2010) found that vanes sloping to the bed from bankfull level at the bank showed better performance than low level ones. Unlike typical groyne structures, which are traditionally emergent (i.e. no regular overtopping) and perpendicular to the flow, the vertical separation of the flow is less significant for barbs because they are submerged and orientated in a more streamline direction (i.e. not perpendicular to the main streamwise flow direction). If a structure (or object) obstructs a high Reynolds number flow, due to the significant velocity gradient created and the corresponding low pressure, the boundary layer developed against the object will separate from the wall. The separated flow will generate a downstream shear layer with the main flow and vertically-orientated vortical structures may develop (i.e. rotation about the vertical axis or z-vorticity). Conversely, the plunging of the flow causes regions of high velocity above the barbs and low velocity between the barbs. This velocity gradient can induce a cross-stream (transverse) mixing which will interact with the primary secondary flow cell (developed as a result of bend geometry), potentially deflecting the secondary flow (along with the maximum velocity core) towards the center of the channel, away from the outer bank. Both Bhuiyan *et al.* (2010) and (Jamieson *et al.*, *submitted – a*; Chapter 5.2) found that plunging action generated a counter-rotating secondary flow cell, but its impact on reducing outer bank erosion was inconsistent.

By comparing the patterns and magnitude of scour and deposition around the barbs with detailed contours of velocity, vorticity and turbulence, it may be possible to estimate the relative magnitude of these flow properties required to generate a scour hole or initiate deposition. Discerning the relative contributions of these to local scour will lead to better understanding and prediction of the changes in bed level for different flow fields associated with different barb geometries and arrangements in series. While Minor *et al.* (2007a) discussed the relationship between local scour and vorticity, the simulated (numerical) results were never validated with measured velocity data. Validation of both the flow field and bathymetry are crucial before any significant relationships between flow field dynamics and sediment transport are revealed through numerical simulation.

The laboratory stream barb investigations in this thesis present the first experimental results to describe the spatial variability of the complex turbulent flow field associated with a series of submerged barbs installed in a channel bend. The most recent studies of fluid and sediment dynamics around spur dikes and barbs have considered straight laboratory channels (Fox *et al.,* 2005b and Kuhnle *et al.,* 2008) and non-simultaneous measurements of flow field and bed morphology (Bhuiyan *et al.*, 2009). The one exception is the recent study of thin bank-attached vanes by Bhuiyan *et al.* (2010). We are not aware of any laboratory or field studies that have investigated the spatial variation in three-dimensional (3-D) turbulent flow structure and associated patterns of scour and deposition around a series of upstream-angled rock stream barbs in a channel bend, where in practice these structures are most typically deployed. The systematic study of the effects of in-stream structures on local flow and sediment transport processes under controlled conditions in a large-scale laboratory flume are rare. Such investigations are critical if we are to understand these complex processes and provide the necessary data for validating numerical models. This is especially true for mobile

bed conditions, where data are most lacking, despite being vital for linking the influence of flow patterns and turbulence to sediment transport processes.

The goal of the laboratory barb studies is to confirm the numerical modelling results of Minor *et al.* (2007a) and also demonstrate the role of three-dimensional flow, turbulence and vorticity on the development of local scour. This research provides quantitative measurements of the 3-D flow field and turbulence in the vicinity of a series of barbs in a channel bend. During overtopping conditions at high flows, a stream barb causes flow separation, which significantly influences the nature of the vortices around the structure. This leads to some significant differences in the geometry of scour holes for in-stream structures with overtopping flow (Kuhnle *et al.,* 1999 and 2002). These observations need to be investigated further. It is not known what impact the plunging (overtopping) flow has on maximum scour depth and hence the function and reliability of different barb shapes, sizes and arrangements. Understanding the flow in detail (i.e. the scale and structure of the vortical and turbulent motions) should provide a better means of predicting the resulting bed level changes for various barb geometries and orientations. It is expected that these results will lead to: (i) improved design of barb structures, (ii) provide necessary data for better validation of numerical simulations of turbulent flow and sediment transport for submerged in-stream structures, and (iii) a better understanding of the role of these coupled processes in general. These results have implications for employing other similarly submerged in-stream structures and for understanding natural fluvial features where similar plunging flow conditions (or horizontal flow separation) are found; such as, forced riffle-pools and dune fields.

2.3.3 Biological and Ecological Significance

The objectives of many river and stream restoration projects do not stop at the physical and morphological requirements, such as reducing bank erosion and maintaining channel stability. Many different types of in-stream structures and features (such as ramps, weirs, groynes, boulders etc.) are added specifically to enhance the quality and quantity of aquatic habitat. Habitat structures are typically designed to increase fish production by providing a suitable combination of physical conditions for spawning and rearing, foraging and reducing predation risk. To achieve this, successful habitat structures are likely to provide three important features: (1) velocity refuge, (2) visual isolation, and (3) overhead cover (Fausch 1993). Stream barbs can provide one or a combination of these features depending on their construction. Not only is it possible that vorticity plays an important role in sediment transport dynamics, but it also plays a crucial role in flow complexity, a necessary component of functioning stream habitats.

Stream barbs provide velocity refuge in the upstream region behind the barb, where velocity is low. If a scour hole forms near the tip of the structure, additional refuge may be found in this deeper flow region. Structures that afford velocity refuge allow fish to hold low-velocity positions adjacent to regions of higher velocity and may thereby maximize their energy intake from drifting invertebrates while minimizing the cost of swimming to maintain position (Fausch 1993). The upstream and downstream regions on either side of a barb may also provide some visual isolation. Visual isolation increases habitat availability because it allows greater densities of fish to occupy a given area without risking harm from each other due to natural hierarchical dominance or territorial conflict (Mesick 1988). Finally, the use of stream barbs over traditional bank protection measures such as riprap promotes a vegetated stream bank, which could increase overhead cover near the bank, depending on the size and

type of vegetation used. Overhead cover reduces predation risk by providing hiding places for fish from terrestrial and aquatic predators through reduced visibility and shade from above (Fausch 1993).

Earlier research, including that of Everest and Chapman (1972), relied on observation to describe the average characteristics and optimum conditions of water depth and velocity for desirable habitat. However, these did not necessarily explain why certain species of fish selected certain locations over others. More recent studies are beginning to rely on direct experimental measurement, and at greater temporal and spatial resolution, in order to better quantify fish behaviour and fish habitat. In particular, studies have shown that spatial habitat diversity, associated with complex flow features such as eddies, wakes and secondary flows, support higher levels of biodiversity (Gorman and Karr 1978; Harper and Everard 1998). These different types of flow features are important for making available a diverse set of habitat conditions across a range of scales, such that stream organisms may rest, feed, reproduce and take refuge (Fausch 1993 and Shields and Rigby 2005).

Using flow variables such as kinetic energy gradients, vorticity and circulation, which were identified by Crowder and Diplas (2000 and 2002) as possible metrics of stream habitat quality based according to flow variability (i.e. flow patterns and velocity gradients), Shields and Rigby (2005) used 3-D velocity measurements to describe and characterize stream habitat. An acoustic Doppler current profiler (ADCP) was used to collect 3-D velocity data in four reaches of the Little Tallahatchie River in northern Mississippi. These reaches were selected to represent three distinctly different flow regimes: (i) downstream of a major flow obstruction (low weir), (ii) downstream from the apex of two bends, and (iii) within a long, straight reach created by channelization. The velocity data were used to calculate spatially-dependent variables (kinetic energy gradients, vorticity and circulation). The authors found

that, while the ADCP has great potential for detailed measurements of aquatic habitat suitability (particularly at the reach scale), it was difficult to collect information near the bed and banks and at the water surface – a known limitation of acoustic instrumentation in the field. Most importantly, the authors note that detailed biological studies are needed to investigate links between ecological processes and the types of flow heterogeneity that can be measured.

One study in Arctic Canada (Jones and Tonn, 2004) examined the effectiveness of four types of habitat structures (ramps, V-weirs, vanes and groynes) at increasing the productive capacity for Arctic grayling (*Thymallus arcticus*) and other fish in a 3.4 km artificial stream, which had been created as compensation for fish habitat lost due to nearby development. The authors used a modified before-after-control-impact (BACI) design to quantify changes in fish density, biomass and growth at two spatial scales; in both the immediate area of each structure and for the artificial stream as a whole. Overall, the authors found contrasting results at the two spatial scales. When comparing densities, biomass and fish growth at the in-stream structures relative to nearby reference sections, it was clear that the structures increased local densities, especially earlier in the season. In contrast, there was no evidence of a stream scale enhancement of Artic grayling in the artificial stream, in either an absolute sense or relative to the performance of reference streams. These results suggest that the addition of habitat structures merely redistributed the fish – they preferred the structurally enhanced sections over the featureless reference sections – without any actual increase in total numbers, growth or survival. Similarly, Shields *et al.* (2000) found that reaches stabilized with stone spurs supported significantly higher densities of large fish and higher levels of fish biomass per unit channel length than reaches with other bank treatments. However, without an assessment of before and after conditions, it is impossible to comment

on whether or not these higher densities of fish and biomass were also merely due to a redistribution of fish to more favourable conditions in the reach, rather than causing a net overall increase to the reach as a whole. Jones and Tonn (2004) suggest that the lack of available organic matter to benthic fauna and fish that was identified on the artificial stream may have been a limiting factor to net growth. This, the authors suggest, emphasizes the importance of riparian vegetation and other functional biotic components for stream ecosystems as factors contributing to stream restoration.

Jones and Tonn's (2004) study is intriguing, as it demonstrates that local features beyond flow variability (i.e. complex flow patterns and velocity gradients) are a significant determinant to successful in-stream structure function and habitat restoration. In addition to complex flow features supporting higher levels of biodiversity, the availability of ecological habitat features, such as organic material, may be equally (if not more) important to supporting fish growth (both number and size). What appears to be missing from many studies of aquatic habitats is the simultaneous measurement and coordinated analysis of flow field heterogeneity and fish behaviour. What impact will the stream barbs at Sawmill Creek have on fish populations and behaviour?

An extensive aquatic habitat monitoring plan by the City of Ottawa's Water Environment Protection Program (WEPP) has been incorporated into the stream barb project at Sawmill Creek, to provide quantitative measures of the environmental impact stream barbs may have to the study site. The monitoring plan has been specifically designed to determine the existing conditions of the aquatic ecosystem within Sawmill Creek, i.e. prior to the construction of stream barbs, to provide a baseline with which to compare post construction conditions. The monitoring will assess temporal and spatial fish and fish habitat conditions

throughout the study area over a three-year period (2008-2010), before and after barb construction.

3 Sawmill Creek

3.1 Design of stream barbs for field scale application at Sawmill Creek, Ottawa

---

Jamieson, E.C., Rennie, C.D. and Townsend, R.D. (2009). Design of stream barbs for field scale application at Sawmill Creek, Ottawa. *WIT Transactions on Ecology and the Environment (Proceedings of River Basin Management V*, Malta, September 2009), 124, pp. 281-292.

3.1.1 Abstract

A three-dimensional numerical model *Simulation in Intakes with Multiblock option* (SSIIM) was used to model the effects of placing a series of barbs along an unstable section of Sawmill Creek, a small urban stream in the city of Ottawa, Canada. Stream barbs (a type of submerged groyne) are low-profile linear rock structures that prevent the erosion of stream banks by redirecting high velocity flow away from the bank. As they can be built at a relatively low cost and also provide significant ecological benefit, these structures are an important and relatively new method of stream bank protection. The numerical model was used to assess various design alternatives for a series of seven stream barbs at two consecutive channel bends requiring stabilization measures along their outer banks. Design criteria were principally based on the goals of reducing local velocities, shear stress and subsequent erosion at the outside bank of each bend, and on moving the thalweg away from the (existing) outside bank regions towards the centre of the channel. This paper reports on (i) the unique site conditions and environmental protection requirements, (ii) the results of the numerical simulation, and (iii) the design methodology.

3.1.2 Introduction

Stream barbs (a type of submerged groyne) are low-profile linear rock structures, which are generally located as a series of two or more structures on the outside bank of meander bends, and which prevent the erosion of stream banks by redirecting high velocity flow away from the bank. The construction of stream barbs in Sawmill Creek, Ottawa, Canada will serve as a demonstration project for the use of barbs as a new bank stabilization technique that will contribute to the rehabilitation of urban creeks while reducing erosion threats to property and infrastructure. Stream barbs are a relatively low cost technique for bank protection, as compared to traditional revetment, due to reduced construction material requirements and maintenance costs. Moreover, as well as providing bank protection, these structures promote vegetated stream banks, maintain deep pool habitats through the development of scour holes at barb tips and increase bio-diversity for aquatic species (Shields *et al.*, 1998; Engelhardtm *et al.*, 2004).

Stream barbs have been used by the United States Natural Resources Conservation Service (NRCS) in Oregon since the late 1980s (USDA, 2005) and by the Washington State Department of Transportation (WSDOT) (Papanicolaou *et al.*, 2004) for river and stream bank protection along highways and river crossings and in some cases also to improve aquatic conditions, especially in shallow gravel bed streams. However, despite their relatively extensive use, documentation of long-term performance and specific design criteria are limited. The most authoritative guideline is provided by the United States Department of Agriculture (USDA, 2005), which is recommended for meandering, alluvial river systems, and which was followed closely when establishing initial barb layouts for the present design at Sawmill Creek.

As a field test site, Sawmill Creek presents a unique opportunity to study the interesting flow field and sediment transport processes associated with a submerged structure. The submerged nature of these structures and the fact that they are typically placed in channel bends (where secondary flow dominates) creates a unique combination of vertical flow separation and overtopping (plunging) flow conditions, causing large and small scale three-dimensional (3-D) eddies to form. Quantifying the influence of these 3-D turbulent eddies on the bed will improve predictions of sediment transport and as a result, will allow for better estimates of scour, bank erosion and overall channel morphology.

The chosen field test site also has the added complexity of having a clay bed and banks, which will allow further study of the erosional behaviour of cohesive soils, a topic which remains poorly understood. Clay bed channels are common in the Ottawa area and it is anticipated that successful implementation of stream barbs at this site will provide a good opportunity for promoting this method of bank protection at other sites in the municipality. The objective of this research is to use the Sawmill Creek test site as a case study for stream barb design and installation practices with the ultimate goal of developing design guidelines for routine employment of these structures to stabilize banks and improve aquatic habitat for semi-alluvial (clay) channels.

Site Information

Sawmill Creek is located in the City of Ottawa, Canada, south of the Rideau Canal and drains north into the Rideau River. It has a total watershed area of 27.7 km^2 and an approximate length of 10 km (Parish Geomorphic, 2005). Sawmill Creek has a highly urbanized watershed that responds quickly to rainfall, experiencing large and rapid fluctuations in discharge and water depth following heavy rainfall events.

A 50 m section of Sawmill Creek (which receives approximately 90 % of the contributing watershed area) is experiencing bank erosion and mass wasting at two particular bends, referred to here as bend 1 and bend 2 (Figure 3.1.1). The proposed remedial work will provide measures for both bank stabilization and bank protection through the construction of a series of submerged stream barbs coupled with vegetative planting.

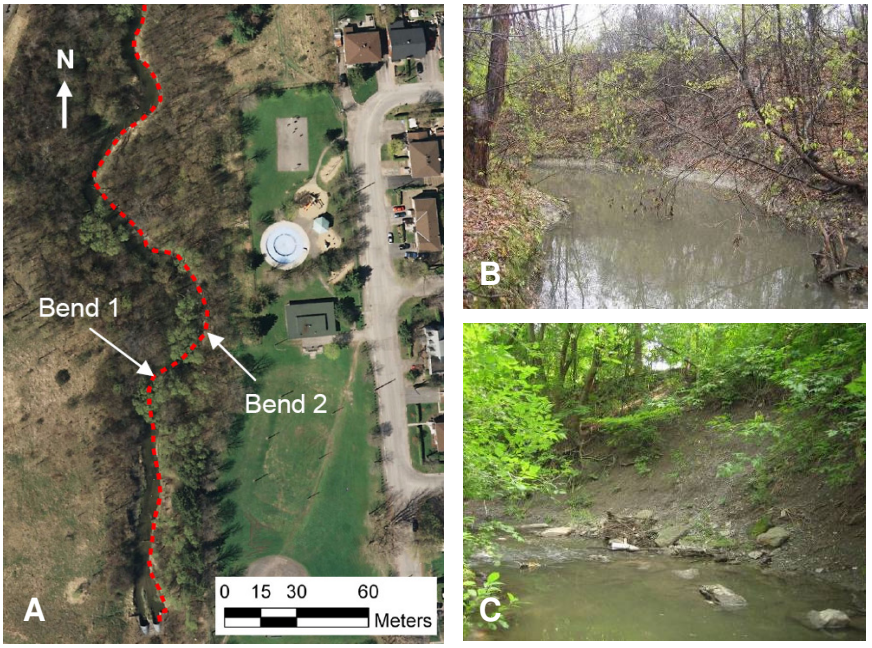

Figure 3.1.1. (A) Aerial photo of the Sawmill Creek study area; red dashed line indicates right bank and flow is from south to north. (B) Bend 1 looking upstream, and (C) outside bank of bend 2 looking downstream.

Sawmill Creek is a predominately clay bed channel, with a mix of coarse sand and gravel in the riffles. In the bend 2 section, a number of large boulders dominate and form a riffle, close to the apex of the bend (Figure 3.1.1 C). In typical river morphology, larger sediment sizes and an established riffle at the apex of the bend is unexpected. It is speculated that these boulders are the remnants of previous bank hardening measures, which over time fell from

the steep side slope into the channel to create the riffle. (Pieces of concrete and asphalt found in the riffle area support this hypothesis).

Low flow and bankfull water depth and channel width at each bend apex are given in Table 3.1.1. Low flow and bankfull conditions were designated based on field observations and hydrological data from a gauging station located approximately 1.2 km downstream of the site. Hydrological data were obtained for the period of 2002-2007 (excluding 2003) and indicate that the average base (low) flow is approximately 0.20 m^3/s.

Table 3.1.1. Summary of flow conditions at the study site. (*Q* is discharge; *WSE* is water surface elevation; *h* is water depth; *B* is water surface width).

Location	Condition	*Q* (m^3/s)	*WSE* (m)	*h* (m)	*B* (m)
Bend 1 apex	Low flow	0.20	65.0	0.70	5.0
Bend 1 apex	Bankfull	9.0	65.7	1.40	7.4
Bend 2 apex	Low flow	0.20	65.0	0.30	4.3
Bend 2 apex	Bankfull	9.0	65.7	1.00	7.7

Based on an interpretation of available hydrological data and channel indicators surveyed at the site immediately following a bankfull event during July 2007, the current bankfull discharge at the gauge is estimated to be about 9.0 m^3/s. The associated water surface elevation for bankfull discharge is estimated to be 65.7 m, based on field measurements from the July 2007 storm event where maximum discharge at the downstream gauging station was 8.86 m^3/s. For design purposes, a bankfull discharge of 9.0 m^3/s at the site has been employed, which is considered conservative since the gauge is downstream of the site, wherein the contributing watershed at the site is 92 % of the watershed at the gauge.

3.1.3 Numerical Model

The 3-D numerical model used in this study was Sediment Simulation in Intakes with Multiblock option (SSIIM), Version 1.1. This model, which was developed at the Norwegian University of Science and Technology (Olsen, 2005), uses a 3-D structured and non-orthogonal grid to simulate flow and sediment transport. The 3-D Reynolds-averaged Navier-Stokes equations are solved to calculate water flow, with the k-ε turbulence model to resolve the Reynolds stresses. The SIMPLE method is used to solve the pressure term. The suspended sediment transport is calculated with the convection-diffusion equation and the volumetric bedload transport is calculated using van Rijn's bedload transport formula. (Other sediment transport formulas are available, but have not been tested in SSIIM). SSIIM has been successfully used to model flow and sediment transport in meandering self-forming channels (Olsen, 2003); 90 and 135º bends (Ruther and Olsen, 2005; Minor *et al.*, 2007b); and overbank flow in a meandering channel (Wormleaton and Ewunetu, 2006).

Without detailed field measurements of the flow field and change in channel geometry over time, it is difficult to calibrate correctly the numerical model to simulate the current field conditions. Therefore, the modelling was used as a tool for testing different configurations of barb layouts and orientations. The modelling results represent a relative comparison of the change in bathymetry and patterns of velocity before and after the addition of stream barbs and, considering the criteria discussed in Section 3.1.4, an optimum design was achieved on this basis.

Model Development

The numerical model (SSIIM version 1.1) uses a structured grid to define the model boundaries, channel geometry and computational domain. The entire length of the modelled reach is 167 m, with the first bend approximately 83 m downstream of the model's upstream boundary and the second bend approximately 55 m upstream of the downstream boundary. To generate the grid, a digital elevation model was developed based on the interpolation of 500 topographical survey points, from 29 cross sections and additional top-of-bank and thalweg survey points. To generate the grid mesh for use in SSIIM, 228 cross sections, with 21 nodes per cross section, were digitized on the interpolated ground model and used to define the location of each grid node in the model. In the vertical direction, 10 grid points (9 cells) were defined from bed to water surface, with a higher resolution of points near the bed. The model grid is shown in Figure 3.1.2 A. The grid spacing in the two bend sections in the vicinity of the proposed barbs was also reduced to improve the resolution in these regions for better flow and sediment transport calculations, and to allow greater flexibility when testing various barb geometries and spacing (Figure 3.1.2 A).

The initial bathymetry is shown in Figure 3.1.2 B and represents the current bathymetry of the channel (i.e. before any numerical simulation), based on the interpolated ground model from the topographical survey data. The topographical survey was also used as a base map for the design plans.

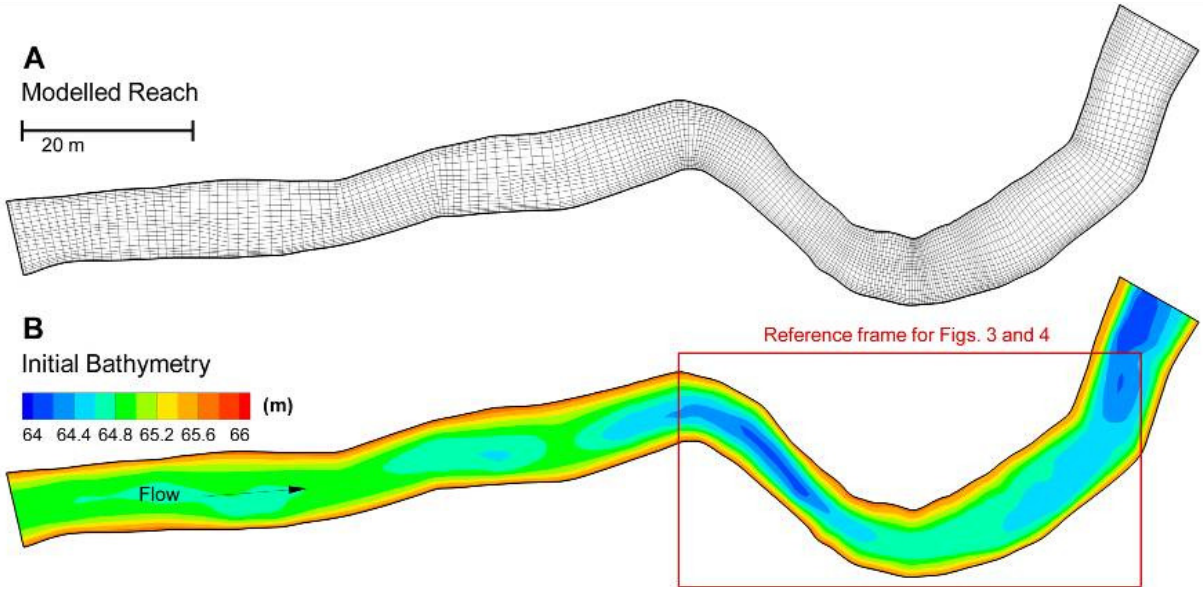

Figure 3.1.2. Modelled reach and initial bed elevations: (A) Mesh of modelled reach; (B) Initial bathymetry. (Reference frame for Figs. 3 and 4 refers to Figure 3.1.3 and Figure 3.1.4 respectively).

To calculate the water surface, SSIIM requires the following model input parameters: downstream water level, discharge and roughness. Downstream water surface elevation was set at 65.5 m in order to achieve a bankfull water depth of 65.7 m near the two channel bends; discharge was set at 9.0 m^3/s (design bankfull discharge); roughness (which is defined in the model as equivalent to a diameter of particles on the bed) was set at 0.005 m; and Shield's coefficient (used for defining critical shear stress for particle transport) at 0.055. The most sensitive parameter to bed level changes was found to be the Shield's coefficient. Rather than estimate a Shield's coefficient based on the mean particle size from field samples, which would be difficult to define accurately due to the cohesive properties of the soil at the study location, this parameter was specified on the basis of establishing minimal sediment transport in the reference run (i.e. no barbs). Therefore, when the barb structures

were added to the model, any change in flow and channel morphology would be considered due to barb layout, geometry and orientation alone.

The barb structures were modelled in SSIIM using a procedure described in Olsen (2005), where cells defining the location of the barbs in the computational grid are blocked out. These cells are defined by fixed grid points with no slip conditions specified along the cell. This method of "out blocking" was successfully used in past numerical simulations to model submerged stream barbs in a laboratory channel bend, wherein a statistical comparison of the measured bed elevations from laboratory experiments (Matsuura and Townsend, 2004) and predicted values from numerical simulation (Minor *et al.*, 2007b) gave a regression coefficient of determination (r^2) of 0.8 (Minor *et al.*, 2007b). Details of the current numerical modelling results are presented in the next section.

3.1.4 Stream Barb Design

The primary objective of the hydraulic modelling was to test different configurations of barb layout, geometry and orientation on this particular reach of Sawmill Creek such that an optimum design could be achieved. The criteria for optimum barb design were:

- reduce flow velocity and shear stress along the outer bank of each bend;
- prevent erosion at the outer bank of each bend;
- shift thalweg to the center of the channel and make thalweg deeper (more stable);
- cause no morphological changes to the channel upstream or downstream of the two bends.

To satisfy these criteria, the modelling approach taken was to: (1) use the hydraulic model to establish base conditions of the channel (i.e. a stable reference simulation without

barbs) and then; (2) test different configurations of barb layouts to ensure these criteria are met.

Using a combination of current guidelines (USDA, 2005) for the initial barb system layout and the results of intermediate numerical simulations for optimization, a final system layout was established. The layout was considered final when it successfully met the design criteria outlined above. Details of the final barb system layout (barb number, length, angle and spacing) are provided in Table 3.1.2. The final design incorporates the placement of seven barbs, three in the first bend and four in the second bend (Figure 3.1.3).

Barb length is measured from the barb key at bankfull elevation to barb tip and barb alignment angle is the angle between the centerline of the barb and the tangent to the local stream-bank at bankfull elevation (Figure 3.1.5). Barb spacing is the distance between the midpoint of consecutive barbs along one bend.

Table 3.1.2. Summary of barb details. Barbs are numbered in order in downstream direction (refer to Figure 3.1.3).

Barb No.	Bank Location	Length (m)	Angle (º)	Spacing (m)
1	Left	2.6	35	
				8.1
2	Left	2.6	35	
				7.0
3	Left	2.6	35	
				-
4	Right	2.9	35	
				6.3
5	Right	2.8	30	
				9.1
6	Right	3.4	30	
				11.5
7	Right	3.3	25	

The results of previous laboratory experiments (Matsuura and Townsend, 2004) and numerical modelling (Minor *et al.*, 2007b) found that barb alignment angle plays an important role in barb system performance. In these experiments, which considered 90 and 135º channel bends, optimum bank protection was achieved for a series of three barbs, each with an alignment angle of 30º.

Stream barb length in the first bend is less than in the second bend in order to accommodate the narrower channel width through this bend: USDA guidelines recommend that barb lengths should not exceed one-third of the cross section top width at bankfull flow. However, to ensure sufficient flow is captured by the shorter barb lengths, the angle of the three barbs in the first bend were specified as 35º (i.e. greater than the recommended 30º). Erosion in bend 1 was more significant than bend 2 (Figure 3.1.3), requiring greater deflection of high velocity flow away from the bank, and therefore greater barb angles.

Barb spacing varies according to bend curvature; the sharper the radius of curvature, the more closely spaced the barbs should be placed (USDA, 2005). Observance of this guideline is reflected in the specified barb spacing of the final design (Table 3.1.2, Figure 3.1.3 and Figure 3.1.4).

Simulation Results

Numerical modelling results are presented in Figure 3.1.3 and Figure 3.1.4, for both the reference simulation, Case 1 (without barbs) and the final barb layout, Case 2. Figure 3.1.3 illustrates the bed level changes (ΔZ) and distribution of bed shear stress (τ) for each simulation case. A comparison of these plots reveals the effect that the barbs have on ΔZ and on the distribution of τ: erosion at the outside bank of each bend has been prevented (A2

versus A1); and bed shear stress alongside the outer banks of each bend has been reduced (B2 versus B1). The bed shear stress in the centre of the channel has increased and become more concentrated in the centre for the case with barbs, suggesting that this barb arrangement would promote the development of a new, more stable thalweg in the channel centre through increased transport in this region.

Figure 3.1.4 shows the distribution of streamwise velocity (U) before and after the addition of barbs (A1 verses A2). As expected, the barbs cause a noticeable reduction in streamwise velocity along the outer bank, which corresponds with the observed reduction in bed shear stress in the same outer bank regions.

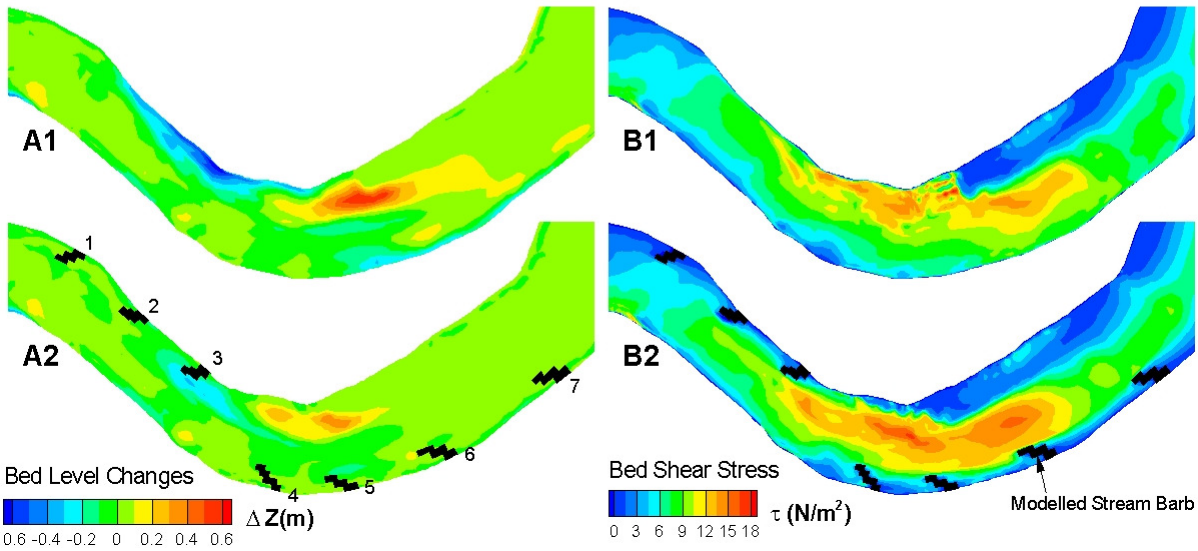

Figure 3.1.3. Contours of bed level changes (ΔZ) and bed shear stress (τ) before (A1, B1) and after (A2, B2) the addition of barbs. Flow is from left to right. Barb numbers are labelled in A2.

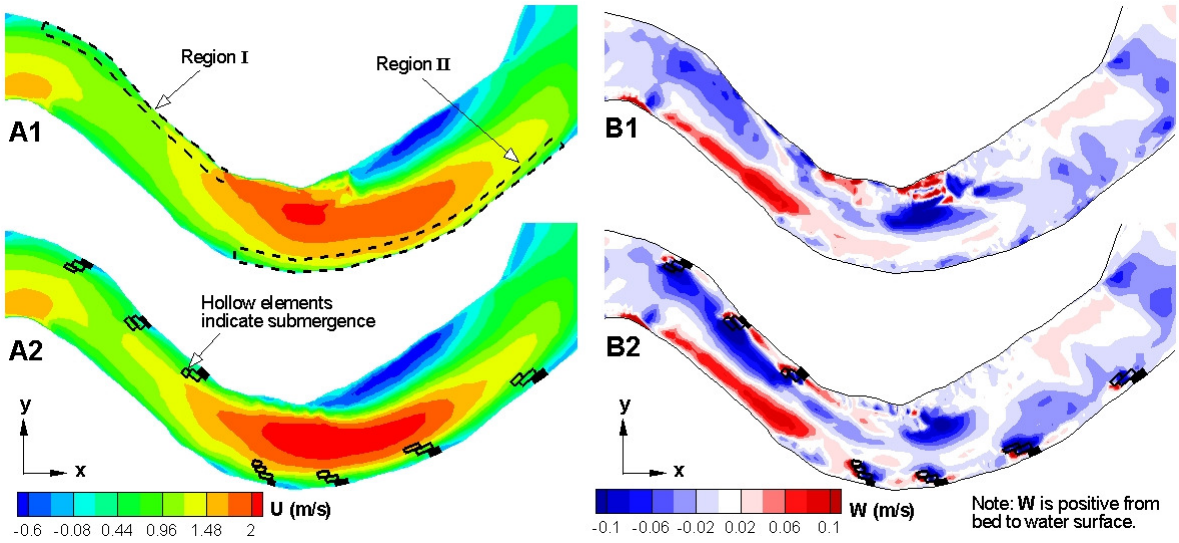

Figure 3.1.4. Contours of streamwise (U) and vertical velocity (W) at 60% of the flow depth before (A1, B1) and after (A2, B2) the addition of barbs. Flow is from left to right.

Figure 3.1.4 also shows the change in vertical velocity through the bend (B1 and B2). The presence of secondary flow, which is characteristic of flow in a bend, is best seen in the regions of high negative (blue) and positive (red) contours of vertical velocity at the inside and outside regions of bend 1, respectively (Figure 3.1.4 B1). Secondary flow is less pronounced in the second bend, most likely due to the shallowing of the local topography (due to the spurious riffle), which has disrupted this flow pattern. Despite this, the addition of stream barbs has clearly lead to a more complex, 3-D velocity pattern in the near vicinity of each structure. Extreme positive and negative values of vertical velocity, upstream and downstream of each barb structure respectively, illustrate the plunging action of the flow as it passes over the submerged structure. This resultant 3-D flow pattern is essential to the effectiveness of these structures in disrupting and redirecting the erosion-causing outer bank velocities (i.e. high streamwise and secondary flow velocities) and promoting the development of scour at the barb tips.

A quantitative comparison between each simulation case can be made by calculating the mean values of ΔZ, τ and U in the vicinity of each series of stream barbs along each bend. Two regions, which represent the near bank flow field for each series of barbs along the left (Region I) and right (Region II) banks have been defined and are shown in Figure 3.1.4 A1. The calculated mean values of each variable (ΔZ, τ and U) for each case (Case 1 = no barbs; Case 2 = with barbs) and region (I or II) are given in Table 3.1.3. These results confirm the substantial reduction in erosion, ΔZ (68 and 98 %), bed shear stress, τ (56 and 59 %) and streamwise velocity, U (51 and 51 %) achieved by the addition of the proposed barb layout for Regions I and II respectively.

Table 3.1.3. Mean values and percentage change for near bank Regions I and II. Case 1 and 2 represent modelling results for before and after the addition of barbs respectively. ΔZ is bed level change, τ is bed shear stress and U is streamwise velocity at 60% of the flow depth. (Region I and II boundaries are shown in Figure 3.1.4 A1).

	ΔZ (m)			τ (N/m^2)			U (m/s)		
Region	Case		Change	Case		Change	Case		Change
	1	2	(%)	1	2	(%)	1	2	(%)
I	-0.222	-0.068	-68	6.575	2.877	-56	0.990	0.490	-51
II	-0.083	-0.002	-98	5.676	2.302	-59	1.028	0.501	-51

The simulation results show that all but one criterion have been satisfied; the thalweg did not get noticeably deeper (Figure 3.1.3). While the barbs have reduced outer bank erosion, there is no obvious increase in scour at the barb tips (except for the case of barb 3), which would be required for the formation of a new, more stable and centered thalweg. This is likely due to the model parameters (i.e. Shield's criterion) that were specified purposely to inhibit sediment transport in the reference run scenario, thereby potentially under-predicting

the sediment transport in the vicinity of the structure. Without detailed field measurements for calibration, morphological changes are difficult to quantify substantively. Therefore, this criterion (thalweg shift) was not considered critical during the model testing as it is largely dependent on the specified sediment transport parameters, which could not be modelled exactly.

Design and Installation Plans

Stream barbs reduce bank toe scour and velocity induced erosion; however, these structures do not address bank failure due to soil instability and drawdown/saturation (USDA, 2005). Therefore, as part of the overall strategy for stream restoration and the prevention of stream bank erosion at Sawmill Creek, additional work is proposed, including: stream cleanup; vegetative planting; and site monitoring. The plan is to incorporate vegetative planting and other bioengineering practices during the construction phase to address these additional mechanisms of bank failure. Moreover, vegetation provides additional roughness to dissipate energy along the stream bank and enhances wildlife habitat and water quality.

The design reach will be monitored for flow hydraulics and fish utilization. Specifically, the 3-D flow field, bed and bank morphology, fish habitat, and fish and benthic invertebrate populations will be measured throughout the design reach, for both pre- and post-installation conditions, for a period of three years.

Figure 3.1.5 illustrates the design details of a single barb structure in plan, elevation and cross-section views. Barbs will be constructed out of large rock riprap, between 500 and 600 mm in diameter, with additional smaller riprap (d_{50} ~ 230 mm) along the bank side slope (50 % above/below bankfull) upstream of each barb to provide additional protection in this area.

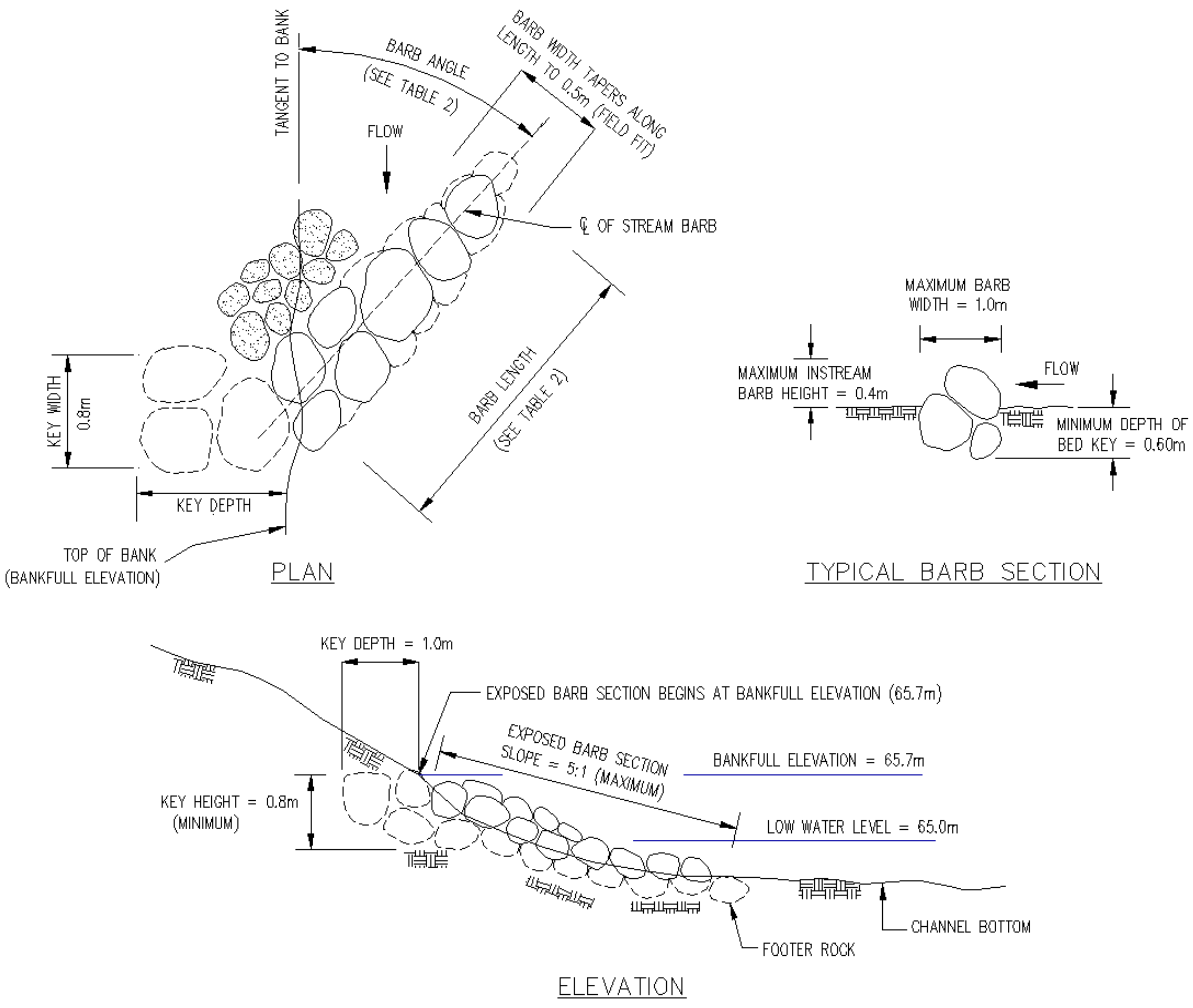

Figure 3.1.5. Barb design details: Plan (top left); Section (top right); and Elevation (bottom) views. Table 2 refers to Table 3.1.2.

According to the USDA Design Guidelines (USDA, 2005) and based on field observations, there are four common modes of barb structure failure. In the past, barbs were installed throughout the United States with limited or no guidance and as a result, several failures could have been avoided (USDA, 2005). These failure modes are: (1) flanking of the barb, which occurs when the horizontal angle is too large, the key length too short, and/or the spacing between barbs is too large; (2) the structure is undermined downstream, which

occurs when the footer rock depth is too shallow; (3) Erosion occurs between barbs, which happens when the barb spacing is too great or the horizontal angle is too large, causing greater capture of the stream flow and promoting an area of recirculating flow behind the structure; (4) rock displacement, which occurs as a result to poor construction techniques leading to weir section rocks that are not locked together.

To ensure that the proposed barb design for Sawmill Creek is not susceptible to failure, the following steps have been incorporated during the design process:

- The key length for each barb has been specified as greater than one-third the barb length which, according to USDA guidelines (USDA, 2005) is a conservative value.
- A threshold stability analysis has been carried out to test the (1) sliding and (2) overturning or moment stability of the riprap elements. The numerical modelling results were used to identify the maximum anticipated local velocities. This analysis represents a conservative scenario, as lateral anchoring and shielding of surrounding boulders provide for an additional factor of safety.
- The riprap at the base of each barb should be placed a minimum of 0.6m into the bed. This is referred to as the bed key and is necessary to prevent scour in the vicinity of the structure from causing the rock to fall into the scour hole.

3.1.5 Conclusions

The 3-D numerical model was capable of reproducing the expected distribution of secondary flow in a channel bend, the unique 3-D flow field in the vicinity of a series of stream barbs and the associated patterns of soil erosion and deposition. The numerical modelling was also demonstrated to be a useful tool for optimizing barb design for stream bank protection at the

proposed field test site. Details of the numerical modelling results, final barb design and rationale behind the design process have been presented.

A comprehensive measurement campaign is planned for Spring 2009, wherein detailed velocity measurements through the two bends will be used for improved calibration of the numerical model base-case scenario. Installation of the stream barbs is tentatively scheduled during a period of dry weather and low flow conditions in August 2009.

3.2 Stream barb performance in a semi-alluvial meandering channel

Jamieson, E.C., Rennie, C.D. and Townsend, R.D. (2011). Stream barb performance in a semi-alluvial meandering channel. *Proceedings of River Basin Management VI*, California, USA, May 2011.

3.2.1 Abstract

A series of seven stream barbs were installed at two consecutive channel bends in Sawmill Creek, a semi-alluvial stream located in Ottawa, Canada. Stream barbs (also known as submerged groynes) are low-profile linear rock structures that extend from the outside bank regions of channel bends in an upstream direction, to redirect the attacking currents and prevent erosion of the bank. As well as providing bank protection, these structures promote vegetated stream banks, create resting pools and scour holes for fish habitat, and increase bio-diversity for aquatic species. Despite these benefits, because of their relative novelty as river training structures, stream barbs are not a common means of stream bank protection in Canada and possibly non-existent for semi-alluvial or clay channels. Three years of monitoring and measurement of flow conditions (discharge, water velocity and depth) and bathymetry, before (2 years) and after (1 year) the construction of the barbs, have been collected at the Sawmill Creek study site, providing valuable data for understanding their performance in a semi-alluvial channel. Sawmill Creek has a predominately clay bed and banks, presenting a rare opportunity to study the unique dynamics between flow and sediment transport within a clay channel. This paper reports on (i) the unique site conditions and monitoring methodology; (ii) preliminary results of the 3 year monitoring program; and (iii) recommendations for future design and implementation of these structures.

3.2.2 Introduction

In September 2009, a series of seven stream barbs (or barbs) were installed in Sawmill Creek, an urban, meandering stream located in Ottawa, Ontario, Canada. The project was principally undertaken to serve as a demonstration project for the use of these structures in a semi-alluvial channel. Barbs are a relatively new form of bank protection that, unlike traditional emergent groynes, are designed as low-profile linear rock structures that allow continuous overtopping weir-type flow at bankfull (or higher) water levels. Barbs extend in an upstream direction away from the bank into the flow, and are typically anchored, in series, to the outside bank in bends (USDA, 2005). This configuration redirects the attacking current away from the outer bank towards the center of the channel and also disrupts the velocity gradient close to the outer bank. With time, the thalweg in a channel bend migrates away from the outside bank region (an undesirable and unstable location) to a new more stable location closer to the channel centreline. Unlike traditional bank protection measures such as riprap, concrete paving or gabion walls; these structures require less material, promote vegetated stream banks, create resting pools and scour holes for fish habitat, and increase bio-diversity for aquatic species (Shields *et al.*, 2000; Piper *et al.*, 2001).

A number of case studies are available for the West and Midwestern United States, where alluvial (sand and gravel) rivers predominate (Shields *et al.*, 2000; Piper *et al.*, 2001; and Papanicolaou *et al.*, 2004). No such case studies are available for semi-alluvial streams, which highlights the absence of barbs (or equivalent) as a design option for bank protection in these rivers. The performance of these structures and their long term effects on morphology and habitat will largely depend on the local sediment transport characteristics, which are inherently different when cohesive sediments are present: there may no longer be a supply of alluvial sediment upstream and the mechanisms of soil erosion and transport are

more complex than for sands or gravel. Moreover, available case studies all consider rural or semi-rural streams. The impact of urbanization (i.e. increased runoff and shorter time of concentration) on the functionality of stream barbs, where the estimation and behaviour of bankfull flow conditions is critical for successful barb design, appears to have been excluded from both previous field testing and monitoring, and design documentation. The installation of stream barbs at Sawmill Creek presents a unique opportunity to study the impacts of these structures on a predominately clay bed and bank channel, in a heavily urbanized watershed.

Details of the barb design at the study site, including three-dimensional (3-D) (flow and sediment transport) numerical simulation results of the proposed layout are presented elsewhere (Jamieson *et al.*, 2009; Chapter 3.1). This paper focuses on (i) the unique site conditions and monitoring methodology; (ii) preliminary results of the 3 year monitoring program; and (iii) recommendations for future design and implementation of stream barbs.

3.2.3 Study Site and Monitoring Program

Sawmill Creek is located in the City of Ottawa (Canada) and has a total watershed area of 27.7 km^2 and an approximate length of 10 km. The study site includes two consecutive channel bends along a 50 m section of the channel, which are each experiencing bank erosion and mass wasting along their outer banks (Figure 3.2.1). Sawmill Creek is a predominately clay bed channel, with a mix of coarse sand and gravel in the riffles. During low flow conditions from September 16-26, 2009 (Figure 3.2.2), a series of seven barbs were constructed in the two bends (3 barbs in bend 1, upstream and 4 barbs in bend 2, downstream). The barbs were constructed using large rock riprap (500 mm $\leq d_{50} \leq$ 600 mm), with additional smaller riprap (d_{50} ~ 230 mm) placed along the bank side slope (50 % above/below bankfull) upstream of each barb to provide additional protection in these areas.

Figure 3.2.1 A and B shows photos of the seven barbs, which are numbered in the downstream direction. Additional field site information and barb design details are provided in Jamieson *et al.* (2009) (Chapter 3.1).

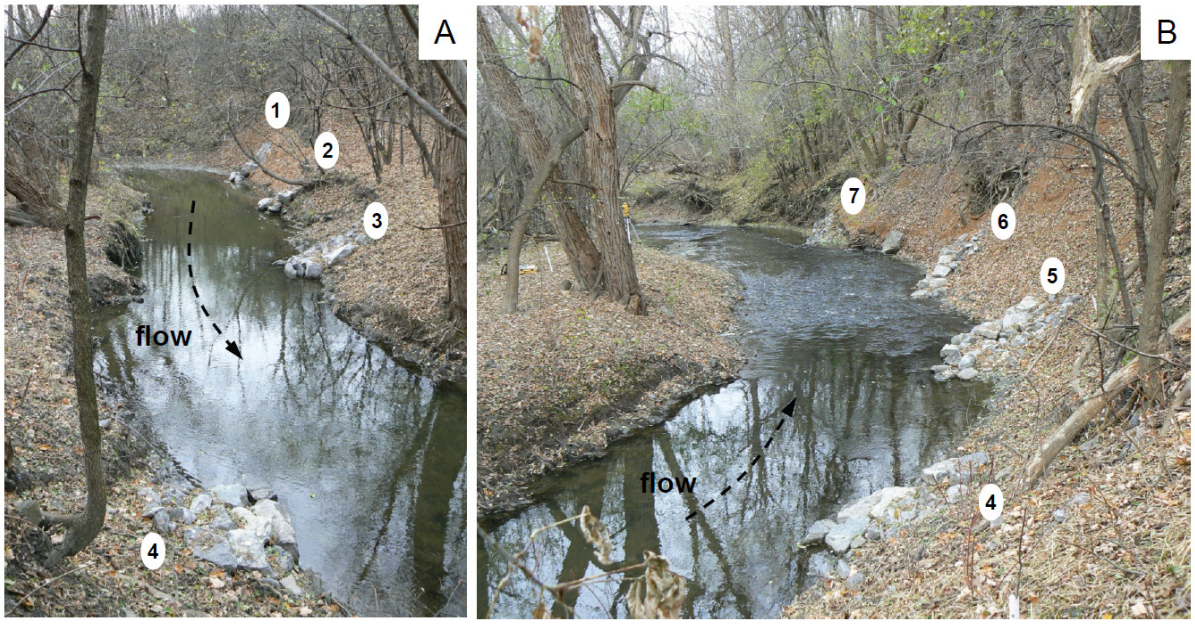

Figure 3.2.1. Stream barbs at Sawmill Creek; (A) bend 1 and (B) bend 2. Barbs are numbered in the downstream direction. Photos taken on 9 November 2009, during low flow conditions.

Discharge data for the past three years (2008-2010) were collected at a stream gauging station (CK18-Q1), approximately 1.2 km downstream of the study site, where the contributing watershed at the site is 92 % of the watershed at the gauge. Daily minimum, mean and maximum discharge are shown in Figure 3.2.2 and are based on stage data recorded continuously through each season at 15 minute intervals using a HOBO water level logger (submersible pressure transducer). Situated in a highly urbanized watershed, Sawmill Creek responds quickly to rainfall, experiencing large and rapid fluctuations in discharge and water depth following heavy rainfall events. Extreme summer rain events may even exceed

the spring freshet (Figure 3.2.2). However, it should be noted that the upper limit of the discharge rating curve is 4.3 m^3/s, and it is not currently possible to estimate discharge beyond this point (City of Ottawa, 2010).

Beginning in April 2008, continuous water level measurements were collected each season (typically mid-March to mid-November) using two HOBO water level loggers located upstream and downstream of the study site (CK18-T and CK18-U respectively). These loggers were used to monitor local water surface elevation and temperature at 15 minute intervals. Water surface slope through the study site was calculated as the difference between the daily mean water surface elevation data at each (upstream and downstream) location, divided by the distance between loggers, as measured along the channel thalweg. Distances varied from season to season from 67.2 m (2008) to 82.2 m (2010). A plot of mean daily discharge versus water surface slope for each measurement day for each season is shown in Figure 3.2.3 (excluding data from the barb construction period, September 16-26, 2009).

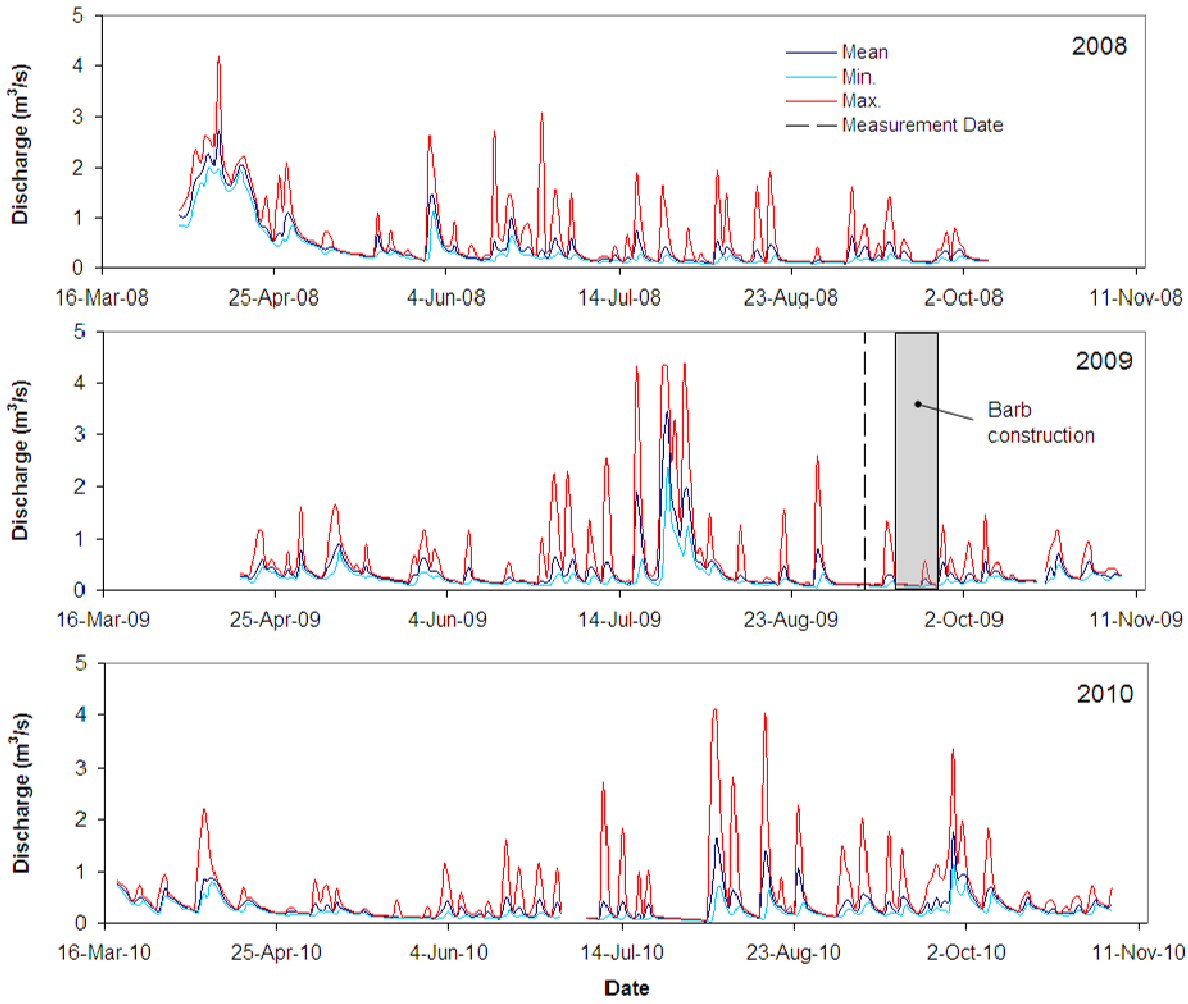

Figure 3.2.2. Daily mean, minimum and maximum discharge for 2008, 2009 and 2010 seasons. Measurement date indicates Sept. 9th ADP survey. The two other ADP surveys were on Nov. 21, 2009 and March 1, 2010. Note that the upper limit of discharge estimates was 4.3 m^3/s (City of Ottawa, 2010).

Water velocity and discharge data at the study site were collected using SonTek's M9 RiverSurveyor Acoustic Doppler Profiler (ADP). The ADP is an acoustic profiling device, which captures simultaneous measurements of velocity along a single vertical profile. The instrument was mounted on a small boat (photo, Figure 3.2.4) to map the 3-D flow field and depth at the study site. The ADP has a 9 beam system, with two sets of four profiling beams

(each set having its own frequency, 3 and 1 MHz) and one vertical beam for measuring depth (RiverSurveyor Manual, 2010). The multiple acoustic frequencies allow optimum cell size and operating frequencies to be used for conditions of varying depths. This type of instrument also has a unique advantage in that it is relatively quick and easy to set up and deploy in the field (3-4 hours). This was most critical for collecting spatial surveys in an urban creek that responds rapidly to heavy rainfall events, to ensure data were collected for relatively steady flow conditions and water levels.

Velocity data from three different spatial surveys are presented: September 9, 2009 (pre-barbs), November 21, 2009 (post-barbs) and March 1, 2010 (post-barbs). Discharge on these dates was measured based on repeated ADP transects at the study site and were 0.08, 0.30 and 0.50 m^3/s, respectively. These surveys focus on the flow field in bend 1 only, where it was expected the barbs would have the greatest influence on the flow and morphology. This expectation was based on; (1) the more typical pool geometry in this bend versus the second bend, and (2) the results of the numerical modelling that established the optimum barb design for the site (Jamieson *et al.*, 2009; Chapter 3.1). The numerical study found that the outer bank of the first bend (from T20 – T16, Figure 3.2.5) was most susceptible to erosion.

Lastly, to monitor any changes in bathymetry at the study site, three annual topographical surveys were performed; before (2007 and 2009) and after (2010) the installation of barbs. Surveys were conducted using a total station over a period of 2-3 days in November of each year, for the purpose of identifying any changes that might have occurred from season to season of each year. The surveyed sections (transects) and select results are presented in Figure 3.2.5. Results from the 2009 survey are considered to represent "as-built" conditions as very little time had passed between barb construction and the survey, and no extreme rainfall or flow events occurred between these activities. Transect locations were selected to

monitor changes immediately upstream and downstream of each barb, and in the zones between adjacent barbs. Typically, ~30 points were measured in each section, and an example of point density is shown for transect 23 (T23) in Figure 3.2.5. Barb boundaries and crest elevations were also surveyed to confirm as-built barb dimensions (Figure 3.2.5 and Figure 3.2.6).

3.2.4 Results

From Jamieson *et al.* (2009) (Chapter 3.1), the channel stability criteria for optimum barb design at Sawmill Creek were to:

- reduce flow velocity and shear stress along the outer bank of each bend;
- prevent erosion at the outer bank of each bend;
- shift the thalweg at the bend apex to a new location closer to the center of the channel and make the thalweg deeper (more stable);
- cause no morphological changes to the channel upstream or downstream of the two bends.

Monitoring results are presented in the context of satisfying these criteria while evaluating overall barb performance.

Velocity and Shear Stress

A plot of daily mean discharge versus daily mean water surface slope through the study site is presented in Figure 3.2.3. This figure shows that with the addition of barbs (2009 (post-barb) and 2010 data), water surface slope decreases for all discharges. Without barbs, mean water surface slope was 0.004, while with barbs the mean was 0.002, with the means being

statistically different at the 95% confidence interval. Bed slope through the two bends (for all years) is 0.004; therefore, before barbs, flow was uniform. The change in mean water surface slope indicates that the barbs (or barb construction) reduced the water surface slope and that for little to no changes in cross-sectional geometry (i.e. hydraulic radius, R), bed shear stress ($\tau_o = \gamma RS$) through the two bends is reduced. While the reduction in water slope could be due to the barbs causing a local backwater effect due to channel blockage, water levels upstream of the site were consistently lower following the barb construction. A shallow riffle at the apex of the second bend (between T12 – T11) (Figure 3.2.5) was lowered (~ 0.2 m) during barb construction when large debris (including a car axle) were removed. This alteration likely caused the reduction in upstream water levels. Therefore, the change in slope is more likely due to the lowering of the upstream water level, due to the removal of debris and riffle in the second, downstream bend. There appears to be slight positive trend between discharge and water surface slope in the post-barb construction data, where slope decreases with increasing discharge. This trend is not as notable in the pre-barb data.

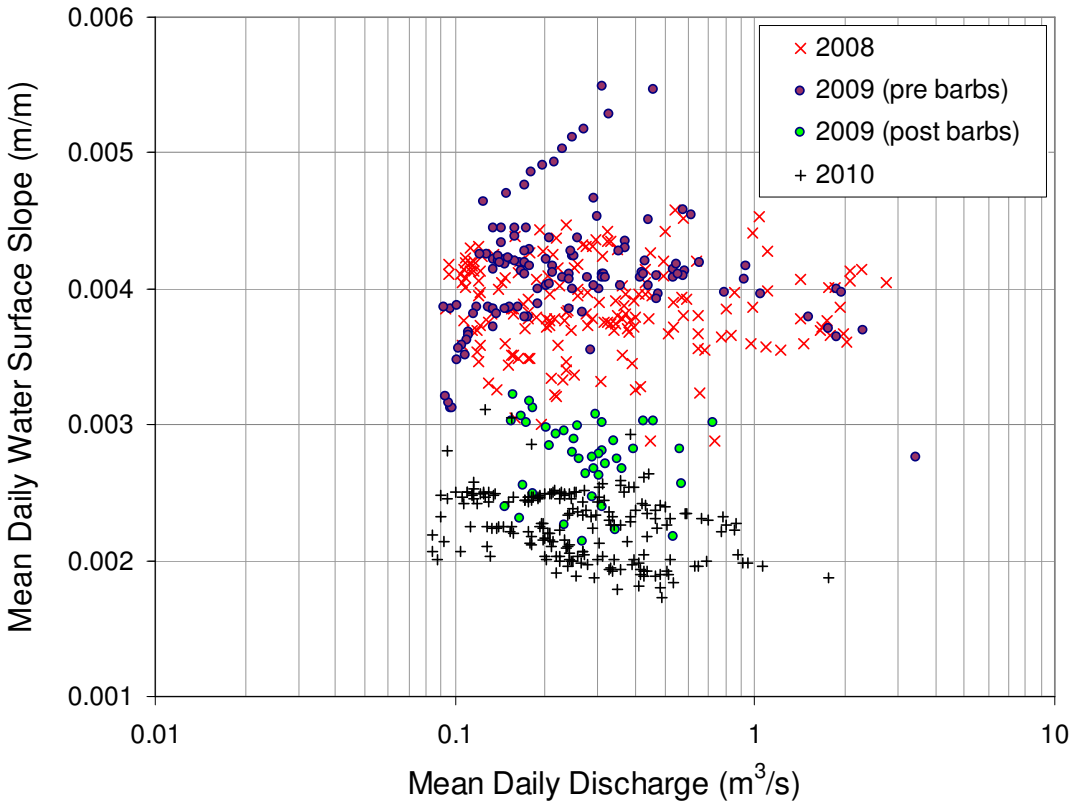

Figure 3.2.3. Mean daily discharge versus water surface slope for 2008, 2009 and 2010 season.

Velocity contours from the three spatial surveys are presented in Figure 3.2.4. The contours represent the average horizontal velocity from the top two 5 cm cells measured by the ADP using pulse coherent methods. The ADP has a submergence plus blanking distance (which comprise the distance below the water surface that can not be measured) of 0.15 m. Therefore, the top two cells represent measurements between 0.15-0.20 m and 0.20-0.25 m below the water surface. It was found that velocity data below the two 5 cm cells were less reliable, probably due to employment of pulse incoherent (narrowband) methods, (cells were also larger at 10 and 20 cm) and therefore, only the near surface average (data from the top two cells) have been presented. As well, despite the instrument being integrated with real-

time kinematic Global Position System (RTK-GPS), a lack of visible satellites (due to the creek's location in a heavily wooded and deep valley) failed to produce reliable GPS data. Therefore, all surveys are referenced according to bottom tracking (see RiverSurveyor Manual (2010) for further details on bottom tracking). For spatial referencing between surveys and an indication of the density of measured data, the distribution of sampled profiles for each spatial survey are plotted with respect to the channel bathymetry (bankfull elevation indicated by the dark blue line) in the inset plot in Figure 3.2.4, and coloured according to survey date. To best facilitate comparison, the contour plots in Figure 3.2.4 have each been shifted and overlapped in the easting direction, where the easting coordinates for each plot correspond to the coloured labels purple, red and black, for 2009-09-09; 2009-11-21 and 2010-03-01 respectively (in yyyy-mm-dd format). The topographical survey transects are also shown in Figure 3.2.4; however, these have been shortened to bankfull extents.

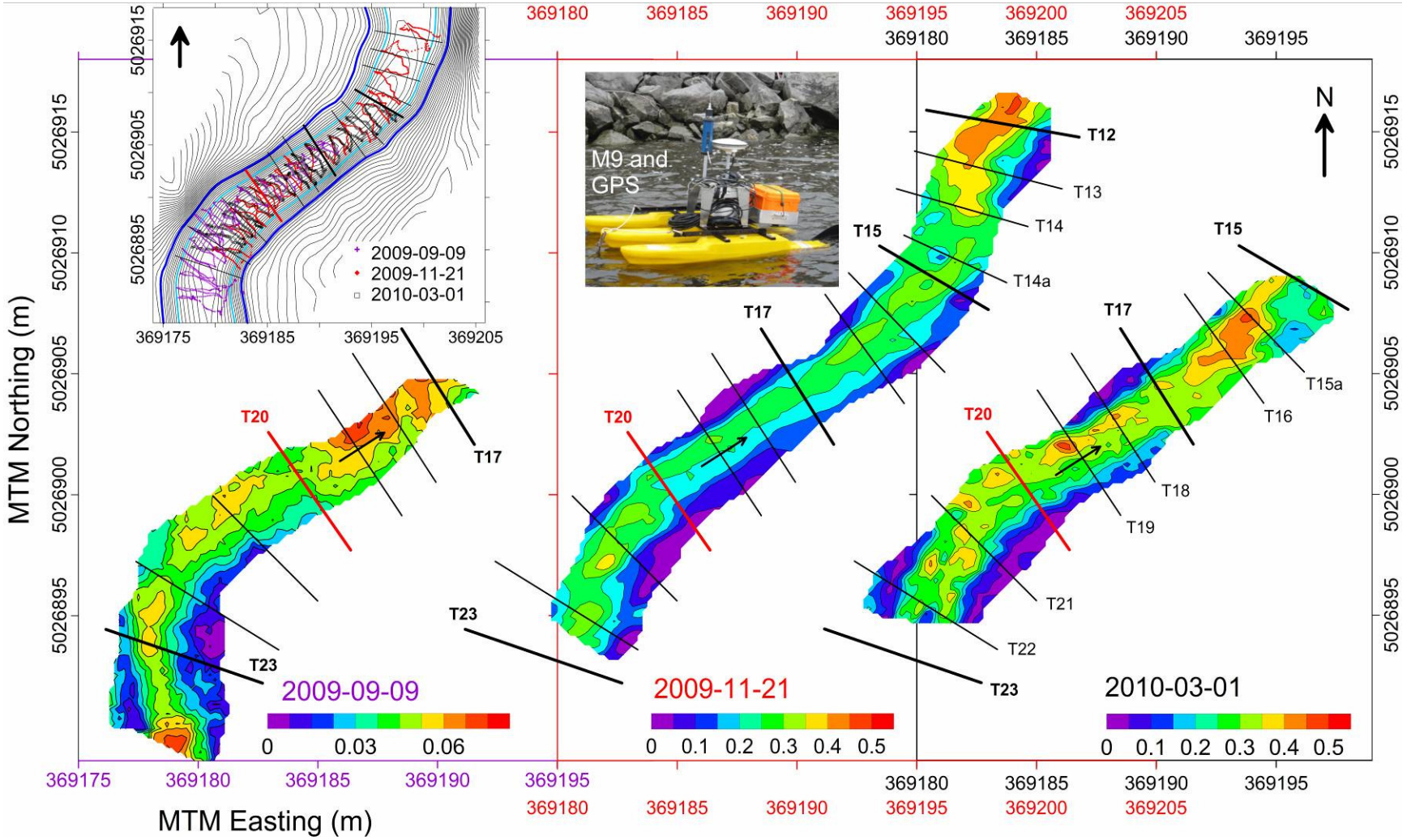

Figure 3.2.4. Contours of near surface horizontal velocity magnitude (m/s) for three different spatial surveys (no barbs, Sept. 9, 2009 (Q ~ 0.1 m^3/s); and with barbs, Nov. 21, 2009 (Q ~ 0.3 m^3/s) and March 1, 2010 (Q ~ 0.50 m^3/s)).

The velocity contours show that without barbs (2009-09-09 survey) the core of maximum velocity was along the outer (left) bank, with maximum velocity located near the bend exit or cross-over, between transects T19 and T17. With barbs (2009-11-21 and 2010-03-01), velocity magnitude along the outer bank was reduced and maximum velocity (while still near the bend exit (T16) in 2010-03-01) was shifted away from the bank and towards the center of the channel. The one exception was a portion of the outer bank on 2010-03-01, between T21 and T19, where a region of high velocity was found between regions of low velocity. This location is in the vicinity of the second barb (B2, Figure 3.2.5) and is discussed more in the following section. The two regions of low velocity correspond with flow in the vicinity of B1 (T22) and B3 (T17) (Figure 3.2.5), where the velocity reduction was assumed to result from the presence of these barbs. In all three surveys, flow at the inner (right) bank at the bend entrance was near zero.

Channel and Barb Topography

Topographical survey data along select transects (Figure 3.2.5) and for each barb crest (Figure 3.2.6) are presented. Survey results for 2007 are not presented as little to no change was observed in these sections between 2007 and 2009 (with the exception of bed level lowering at T12 and T11 due to barb construction), despite several high flow events in 2009 (Figure 3.2.2), when the discharge rating curve was exceeded (> 4.3 m^3/s). The highest recorded stage in 2009 was 0.54 m higher than the upper limit of the gauge rating curve (City of Ottawa, 2010), during an event that was 0.9 m above bankfull in the study reach. Instead, cross-sectional data are presented for the first bend (T23 – T18) for 2009 and 2010, where

the greatest amount of change did occur. However, the contours in Figure 3.2.5 are based on the 2007 survey.

The greatest amount of bed level change occurred in sections T23 and T22 in the center of the channel, where the bed elevation dropped ~ 0.2 m from 2009 to 2010 (Figure 3.2.5). It should be noted that the slight change along the right bank of T23 is not due to erosion, but a slight misalignment of section points along the transect (see surveyed points in Figure 3.2.5). One objective of employing barbs is to shift (and maintain) the thalweg to the center of the channel, through scour at the barb tips. This appears to have occurred at T22 (tip of barb 1, B1), where scour is concentrated in the channel center (Figure 3.2.5). The same amount of scour is present in T23, which is ~ 4 m upstream of the barb, suggesting that the barb may cause the scour to progress upstream. By T21, downstream of the barb, the channel exhibited no change in bed levels.

The second location of maximum change occurred at T19, where erosion of the outer bank and channel center was observed. T19 is located immediately downstream of B2 and close to the bend exit or cross-over between bends. Previous laboratory experiments with stream barbs in a channel bend (Jamieson *et al.*, submitted – a; Chapter 5.2) found that the outer bank was most susceptible to erosion immediately downstream of a barb. This was largely attributed to the increased turbulence and secondary velocities that result from the overtopping flow and flow deflection (Jamieson *et al.*, submitted – a; Chapter 5.2). Survey results at T19 appear to confirm this behaviour; there was ~ 0.3 m change along the side slope and ~ 0.2 m on the top of the bank. However, this outer bank erosion was not observed downstream of any of the other barbs. This singular occurrence of outer bank erosion was likely due to: (1) B2 being located in the most dynamic region of the two bends, as determined by the numerical modelling (Jamieson *et al.*, 2009; Chapter 3.1); and (2)

compared to the other barbs, the barb crest slope at T19 (B2) was the steepest (> 50 %) (Figure 3.2.6), and therefore permitted the greatest amount of overtopping flow in this region. Indeed, while velocity was reduced along the entire outer bank at 0.3 m^3/s (2009-11-21, Figure 3.2.4), at higher water levels (2010-03-01, Figure 3.2.4), there is a section in the middle (from T21 – T19) where velocity remains highest along the outer bank.

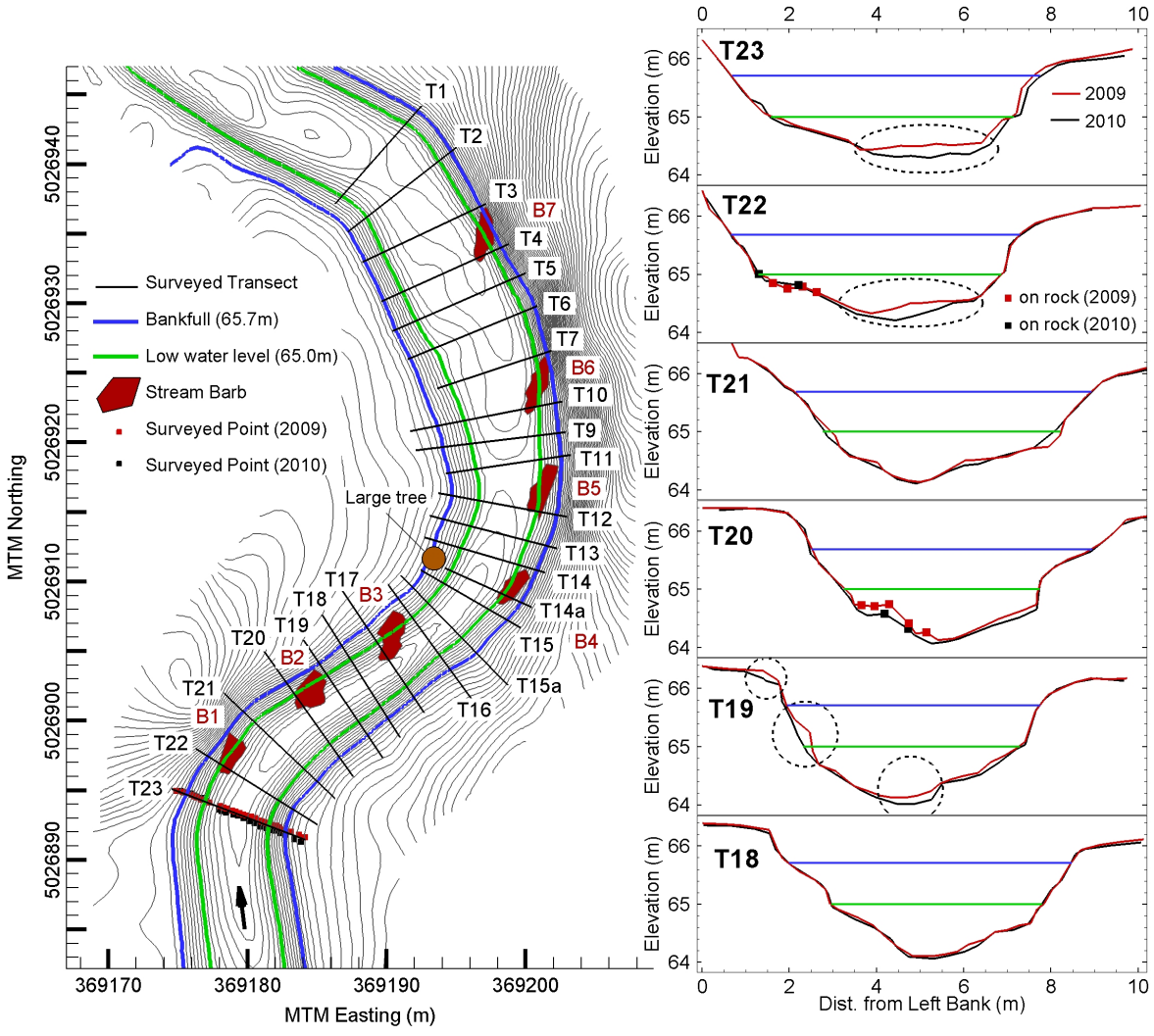

Figure 3.2.5. Topographical survey sections (Transects) at the study site and the location of "as-built" barbs. Contour lines are at 0.1 m intervals. Dashed circles represent areas of notable bathymetry change.

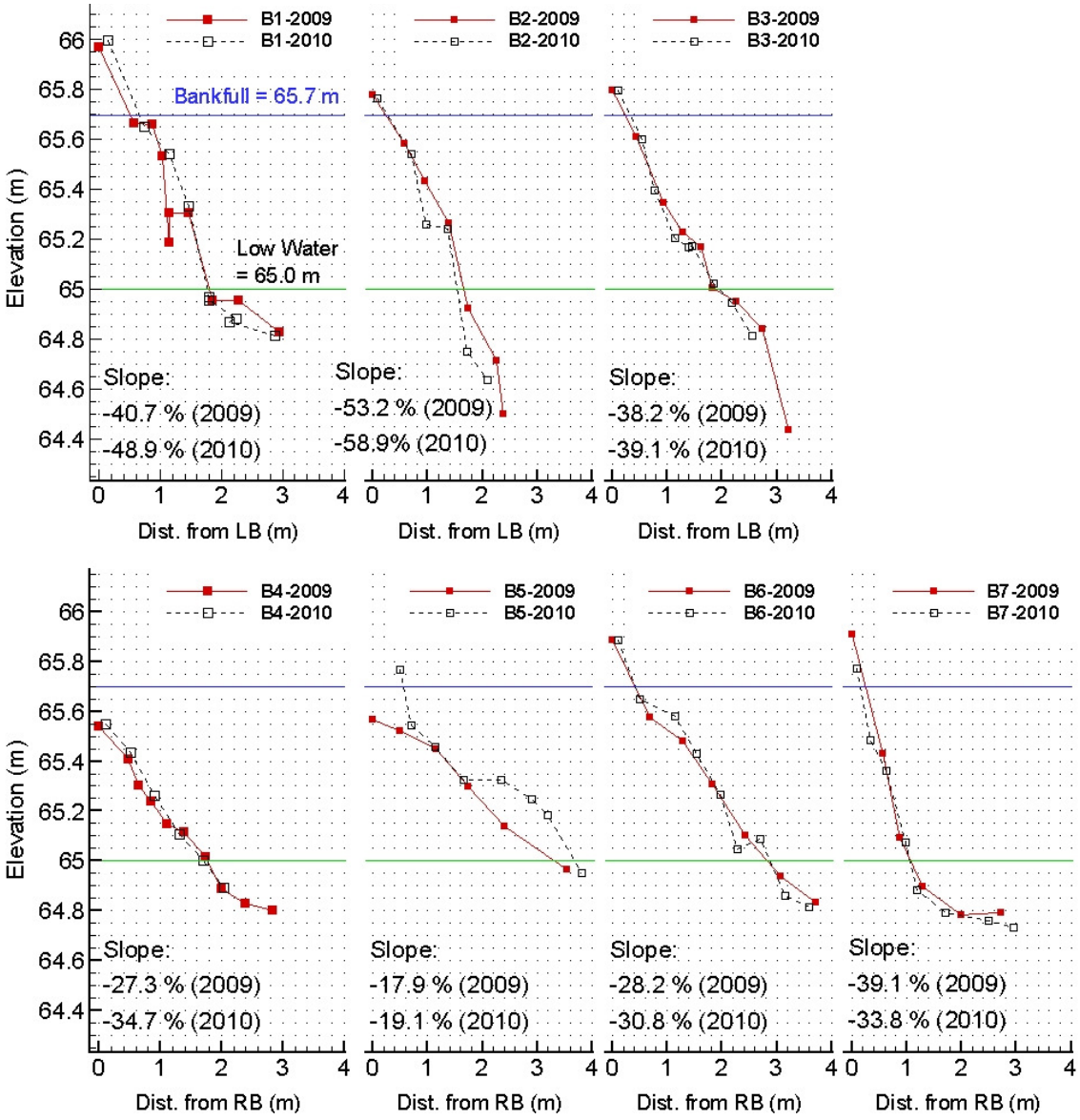

Figure 3.2.6. Survey results for barb crests (B1-B3) in bend 1 (top) and barbs (B4-B7) in bend 2 (bottom). The x-axis represents the distance from the left bank (LB) (top) and from the right bank (RB) (bottom).

Overall, barb crest slopes showed little change from 2009 to 2010 (Figure 3.2.6). Some slight variations in elevations were expected as it was not possible to survey in the same

location on each rock each year. The one exception was B5, where the barb rocks were moved and the crest height increased between the 2009 and 2010 survey. This change was due to the need to rebuild the barb following the discovery that the crest stones had moved to the center of the channel. Based on the layout and size of the moved stones (smaller stones were found to be deposited in a row across the stream immediately adjacent to the barb) and the fact that no extreme flow events occurred prior to the stones moving, it was assumed that the stones were moved by human means. Given the site's urban location, the project and monitoring efforts have been continually affected by vandalism. It is believed the stones were not moved by the flow but by individuals wanting to create a shallower crossing of the creek.

Design Recommendations

Based on the results of this field study, the following recommendations on barb design (beyond the existing design guidelines (USDA, 2005)) are made:

- Additional stream bank protection immediately downstream of each barb should be provided. This could be achieved by either widening the barb's bank key, or adding additional riprap downstream of the barb, above and below the bankfull elevation.
- Barb crest slope should not exceed 50%, as this could cause excessive overtopping flow, providing less flow deflection and consequently affording less protection of the outer bank. However, in most cases, barb crest slope will depend, in part, on local channel geometry. For example, in our study, due to the steeper side slopes of the outer bank in the first bend, the crest slopes in the first bend are steeper than in the second bend (Figure 3.2.6).

- For urban settings, minimum rock size criteria should also include a clause specifying that the smallest stones are sized such that they can only be moved with equipment (to deter vandalism).
- Longer monitoring (> 3 years) of bed topography is required for cohesive or semi-alluvial channels to determine conclusively barb effects on channel morphology. This is particularly important for streams where runoff and flow rates may be less consistent from year to year. For example, in our study, due to a combination of higher than average early spring temperatures and lower than average winter snowfall accumulation, there was no spring freshet in 2010 (Figure 3.2.2).

3.2.5 Conclusions

In summary, the interim results of our field monitoring program indicate that the installation of barbs at Sawmill Creek successfully (1) reduced velocity magnitude along the outer bank, but were slightly less successful at higher flows, when water levels were higher and more overtopping occurred; (2) shifted the high velocity core to the centre of the channel, away from the outer bank; (3) did not appear to alter the flow field along the inner bank; and (4) with a few exceptions, had little to no change in bed and bank topography, suggesting that semi-alluvial channels are resistant to change and/or a longer monitoring period (>3 years) is required to record meaningful changes in semi-alluvial or clay-type channels.

4 Missouri River

4.1 Evaluation of ADCP apparent bed load velocity in a large sand-bed river: Moving versus stationary boat conditions

---

Jamieson, E.C., Rennie, C.D., Jacobson, R.B. and Townsend, R.D. (*in press*). Evaluation of ADCP apparent bed load velocity in a large sand-bed river: Moving versus stationary boat conditions. *Journal of Hydraulic Engineering,* accepted December 2010.

4.1.1 Abstract

Detailed mapping of bathymetry and apparent bed load velocity using a boat-mounted acoustic Doppler current profiler (ADCP) was carried out along a 388 m section of the Lower Missouri River near Columbia, Missouri. Sampling transects (moving-boat) were completed at 5 and 20 m spacing along the study section. Stationary (fixed-boat) measurements were made by maintaining constant boat position over a target point where the position of the boat did not deviate more than 3 m in any direction. For each transect and stationary measurement, apparent bed load velocity (v_b) was estimated using ADCP bottom tracking data and high precision real-time kinematic global positioning system (RTK GPS). The principal objectives of this research are to (i) determine whether boat motion introduces a bias in apparent bed load velocity measurements; and (ii) evaluate the reliability of ADCP bed velocity measurements for a range of sediment transport environments. Results indicate that both high transport ($\overline{v_b}$ > 0.6 m/s) and moving-boat conditions (for both high and low transport environments) increase the relative variability in estimates of mean bed velocity. Despite this, the spatially dense single transect measurements were capable of producing detailed bed velocity maps that correspond closely with the expected pattern of sediment transport over large dunes.

4.1.2 Introduction

Recent advancements in acoustic instrumentation have provided the means for capturing high quality data in a range of aquatic environments. However, limitations remain concerning deployment methods, post-processing and data interpretation, and, in the case of bed load transport, reliable and adequate validation. Previous studies have attempted to validate ADCP measured bed load transport by correlating ADCP moving-bed bias (apparent bed load velocity, v_b) with traditional bed load samplers (Rennie *et al.*, 2002; Rennie and Villard, 2004) and found strong correlations for gravel-bed conditions, but for sand-beds, correlations were either poor or limited to low sediment transport conditions (i.e. $v_b < 0.2$ m/s). More recent research for sand-beds (Gaeuman and Jacobson, 2006 and 2007b) has shown higher correlations between v_b and bed load capture rates from bed load samplers (g_b) for higher bed velocities ($0.1 < v_b < 1.0$ m/s) but found that due to the clustering of data at low ($g_b < 0.0002$ kg/s) and high ($g_b > 0.002$ kg/s) transport rates, relationships were relatively weak. The authors concluded that physical bed load sampling is ineffective as a validation or calibration measure for alternative techniques (such as acoustic bottom track bias) for measuring bed load in large sand-bed rivers.

Bed load transport involves the intermittent entrainment and transport of material from the river bed, and is a function (in part) of the composition of the surface particles. Gravel-beds tend to entrain (and transport) material more stochastically than sand-beds (due to their larger and typically less sorted particle size), and homogeneous transport can not be assumed. Therefore, sand-bed environments should be more suitable for reliable acoustic bed velocity measurements. However, the difficulty with sand is determining the height of the active layer (the zone of highly concentrated moving sediment just above the bed), and where bed forms are present, the presence of heterogeneous transport.

Apparent bed load velocity (v_b) (referred to herein as bed velocity) represents a spatial average of surface particle velocities, including immobile particles that make up the stationary bed, weighted by the backscatter intensity of the various surface particles. The ratio of bed velocity to mean bed load particle velocity depends on a number of factors: the concentration and size of the particles moving in the bed load layer; the bed load layer thickness (active layer); and the backscatter strength from a unit area of moving particles relative to the echo strength from a unit area of unobstructed bed. Controlled laboratory experiments in a mobile sand-bed flume have attempted to quantify bed velocity error and validate ADCP bed velocity measurements through simultaneous measurements of bed load using ADCP bottom track data, automatic weigh pans, dune tracking and high-speed digital video (Jamieson *et al.* 2008; Ramooz and Rennie, 2010). While acceptable correlations were found, a complete analytical solution equating ADCP bed velocity to total bed load transport rates has yet to be realized.

Researchers have recently begun to investigate the significance of moving versus stationary boat ADCP measurements for quantifying mean flow field characteristics (Muste *et al.* 2004a; Dinehart and Burau, 2005; Szupiany *et al.* 2007). Data are typically collected from moving boat transects as they provide greater spatial coverage for less measurement time. However, no study to date has quantified the variation in measured bed velocity under these two different measurement conditions. Rennie and Millar (2004) introduced moving-boat measurements of v_b to map spatial distribution of relative bed load transport. In a sand-bed estuarine distributary channel, it appeared that moving-boat measurements of v_b may have exceeded collocated stationary measurements, but results were inconclusive because flow was unsteady due to tidal influence and the collocated stationary measurements were collected one hour after the moving-boat measurements. It is likely that bed load transport

had diminished by the time stationary measurements were collected, which may have led to the apparent discrepancy.

This paper has two principal objectives: (1) To determine whether boat motion introduces a bias in bed velocity measurements by quantifying the variations in measured bed velocity between stationary and moving-boat conditions; (2) To assess the reliability of bed velocity measurements under a range of sediment transport environments. This research will attempt to evaluate whether or not moving-boat (single transect) data are sufficient for resolving spatially and temporally variable transport in a sand-bed river. These results have implications for improving boat-mounted ADCP measurement techniques and understanding to what extent these instruments can be used for detailed mapping and analysis of sediment transport in large rivers.

4.1.3 Study Site and Methods

Detailed mapping of bathymetry and bed velocity using a boat-mounted ADCP was carried out along a 388 m section of the Lower Missouri River at River Mile 173, near Columbia, Missouri. The Lower Missouri River channel morphology has changed substantially over the last one hundred years as engineering measures such as wing dikes and revetments have been introduced to stabilize the banks and maintain a deep, narrowed, and focused thalweg for barge traffic. ADCP data were collected at the study site (Figure 4.1.1) over three days (May 29, June 2 and 4, 2008) (Table 4.1.1), using a 1200 kHz Workhorse Rio Grande ADCP manufactured by Teledyne-RD Instruments, Inc. (*Any use of trade, product, or firm names is for descriptive purposes only and does not imply endorsement by the U.S. Government*). The ADCP was mounted from a boat along with real-time kinematic (RTK) GPS and configured for a sampling rate of 1.7 Hz, bin size of 0.25 m, Water Mode 1 and Bottom Mode 5, and

bottom track pulse length &R20 (i.e., 20% of the distance to the bed). These parameters were selected based on the default manufacture recommendations for large rivers (TRDI, 2009), laboratory testing (Ramooz and Rennie, 2010) and the experience of the authors. A summary of the data collected is given in Table 4.1.1. A single beam echosounder transducer (sonar) was used for simultaneous measurements of depth for detailed mapping of the bathymetry. Mean daily discharge data (Table 4.1.1) were obtained from the Missouri River at Boonville Gauging Station (USGS 06909000), which is approximately 55.5 km upstream of the study location. Previous ADCP bed velocity research on the Lower Missouri River includes Gaeuman and Jacobson (2006, 2007a and 2007b), who studied a sand-bed bend section approximately 40 km upstream of the present study site. Bed material in the thalweg is primarily fine to medium sand with small amounts of fine gravel (Gaeuman and Jacobson, 2006).

Table 4.1.1. Summary of ADCP data collection. Q is the mean daily discharge and Q_E is the percent daily flow exceedance for years 1967 to 2008.

Date	Q (m^3/s)	Q_E (%)	ADCP Measurements
May 29 2008	3275	12.2	• Spatial survey at 5 and 20m spacing
June 2 2008	4531	5.4	• Moving-boat : 16 repeated transects over P1 and P2 • Stationary: 2 x 10 min. at P1; 2 x 10 min. at P2
June 4 2008	4337	6.1	• Stationary: 1 x 15 min. at P2

Figure 4.1.1. Aerial photo of the study site in 2005, during low flow conditions. Dashed lines represent the survey extents. Points 1 and 2 indicate locations of stationary measurements.

ADCP and single-beam echosounder survey data included 67 transects covering a 388 m long section of the study area. Transects were spaced a combination of 20 and 5 m apart, with the 5 m transects covering the area surrounding the wing dike and adjacent thalweg (see Figure 4.1.2 B for 5 m survey extents). Navigation software (HYPACK) was used to map out the transect locations before the survey and to track the boat's position during measurements to help the driver maintain a position as close to the desired transect line as possible. Lateral variation of the boat position off the transect line rarely exceeded 5 m (i.e. 5 m transects rarely overlapped). Transects were orientated perpendicular to the streamwise flow direction. These data were used for the spatial mapping of bathymetry and bed velocity (Figure 4.1.2).

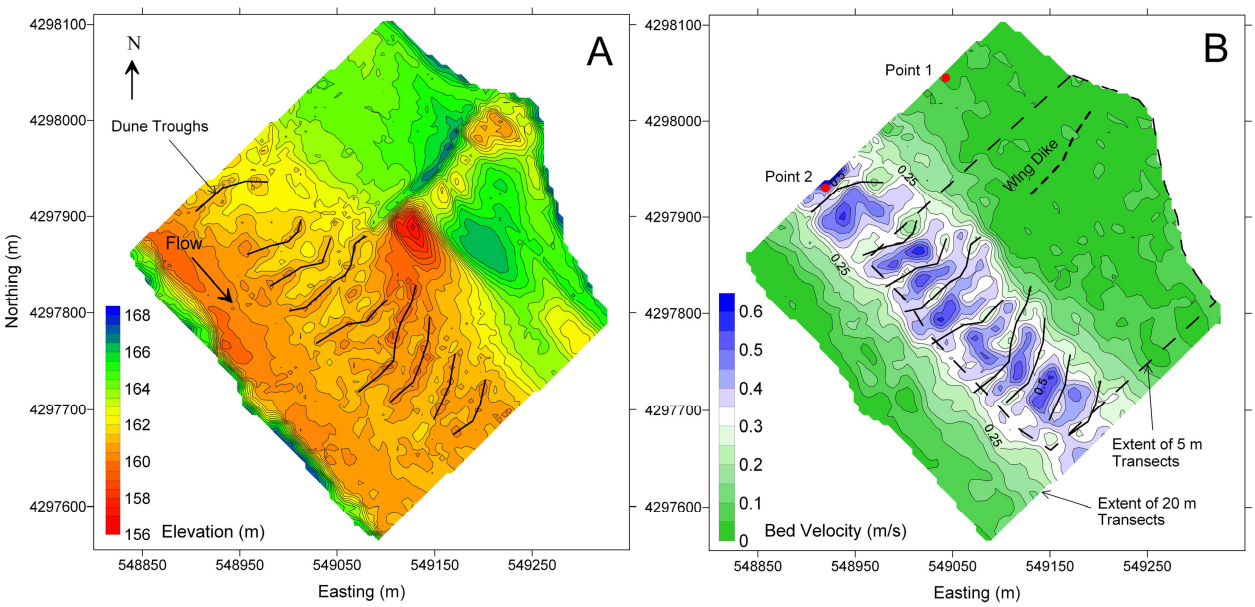

Figure 4.1.2. Contours of bed elevation (A) and bed velocity (B). Solid lines represent topographic troughs. All data are from the May 29 survey and interpolated at 5 m resolution from data collected with 20 m and 5 m transect spacing (as indicated). Elevation data are from single beam sonar and bed velocities are from four beam ADCP.

Stationary measurements were made by manoeuvring the boat to maintain a constant position over a target point (using navigation software) for approximately 10 minutes per measurement. During these measurements the ADCP (mounted on the boat) did not deviate from the target position by more than 3 m (at least 94 % of the time). In total, five stationary measurements were made (Table 4.1.2). For the comparative analysis with stationary data, moving-boat measurements were made by repeated transects (16) perpendicular to the streamwise direction and over the two target points on the same day as four of the stationary measurements (June 2nd data, Table 4.1.2). On this day, the stationary point data were collected over a period of 1 hour, 30 minutes after the moving-boat data, which were collected over a period of 2 hours and 40 minutes (2.7 hrs.). The flow was steady during the

entire measurement program based on data from the Boonville Gauging Station. Average boat speeds during stationary and moving-boat (transect) measurements were 0.14 m/s (σ = 0.11 m/s) and 1.31 m/s (σ = 0.42 m/s) respectively.

Table 4.1.2. Summary of stationary data. No. of Ens. is equal to the number of bottom track ensembles collected over the measurement duration; % Valid = No. of Ens./(Duration/0.6)·100, where 0.6 is the sampling rate in seconds.

Measurement	Date	Location	Duration (s)	No. of Ens.	% Valid	$\overline{v_b}$ (m/s)	σ (m/s)	95% CI
000	June 2	Point 1	618	848	82	0.101	0.080	0.005
001	June 2	Point 1	609	930	92	0.098	0.071	0.005
002	June 2	Point 2	536	303	34	0.835	0.289	0.033
003	June 2	Point 2	590	48	5	1.071	0.472	0.134
050	June 4	Point 2	920	731	48	0.623	0.169	0.012

4.1.4 Bed Velocity

Bottom tracking bias in the ADCP is introduced when the bed surface is mobile. By comparing boat velocity measured with bottom tracking, v_{bt} to an independent measure of boat velocity, v_{ref} (i.e. RTK GPS), an estimate of bed velocity, v_b can be calculated by $v_b = v_{ref} - v_{bt}$ (Rennie *et al.* 2002). Two-dimensional (2-D) surface grids (with a point spacing of 5 m) were interpolated from the bed velocity data using linear kriging and an anisotropic semi-variogram model to best fit the data. Individual maps were interpolated for each component (v_{bE} and v_{bN}, where v_{bE} and v_{bN} represent the easting and northing components of bed velocity respectively) and then combined to generate a contour map of v_b, where $v_b = \sqrt{{v_{bE}}^2 + {v_{bN}}^2}$ (Figure 4.1.2 B). For contours of bed elevation, the same method of linear kriging (with a point spacing of 5 m and anisotropic semi-variogram) was also used to

interpolate a 2-D grid from the single-beam sonar bathymetry data (Figure 4.1.2 A). An anisotropic semi-variogram was used as it provided the best search radius orientation for interpolation in the streamwise direction, given the orientation of the reach (i.e. streamwise direction) with respect to north.

Interpolating each component of bed velocity (v_{bE} and v_{bN}) separately incorporates the importance of a spatially consistent vector direction into the interpolation. A positive bias in bed velocity magnitude could be generated by interpolating bed velocity magnitude alone (i.e. without direction), where inconsistent bed velocity directions (which are typically higher in regions of zero to low bed velocity, where moving bed is more difficult to detect with the ADCP) generates higher than expected bed velocity (Figure 4.1.3 C). This positive bias occurs because the calculated vector magnitude is necessarily a positive value, without consideration of direction. Scatter plots of interpolated bed velocity (coloured according to magnitude) are shown in Figure 4.1.3 B and C, where Figure 4.1.3 C shows the interpolation of vector magnitude ($v_b = \sqrt{v_{bE}^{\ 2} + v_{bN}^{\ 2}}$) and Figure 4.1.3 B shows the interpolation of each component (v_{bE} and v_{bN}) separately and then combined as calculated magnitude. Note that Figure 4.1.2 B and Figure 4.1.3 B are the same, except one shows contours (Figure 4.1.2 B) while one shows points coloured according to magnitude (Figure 4.1.3 B).

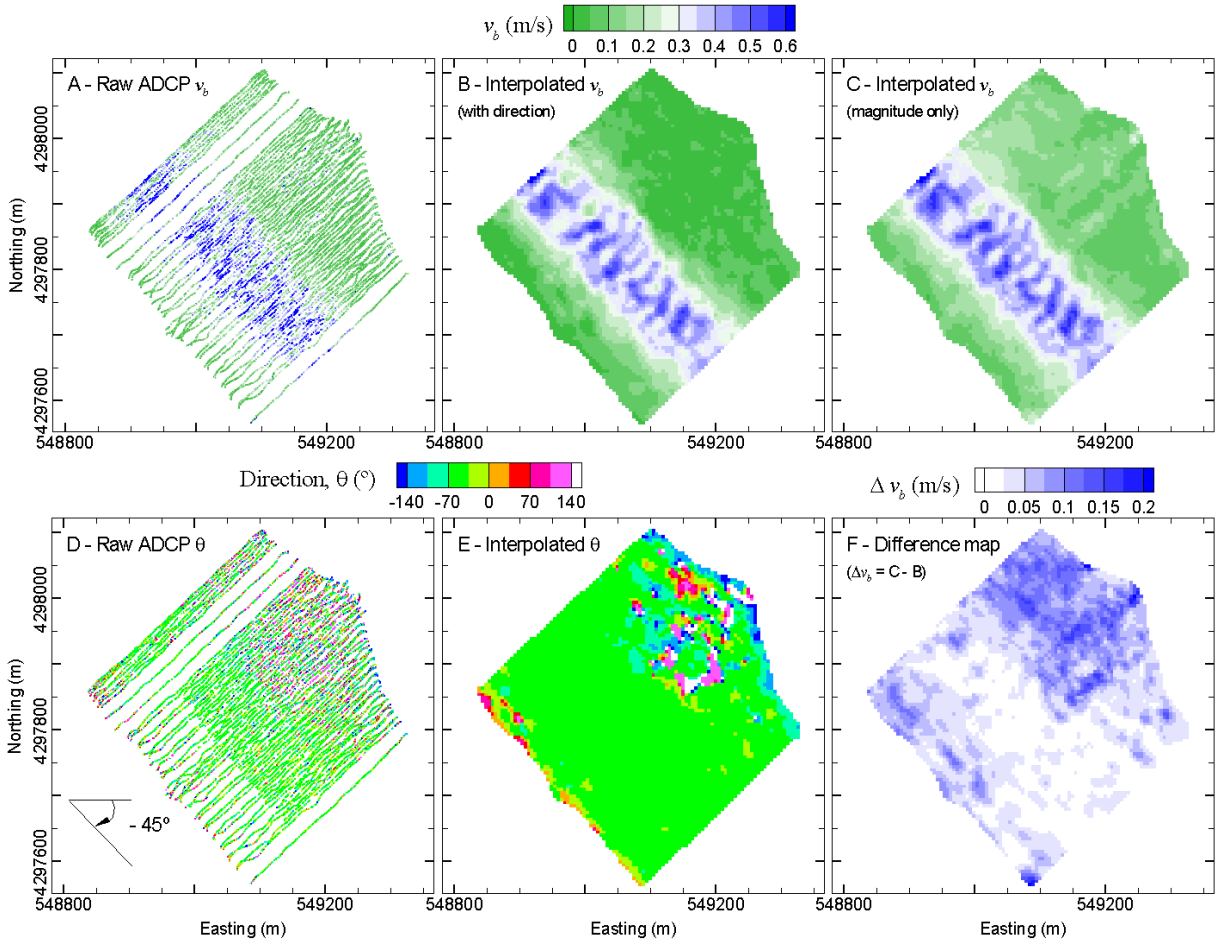

Figure 4.1.3. Scatter plots of raw and interpolated bed velocity (v_b) (A, B and C), bed velocity direction (in degrees) (D and E) and bed velocity difference (Δv_b) (F). Direction angle is measured counter-clockwise from east. Δv_b is calculated as the difference between the interpolation of vector magnitude (C) and the interpolation of each component (v_{bE} and v_{bN}) separately, which are then combined to calculate magnitude (B). The thalweg / dune field region (Figure 4.1.2 A) is dominated by bed velocity vectors with directions between -35 to -70 ° (for both raw and interpolated data) and low to zero difference in bed velocity magnitude (F).

Figure 4.1.3 F provides a difference map between the two interpolation methods (Figure 4.1.3 C minus Figure 4.1.3 B) and shows that there is little to no change in the thalweg region (where bed velocity is highest and greater than 0.3 m/s) compared with a difference of

up to ~ 0.15 – 0.20 m/s in v_b in the shallower region surrounding the wing dike where little to no transport is expected (Figure 4.1.2 B). Bed velocity direction (θ, in degrees) is calculated as $\theta = tan^{-1}\left(v_{bN} / v_{bE}\right)$ (accounting for quadrant) and is plotted for the raw and interpolated bed velocity data (Figure 4.1.3 D and E respectively). The plots of bed velocity direction confirm (i) the uniformity of direction in the thalweg region (direction ranges between -35 to -70º), which is consistent with the assumed streamwise direction (~ -43º) and, (ii) the variability that is present in the shallow region in the vicinity of the wing dike. Together, the interpolated direction plot (Figure 4.1.3 E) and bed velocity maps (Figure 4.1.3 B and C) suggest that there is very little directional noise in bed velocity when transport is approximately greater than 0.3 m/s.

To evaluate the difference in measured bed velocity variability between the two deployment conditions (moving versus stationary boat), individual single-ping data were combined into ensemble groups of varying size, from which mean bed velocity ($\overline{v_b}$) and standard deviation (σ) were calculated as

$$\overline{v_b} = \sqrt{\left(\overline{v_{bE}}\right)^2 + \left(\overline{v_{bN}}\right)^2} \quad \text{and} \quad \sigma = \sqrt{{\sigma_E}^2 + {\sigma_N}^2} \qquad (4.1.1) \text{ and } (4.1.2)$$

where $\overline{v_{bE}}$, σ_E and $\overline{v_{bN}}$,σ_N are the mean and standard deviations of the easting and northing components of v_b for each ensemble group respectively. For comparisons between a range of bed velocity magnitudes, a dimensionless parameter, the coefficient of variation (CV = $\sigma / \overline{v_b}$), was used. The coefficient of variation compares estimates of σ as a proportion of the mean value, with low values of CV representing less relative variability and therefore greater reliability. These variables ($\overline{v_b}$, σ and CV) were calculated for four separate conditions: moving-boat (transect) at Points 1 and 2; and stationary at Points 1 and

2. The location of Points 1 and 2 are shown in Figure 4.1.1 and Figure 4.1.2 B and represent regions of low ($\overline{v_b} \approx 0.1$ m/s) and high ($\overline{v_b} > 0.6$ m/s) bed load transport respectively (Figure 4.1.2 B and Table 4.1.2).

To eliminate any temporal bias, stationary ensemble data were grouped in random temporal order to form group sizes ranging from one ensemble to the maximum (i.e. all ensembles from a 10 min. measurement) (Figure 4.1.4 C). Moving-boat ensembles were grouped according to their spatial proximity to the target point: using a variable search radius from 1 to 30 m (with 0.5 m intervals) with the target point at the center, ensembles within each radius extent were grouped, such that the number of ensembles would increase with increasing search radius size (Figure 4.1.4 B).

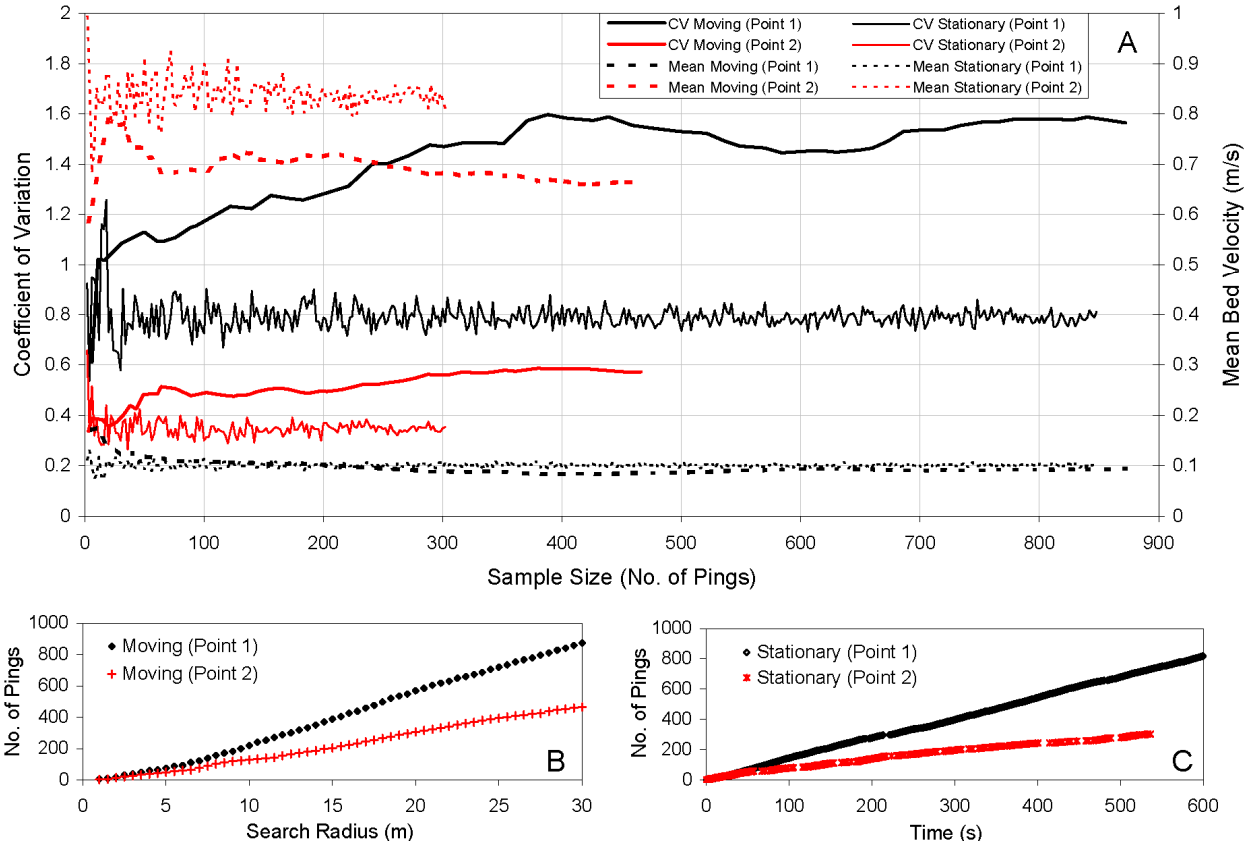

Figure 4.1.4. (A) Coefficient of variation and mean bed velocity verses sample size (no. of single ping ensembles) for moving-boat and stationary ADCP bed velocity measurements. The sample size (No. of Pings) represents the number of valid pings that provided bed velocity data, which varied based on spatial proximity to the center of Point 1 or 2 (B) and the quality of data (C) - at higher bed velocities (Point 2), more data were invalid over the same measurement duration. Stationary at Points 1 and 2 are represented by data 000 and 002 respectively (see Table 4.1.2). Single ping ensemble data were collected every 0.6 seconds.

4.1.5 Results and Discussion

Figure 4.1.2 A provides a detailed map of bed topography of the surveyed area. The thalweg was dominated by large dunes 2-3 m in height with an average wavelength of 39 m, while a number of different scour holes (large and small) can be found in the area surrounding the wing dike. Figure 4.1.2 B shows the spatial variability in bed velocity (measured by moving-

boat transects of the entire study area in just under 5 hours), with regions of high and low bed velocity in the thalweg corresponding closely with dune crests and troughs respectively. Velocity and bed shear stresses are largest in the vicinity of a dune crest (Villard and Kostaschuk, 1998; McLean *et al.*, 1999; Kostaschuk *et al.*, 2004), leading to higher transport over the dune crest.

A comparison of $\overline{v_b}$ and CV between moving-boat and stationary measurements, for regions of low (Point 1) and high (Point 2) transport is shown in Figure 4.1.4. It can be seen that $\overline{v_b}$ was comparable for collocated moving versus stationary data for low bed velocities ($\overline{v_b} \leq 0.1$ m/s) when no bed forms were present (Point 1). Higher bed velocities ($\overline{v_b} \approx 0.8$ m/s) occurred at Point 2, where bed forms were present (and assumed to be migrating). At this location, $\overline{v_b}$ between stationary and moving-boat measurements differed by ~ 0.25 m/s for large sample sizes. On the other hand, for small sample sizes (< 30 ensembles) $\overline{v_b}$ was similar between survey methods. At approximately 25 ensembles (search radius = 3 m), $\overline{v_b}$ ~ 0.80-0.85 m/s for both conditions (Figure 4.1.4 A). In this case, the 3 m measurement domain was common between the moving-boat and stationary data sets.

The range of CV for bed velocity (solid lines, Figure 4.1.4 A) was between 0.3 – 1.6, where only the moving-boat at low transport (Point 1) CV value was greater than 1 (i.e., $\sigma > \overline{v_b}$). CV is sensitive to the magnitude of mean bed velocity (CV = $\sigma/\overline{v_b}$), and as a result, despite a lower standard deviation at Point 1 compared to Point 2 (Table 4.1.2), the relative impact of σ becomes more important at lower values of $\overline{v_b}$. For both low (black) and high (red) transport regions, CV was higher for moving versus stationary boat conditions (Figure 4.1.4 A). Moving-boat data were combined based on spatial proximity to the target point in

order to increase sample size (Figure 4.1.4 B). For large sample sizes, the search radius incorporated a relatively large area with spatially heterogeneous transport, dominated by dunes for Point 2, which increased the variability of bed velocity. This may also explain why the stationary $\overline{v_b}$ was greater than the moving-boat mean at Point 2. It is possible that the stationary measurements collected over a period of 10 minutes were taken over a dune crest while the moving boat measurements collected over a period of 2.7 hours were taken over alternating dune crests and troughs, thereby lowering the moving-boat mean bed velocity since bed velocity is lower in a dune trough. Dune migration rates in the Lower Missouri River (for similar spring discharges to those considered in this paper) range between 1 and 5 m/ hour, with an average of 2.6 m/hour, regardless of dune height and wavelength (Gaeuman and Jacobson, 2007a). Therefore, it can be assumed that stationary measurements were restricted to a relatively stationary dune, while the moving-boat would have measured over both a dune crest and trough as a single dune crest could have passed during the 2.7 hour period. In a more homogenous region of transport (Point 1), where bed forms were not measured (Figure 4.1.2 A), the difference in large sample $\overline{v_b}$ between moving-boat and stationary measurements was less than the standard deviation of the stationary measurement (σ = 0.08 m/s for 000) and close to negligible beyond a sample size (number of ensembles) of 100 (Figure 4.1.4 A). Our results suggest that, like conventional bed load sampling, in the presence of mobile bed forms, stationary measurements should be scaled by migration rate, while moving-boat bed velocity measurements should be scaled by both the bed form dimension (i.e. spatial extent) and migration rate.

Most importantly, similar to the convergence of the mean values at small sample sizes, at sample sizes less than approximately 30 ensembles, CV values for moving and stationary

measurements were similar (at both Points 1 and 2). This convergence of mean and CV values when the measurement domain was comparable between measurement methods suggests data populations for the moving and stationary measurements were similar, and there was no bias between moving and stationary measurements. It should be acknowledged, however, that estimates of the mean and standard deviation are relatively uncertain when calculated using these smaller sampler sizes, which results in spikes in CV at low sample numbers (Figure 4.1.4 A).

The difference in $\overline{v_b}$ (percent difference = 25%) for back-to-back stationary measurements collected only minutes apart at Point 2 (002 and 003, Table 4.1.2), demonstrates the inherent uncertainty of measuring such temporally dependent transport, regardless of the technique employed. Rennie *et al.* (2002) found that a large number of samples (25 min.) were required to estimate the moving-bed bias with reasonable confidence in a gravel-bed river, and Rennie and Villard (2004) found that longer averaging times were required in gravel-bed reaches compared to sand-bed, likely due to the stochastic nature of bed load entrainment in gravels. However, this relatively long sampling time (25 min.) could be inefficient when measuring regions with high temporal and spatial variability.

A comparison between all five stationary measurements (000, 001, 002, 003 and 050) shows a strong exponential relationship (r^2 = 0.989) between σ and $\overline{v_b}$ (Figure 4.1.5 A), where σ increases with increasing $\overline{v_b}$. Rennie *et al.* (2007) also found a similar trend for stationary measurements of sand-bed transport, but used a power function for best fit. The results in Figure 4.1.5 A are also consistent with the observed variations in data quality, where data quality refers to the number of invalid pings (or ensembles). At low transport ($\overline{v_b} \approx 0.1$ m/s), bottom track data are more reliable (i.e. fewer invalid ensembles) compared

to high transport for similar measurement durations (Figure 4.1.4 C and Table 4.1.2). There appears to be a strong linear relationship ($r^2 = 0.982$) between the number of valid ensembles obtained and bed velocity magnitude (Figure 4.1.5 B). Substantial invalid data (> 1 ensemble per second or < 50% valid ensembles) was observed for mean bed load velocities greater than 0.6 m/s (Table 4.1.2).

The reason for more valid ensembles at Point 1 compared to Point 2 (Figure 4.1.4 B and C) was likely a combination of (i) the repeated moving-boat transects being consistently closer to the target (Point 1), because lower water velocities in this region allowed more accurate navigation on the transect line, and (ii) fewer ensembles are lost (invalid) over a less mobile bed with more homogeneous transport (Figure 4.1.2 B). However, the correspondence between Figure 4.1.4 B and Figure 4.1.4 C suggests that poor data quality (i.e. more invalid ensembles over time (Figure 4.1.4 C) or area (Figure 4.1.4 B)), and by extension bed velocity variability, is less a function of measurement technique than of higher bed velocity.

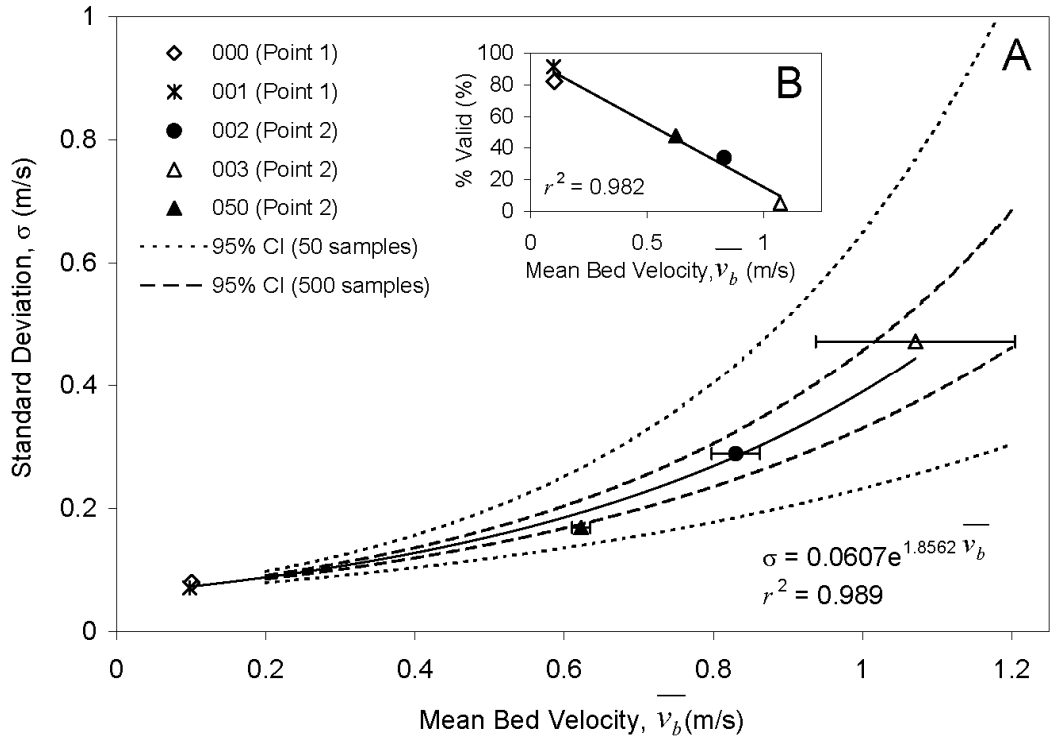

Figure 4.1.5. (A) Standard deviation (σ) versus mean bed velocity ($\overline{v_b}$) for stationary data. Error bars represent +/- 95% Confidence Interval (CI). (B) Percentage of valid ensemble data (% Valid) versus $\overline{v_b}$ for each stationary measurement. Error bars for 000 and 001 are smaller than the symbol size.

The uncertainty in estimates of bed velocity depends on both real temporal variability of transport and measurement error. The increase in standard deviation and reduction in data quality with increasing bed velocity could be for two reasons: instrument limitations (i.e. signal attenuation and decorrelation) and a spatially heterogeneous transport environment, to which the ADCP is particularly sensitive given the divergent beam geometry (typical ADCPs have three- or four-beam sensors with divergent beam angles of 20-30º with the vertical, which results in the sampling area of the ADCP bottom track velocity increasing with depth due to the physical spreading of the beam footprint). In the spatial survey data (moving-boat

transects of the entire study area, Figure 4.1.2 B) 14.6% of the bottom track data were invalid due to exceedance of the error velocity threshold (set at 0.1 m/s), compared to only 0.8% and 0.2% invalid data due to beam correlation and amplitude thresholds respectively. Correlation and amplitude respectively represent measures of the quality and strength of the bottom track return signal, and thresholds were set at instrument default values of 220 and 30 counts respectively, while a three beam solution was allowed. The error velocity acts as a measure of bottom track velocity heterogeneity as it is equal to the difference between the vertical velocity measured by one set of two beams and the vertical velocity measured by the other set of two beams, scaled to be indicative of horizontal velocity error. Of the 14.6% invalid data due to high error velocity, 84% were located in the thalweg region where bed velocity was greater than 0.3 m/s and dunes were present (Figure 4.1.2 B). Therefore, it is assumed that the increase of invalid bottom track signals at higher transport rates is predominately due to the increased bottom track error velocity measured in the thalweg, where the beam spread is largest (flow is deepest) and sediment transport is most heterogeneous.

Despite the low standard deviations at low transport compared to high transport, the relative magnitude of σ to $\overline{v_b}$ is highest at low transport (Table 4.1.2). Even when data quality is highest (valid ensembles > 80% under low transport conditions), the standard deviation of measured apparent bed velocity is 70-80% of the mean (Table 4.1.2).

The spatial survey results (Figure 4.1.2) are in close agreement with previous measurements by Gaeuman and Jacobson (2006 and 2007b) and show that despite the high standard deviations in bed velocity determined from stationary measurements, highly dense single-transect (moving-boat) measurements (i.e. a transect spacing of 5 m, or approximately 1 % of the channel width) are capable of mapping highly variable and spatially diverse

patterns of bathymetry and bed velocity in a large river (at least for maximum bed velocities of up to ~0.6 m/s). It may be possible to obtain equally relevant maps at higher flow rates (and higher transport); however, such data have not yet been collected. These results also indicate that averaging over suitably broad areas can provide useful estimates of bed velocity, for example as a measure of bed mobility at the reach scale (Elliott *et al*., 2009).

In our analysis, the moving boat conditions under investigation were restricted to steady boat movement along a transect, perpendicular to the flow and with minimal accelerations. Other factors such as compass error, boat accelerations and boat motion were not considered. Compass calibration, as well as other factors, such as spatial averaging and a spatially heterogeneous moving bed, has been observed to affect ADCP bottom track data quality (Gaeuman and Jacobson, 2005). However, compass error was not considered to be a factor in the present study because the compass was calibrated *in-situ* to less then 1° error for all surveys conducted (where the RDI User's Manual (TRDI, 2009) recommend a minimum of 2°), and spatial accelerations that locally bias the internal flux-gate compass were minimized during the survey.

4.1.6 Conclusions

ADCP measurements of bathymetry and acoustic bed velocity have been carried out on the Missouri River near Columbia, Missouri (a large sand-bed river), for both stationary and moving-boat conditions. Results show that $\overline{v_b}$ is comparable for collocated moving versus stationary data for low bed velocities ($\overline{v_b} \leq 0.1$ m/s) when no bed forms are present. At higher bed velocities ($\overline{v_b} \approx 0.8$ m/s) when bed forms are present, $\overline{v_b}$ were only comparable at small sample sizes (< 30 ensembles). These results suggest no introduction of bias in

moving-boat measurements in these conditions. A negative bias in large sample $\overline{v_b}$ between moving and stationary measurements at the high transport conditions was observed (i.e. large sample moving $\overline{v_b}$ < stationary $\overline{v_b}$), most likely because of passing bed forms. Indeed, the presence of bed forms at higher bed velocities may explain the clustering of data at high and low transport rates (Gaeuman and Jacobson, 2006 and 2007b), suggesting that for different bed load transport regimes (i.e. uniform transport at low bed velocities versus heterogeneous transport due to bed forms at high bed velocities), the correspondence of bed load transport with acoustic bed velocity should be treated differently.

Results indicated that despite a higher coefficient of variation in bed velocity for moving-boat data versus stationary, the reliability of bed velocity estimates at high bed velocity (v_b > 0.6 m/s) is more a function of data quality than the measurement technique employed. However, even with a higher coefficient of variation, when interpolated to generate detailed 2-D bathymetry and bed velocity maps, highly dense (i.e. 5 m spacing or 1 % of the channel width) single transect (moving-boat) ADCP measurements were capable of describing the expected patterns of bed load transport in an active dune field (dunes 2-3 m in height with an average wavelength of 39 m), when maximum $v_b \approx 0.6$ m/s. When generating contour maps of bed velocity, each component of bed velocity (v_{bE} and v_{bN}) should be interpolated separately to account for direction and avoid any positive bias associated with calculating a vector magnitude from the two bed velocity components. Inconsistent bed velocity directions were greatest in regions of zero to low bed velocity (where moving bed is more difficult to detect with the ADCP), and when bed velocity magnitude was interpolated alone (i.e. without direction), a higher than expected bed velocity was observed in these zero to low transport regions.

A comparison between stationary measurements found a high positive correlation between bed velocity and standard deviation and a high negative correlation between bed velocity and data quality (likely due to instrument limitations and a highly varied transport environment). Results indicate that at $v_b > 0.1$ m/s both data quality and the characteristics of the local transport environment (i.e. degree of temporal and spatial heterogeneity) play an important role in the reliability of bed velocity estimates. At high transport rates ($v_b > 0.6$ m/s), when it is assumed that most of the bed is mobile, more than half of the ensemble data were invalid due to lost bottom track signal. The predominant cause of invalid bottom track data was due to exceeding the error velocity threshold (0.1 m/s).

Overall, results indicate that reasonable estimates of bed velocity are possible for measurements up to ~0.6 m/s, regardless of technique, stationary or moving-boat. Additional data collection at higher transport rates (field and laboratory scale) and for more homogeneous transport conditions are required to understand more conclusively the capabilities of ADCP moving-bed bias for quantifying bed load transport in highly mobile sand-bed environments.

4.2 3-D flow and scour near a submerged wing dike: ADCP measurements on the Missouri River

Jamieson, E.C., Rennie, C.D., Jacobson, R.B. and Townsend, R.D. (2011a). 3-D flow and scour near a submerged wing dike: ADCP measurements on the Missouri River. *Water Resources Research*, 47, W07544, doi: 10.1029/2010WR010043.

4.2.1 Abstract

Detailed mapping of bathymetry and three-dimensional water velocities using a boat-mounted single-beam sonar and acoustic Doppler current profiler (ADCP) was carried out in the vicinity of two submerged wing dikes located in the Lower Missouri River near Columbia, Missouri. During high spring flows the wing dikes become submerged, creating a unique combination of vertical flow separation and overtopping (plunging) flow conditions, causing large-scale three-dimensional turbulent flow structures to form. On three different days and for a range of discharges, sampling transects at 5 and 20 m spacing were completed, covering the area adjacent to and upstream and downstream of two different wing dikes. The objectives of this research are to evaluate whether an ADCP can identify and measure large scale flow features such as recirculating flow and vortex shedding that develop in the vicinity of a submerged wing dike; and whether or not moving-boat (single-transect) data are sufficient for resolving complex three-dimensional flow fields. Results indicate that spatial averaging from multiple nearby single transects may be more representative of an inherently complex (temporally and spatially variable) three-dimensional flow field than repeated single transects. Results also indicate a correspondence between the location of calculated vortex cores (resolved from the interpolated three-dimensional flow field) and the nearby scour holes, providing new insight into the connections between vertically-orientated

coherent structures and local scour, with the unique perspective of flow and morphology in a large river.

4.2.2 Introduction

Identifying large-scale fluid phenomena in the field and characterizing their behaviour at sufficient temporal and spatial resolutions remains a challenge. Recent advancements in acoustic instrumentation have provided the means for capturing high quality data in a range of aquatic environments. However, limitations remain concerning deployment methods, post-processing techniques and data interpretation. The three-dimensionality inherent in turbulent flows and in particular in locations of complex geometry or structures (i.e. channel bends and confluences, wing dikes and abutments) and their associated temporal and spatial variability, play an important role in the transport and distribution of sediment (and pollutants and nutrients) in these environments. A detailed understanding of these complex flows and how they influence sediment transport processes at the large-scale is necessary for improved assessment and prediction of river morphology, aquatic and benthic habitat, and the integrity and design of engineering structures. Mapping and assessment of complex flows in large rivers has gained increasing importance as restoration efforts have emphasized incremental re-engineering of river-training structures to improve ecological conditions (Shields, 1995; Buijse *et al.*, 2002; Muhar *et al.*, 2007; Papanicolaou *et al.*, in press). Optimal designs depend on understanding how re-engineering of river training structures – removal, notching, unrooting from the bank, lowering, or extending – affect the complex flow patterns, consequent erosion or deposition, and ultimately the diversity and quality of aquatic habitat.

In medium to large rivers, the acoustic Doppler current profiler (ADCP) is a common instrument for measuring discharge (Gordon, 1989; Simpson, 2001), water velocity (Muste *et al.,* 2004a; Dinehart and Burau, 2005), bed load transport (Rennie *et al.*, 2002; Rennie and Millar, 2004) and in some cases the availability of aquatic habitat (Shields and Rigby, 2005; Gaeuman and Jacobson, 2007). Recent studies have begun investigating the use of boat-mounted ADCPs for detailed velocity measurements in medium and large rivers using moving boat transect data (Richardson and Thorne, 1998; Muste *et al*., 2004a; Dinehart and Burau, 2005; Parsons *et al.*, 2005; Parsons *et al.*, 2007; Szupiany *et al.*, 2007; Szupiany *et al.*, 2009; Rennie and Church, 2010). Particular interest has focused on the significance of moving versus stationary boat ADCP measurements for quantifying mean flow field characteristics. Data are typically collected from moving-boat transects as they provide greater spatial coverage for less measurement time. It is expected that greater sampling, achieved by either repeated moving transects or longer stationary measurements, is required for adequate representation of the mean velocity flow field (i.e. Muste *et al.,* 2004b; Dinehart and Burau 2005; Szupiany *et al.*, 2007).

Most of these studies have found considerable scatter in velocities from single transects compared to stationary profiles or repeat transects and recommend either an average of five (Szupiany *et al.*, 2007 and Szupiany *et al.*, 2009) or up to six (Dinehard and Burau, 2005) cross sections is necessary to resolve the finer details of the flow, or that in fact only stationary measurements with sufficient sampling time should be used (Muste *et al.*, 2004b). However, Szupiany *et al.* (2007) found that, for a single transect just downstream of a confluence on the Paraná River (Argentina), the main features of the expected secondary flow field were evident. It was "the finer details" of the flow field, including a stronger, more clearly defined secondary flow cell, that were only obtained through the process of averaging

five repeated transects at the same location. In the same river, Parsons *et al.* (2005) measured the three-dimensional (3-D) flow field over dunes from single longitudinal (streamwise) moving-boat transects, and were able to identify a number of flow features, including near-bed flow deceleration (produced by the form drag and dune morphology), and in a few cases, flow separation (or flow reversal) downstream of the dune crests, within the area of the leeside scour. Parsons *et al.* (2007) also presented a spatial analysis of secondary velocities from single ADCP transects, this time from multiple (36) individual cross-stream traverses spaced an average of 150 m apart along a confluence-diffluence unit, again in the Paraná River (Argentina). At this scale, the transects adequately described the general flow field pattern within the confluence-diffluence unit, which was dominated by simple convergence and divergence through the reach, and, contrary to previous laboratory and smaller scale field studies, indicated that no coherent, channel-scale secondary flow cells existed at the confluence.

Typical ADCPs have three- or four-beam sensors with divergent beam angles of 20-30º (with the vertical), resulting in single ping water velocities that are actually the transformation of three (or four) independent single-component velocities sampled in separate bins at spatially discrete locations along the edges of a large (conical) volume of water, which increases with depth. This poses a significant problem for data interpretation and identifying spatially-variable flow features such as coherent flow structures. Trump and Marmorino (2002) present a technique for grouping individual bins of moving-boat ADCP data according to their true spatial location (before averaging to a vertical profile below the instrument), such that only bins occurring within a specified vertical slice (of a given width) through the water column centered at a given horizontal (East-North) location are grouped. However, this technique limits the spatial extent (both vertical and horizontal) of the sampled

area, and would still require repeat transects for adequate coverage of an entire 3-D flow field, particularly one which is not fully characterized by a single two-dimensional slice. As well, it is not clear how all three Cartesian components of velocity are resolved for each overlapping bin location, as three independent overlapping (single-component) beam velocities would be required, which may not always be available when individual bins at various depths and of various direction are combined. Furthermore, even if available, overlapping individual velocity components would not be collected simultaneously and turbulent velocity fluctuations would ensure that each measurement corresponded to a different instantaneous velocity. Therefore, the resolved Cartesian velocity would represent neither an instantaneous nor a mean velocity and would likely not be indicative of the actual velocity within the bin. Moreover, the resolved direction would likely be in error.

In this paper, we present a new method for evaluating large-scale, complex 3-D flow fields from densely spaced single transect ADCP surveys. Some previous studies have used ADCP data for evaluating 3-D flow patterns (such as secondary circulation), but for only discrete, two-dimensional transects or cross-sections (i.e. Parsons *et al.*, 2005; Szupiany *et al.*, 2007; Szupiany *et al.*, 2009). With the exception of Parsons *et al.* (2007) and Movafagh Kerman and Rennie (2007), where individual transects were spaced over 100 m apart, we are not aware of any previous studies that used ADCP measurements for densely mapping the entire 3-D flow field. In the present work, closely-spaced single-transect data are combined using kriging to interpolate a spatially continuous volumetric (3-D) grid from which additional fluid flow features can be calculated, such as contours of vorticity magnitude and the presence of vortex cores in the vicinity of the wing dikes. We believe our method presents the best compromise of capturing large-scale 3-D features of the flow field with an

acceptable measurement time (i.e. 5 hours), allowing one to assume stationarity of discharge and bathymetry, even at high flows.

This research has two principal objectives: (1) to evaluate whether an ADCP can identify and measure large-scale flow features such as recirculating flow and vortex shedding that develop in the vicinity of a submerged wing dike; and (2) to describe the unique 3-D flow patterns and associated morphology (for example, scour holes) occurring in the vicinity of a submerged wing dike on a large sand-bed river. These results have implications for improving boat-mounted ADCP measurement and analysis techniques and for understanding to what extent these instruments can be used for detailed mapping and analysis of complex flows in large rivers. The submerged nature of these structures creates a unique combination of vertically-orientated flow separation from wing dike tips and overtopping (plunging) weir-type flow conditions, causing large and small scale 3-D eddies to form. Quantifying the influence of this highly 3-D flow field and associated complex features on a mobile bed (i.e. during threshold conditions for sediment entrainment) provides new and valuable data for understanding the impact and performance of these structures on the flow and morphological dynamics in a large river.

In this paper we describe the study site and measurement methodology, including a new technique for processing and analysing three-dimensional velocities through interpolation and the calculation of additional flow features such as vortex cores. A discussion follows, including an assessment of the interpolation technique, and implications for measuring and understanding large-scale complex flow fields and their role in scour hole dynamics.

4.2.3 Study Site and Methods

The Missouri River is the longest river in North America, draining 1,371,000 km^2 (or ~ 6 %) of the continent (Galat *et al.*, 2005). From St. Louis, Missouri (River Mile 0) to Sioux City, Iowa (River Mile 735), the Lower Missouri River channel morphology has changed substantially over the last one hundred years as engineering structures such as wing dikes and revetments have been introduced to stabilize the banks and maintain a deep, narrowed and self-dredging thalweg for barge traffic. Wing dikes and revetments now stabilize 1,200 km of riverbanks, in what was historically a shallow river characterized by interspersed braided, anabranched, and single-channel reaches (Elliott *et al.*, 2009). The two sites surveyed in the present study are located on the Lower Missouri River near River Miles 178 (Site A) and 173 (Site B), near Columbia, Missouri (Figure 4.2.1).

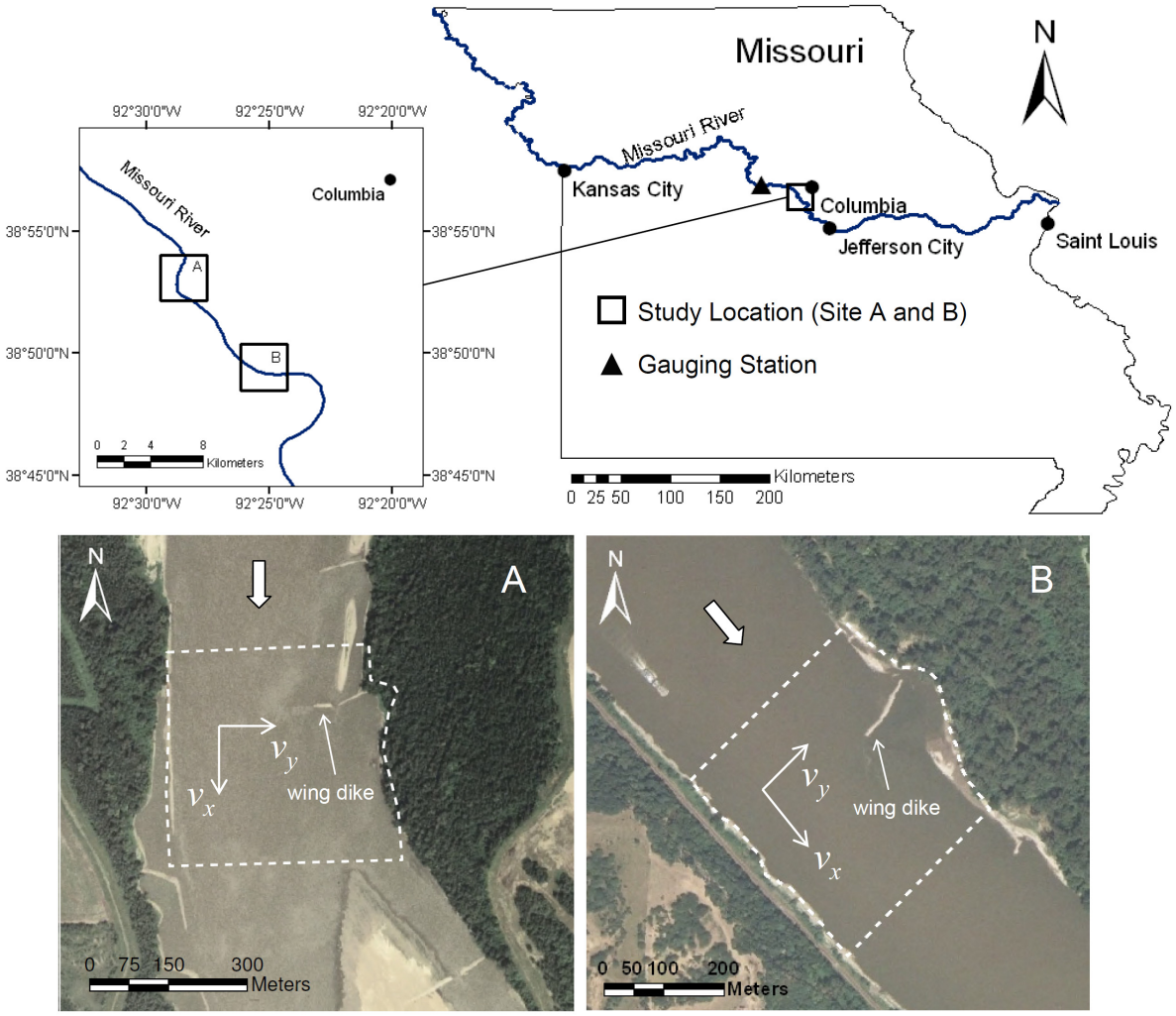

Figure 4.2.1. Map of ADCP survey location and streamflow gauging station (USGS 06909000) (top) and air photos of each site during low flow conditions, when wing dikes are exposed: (A) Site A (Huntsdale) taken August 2006 when discharge was 1166 m^3/s (75% exceedance) and (B) Site B (Plowboy) taken August 2005 when discharge was 1070 m^3/s (81% exceedance). Site B is 7.5 km downstream of Site A. Dashed lines represent survey extents. v_x and v_y represent the streamwise and cross-stream flow directions respectively.

Using a boat-mounted single-beam echosounder transducer (sonar) and four-beam ADCP, detailed mapping of bathymetry and water velocity was carried out in the vicinity of two submerged wing dikes at each of the two study sites (Figure 4.2.1 A and B). Data were

collected over a period of three days between May 28 and June 4 2008, when high spring flows lead to overtopping conditions at both wing dikes (Table 4.2.1 and Figure 4.2.2). The wing dikes are not perfectly horizontal, sloping toward the thalweg, with notches or gaps allowing some through-flow of water (Figure 4.2.3). Generally, the wing dikes are just submerged at 1980 - 2120 m^3/s (30-35% flow exceedance and 110-130 days per year on average). The echosounder was a 208 kHz Odom, 8-degree transducer, with a depth accuracy of 0.07m (Elliott *et al.*, 2004) and sampling rate of 5Hz. ADCP data were collected using a 1200 kHz Workhorse Rio Grande ADCP manufactured by Teledyne-RD Instruments, Inc.[2], which was mounted from a boat along with real-time kinematic Global Position System (RTK-GPS) (collecting position data at 10 Hz), and configured for a sampling rate of 1.7 Hz, bin size of 0.25 m, blanking distance of 0.25 m, Water Mode 1 and Bottom Mode 5 (TRDI, 2008). The ADCP transducer was submerged 0.24 m below the water surface and the depth of the centre of the first bin was 0.78 m. The RTK-GPS used real-time base station corrections providing sub-decimeter horizontal and vertical accuracy. Water velocity data were referenced to the RTK-GPS position data. Mean daily discharge and turbidity data (Figure 4.2.2) were obtained from the Missouri River at Boonville Gauging Station (USGS 06909000), which is approximately 48 km upstream from the first study site at Huntsdale (Figure 4.2.1). There are no significant inflows between the Gauging Station and the study sites.

[2] Any use of trade, product, or firm names is for descriptive purposes only and does not imply endorsement by the U.S. Government

Table 4.2.1. Summary of flow conditions and data collection. Q is the mean daily discharge, Q_E is the percent daily flow exceedance for years 1967 to 2009, depth is the average depth of the surveyed area, WSE is the water surface elevation at the upstream end of each surveyed area, and Thalweg is a representative thalweg elevation, not accounting for scour holes.

Date	Location	Q (m^3/s)	Q_E (%)	Depth (m)	Wing Dike Elevation (m)	WSE (m)	Thalweg (m)	Transect Data
May 28, 2008	Site A (Huntsdale)	3030	14.4	5.1 (14.0 max.)	168.5-169.5	172.0	162	• 66 Transects over 380 m • 5 and 20 m spacing (separate surveys)
May 29, 2008	Site B (Plowboy)	3030	14.4	5.9 (11.8 max.)	166.0-166.5	168.5	160	• 66 Transects over 388 m • 5 and 20 m spacing (concurrent survey)
June 4, 2008	Site B (Plowboy)	4332	6.2	7.3 (12.4 max.)	166.0-166.5	169.6	160	• 33 Transects over 230 m • 5 and 10m spacing (concurrent survey)

Spatial surveys of the two sites were carried out using densely spaced moving-boat transects that were orientated perpendicular to the streamwise flow direction (v_x) at each site (Figure 4.2.1). Transects were spaced a combination of 5 and 20 m apart (approximately 1 and 5 % of the channel width respectively), with the 5 m transects covering the area surrounding the wing dikes and the adjacent thalweg (see Figure 4.2.3 for indication of survey extents). Navigation software (HYPACK) was used to map the transect locations before each survey and together with RTK-GPS, was used to track the boat's position during measurements and help the driver maintain a position as close to the desired transect line as possible. Lateral variation of the boat position off the transect line rarely exceeded 5 m (i.e. 5 m transects rarely overlapped). Based on an average measured boat speed of 1.3 m/s during transect measurements, ADCP single-ping ensemble data were collected every 0.6 s, with an average distance between ensembles of approximately 0.8 m, while the average distance between pings for the 5 Hz vertical beam echosounder data was 0.26 m. At Site A (May 28) the 5 and 20 m transect surveys were measured independently (one after the other respectively), while the data at Site B (May 29 and June 4) were collected concurrently (Table 4.2.1). On each day of measurement, the surveying was completed in less than 5 hours, during which time the discharge remained constant and steady flow was assumed. A summary of the data collected is given in Table 4.2.1.

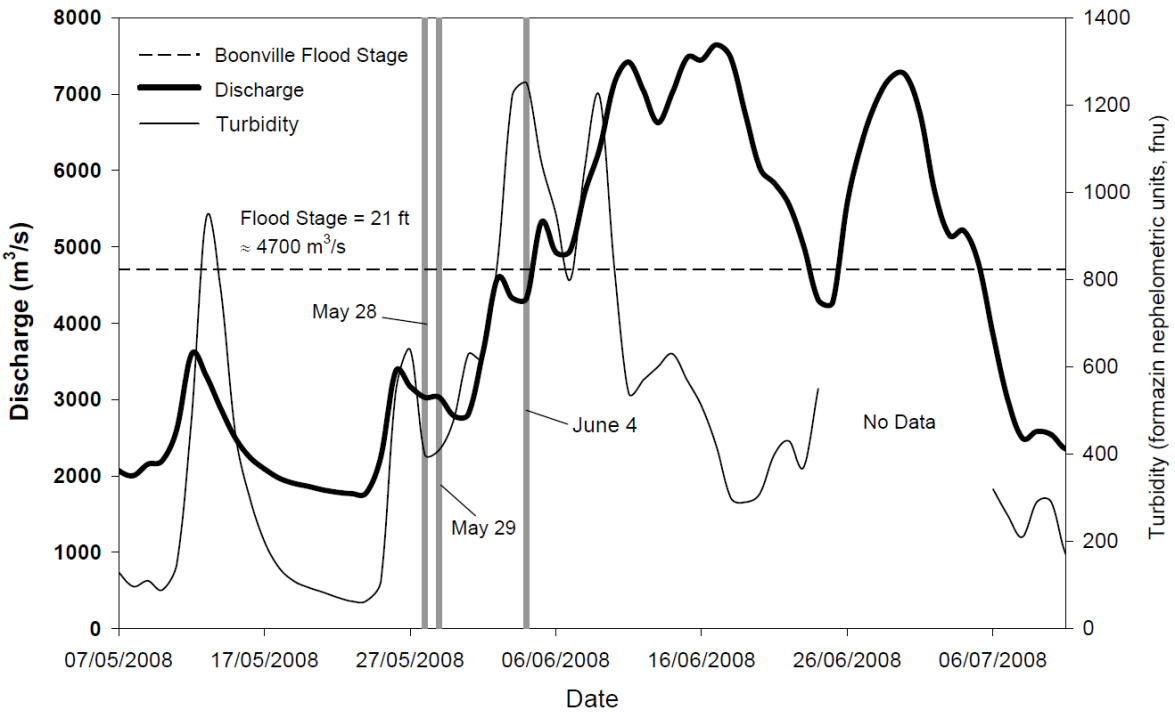

Figure 4.2.2. Hydrograph of daily mean discharges and turbidity for Missouri River at Boonville, Missouri (USGS 06909000), along with the date of each ADCP survey (vertical lines). Note the peak in flow between survey dates May 29 and June 4, and the extreme peak in turbidity on June 4th.

Bathymetry Data

The single-beam echosounder transducer (sonar) was used for simultaneous measurements of bed elevation for detailed mapping of the bathymetry. Single vertical-beam sonar data (sampling rate = 0.2 s) were used as they provide superior bathymetric detail (particularly in areas of abrupt slope changes), compared to the ADCP bottom-track depth (sampling rate = 0.6 s), which not only has a greater distance between data, but is also the average depth from four divergent beams. [However, it is also possible to use individual beam depths for a higher resolution bathymetry]. For each spatial survey, a two-dimensional (2-D) surface grid with a point spacing of 5 m was derived from interpolating the single-beam sonar data using

linear kriging, with a semivariogram model to fit best the data (Figure 4.2.3). Additional grid point spacings (3, 12 and 20 m) were also created (depending on the transect spacing of the original data), to asses the effect of grid spacing on the interpolated velocity field (Table 4.2.2). Figure 4.2.3 provides a detailed contour map of bed topography of the surveyed area at each site for two of the days where extensive spatial data were collected (May 28 and May 29). Figure 4.2.3 also indicates the survey extents of the 5 and 20 m transect spacing data, and the survey extents for the June 4 survey. The grid spacing for both contour plots in Figure 4.2.3 is 5 m by 5 m.

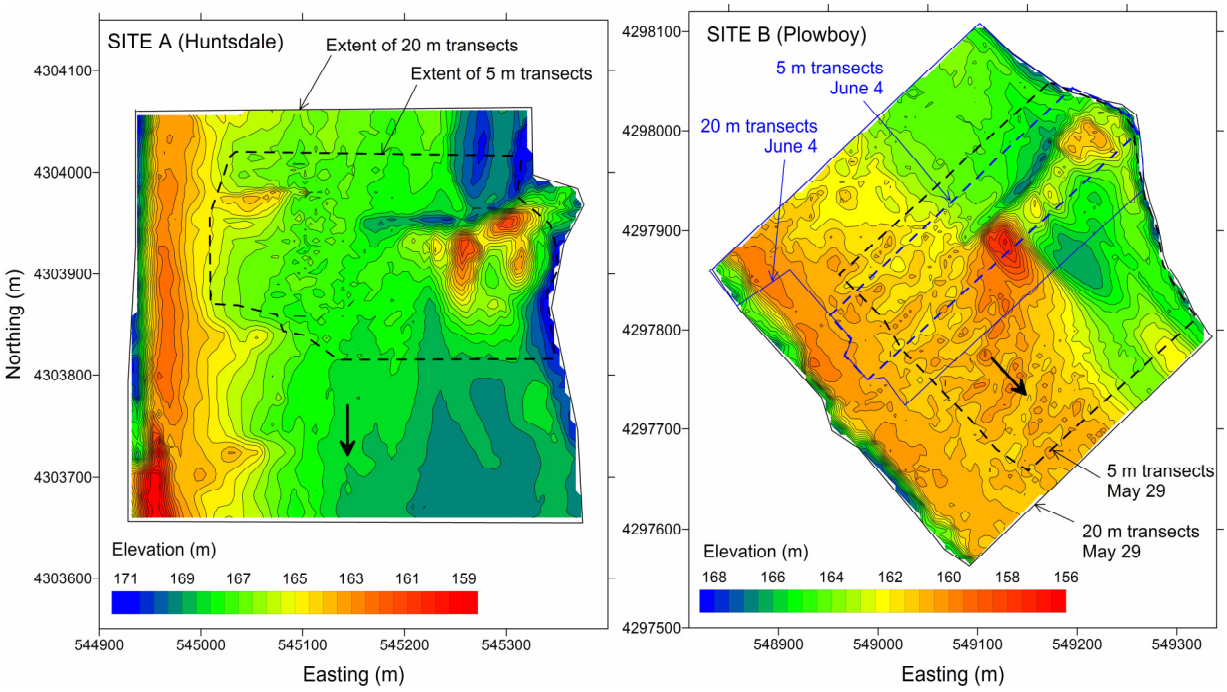

Figure 4.2.3. Contours of bed elevation and indication of survey extents at Site A (May 28) and B (May 29). All data are interpolated at 5 m resolution from data collected with 5 m and 20 m transect spacing (as indicated). Elevation data are from single beam sonar, using sea level (0 m) as datum. The survey extent for June 4 is also indicated for Site B.

Velocity Data - Processing and Interpolation

The ADCP has four divergent transducers spaced at 90º from each other and all orientated with a 20º angle with respect to the vertical. A velocity profile (single ensemble of multiple bins in the vertical direction) is calculated by assuming that the divergent beams are all sampling at the same horizontal location at the center of the beam pattern. In fact, the individual radial components of velocity along each beam (and for each bin), are combined (along with heading data from the internal compass) to calculate the easting, northing and vertical components of water velocity; v_e, v_n and v_z respectively for each 0.25 m high bin in the averaged velocity profile. The spatial position of the averaged profile is assigned using navigation data from RTK-GPS. Calculating an averaged velocity profile from divergent beams requires the assumption that the flow is homogenous over the lateral separation of the beams, which increases with depth. For the four-beam Workhorse Rio Grande ADCP, the diameter of the circle that encloses the insonified sampling areas of each beam (D_s) varies (linearly) from 1.1 m at a depth of 1 m to 8.3 m at a depth of 10 m (based on equation 4 from Rennie *et al.* (2002)). Since only three beam velocities are required to determine the three components of velocity, the fourth beam of a four-beam ADCP provides a redundant measurement of vertical velocity, from which error may be quantified. The error velocity (v_ε) is the difference between the vertical velocity measured by one set of two beams and the vertical velocity measured by the other set of two beams, scaled to be indicative of the variance of the horizontal velocity. Mean depth-averaged streamwise velocity (U) for each spatial survey was 1.3 m/s for both May 28 (5 and 20m transect data) and May 29, and 1.5 m/s for June 4.

For plotting, calculation and overall flow structure evaluation purposes, easting and northing components of velocity (v_e and v_n) were used to determine steamwise (v_x) and cross-stream (v_y) components of velocity at each site (Figure 4.2.1 A and B). Streamwise and cross-stream velocity directions were designated as parallel and perpendicular to the river banks, respectively. Therefore, given the orientation of each site with respect to north; v_x and v_y were set equal to negative v_n and positive v_e at Site A, while v_e and v_n at Site B were rotated using simple vector rotation to determine v_x and v_y, where the angle of rotation was 43º counter-clockwise (0.7505 radians). The true vertical velocity component (v_z) was assumed to equal the measured value since ADCP vertical velocity was corrected for pitch, roll and vertical boat motions. Vertical velocity was corrected for vertical boat motion equal to or greater than 0.1 m based on changes in boat elevation from the GPS data, while the ADCP is internally calibrated to compensate for pitch and roll. Less than 10 % of all the data required correction for vertical boat motion. The bottom 6 % of bins in each profile were rejected in post-processing to eliminate any water velocity error or bias due to side-lobe interference.

In order to maintain a uniform and structured grid with points (and therefore grid lines) orientated in the streamwise (x) and cross-stream (y) direction (for better interpolation of fluid flow properties), the bathymetry data at Site B were first rotated before interpolation to the surface grid and then rotated back to the original Earth coordinates, since the software used for interpolation of the surface grid is by default orthogonal in the East-North direction. A 3-D volume grid was then generated from each of the 2-D surface grids (one for each set of spatial data), with a vertical spacing of 20 cells and a top elevation of 170.5 m (Site A), 167 m (Site B, May 29) and 168.1 m (Site B, June 4). A constant top grid elevation assumes zero water surface slope, which is consistent with the GPS data, where the drop in water

surface elevation recorded along each of the surveyed reaches did not exceed 0.15 m (or less than one measured ADCP bin height = 0.25 m). The top elevation of each grid was 1.5 m below the upstream water surface elevation (172 m at Site A, 168.5 m at Site B on May 29 and 169.6 m at Site B on June 4) and was specified as such in order to eliminate erroneous data that were found near the water surface. Despite correction based on GPS elevation changes (due to boat motion), data from the top 3-4 bins of each ensemble were found to have unusually high negative vertical velocities, and in some cases v_z < -0.5 m/s. It is possible that during transect data collection, the local flow field immediately surrounding the ADCP was affected by the boat-generated wake or flow disturbance from the submergence of the ADCP itself, and without any physical justification for the observed vertical velocities, these data points were excluded from the interpolation. This negative bias in vertical velocity immediately below boat-mounted ADCPs has also been observed elsewhere (Dinehart and Burau, 2005; Muste *et al.*, 2010) and the data are typically rejected.

Single-ping ensemble velocity data (v_x, v_y, v_z and v_ε) were interpolated into each 3-D grid using kriging. The kriging parameters included an eight-point octant search, a range of 0.3, no-drift and a zero value of 0.05. The range is the distance beyond which source points become insignificant when kriging and is equal to the fraction of the length of the diagonal of the 3-D volume which contains the data points. A range of zero means that any point not coincident with the destination point is statistically insignificant, while a range of one means that every point in the dataset is statistically significant for each point. The zero value is a non-dimensional measure of variance (from 0-1) of the certainty of the value at a data point. A value of 0 will specify an exact fit with the source points, while any value above zero will allow some variance and essentially a smoothing of the data. Continuity within the interpolated grids was checked by integrating streamwise velocity over select slices taken at

the upstream and downstream extents of each grid. The two 20 m survey grids for May 28 and May 29 were checked (since these were the only surveys to span the entire width of the river) and the percentage differences in discharge were 1 and 3 % respectively.

To quantify the smoothing and overall effect of the interpolation on the velocity data, interpolated (grid) data were extracted at every point location corresponding to each measured bin in the ADCP profile measurement, for direct comparison between interpolated (grid) and measured (ADCP) values. Joint probability density plots comparing these data for each of the 5 and 20 m transect spatial surveys on May 28 are shown in Figure 4.2.4. The joint probability frequencies have been normalized by the total population of compared points for each set of variables, such that the cumulative joint distribution of each joint probability density plot equals 1. These plots confirm that all compared data, and in particular the highest frequencies, are centered on the identity line. In both transect cases, the streamwise and cross-stream velocity components have roughly the same extent of divergence from unity (over 99% of all data are within +/- 1 m/s, while 90% of all data are within +/- 0.5 m/s for both v_x and v_y). One difference between these components is the extent of velocity magnitude and subsequent spread represented by the joint probability plot: v_x values range from approximately -1 to 3 m/s, while v_y values range from approximately -1.6 to 1.6 m/s. This difference in range alters the appearance of the v_x plots compared to v_y in Figure 4.2.4. In both cases, the vertical velocity shows very little deviation from the identity line (< 0.2 m/s). The lack of smoothing to the vertical velocity is most likely because the range of velocity magnitudes in the vertical direction is low, and because the vertical velocity is actually the average of two independent measurements of vertical velocity (two redundant measurements of v_z from two different beam pairs). The flatness of the joint probability plots

in the horizontal direction, which is most apparent for v_x and v_y, demonstrates the magnitude of smoothing for the extreme (positive and negative) values.

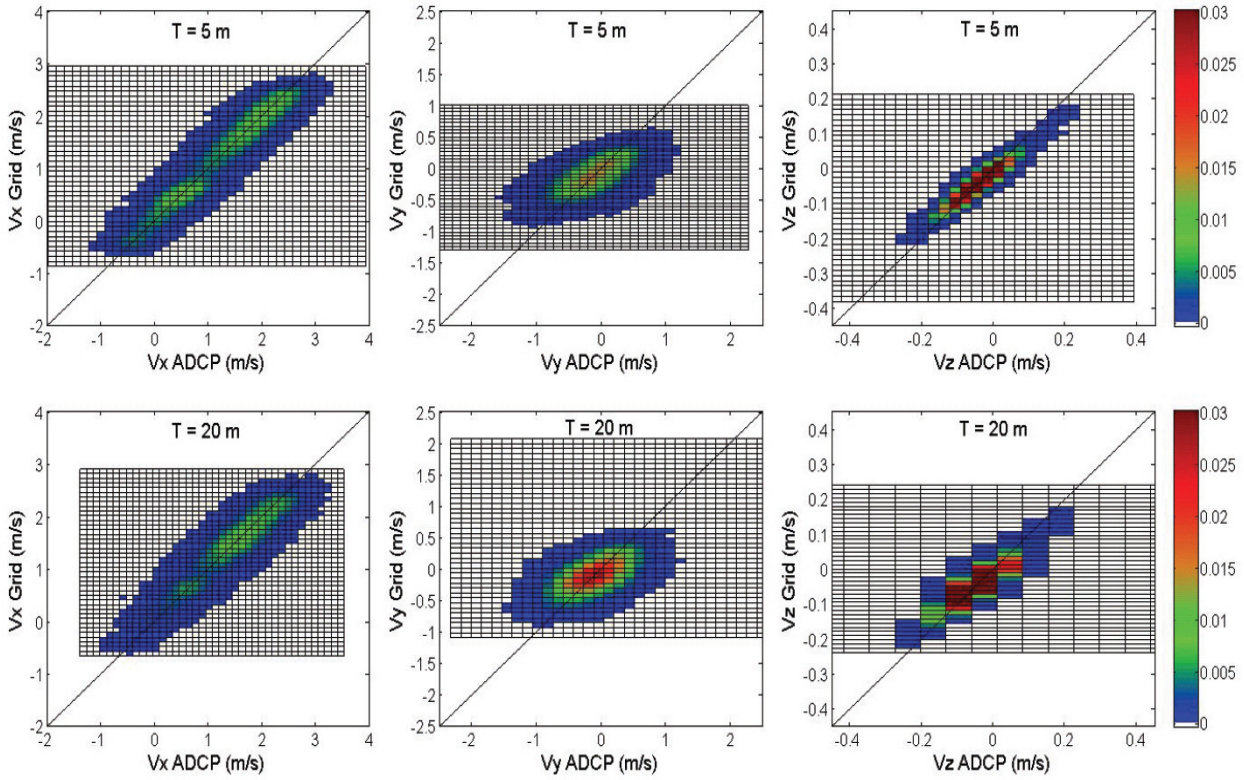

Figure 4.2.4. Joint probability density plots comparing interpolated (grid) and ADCP velocity data for transect spacings (T) of 5 and 20 m for May 28 data. Velocity data are represented by streamwise (v_x), cross-stream (v_y) and vertical velocity (v_z). Joint probability frequencies have been normalized by the total population of compared points for each set of variables, such that the cumulative joint distribution of each plot equals 1.

The mean absolute difference for each velocity component ($\overline{\Delta v_x}$, $\overline{\Delta v_y}$ and $\overline{\Delta v_z}$) between all compared points is calculated as

$$\overline{\Delta v_m} = \frac{\sum_i^n \left| v_{m,grid_i} - v_{m,ADCP_i} \right|}{n} \qquad \text{for } m = x, y \text{ and } z \qquad (4.2.1)$$

where n represents the total number of compared (coincident) data points; and $v_{m,grid}$ and $v_{m,ADCP}$ are the velocity components in the x, y and z direction for the interpolated grid and ADCP data respectively. Similarly, the root mean square error (*RMSE*) can be calculated as

$$RMSE_{(m)} = \sqrt{\frac{\sum_{i}^{n}\left(v_{m,grid_i} - v_{m,ADCP_i}\right)^2}{n}} \qquad \text{for } m = x, y \text{ and } z \qquad (4.2.2)$$

A summary of results for various grid sizes, zero values and range values is provided in Table 4.2.2. It should also be noted that the mean of the estimation error ($\overline{\varepsilon_{(m)}}$), where estimation error, $\varepsilon_{(m)} = v_{m,grid_i} - v_{m,ADCP_i}$ was zero ($\overline{\varepsilon_{(m)}} = 0.00$) for all velocity components (except for the 20 x 20 grid, 20 m transect data, where $\overline{\varepsilon_{(y)}} = 0.01$), confirming the interpolation estimates were unbiased by drift.

Table 4.2.2. Summary of sensitivity analysis for interpolation of May 28 velocity data. Dark grey highlighted results indicate the grid used for velocity contour plots and vortex core analysis.

Data	Grid Spacing[1] (m)	n[2]	Zero Value[3]	Range[4]	Mean Absolute Difference[5] (m/s)			Root Mean Square Error[6] (m/s)		
					$\overline{\Delta v_x}$	$\overline{\Delta v_y}$	$\overline{\Delta v_z}$	$RMSE_{(x)}$	$RMSE_{(y)}$	$RMSE_{(z)}$
5 m transects	3 x 3	163,392	0.01	0.3	0.23	0.25	0.02	0.30	0.32	0.02
			0.05	**0.3**	**0.24**	**0.25**	**0.02**	**0.30**	**0.32**	**0.02**
				0.1	0.23	0.25	0.02	0.30	0.32	0.02
	5 x 5	162,739	0.01	0.3	0.26	0.27	0.02	0.33	0.35	0.02
			0.05	0.3	0.26	0.27	0.02	0.33	0.35	0.03
20 m transects	5 x 5	129,023	0.01	0.3	0.25	0.25	0.02	0.32	0.33	0.03
			0.05	**0.3**	**0.25**	**0.25**	**0.02**	**0.32**	**0.33**	**0.03**
				0.1	0.25	0.25	0.02	0.32	0.33	0.03
	12 x12	124,164	0.01	0.3	0.28	0.27	0.02	0.35	0.35	0.04
			0.05	0.3	0.28	0.27	0.02	0.35	0.35	0.04
	20 x 20	117,348	0.01	0.3	0.28	0.28	0.03	0.36	0.36	0.04
			0.05	0.3	0.28	0.28	0.03	0.35	0.36	0.04

[1] Grid spacing refers to bathymetry grid and represents cell spacing in the x and y direction. All interpolated volumes had 20 cells in the vertical, except for the 20 x 20 grids, which had only 10 cells in the vertical.
[2] n represents the total number of matched points.
[3] See text.
[4] See text.
[5] Mean absolute difference based on Equation 4.2.1.
[6] Root mean square error of the estimate based on Equation 4.2.2.

The results in Table 4.2.2 quantify the difference between interpolated and ADCP data and represent a sensitivity analysis for the interpolation technique employed. For both the 5 and 20 m transect data, the results indicate that as grid size is reduced there is a slight improvement in the interpolated results, while the zero value and range had little to no effect. For the grid sizes tested, both mean absolute difference and root mean square error are reduced by 0.03 m/s for v_x and v_y and by 0.01 m/s for v_z (for both data sets). Overall, mean absolute differences (and mean absolute percentage differences) for v_x and v_y ($\overline{\Delta v_x}$ and $\overline{\Delta v_y}$) ranged between 0.23 – 0.28 m/s (76 - 130 %) and 0.25 – 0.28 m/s (300 - 330 %) respectively, while the root mean square error ranged between 0.30 – 0.35 m/s and 0.32 – 0.36 m/s for $RMSE_{(x)}$ and $RMSE_{(y)}$ respectively. Absolute errors in the streamwise and cross-stream components were similar. The large mean absolute percentage differences were the result of a few high percentage difference values, due to division by near-zero values of the local measured velocity component. This was more common for the cross-stream component because v_y was centred on zero, resulting in larger mean absolute percentage differences for v_y than v_x.

Comparing the 5 and 20 m data, the mean absolute difference and root mean square error were uniformly lower for all velocity components for the 5 m transect data compared to the 20 m data. Together, these results suggest that aside from grid spacing, the interpolated velocities are not sensitive to the range of parameters tested.

Rennie and Church (2010) estimated single-ping, single-bin local mean streamwise velocity uncertainty in the Fraser River (gravel-bed river) to be 0.3 m/s, based on variance due to both measurement error and real fluctuations (temporal variability) due to turbulence. Similar values were found for the same section of the Missouri River studied in this paper

(Rennie, *accepted*). Thus, the spatial smoothing provided by kriging reported above can be assumed to be within (or no greater than) the estimated uncertainty of ADCP water velocity measurements. In our case, the smoothing due to kriging is reducing (or countering) the inherent uncertainty of single-ping measured velocity. Furthermore, Rennie and Church (2010) found the mean uncertainty of depth-averaged velocity to be 0.1 m/s, which would represent 13 and 15 % of the mean depth-averaged streamwise velocity (U) for May 28 and 29 (U = 1.3 m/s) and June 4 (U = 1.5 m/s) respectively.

To demonstrate the smoothing effect on velocity data, a direct comparison between single-ping ADCP data and the interpolated values was made along select individual vertical profiles. Two such sets of profiles are shown in Figure 4.2.5, where profiles of raw ADCP data are compared to interpolated (grid) profiles and 11 ensemble averages, for two different geographical locations (Points 1 and 2, see Figure 4.2.7 and Figure 4.2.11) for each of the 5 and 20 m transect data. The 11 ensemble average profile incorporated the central (single ensemble) ADCP profile and five profiles on either side of the same transect line (approximately 4 m on either side). Overall, the interpolated (grid) and 11 ensemble average results show a good fit with the single-ping ADCP data. The general shape of the three profiles match, including changes in local maxima and minima with depth, with both the interpolation and ensemble-averaging providing some smoothing of the extreme (outlying) points along each profile. The interpolated 3-D grid values fit closely with the 11 ensemble average profiles. Interestingly, the best fit among all three profiles (single ping ADCP data, 11 ensemble average and the interpolated grid) is found (for both transect spacings) in the vertical velocity component.

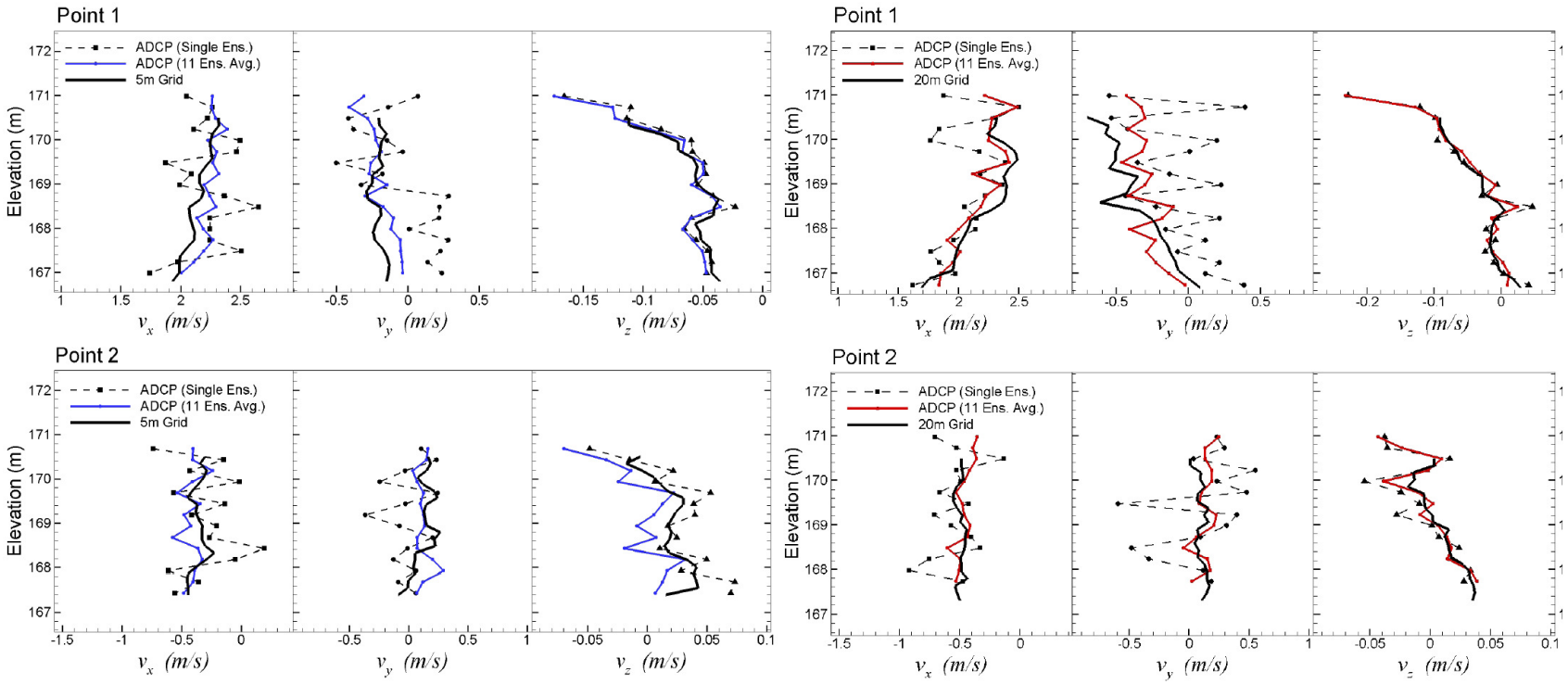

Figure 4.2.5. Direct comparison between single ping ADCP data (dashed line); 11 ensemble average (blue and red) and the interpolated grid (black) along two individual vertical profiles, located at Points 1 and 2, for 5 m (left, blue) and 20 m (right, red) data. (Refer to Figure 4.2.7 and Figure 4.2.11 for the point locations).

To demonstrate the smoothing effect spatially, another comparison is made using ADCP data from a single transect and the interpolated values for a 2-D slice from the 3-D (interpolated) grid, taken along the same transect line (Figure 4.2.6). Overall, all three components of velocity show good agreement: corresponding regions of comparable velocity (magnitude and direction) can be seen between the measured data and the interpolation. In some regions, the magnitude of velocity is slightly lower in the interpolated results, which is expected due to the spatial smoothing. Distinct flow patterns, such as the neighbouring regions of highly positive and negative velocity (which is evident in all three velocity components) are found over the left hand scour hole, for both the ADCP data (Figure 4.2.6, left) and interpolated results (Figure 4.2.6, right). Error velocities (raw and interpolated values) are also shown in Figure 4.2.6 to illustrate the distribution and magnitude of error velocity through the same selected transect and associated scour holes. Error velocity (positive and negative) is highest over the left hand scour hole, where beam spread is greatest and depth most variable, and where velocities are most heterogeneous. The error velocity plots in Figure 4.2.6 demonstrate how the smoothing due to interpolation reduces the spatially averaged error velocities considerably, with most of the interpolated section having $|v_\varepsilon| < 0.2$ m/s except for the region over the left hand scour hole. How much smoothing is applied to all of these distinct velocity patterns will not only depend on the velocity data along the section, but also on the strength (or presence) of the same patterns in the neighbouring upstream and downstream transects.

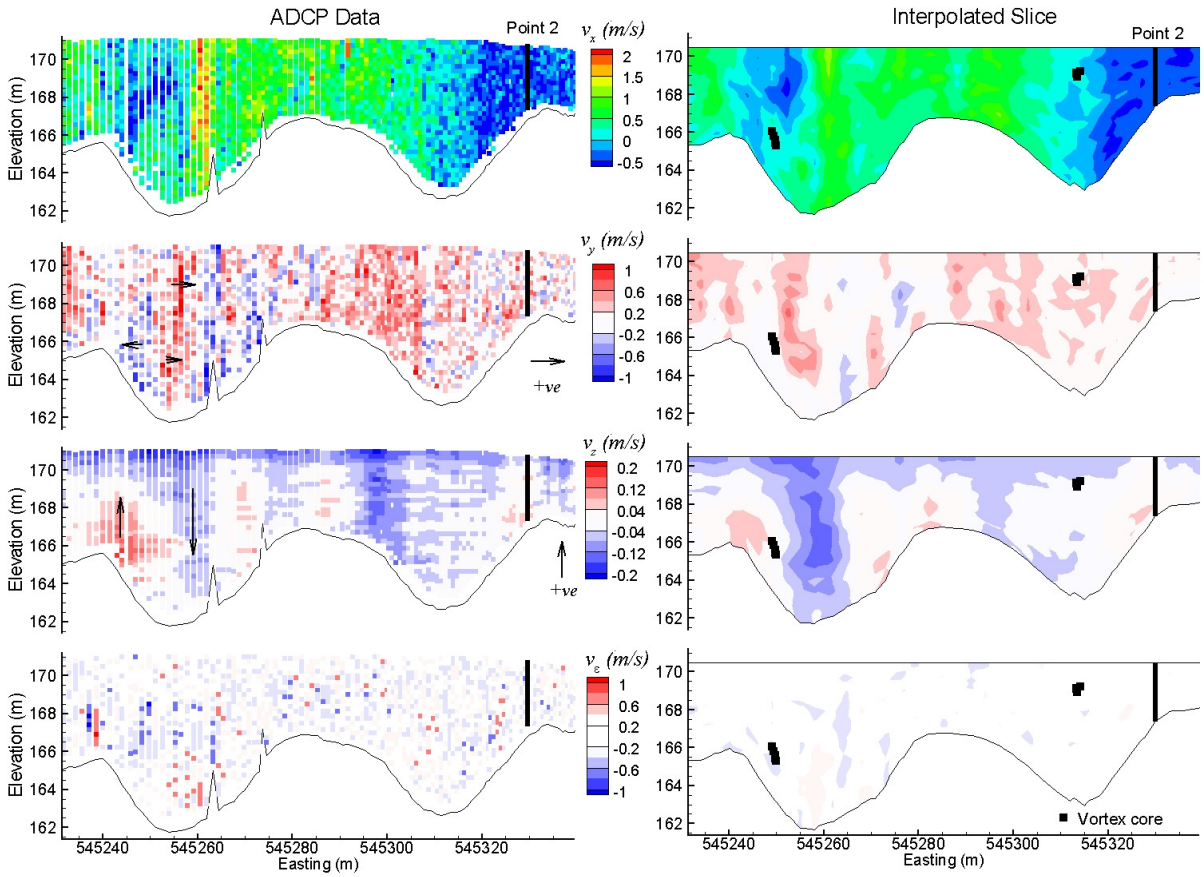

Figure 4.2.6. Comparison between ADCP velocities (left) and interpolated results (right) for a portion of one transect on May 28th. The ADCP transect is from the 5 m (transect spacing) survey and corresponds with the location of slice 4 in Figure 4.2.7 and Figure 4.2.11. The interpolated data represents a portion of a single slice from the 3-D volume interpolation (a portion of slice 4 in Figure 4.2.11). Vertical dimension is scaled at 4:1 with the horizontal. The location of the velocity profile at point 2 (Figure 4.2.5) is shown for reference. Cross sections are viewed looking upstream. Black arrows indicate neighbouring regions of opposite flow direction and are not scaled according to magnitude. Irregularities (i.e. spikes) in the bed contours represent measurement error in the raw ADCP data.

Identifying a vortex

In most open channel flow examples, turbulence is characterised by the measurement of velocity fluctuations, from which statistical parameters such as turbulence intensity,

Reynolds shear stresses, and turbulent kinetic energy may be calculated. However, these parameters are based on long-term averaging from stationary time series measurements of velocity, which is not compatible with the objectives of spatially mapping complex flow fields in large rivers using moving-boat ADCP measurements. Nevertheless, turbulent components are never independently random; they are always correlated with each other in both space and time (Nezu and Nakagawa 1993) and it may be possible to identify dynamically significant, large-scale vortical regions from the mean (spatially averaged) flow field.

In complex turbulent flows, coherent structures may be identified by the presence of vortices, where turbulent (or in this case velocity) components are correlated with each other in both space and time. By this definition, the interpolated volume of 3-D velocities (generated from individual transect data) may be combined to extract such flow features by determining spatial correlations (if any) in velocity gradients. For a 3-D velocity field, the most common criteria for identifying the presence of vortices are the *Q–criterion* (Hunt *et al.*, 1988), the *Δ-criterion* (Chong *et al.*, 1990), and the λ_2*-criterion* (Jeong and Hussain, 1995). For comparison, a fourth criterion based on absolute vorticity magnitude ($|\omega|$) may also be added to this list. Each of these criteria is defined below:

- *Q–criterion* (Hunt *et al.*, 1988): $$Q = \frac{1}{2}\left[|\boldsymbol{\Omega}|^2 - |\boldsymbol{S}|^2\right] > 0 \qquad (4.2.3)$$

- *Δ-criterion* (Chong *et al.*, 1990): $$\Delta = \left(\frac{Q}{3}\right)^3 + \left(\frac{\det \nabla v}{2}\right)^2 > 0 \qquad (4.2.4)$$

- λ_2*-criterion* (Jeong and Hussain, 1995): $$\lambda_2\left(\boldsymbol{S}^2 + \boldsymbol{\Omega}^2\right) < 0 \qquad (4.2.5)$$

- $|\omega|$*–criterion*: the region of absolute vorticity magnitude ($|\omega|$) is greater than a certain threshold

where $\boldsymbol{S} = \frac{1}{2}\left[\nabla \upsilon + (\nabla \upsilon)^T\right]$ is the rate-of-strain tensor, $\boldsymbol{\Omega} = \frac{1}{2}\left[\nabla \upsilon - (\nabla \upsilon)^T\right]$ is the vorticity tensor, $\nabla \upsilon$ is the velocity gradient, $(\nabla \upsilon)^T$ is the transpose of the matrix $\nabla \upsilon$, and $\lambda_2(\mathrm{A})$ denotes the intermediate eigenvalue of a symmetric tensor (A). Vorticity magnitude (ω) is defined as the vector sum of the three components of rotation (ω_x, ω_y and ω_z) about the *x*, *y* and *z*-axis respectively. The rotation about each axis is defined as the average of the angular velocities perpendicular to the axis of rotation such that

$$\omega_x = \frac{1}{2}\left(\frac{\partial v_z}{\partial y} - \frac{\partial v_y}{\partial z}\right),\ \omega_y = \frac{1}{2}\left(\frac{\partial v_x}{\partial z} - \frac{\partial v_z}{\partial x}\right) \text{ and } \omega_z = \frac{1}{2}\left(\frac{\partial v_y}{\partial x} - \frac{\partial v_x}{\partial y}\right) \qquad (4.2.6)$$

where $\partial v_y/\partial x$ and $\partial v_z/\partial x$, $\partial v_x/\partial y$ and $\partial v_z/\partial y$, and $\partial v_x/\partial z$ and $\partial v_y/\partial z$ are the angular velocities along the *x*, *y* and *z*-axis respectively (assuming counter-clockwise rotation is positive).

Vortex cores are often associated with regions of high vorticity and vorticity magnitude (ω) has often been used to represent the presence of vortex cores. However, there is no universal threshold over which vorticity is to be considered high and so the $|\omega|$*–criterion* is subjective as it relies on an arbitrary threshold of $|\omega|$. Further, vorticity may be high in parallel shear flows where no vortices are present (Haller, 2005). Indeed, when the background shear is comparable to the vorticity magnitude within the vortex core (as is likely the case in a shear flow), the $|\omega|$*–criterion* may not be sufficient (Jeong and Hussain, 1995). In our case, high shear flow is expected in the vicinity of the submerged wing dike, which suggests the $|\omega|$*–criterion* would be inadequate for identifying vortices. We found that

when the vorticity vector ω was used to identify vortex cores, the location of these vortices was similar to the other criteria (concentrated along and downstream of the wing dikes where shear flow was expected), but a noticeably greater number were found (in some cases nearly double the number found by the other criteria). These results, combined with the findings of others (Jeong and Hussain, 1995 and Haller, 2005) confirm the potential ambiguity of using ω to identify vortices.

In the λ_2-*criterion* vortex determination, Jeong and Hussain (1995) justify their method over others through testing of the four above criteria using a number of different analytic flow examples and direct numerical solution (DNS) databases. The authors found that among these criteria, only the λ_2-*criterion* was able to represent the topology and geometry of vortex cores for a large variety of flows. However, in most of the flow cases tested, the *Q-, Δ-* and λ_2-*criterion* resulted in similar vortex cores, particularly in the case of vortices in a shear layer. Most recently, Sanjou and Nezu (2009) successfully used the *Δ-criterion* for indentifying coherent horizontal vortices in a meandering compound open channel flow. It is the $|\omega|$*–criterion*, which requires an arbitrary cutoff, that is the least appropriate. Given, (i) that all three (*Q, Δ* and λ_2) criterion produce similar results for vortices in a shear layer, (ii) the success of the λ_2-*criterion* where other criteria are inadequate, and (iii) that overall, this method tends to give fewer spurious vortex cores (Jeong and Hussain, 1995), the λ_2-*criterion* was chosen for identifying vortex cores in the present study.

4.2.4 Results

Bed Morphology

Contour plots of the bathymetry and depth (Figure 4.2.3 and Figure 4.2.7) show a number of different scour holes (large and small) in the area surrounding both wing dikes. At Site B (May 29), one large scour hole (~ 11 m deep) was found directly at the wing dike tip, near the center of the channel. Flanking of the wing dike along the left bank (at both Site A and B) produced relatively large scour holes (~ 8 to 10 m) and likely has been responsible for the observed bank erosion at these locations. At both sites, the regions of scour directly downstream of the wing dike are likely due to engineered notches in the wing dike and/or the plunging action of the flow. At Site A, the notches in the wing dike are more pronounced, along with the corresponding scour holes immediately downstream of the structure. The lack of any scour hole at the tip of the wing dike at Site A is likely due to the larger notches at this site, one of which can be seen at lower flow (near the middle of the structure) from the 2006 air photo (Figure 4.2.1 A). These larger gaps at Site A provide more through-flow and therefore less constriction of the flow at the wing dike tip.

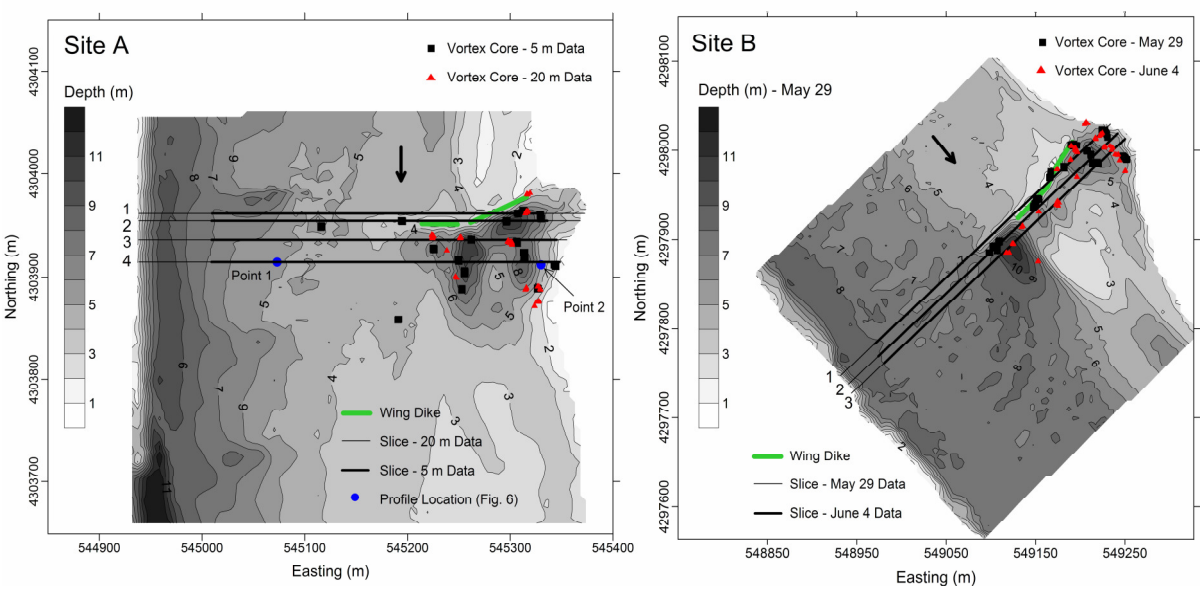

Figure 4.2.7. Contours of depth and the location of vortex cores at Site A (left) and Site B (right). Vortex cores are concentrated downstream of the wing dike and over individual scour holes. Vertical slices are labelled 1, 2, 3 and 4 (Site A) and 1, 2 and 3 (Site B). The location of vortex cores in cross-section are shown in Figure 4.2.10 and Figure 4.2.11.

The change in bathymetry between the two surveys at Site B is represented by a difference map (Figure 4.2.8 A). The maximum change occurred at the tip of the wing dike, where the depth of the upstream edge of the scour hole was reduced by up to 5 m between May 29 and June 4. Between May 29 (Q = 3030 m^3/s) and June 4 (Q = 4332 m^3/s) the flow peaked on June 2 at 4587 m^3/s (Figure 4.2.2). It is possible that this higher flow event between the two surveys caused enough transport to infill the upstream end of the scour hole. Bed velocity data at this site (determined using the bias in ADCP bottom track data (Rennie *et al.*, 2002)) show no bed load transport at the wing dike tip for May 29 (Jamieson *et al.*, *in press*), while some transport in this region (~ 0.1 – 0.3 m/s) was found for June 4 (Figure 4.2.8 B), when flow was slightly higher. However, there was some loss of ADCP bottom-tracking data immediately downstream of the wing dike tip (Figure 4.2.8 B), likely due to the

combination of higher turbidity on this day of measurement (Figure 4.2.2) and the naturally occurring turbulence in this region (i.e. vortex shedding at the wing dike tip). High concentrations of suspended sediment cause high absorption and scattering of the acoustic signal, resulting in weak bottom reflections that may be insufficient to detect the threshold required for identifying the bottom (Simpson, 2001). Both the elevation difference and bed velocity maps (Figure 4.2.8) confirm that the most dynamic region of bed load transport is concentrated within the thalweg, which is consistent with previous bed velocity maps (Jamieson *et al.*, *in press*) and the measured bed forms (Figure 4.2.3 B). The correspondence of bed features (such as scour holes) with the flow field will be examined in the next section.

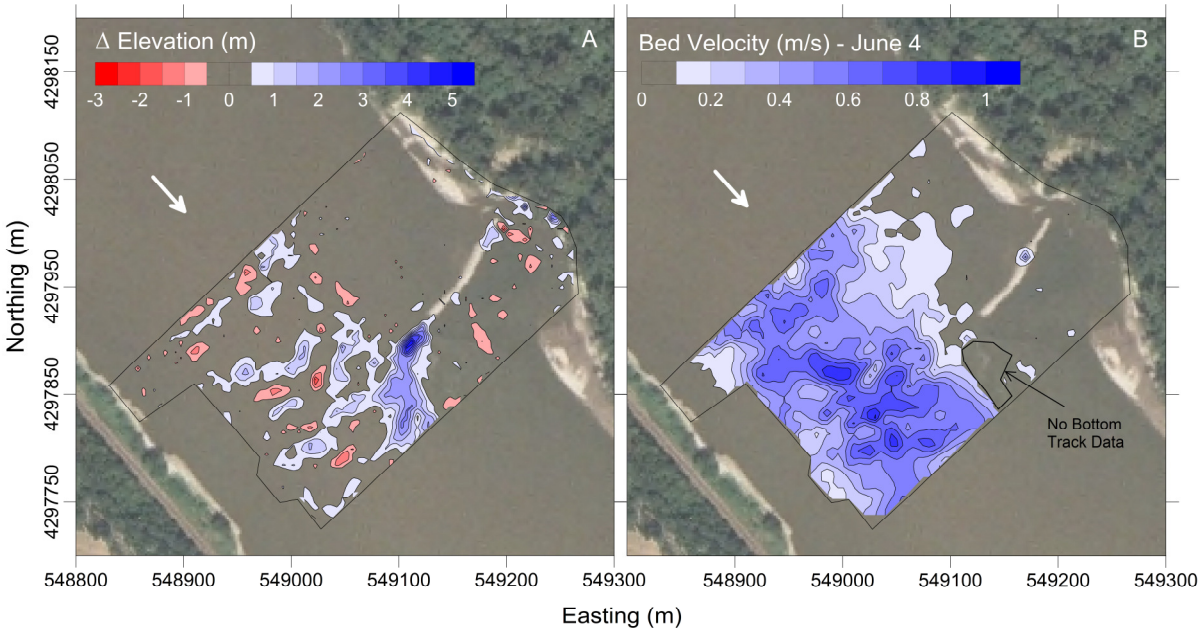

Figure 4.2.8. (A) Contours of the change in bed elevation from May 29, 2008 (Q = 3030 m^3/s) to June 4, 2008 (Q = 4332 m^3/s). The increase in elevation at the wing dike tip (blue contours) represents the infilling of the scour hole (Figure 4.2.3 B) between the two dates. (B) Contours of bed velocity for June 4. All data are interpolated at 5 m resolution.

Three-Dimensional Flow Field

To illustrate the 3-D flow field measured in the vicinity of the wing dike at Site A, the entire 3-D volume of interpolated velocity data for the 5 m transect data on May 28 is shown in Figure 4.2.9. In this figure, two 3-D views are presented to show contours of streamwise velocity (v_x) and select calculated stream traces. The stream traces are possible trajectories of neutrally buoyant particles calculated from the interpolated flow field and provide effective flow visualization of the plunging flow over the wing dike (Figure 4.2.9 A) and recirculating flow downstream of the wing dike and near the left bank (Figure 4.2.9 B). To illustrate the 3-D flow field at Site B, cross-sectional contours of v_x, v_y and v_z for three different slices (1, 2 and 3) have been extracted from the interpolated May 29 3-D volume data and are shown in Figure 4.2.10 (slice locations are shown in Figure 4.2.7). By progressing downstream from slice 1 to 3, it is possible to observe the individual changes in magnitude and sign of each velocity component as flow passes directly over the wing dike. Of particular interest are the reverse flow in streamwise velocity ($v_x < 0$) and the variation in cross-stream and vertical velocity components (referred to herein as secondary velocities), v_y and v_z. Neighbouring regions of highly positive and highly negative v_x, v_y and v_z velocity demonstrate local areas of dynamic mixing, recirculation and highly 3-D flow. The highest magnitudes of secondary velocity appear to occur at the wing dike tip (slice 1), directly above the wing dike crest (slice 1) and inside the scour hole (slice 2 and 3). The high positive vertical velocity in slice 1, coupled with high negative vertical velocity in slice 2 approximately 13 m downstream, reveal the plunging action of the flow that is dominating this region. Similarly, the regions of sharp horizontal velocity gradients that are evident from the contours of streamwise velocity (particularly in slice 2), support the assumption of complex mixing and recirculating flow

being generated by flow separation at the wing dike. Neighbouring regions of positive and negative streamwise velocity are most pronounced in the scour hole near the wing dike tip (slice 2) and behind the wing dike near the left bank (slices 2 and 3).

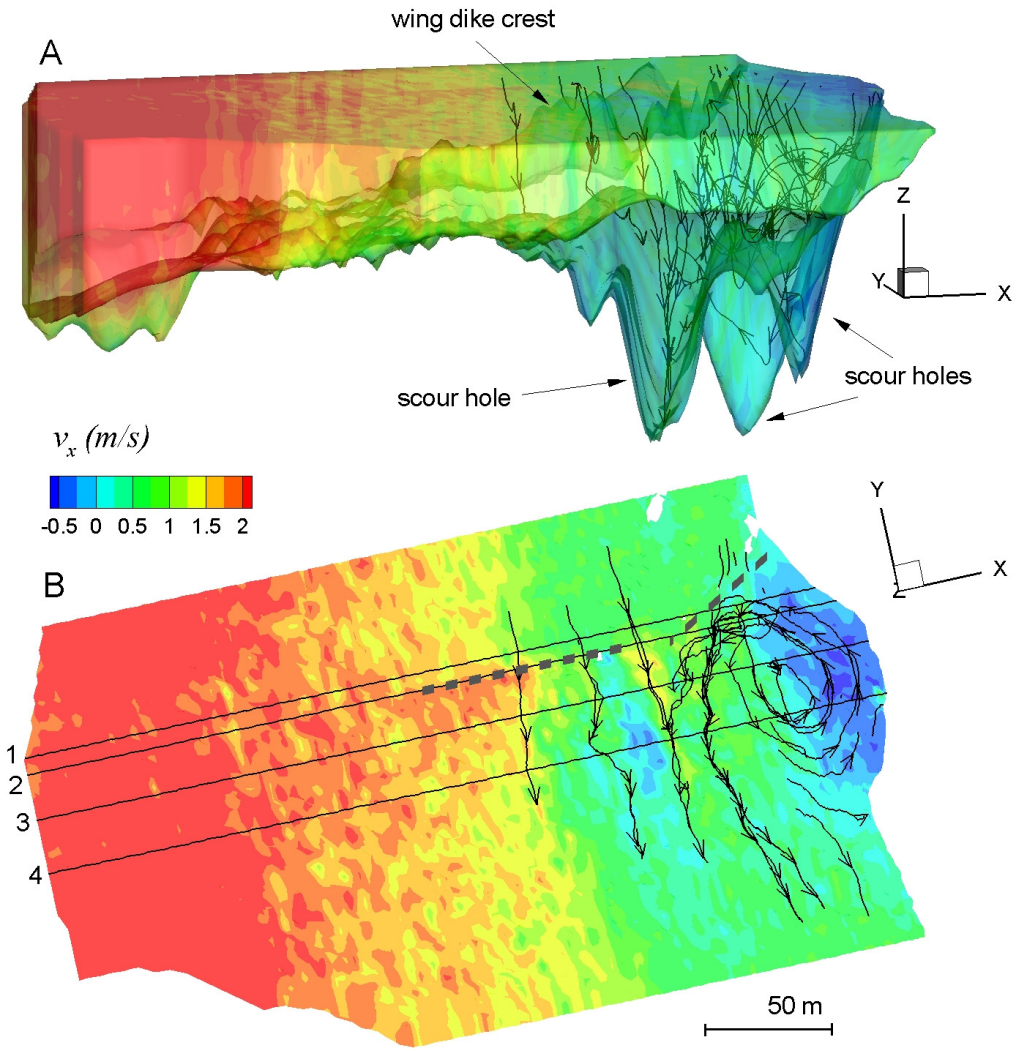

Figure 4.2.9. Three-dimensional views of the interpolated velocity field, for the 5 m transect data on May 28: (A) oblique view of downstream velocity contours (v_x) and calculated stream traces; and (B) plan view of the same stream traces in (A) superimposed on contours of downstream velocity taken near the water surface (at z = 170.25 m). The vertical dimension in (A) is scaled 10:1 with the horizontal. In (B) the slices 1, 2, 3 and 4 are shown for reference, and the grey dashed line represents the approximate location of the wing dike crest. The X and Y direction refer to the Easting and Northing directions respectively.

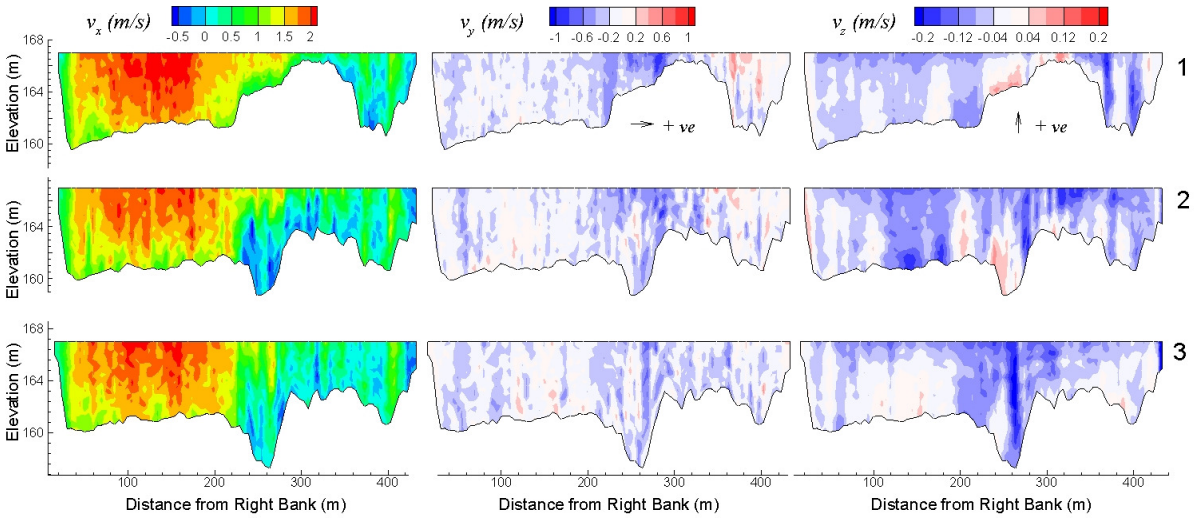

Figure 4.2.10. Interpolated contours of streamwise (v_x), cross-stream (v_y) and vertical velocity (v_z) at three slices (1, 2 and 3) for May 29 data. See Figure 4.2.7 B for slice locations. Vertical dimension is scaled at 15:1 with the horizontal. Cross sections are viewed looking upstream.

Contours of streamwise velocity are very similar between the 5 and 20 m transect data (Figure 4.2.11). In particular, distinct regions of vertical shear (as evidenced by neighbouring regions of highly negative and highly positive streamwise velocity) are found in the same location for both sets of data (see contours of velocity behind the wing dike in slices 3 and 4, Figure 4.2.11). The most notable difference between the two sets of data is the resolution of the bathymetry near the wing dike crest (slices 1 and 2, Figure 4.2.11). Here, the denser (5 m) transect spacing was better able to map the abrupt changes in elevation that are most pronounced in the immediate areas surrounding the wing dike (Figure 4.2.7). Unless a transect traverses directly over the wing dike (which is approximately 5 m wide) then the crest of the wing dike will not be adequately represented, nor resolved through interpolation. During the 20 m survey, the two closest transects to the wing dike were approximately 10 m upstream and downstream of the crest. On the other hand, one transect during the 5 m survey

passed directly over the crest and two others directly upstream and downstream of the crest, 5 m away. The proximity of transect locations relative to the position of the wing dike was only determined after the survey data were analysed as it was not possible to see the wing dike during measurements due to high turbidity. A similar comparison is made for three slices at Site B, comparing the May 29 and June 4 data (Figure 4.2.12). In this figure, the difference in bathymetry and contours of streamwise velocity for both days are compared. These results are discussed in more detail in the following sections.

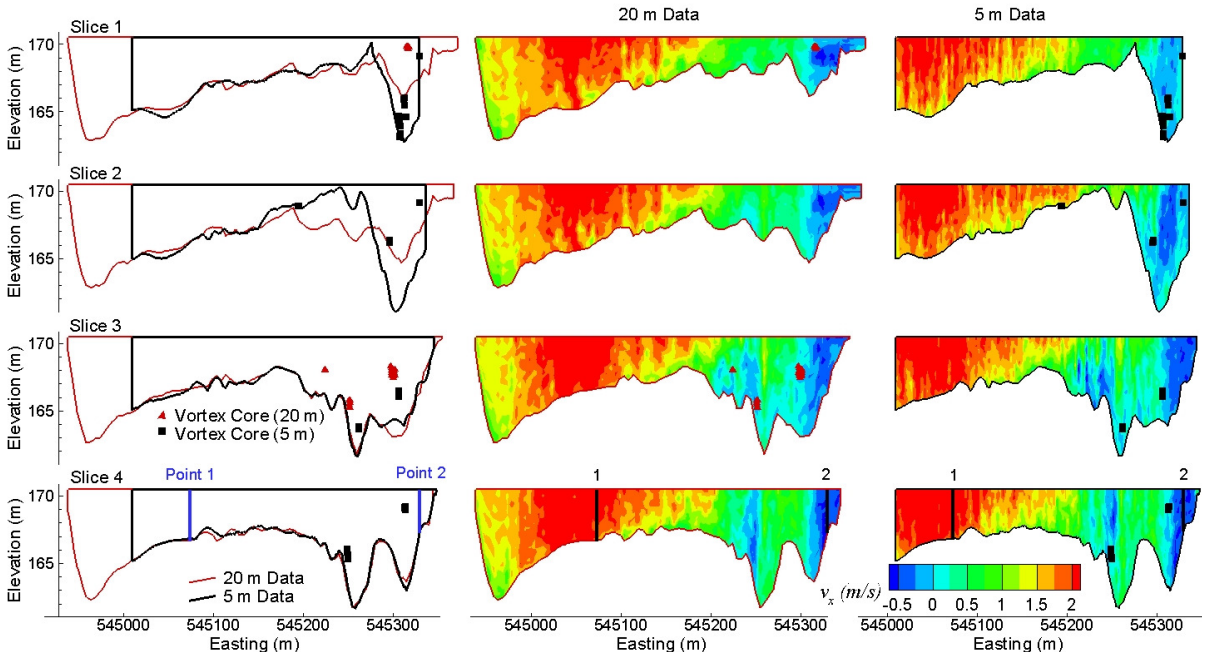

Figure 4.2.11. The presence of vortex cores near the wing dike at Site A (May 28) for four different slices (left) and corresponding contours of streamwise velocity (v_x) (right). Red and black lines and symbols refer to the 20 m and 5 m transect data respectively. Velocity profiles at Points 1 and 2 of slice 4 are provided in Figure 4.2.5. The location of vortex cores and slices in plan view are provided in Figure 4.2.7. Vertical dimension is scaled at 15:1 with the horizontal. Cross sections are viewed looking upstream.

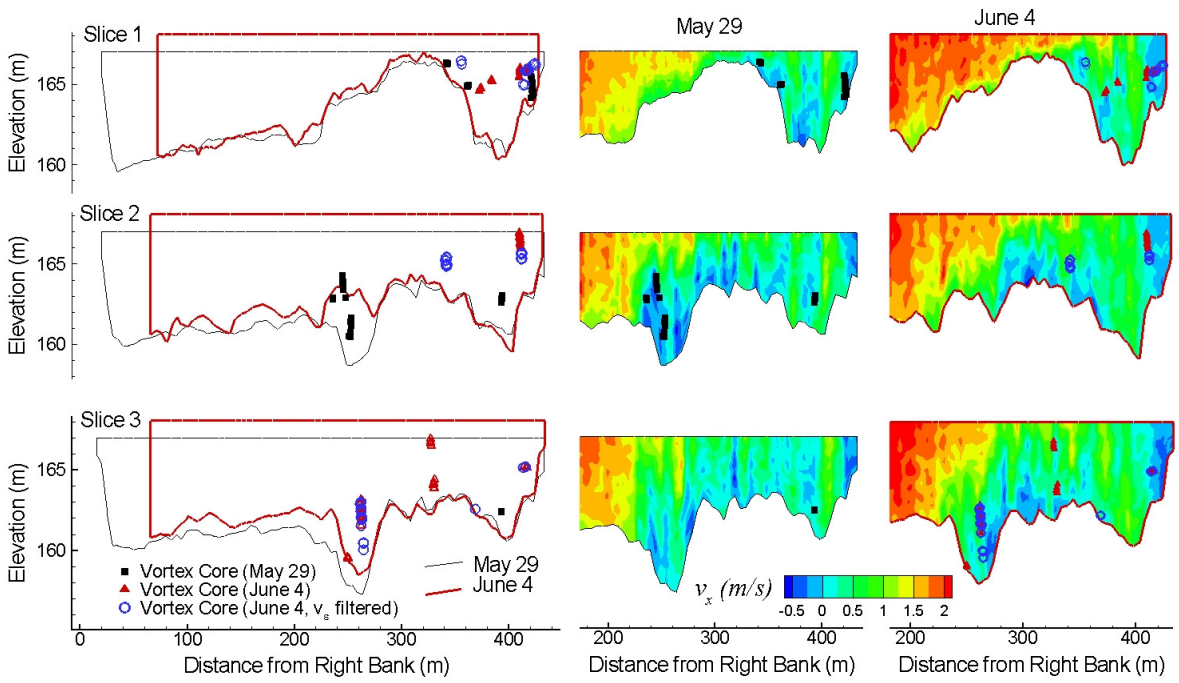

Figure 4.2.12. The presence of vortex cores near the wing dike at Site B (May 29 and June 4) for three different slices (left) and corresponding contours of streamwise velocity (v_x) (right). Red and black lines and symbols refer to the June 4 and May 29 transect data respectively. The location of vortex cores and slices in plan view are provided in Figure 4.2.7. Blue circles refer to vortex cores indentified when data with absolute error velocity ($|v_\varepsilon|$) > 0.5 m/s are removed. Vertical dimension is scaled at 15:1 with the horizontal. Cross sections are viewed looking upstream.

Vortex Cores

The calculation of vortex cores, which results in a point or series of connected points defining the vortex core locations, reveals the concentration of vortices along the wing dike and near individual scour holes for both sites and for all three days of measurements (Figure 4.2.7). Shear layers, which may develop at the wing dike tip and near possible notches (or gaps) in the structure, are likely responsible for the generation of these vortices. The location of gaps in the wing dikes (Figure 4.2.1) also appear to correspond with the nearby scour

holes (Figure 4.2.7). When viewed in cross-section (Figure 4.2.6, Figure 4.2.11 and Figure 4.2.12) some vortices appear to be clustered in the vertical direction and positioned over individual scour holes.

With respect to the flow field, the location of vortex cores appears to correspond with regions of sharp velocity gradients, which is to be expected (Eqns. 4.2.3 - 4.2.5). Figure 4.2.6, Figure 4.2.11 and Figure 4.2.12 all show the location of vortices at select cross sections superimposed with contours of streamwise velocity (Figure 4.2.11 and Figure 4.2.12) and all three components of velocity (Figure 4.2.6). Note that contours of secondary velocity (v_y and v_z) in Figure 4.2.11 and Figure 4.2.12 were not shown due to space limitations, but are provided for three of the slices in Figure 4.2.10. Regions of recirculating flow (i.e. negative streamwise velocity), which are sharply delineated in the vertical dimension, are most pronounced near the eastern tip of the wing dike (near the left bank) at both sites, where flow is constricted between the bank and the wing dike. During data collection, reverse flow was observed on the water surface at this location (for both sites), as well as a collection of floating woody debris caught up in a large eddy immediately downstream of the wing dike. Both transect spacings at Site A were capable of illustrating this recirculation (Figure 4.2.11). However, a greater number of vortex cores (in both plan and profile view) were identified in the 5 m transect data compared to the 20 m data, particularly in regions where sharp velocity gradients were most pronounced. Calculated streamlines from the 3-D volume also indicated recirculating flow was present behind the wing dike and near the left bank for the 5 m (Figure 4.2.9) and 20 m transect data (not shown).

By mapping vortex core locations with bathymetry, a close connection between these vertically-orientated coherent structures (i.e. structures orientated with a vertical axis) and

local scour is found. Further evidence to support this correspondence is obtained by comparing the results of the two surveys at Site B, where a change in flow conditions and bed morphology was measured between the survey dates. When the upstream edge of the large scour hole at the wing dike tip becomes in-filled between the two measurement dates, the vortex cores, which are most pronounced in this region on the first day (May 29) (slice 2, Figure 4.2.12 and Figure 4.2.13), have moved downstream to the next slice (slice 3, Figure 4.2.12 and Figure 4.2.13), above the new upstream edge of the scour hole. In other locations, the presence of some vortices remains consistent between the two dates (Figure 4.2.7 B). For example, there is the collection of vortex cores along the left bank near slices 1 and 3 (Figure 4.2.12 and Figure 4.2.13) and a similar group of vortex cores at the eastern tip of the wing dike, closest to the left bank, for both May 29 and June 4.

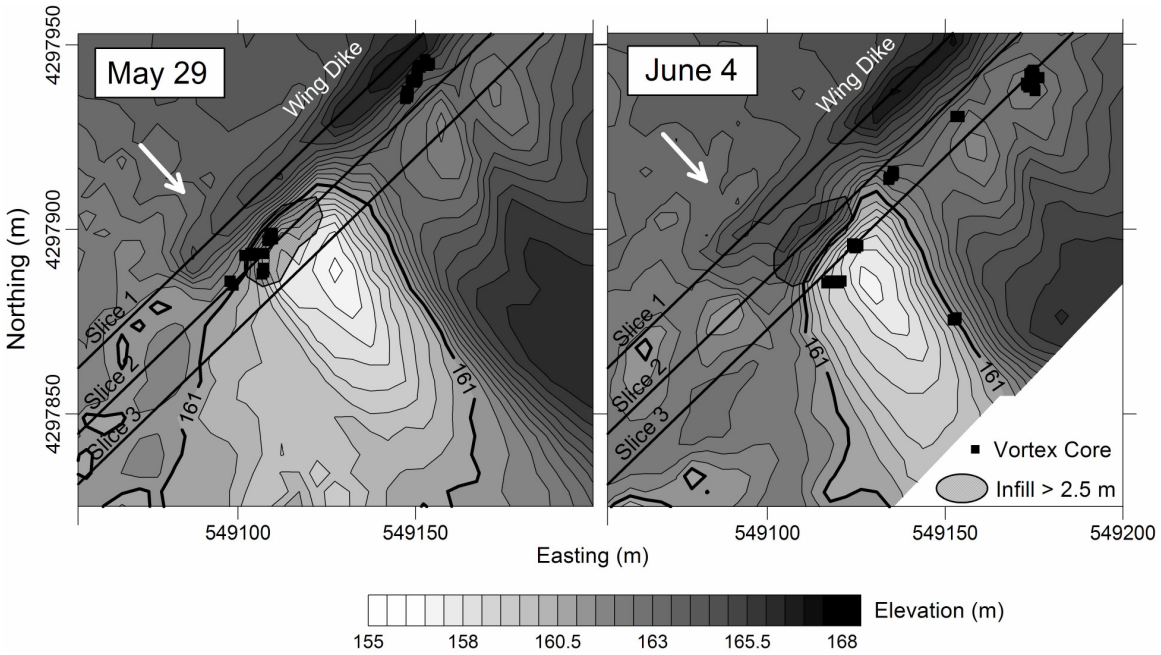

Figure 4.2.13. Close up of vortex core locations and region of substantial bathymetry change (> 2.5 m) at the wing dike tip at Site B for May 29 (left) and June 4 (right). Slices 1, 2 and 3 are shown for reference and correspond to slices in Figure 4.2.7, Figure 4.2.9 and Figure 4.2.11. White arrow indicates general flow direction.

The dominance of vertically-orientated vortex cores suggests that the vertical shear developing around the wing dike (and through any gaps) is dominating the mixing and turbulence structures in this region. Indeed, contour plots of z-vorticity (ω_z, Equation 4.2.6) confirm the dominance of highly-positive vertically-orientated vorticity along the downstream edge of the wing dike and at the tip of the structure, over the prominent scour hole at Site B (Figure 4.2.14). These regions of high z-vorticity correspond with the location of vortex cores as would be expected. Figure 4.2.14 also shows how ω_z was uniformly higher on June 4, compared to May 29, when flow and water surface elevation were higher, resulting in higher velocities and greater overtopping.

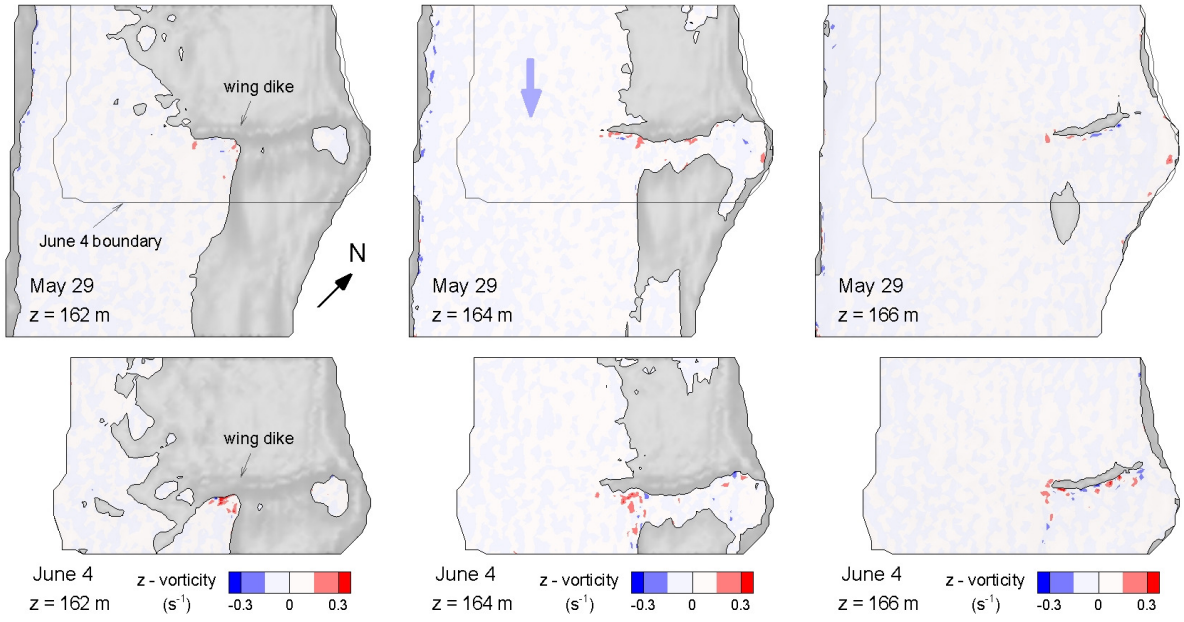

Figure 4.2.14. Contour plots of z-vorticity (ω_z) at Site B, for both May 29 (top) and June 4 (bottom), for three different horizontal slices at elevations (z = 162, 164 and 166 m). Gray shading of the bathymetry is provided for visualization of the bed features and wing dike. General flow direction is from top to bottom.

Our results suggest a correspondence between the locations of scour holes and the presence of vertical vortex cores and high vertical vorticity. The plunging action and flow separation are likely to contribute to higher near-bed shear stresses downstream of the wing dikes, but our results suggest that it is the near-bed shear due to 3-D rotation of the local flow field that contributes most to scouring action. Bed shear stress was not estimated given the non-uniform distribution of flow around the wing dike. Standard methods for estimating shear stress assume a log-linear velocity profile and/or linear regression of principal Reynolds stresses, both of which would not apply for the highly 3-D flow in the vicinity of the wing dike. In the complex flow field around deflectors, Biron *et al*., (2004) found that the turbulent kinetic energy method, which is widely applied in oceanography, provided the best estimate of shear stress, compared to other more conventional methods. However, this method relies on obtaining velocity fluctuations, which is not possible with the profiling ADCP.

4.2.5 Discussion

Measurement and Interpolation Methodology

Many authors have argued that only repeated transects should be used for reliable measurements of moving-boat ADCP water velocities. However, in most cases, spatial variance is at least as great as temporal variance, thus it seems reasonable that tighter spacing of single transects should prove to be more useful for generating reliable spatial distributions. Rennie and Church (2010) found that, for spatial mapping of single transect depth-averaged ADCP water velocities, the uncertainty in velocity measurement was limited by interpolation (not measurement error), suggesting denser transect spacings may reduce the uncertainty (at

least for depth-averaged velocities). Kriging provides spatial smoothing, which helps overcome the variance in ADCP velocities, and when coupled with dense transects, reduces the uncertainty. However, in their case, transects were considerably farther apart (over 100m or > 20 % of the channel width) and traversed diagonally downstream in a zigzag pattern, such that transects were not evenly spaced.

As many previous studies have found, the averaging of multiple repeat transects will reduce velocity variance. However, averaging would likely also eliminate the real (temporal) fluctuations, and eliminating this natural variance may reduce our capacity to measure and understand complex flow fields. Szupiany *et al.* (2007) conclude that, in their case of moving-boat transects downstream of a confluence on a large river, a minimum number of 5 repeated transects are required to resolve specific features of secondary velocities and reduce the variations in streamwise velocity. However, in their moving-boat transects, lateral deviation of the measured transects from the cross-section lines were on the order of ± 30 m. Therefore, in this example, averaging repeated transects necessarily incorporates some spatial smoothing, at least over the measurement extent containing the lateral deviations of each transect. In this sense, the smoothing resulting from the kriging of, for example, 5 nearby transects only 5 m apart, may be no different than the averaging of 5 repeated transects, when lateral deviations of up to 30 m are experienced. In fact, the kriging of nearby single transects may provide a slight advantage since the resultant region of investigation is a continuous 3-D volume (versus a single 2-D cross-section), a form better able to demonstrate spatially variable flow and limit temporal averaging. Indeed, in Parsons *et al.*'s (2005) case (single streamwise ADCP transects employed to study river dune dynamics on the Paraná River), time was a factor and repeat transects would not have been

suitable if dunes were actively migrating at the time of measurement. Both the scale of the river or region of interest and time are important factors to consider when choosing an ADCP surveying methodology.

The magnitude of smoothing and the root mean square error of the interpolation were comparable for both transect spacings (Table 4.2.2, Figure 4.2.4 and Figure 4.2.5), suggesting that, for mean flow patterns, less dense transect spacings (at least up to 5 % of the channel width) may be acceptable and more desirable if a larger survey extent is to be mapped. To support this, qualitative comparisons of velocity contours between the two transect spacings indicate little improvement is achieved in resolving the three-dimensional mean flow field around the wing dike (Figure 4.2.11). However, for mapping more complex flow features such as vortex cores, our results indicate a denser transect spacing is required, since a greater number of vortex cores (in both plan and profile view) were identified in the 5 m transect data (where 5 m ≈ 1 % of the channel width) compared to the 20 m data (Figure 4.2.7 A and Figure 4.2.10). Despite this, it is worth noting that in some locations, the less dense 20 m transect data were still capable of resolving vortex cores in locations matching the 5 m transect data. For example, in Figure 4.2.11, slice 3, we see that both data sets show vertically-aligned vortex cores over the two scour holes near the left bank. It is likely that the scale of these coherent structures are large enough to span at least the 20 m gap between transects. Indeed, our observations of a large eddy downstream of the wing dike and near the left bank at the time of measurement (and the calculated streamlines (Figure 4.2.9)) would support this.

The results also show that a tighter transect spacing is also required for detailed mapping of the bathymetry, particularly if specific features such as scour holes, wing dike crests and

dunes are to be accurately resolved. As well, for regions of abrupt elevation changes, a single vertical beam should be used for mapping bathymetry (unless ADCP depth is represented by each individual beam depth). In addition to providing a second and more accurate depth measurement, the external depth sounder was also useful for determining depth when the ADCP could not detect the bottom. For example, on the last day of measurement (June 4) when turbidity was highest (Figure 4.2.1), many regions of bottom-track data were missing from each transect due to signal attenuation (due to high concentrations of suspended sediment), and therefore failed to resolve the location of the bed (which was particularly noticeable in regions of higher water velocity and/or turbulence, and higher bed velocity). Therefore, where ADCP bottom track was lost (i.e. June 4), it was possible to process the ADCP water velocity data using the external depth data as a reference for the lowest bin in each profile.

Measuring Large-Scale Coherent Structures

In rivers, large-scale vortical motions can form naturally from the turbulent boundary layer (for example, kolk-boil vortices, a ubiquitous form of turbulence in rivers), or due to the presence of bed features (i.e. dunes and ripples) or structures placed in the flow (i.e. bridge abutments, groynes or wing dikes), all of which act to disrupt the mean flow pattern. For example, when flow separates from the tip of a wing dike, creating a recirculation zone behind the dike, a shear (mixing) layer develops where the differing velocities of the main downstream flow and the recirculation zone meet. This mixing can be characterized by vertically-oriented vortices that advect in the direction of the main downstream flow (also known as vortex shedding). By definition, these vortical motions (or coherent structures)

have a life cycle including birth, development, interactions and decay (Nezu and Nakagawa 1993). In identifying coherent flow structures through the presence of vortex cores, calculated from a spatially (and somewhat temporally) averaged flow field, it is impossible to capture this life cycle. However, in a time-averaged flow field it may be possible to identify statistically stationary large-scale flow patterns such as secondary currents and gyres. These circulating flow patterns are said to be stationary as they maintain the same position and orientation in space and time. While the individual transects together represent neither an instantaneous nor a time-averaged flow field, they are still capable of identifying stationary patterns (such as the recirculating flow downstream of the wing dike, Figure 4.2.9) and therefore assumed sufficient for indentifying stationary coherent structures. In this paper we have focused solely on identifying the location of vortices. Determining length scales, size and frequency characteristics of smaller and non-stationary structures (i.e. vortex shedding) would require stationary measurements, full consideration of the ADCP's divergent beam geometry and water velocity measurement uncertainty.

The "raw" ADCP data presented in this paper (i.e. Figure 4.2.4, Figure 4.2.5 and Figure 4.2.6) are necessarily averaged to a central location below the instrument. We have not addressed the effect of a divergent beam geometry on interpreting the results of the measured flow field. This is particularly relevant for the determination of coherent structures, which may not be detected if smaller than the horizontal separation of the four divergent beams, or where the flow field is spatially heterogeneous over the spread of the beams. Within a scour hole, the depth increases rapidly, causing the location of each measured beam velocity to diverge equally rapidly (the ratio of water depth to beam spread is > 1). The fact that vortex cores were resolved within the scour holes (which in some cases were twice as deep as the

mean flow depth) and for two different transect spacings, suggests that in some cases, divergent beams may not be completely limiting in complex flows.

Transect spacing will also play a role in the scale (size and extent) of the vortices that can be detected. In one case, where vortex cores are found over the same two scour holes for both data sets (i.e. Figure 4.2.11, slice 3), it is likely that the coherent structures here are large (i.e. on the order of magnitude of 10s of meters) and therefore resolved for both transect spacings. Obviously, only coherent structures larger or equal to the transect spacing (including the increase in the lateral separation of beams with depth) will be (or should be) resolved, because spatial gradients in velocity due to the coherent structure must be resolved (refer to Equations 4.2.3 – 4.2.6). Therefore, depending on the local, site specific conditions of the flow field being measured, it may be necessary to reduce the transect spacing in order to resolve smaller flow structures.

Coherent structures are by definition regions of heterogeneous flow and the simplest way to quantify flow heterogeneity is the error velocity (v_ε). Error velocity magnitude may act as an indicator of complex flow and coherent structures, since error velocity is likely to be highest in regions of extreme velocity gradients. To determine the sensitivity of our method for calculating vortex core locations to measured ADCP error velocity, vortex cores for the June 4 data were also calculated using filtered data sets, where data with absolute error velocities exceeding 1 m/s and 0.5 m/s were filtered and then vortex core locations re-calculated for the filtered data sets. Note that the default ADCP error velocity threshold is 1.5 m/s, and all other data have employed this threshold. The results showed no change in both the number and location of calculated vortex cores when data with $|v_\varepsilon| > 1$ m/s were rejected (which represented 0.6 % of the data), but noticeable changes were observed when $|v_\varepsilon| > 0.5$

m/s (11.3 %) were rejected (Figure 4.2.12). Overall, fewer vortex cores were indentified with the $|v_\varepsilon| > 0.5$ m/s threshold, but where vortices were most pronounced (for example over the scour hole in slice 3, Figure 4.2.12), results were consistent, indicating extreme error velocities do not necessarily identify the location of vortices. Interestingly, there were also some new vortices indentified for the $|v_\varepsilon| > 0.5$ m/s filtered data, which would suggest that there may be even less of a connection between measured error velocity and the location of calculated vortex cores. Possibly, filtering of erroneous velocities allowed for detection of weaker spatial velocity gradients, which resulted in identification of these additional vortex cores. While we acknowledge error velocity is an indicator of heterogeneous velocity, and could be used to indentify coherent structures, some types of flow heterogeneities may not be detected using an error velocity criterion. For example, when the vertical velocity components in the flow are unaffected by the flow heterogeneity, or when they contain the same error in both beam pairs. As well, it appears that it is possible to identify vortices in regions where error velocity is less than 0.5 m/s.

Understanding Flow Field and Scour Hole Dynamics

The presence of a scour hole at the wing dike tip is to be expected and is consistent with the extensive literature for experimental scour studies on groynes (Uijttewaal *et al.,* 2001; Weitbrecht *et al.,* 2002; Sukhodolov *et al.,* 2002); abutments (Melville, 1992; Lim, 1997) and spur dikes (Garde *et al.*, 1961; Gill, 1972; Kuhnle *et al.*, 1999). However, the contribution of the plunging action of the flow during submerged conditions is less certain, as only a few experimental studies have considered the fluid-sediment dynamics for non-emergent structures (Fox. *et al.,* 2005a; Jia *et al.,* 2005; Uijttewaal, 2005; Kuhnle *et al.,*

2008), all of which involved laboratory-scale investigations. Further, the geometry of the Missouri River wing dikes is irregular, with uneven crest heights and gaps or notches that have been created to improve habitat diversity, making the comparison of the resulting flow fields with previous experimental data (where geometries were comparatively uniform and organized) difficult.

Channel constricting structures such as wing dikes, bridge abutments and groynes are known to cause substantial local scour, due in part to the mean flow features such as secondary velocities. As flow approaches the structure, a principal helical structure forms along the interface between the "dead water" region upstream of the structure and the main flow. As this secondary current passes the structure it is forced downwards and along the bed in a transverse direction, which (similar to the secondary current in channel bends), leads to local scour of the bed at the tip of the structure (Raudkivi, 1998). Locally, the scour hole develops due to increased shear stress along the channel bed, due to the magnitude and direction of the secondary current which is towards and along the bed. This process appears to be confirmed by the velocity contours in Figure 4.2.10 and the corresponding patterns of bathymetry.

Turbulence also plays a role in sediment transport and scour. Jackson (1976) first hypothesized that the turbulent 'bursting' motions observed in turbulent boundary layers of large natural rivers (called kolk-boil vortices) play a major role in how alluvial sediment is entrained and suspended in the flow. Strong upward flow in a burst provides the vertical anisotropy in the turbulence which is needed to suspend sediment. Bursting also promotes the entrainment of more and coarser sediment beyond that which can be accomplished by tractive forces alone (Jackson, 1976). It is possible that the generation of vortex shedding

around a structure (such as a submerged wing dike) helps to establish a certain degree of periodicity (or predictable recurrence) in these burst-like events. More recent research has also shown that near-bed fluctuations, like those found in regions with vortex shedding, create instantaneous forces greater than time-averaged values, which results in sediment transport at flows where the time-averaged conditions are below the critical entrainment threshold for sediments (McLean et al, 1994; Roy *et al*., 1999; Thompson, 2006) and a non-linear increase in transport as the amplitude of velocity fluctuations increases (Schmeeckle and Nelson, 2003).

Together, the results of the present work and previous observations suggest there is a close connection between vertically-orientated vortex cores (which are typical of a free surface shear layer) with high z-vorticity, and local scour. However, by using effectively time-averaged velocity data and stationary bed conditions (the bed is considered stationary since spatial surveys were not repeated during the same flow event), it is difficult to assess what came first: the vortical motion leading to local scour, or increased vorticity as a result of the morphology and development of the scour hole. Most likely, the two processes (local scour and vortex/vorticity magnitude) are developing simultaneously, exhibiting positive feedback. In numerical investigations, Koken and Constantinescu (2008a and 2008b) found that the horseshoe vortex system forming around the upstream base of a single emergent spur dike (which they describe as the main driving mechanism behind the growth of a scour hole at the structure's tip) was present during both the initial and final stages of the scouring process. The authors found that, compared to the initial stage when the bed was flat, the presence of the scour hole stabilized the horseshoe vortex system.

Admittedly, the vortex core locations do not appear to correspond with regions of higher bed load transport; little to no transport is measured in the immediate vicinity of both wing

dikes (Figure 4.2.8 B and Jamieson *et al., in press*). However, this may not necessarily indicate a lack of correspondence between vorticity and scour, but rather (1) that sediment may be removed from the scour holes by suspension (Jackson, 1976) and would therefore not be measured as bed movement (or bed load); (2) that at the time of measurement, flow conditions were simply below threshold conditions for vortex-generated scour; and (3) that in some cases, there is simply no correspondence between bed load transport and local scour.

Measurements at higher flow rates, when the bed is mobile in the vicinity of the wing dike would be required to confirm this second point. However, the more than 5 m elevation change at the wing dike tip at Site B that occurred between May 29 and June 4 (where vortex cores and z-vorticity are most pronounced on both days) suggests that (1) there could be a correspondence between vorticity and scour; and (2) that, in this case, the required flow may be just below the flood stage (4700 m^3/s), given the peak in the hydrograph between these dates (Figure 4.2.2) and subsequent changes to the scour hole shape and depth. Indeed, the most active region of bed mobility – the upstream scour hole crest (Figure 4.2.8 and Figure 4.2.13) – corresponds with the most concentrated contours of high positive z-vorticity (i.e. June 4, Figure 4.2.14), supporting previous numerical results that indicate a correspondence between vorticity and local scour at submerged groyne tips (Minor *et al.*, 2007a).

Flume experiments by Radice *et al*. (2009), of clear water scour at a vertical wall abutment, support the idea of a lack of correspondence between bed load transport and local scour (point three above). The authors found that maximum bed load transport occurred at the abutment tip and wake region, which was consistent with calculated stress contours (Koken and Constantinescu, 2008b); while maximum scour depth was located in the corner between the upstream abutment face and the channel side wall.

4.2.6 Conclusions

Unlike previous studies, where multiple transects at the same location were averaged for identifying secondary flow features (i.e. Dinehart and Burau, 2005; Szupiany *et al.,* 2007), we present a new technique for observing and quantifying 3-D flow fields in large rivers, where complex flow features exist. Our results indicate that interpolating the flow field from multiple nearby single transects (i.e. 5 m spacing) may be more representative of an inherently complex 3-D flow field, particularly when the lateral deviation in repeated transects is great (for example, Szupiany *et al*. (2007) experienced maximum lateral deviations during their moving-boat transects of up to ± 30 m). Too much averaging of repeated transects could eliminate the true variability in velocity that is a characteristic of naturally turbulent flows, thereby essentially removing the spatially (and temporally) dependent features of the flow field.

Our analysis of detailed bathymetry data and densely-spaced velocity data indicate a correspondence between the calculated vortex cores and vorticity (resolved from the interpolated 3-D flow field) and the nearby scour holes. This analysis provides new insight into possible connections between vertically orientated coherent structures and local scour. Single-transect data were capable of describing complex three-dimensional flow field features beyond contours of mean velocity. However, limitations for resolving coherent structures in large rivers may remain due to the ADCP's divergent beam geometry and the subsequent spatial averaging that is associated with the instrument's profiling setup. This may be most acute where depth varies suddenly (i.e. a scour hole) or where coherent flow structures are smaller than the sampling area. Despite this, calculated vortex cores were consistently found in scour holes. The ADCP error velocity measurement does provide some

measure of flow heterogeneity across the divergent beams. However, error velocity alone did not appear to be a sufficient indicator for locations of coherent structures.

This research has relevance for; (1) understanding spatially variable flow fields and their corresponding morphology and sediment transport regime, particularly at the field scale; (2) providing spatially detailed descriptions of the velocity field for quantifying the availability of preferred zones for aquatic habitats across a range of scales (Shields *et al.*, 2003; Reuter *et al.*, 2009); and (3) providing comprehensive measurement data for supporting numerical model validation.

5 Experimental Channel Bend

5.1 Spatial variability of three-dimensional Reynolds stresses in a developing channel bend

---

Jamieson, E.C., Post, G. and Rennie, C.D. (2010). Spatial variability of three-dimensional Reynolds stresses in a developing channel bend. *Earth Surface Processes and Landforms*, 35, 1029-1043.

5.1.1 Abstract

Experimental results of the mean flow field and turbulence characteristics for flow in a model channel bend with a mobile sand bed are presented. Acoustic Doppler velocimeters (ADVs) were used to measure the three components of instantaneous velocities at multiple cross sections in a 135º channel bend for two separate experiments at different stages of clear water scour conditions. With measurements at multiple cross sections through the bend it was possible to map the changes in both the spatial distribution of the mean velocity field and the three Reynolds shear stresses. Turbulent stresses are known to contribute to sediment transport and the three-dimensionality inherent to flow in open channel bends presents a useful case for determining specific relations between three-dimensional turbulence and sediment entrainment and transport. These measurements will also provide the necessary data for validating numerical simulations of turbulent flow and sediment transport. The results show that the magnitude and distribution of three-dimensional Reynolds stresses increase through the bend, with streamwise-cross stream and cross stream-vertical components exceeding the maximum principal Reynolds stress through the bend. The most intriguing observation is that near-bed maximum positive streamwise-cross stream Reynolds stress coincides with the leading edge of the outer bank scour hole (or thalweg), while

maximum cross stream-vertical Reynolds stress (in combination with high negative streamwise-cross stream Reynolds stress near the bend apex) coincide with the leading edge of the inner bank bar. As well, maximum Reynolds stress and average turbulent kinetic energy appear to be greater and more localized over the scour hole before final equilibrium scour is reached. This suggests that the turbulent energy in the flow is higher while the channel bed is developing, and both lower turbulent energy and a broader distribution of turbulent stresses near the bed are required for cessation of particle mobilization and transport.

5.1.2 Introduction

Turbulence is a natural characteristic of flow in rivers and plays an important role in how materials such as sediment, pollutants and nutrients are dispersed and deposited in the surrounding environment. Advances in understanding turbulence in open channel flows have provided the theoretical and physical framework for researchers to acknowledge the importance of turbulent velocity and stress to sediment entrainment and transport (Bagnold, 1956; Sutherland, 1967; Grass, 1971; Leeder, 1983). However, a complete understanding of turbulence in rivers and the extent to which it influences mass transport processes such as sediment entrainment and transport remains elusive.

Turbulent fluctuations in a fluid (and by extension turbulent stresses) are the consequence of the momentum flux of the fluid, which, within turbulent boundary layers, is dominated by a range of fluid motions that impose a degree of intermittency to momentum transfer. These intermittent motions (which also exhibit some degree of coherence) are associated with short term variations in pressure and near bed stress and are believed to contribute to sediment entrainment. Studies have shown that the initiation of sediment

motion occurs in response to peak instantaneous principal Reynolds stresses and lift forces exerted by the flow. Grass (1971) and others (Lu and Willmarth, 1973 and Brodkey *et al.*, 1974) demonstrated through laboratory measurements of streamwise and vertical velocity that in the outer zones of the turbulent boundary layer, burst like events had a significantly greater contribution to principal Reynolds stress than sweep like events (reported in Jackson, 1976). The strong upward flow in a burst provides the vertical anisotropy in turbulence which is needed to mobilize and suspend sediment (Drake *et al.*, 1988 and Lapointe, 1992). On the other hand, highly negative vertical fluctuations indicate motion towards the bed and are associated with bed load transport (Grass, 1983).

The spatial distribution of erosion and deposition in sedimentary environments such as channel bends is largely driven by stresses imposed by the mean flow field (i.e. streamwise velocity and secondary currents). However, since turbulent stresses are known to play a role in sediment mobility, the difficulty remains in understanding the influence of turbulence on the mean flow field, which for a channel bend is highly three-dimensional. Flow in a channel bend can be characterized by the secondary (or helical) flow that develops as a result of the superelevation of the water surface and centrifugal forces imposed on the flow due to the bend geometry. While secondary flows are a natural feature in all channels (including straight channels) their magnitude and subsequent effects are most pronounced in channel bends. Secondary flow introduces a transverse shear that alters the distribution of shear stress across a channel section and consequently influences the distribution of sediment. As the secondary flow interacts with the primary streamwise flow the result is maximum shear stress on the outside of the bank downstream of the channel bend, leading to increased erosion in the outer bank region. The distribution of shear stress, which is affected by the

distribution and pattern of fluid velocity on the bed, will also affect the magnitude and location of bed load transport (Dietrich and Whiting, 1989).

Work on meandering channels and sediment transport in the 1980s by Dietrich and Smith (1983, 1984) (and others, see Ikeda and Parker (eds.), 1989) documented in detail the key characteristics of the mean flow field and patterns of shear stress and bed load transport in a meander bend. These authors demonstrated through detailed field measurements and analytical assessment that the complex interactions that lead to the characteristic bed topography and sediment sorting in river bends is due to three components: (1) spatial variation in the boundary shear stress, which is both induced and reinforced by channel curvature and bed topography; (2) cross stream bed slopes that cause cross stream transport - large particles are transported toward the pool (i.e. down-slope via gravity), against the inward secondary circulation that is transporting the finer particles inward to the point bar top; (3) spatial variation in surface grain sizes (due to point (2) above), which control the local relationship between boundary shear stress and sediment transport rate (Dietrich and Whiting, 1989). Lacking measurements of turbulence, these authors did not evaluate to what extent turbulent stresses contribute to the spatially variable mean boundary shear stress and the role they play in initiating cross stream transport.

A review of experimental research for flow in open channel bends by Blanckaert and Graf (2001) highlighted the limited number of mobile bed experiments, the limited spatial coverage of data collected in each study (typically, measurements were taken at only one cross section in the bend) and the lack of three-dimensional turbulence data (i.e. Dietrich and Smith, 1983 and Odgaard and Bergs, 1988). Experimental mobile bed bend studies since 2001 include: Matsuura and Townsend (2004), Blanckaert *et al.* (2008), and Shiono *et al.* (2008). A recent study by Zeng *et al.* (2008) presents both experimental and numerical

results for flow and bathymetry throughout a sharp bend, but does not discuss turbulence characteristics in great detail. Most recently, Roca *et al.* (2009) provide experimental results of mean velocity and turbulence (turbulent kinetic energy and shear stress) at individual cross sections through a sharp (186º) mobile-bed open channel bend, with and without an outer bank footing. Interestingly, some of the most recent and comprehensive experimental meander bend studies are not fluvial (i.e. open channel), but devoted to the case of density currents in submarine meandering channels (i.e. Corney *et al.*, 2006 and Keevil *et al.*, 2006). In their own experiment, which involved detailed acoustic Doppler velocity profiler (ADVP) measurements at one half of a single cross section (the apex of a 120º bend), Blanckaert and Graf (2001) found a reduction in turbulent activity at the outer bank, corresponding to a reduction in the bank shear stress. This result does not appear to conform to the general understanding of maximum shear stress and increased erosion at the outer bank discussed above. The authors also identified a second circulation cell near the outer bank (Bathurst *et al.*, 1977), which has an opposite sense of rotation than the principal secondary circulation cell in the center of the channel. The opposite sense of this smaller cell would indicate it has a protective effect on the outer bank and the adjacent channel bottom, thus providing an explanation for the reduced outer bank shear stress. However, without details of the mean velocity and turbulent flow field at other cross sections, it is not possible to comment on the spatial extent (and therefore relative importance) of these features through the length of the bend.

In the present study, two separate laboratory flume experiments have been carried out to measure the spatial distribution of velocity and turbulence throughout a 135º channel bend with a mobile sand bed. Acoustic Doppler velocimeters (ADVs) were used to collect measurements at a high spatial density throughout the channel bend to resolve fully the

three-dimensional distribution of Reynolds stresses and turbulent kinetic energy near the bed and through the bend as it was developing (Run 1) and once it reached equilibrium (Run 2).

Most turbulence studies have focused on identifying and measuring the principal Reynolds shear stress, in part due to the difficulties of collecting high frequency three-dimensional turbulence data. The added complexity of secondary flow in a channel bend affects the magnitude and spatial distribution of three-dimensional turbulent shear stress, making the measurement of each component of Reynolds stress essential. With three-dimensional turbulence data it is possible to quantify the relative contributions of each Reynolds stress component and other turbulence parameters to describe better the overall characteristics of the three-dimensional turbulent flow field. Extending these results to analyse the corresponding changes in bed topography sheds new light on the role of turbulent stresses on sediment transport. Furthermore, the comparison of two experiments, each with the same initial conditions but different durations, provides evidence of the temporal variation in bathymetry, mean flow field and turbulence activity before and at equilibrium scour.

The current literature lacks a comprehensive experimental study of near bed velocity and turbulent stresses for three-dimensional bend flow with a mobile bed. This paper has two principal objectives: (i) to describe the distribution of the three-dimensional velocity field and turbulent stresses through a channel bend; and (ii) to describe the significance of three-dimensional Reynolds stress distribution and turbulent kinetic energy on sediment transport and equilibrium scour.

The direct measurement of the three-dimensional velocity field and corresponding turbulence parameters in a mobile bed channel bend will also provide the necessary data for better validation of numerical simulations of turbulent flow and sediment transport. A fully

resolved three-dimensional numerical solution for open channel flow problems which adequately incorporates the behaviour of turbulence and sediment transport has yet to be realized. Even the most recent attempts (i.e. Zeng *et al.*, 2008) have acknowledged the weaknesses of present numerical models for predicting flow, sediment transport and morphodynamics in alluvial bends, likely due to an incomplete characterization of turbulent stresses. The added sophistication of new large-eddy simulation (LES) models (i.e. Van Balen *et al.*, 2009) has improved the predictions of turbulent stresses in curved open channels; however, these models remain limited to simulations with fixed bed conditions.

5.1.3 Experimental Methods

Experiments have been carried out in a channel bend flume located in the Civil Engineering Hydraulics Laboratory at the University of Ottawa. The flume has a centerline length of 18.5 m, with a 12.19 m long approach section, followed by a 135º bend section with a constant radius of curvature of 1.5 m (at the channel centerline) and a straight 2.4 m long exit section (Figure 5.1.1 A). The flume is 1.0 m wide with 0.9 m high vertical plexiglass walls, which contain a 0.3 m deep sand bed (Figure 5.1.1 B). The sand has a mean diameter (d_{50}) of 1.1 mm with a range of particle diameters between 0.6 to 1.8 mm. (Further details of channel design and experimental setup are provided in Post, 2007).

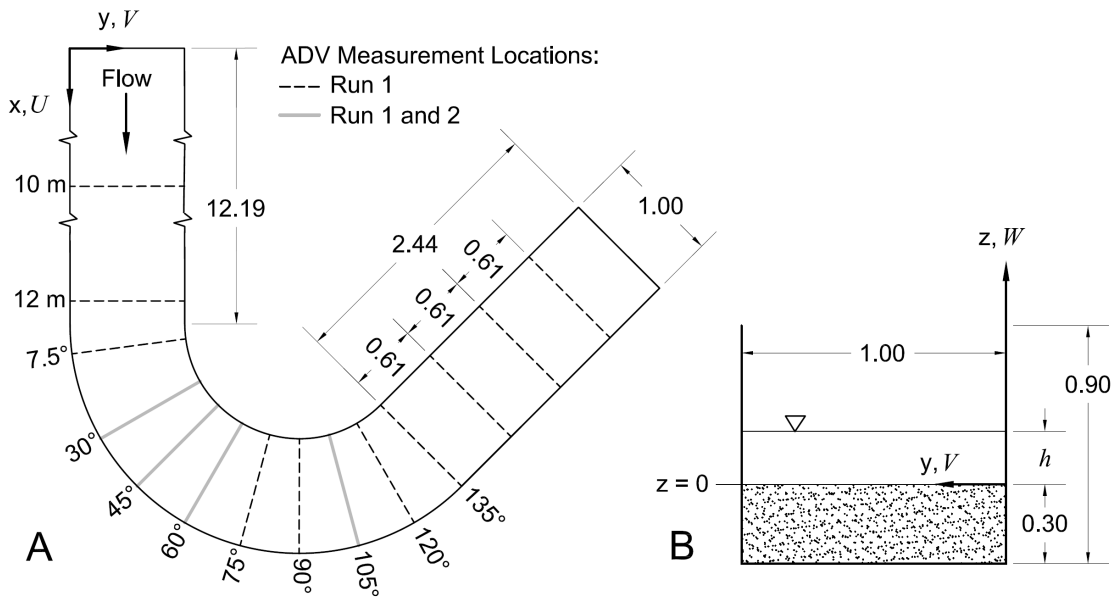

Figure 5.1.1. (A) Plan view of 135º bend flume. Cross sectional locations of ADV measurements are indicated by the dashed (Run 1) and grey solid lines (Run 1 and 2). (B) Cross sectional view (looking downstream) of channel with initial 0.30 m deep sand bed and water depth, *h*. All dimensions are in meters. Streamwise velocity component (*U*) is parallel to flume wall throughout the domain.

Two experiments with the same initial setup and identical flow conditions were run, with the only difference being the total run times of 70 and 122 hours. Table 5.1.1 provides a summary of the experimental parameters. Each experiment began with a constant slope (uniform flow) and a horizontal cross stream bed slope. Experiments were conducted under clear water scour conditions, wherein flow in the approach section was near the threshold for initiation of particle motion and negligible movement of sand grains was observed. Therefore, scour and deposition in the bend section was due to the presence of the bend alone.

Table 5.1.1. Summary of experimental conditions. Q is discharge, h is water depth in the straight approach section, S is initial bed and water surface slope, d_{50} is mean sediment diameter, U is reach-averaged velocity, and $\overline{U_*}$ is reach averaged shear velocity.

Run	Q (m^3/s)	h (m)	S	d_{50} (mm)	U (m/s)	$\overline{U_*}$ (m/s)	*Duration* *(hrs)*
1	0.072	0.200	0.00044	1.1	0.36	0.025	70
2	0.072	0.195	0.00044	1.1	0.37	0.025	122

Instantaneous velocity measurements were made using three Nortek Vectrino (4-beam) acoustic Doppler velocimeters (ADVs). The ADVs were mounted on a movable carriage, with each mount providing adjustment of the instruments in the lateral (cross-stream) and vertical directions. The ADVs were orientated orthogonal to the flume walls and to the original (flat) bed (i.e. vertical) in the straight approach section and through the channel bend. This arrangement provided a consistent frame of reference from which the spatial patterns of the mean flow field and turbulence parameters through the entire bend could be assessed. Data are sometimes rotated to limit the error in Reynolds stress (McLelland and Nicholas, 2000). However, in complex flow fields where the local streamline may vary markedly from one point of measurement to the other, applying such a rotation may unnecessarily complicate the analysis (Roy *et al.*, 1996). Figure 5.1.1 shows the ADV measurement locations (in plan view) for each experiment.

In order to collect data, the ADV transducers must be fully submerged in the flow, and since the sample volume is remote from the sensors and 50 mm from the central (emitting) transducer, it is not possible to collect data in the top 60 mm of the water depth. The regions of the flow where no ADV data were collected are indicated in the cross sectional plots (Figure 5.1.6, Figure 5.1.9 and Figure 5.1.10). ADV measurement locations for each cross

section are shown in Figure 5.1.6, Figure 5.1.8, Figure 5.1.9 and Figure 5.1.10. The ADV configuration parameters were identical for each run (sampling time = 120 s; nominal velocity range = 0.30 m/s; transmit length = 1.8 mm; sampling volume = 5.5 mm) except for sampling frequency (f) which was 200 and 50 Hz for Run 1 and 2 respectively. Run 1 data were box car averaged (every 4 samples were averaged) in order to convert data to 50 Hz for reliable comparison with Run 2 data. This approach is appropriate since the ADV internally averages multiple pulse-pairs to the specified sampling frequency (i.e. 50 or 200 Hz). Data collected in the same measurement locations in each Run were compared and confirmed: (1) the observed frequency range of the inertial subrange is unaffected by the choice in sampling frequency based on spectral density plots of velocity components; and (2) Reynolds stress contributions occurred at frequencies less than 25 Hz (which is the Nyquist frequency for a sampling frequency of 50 Hz) based on coherence spectra (cospectra) plots of streamwise and vertical velocity (Gross and Nowell, 1985).

The spatial coverage of measurement points in each experiment varied based on a compromise between overall coverage of the channel bend and the density of measurement points in each cross section. Run 1 data were collected at fourteen different cross sections through the bend: 10 and 12 m from the flume inlet; 7.5, 30, 45, 60, 75, 90, 105, 120 and 135º through the bend; and 0.61, 1.21 and 1.83 m from the bend exit (Figure 5.1.1 A). These cross sections provide enough spatial coverage to describe the distribution of velocity and turbulence through the entire bend. In this run, measurements at each cross section (except 105º) consisted of five evenly spaced vertical profiles, with measurements in the vertical direction at 5, 10, 20, 40, 70, 100 and 140 mm above the bed. Where flow became deeper due to scour, measurements continued upwards at intervals of 20 mm until 60 mm below the water surface.

In Run 2, data at six cross sections were collected: 11 m from the flume inlet and 0, 30, 45, 60 and 105º through the bend. In this run each cross section had a greater density of measurement points; each cross section consisted of at least nine evenly spaced profiles with measurements in the vertical direction at intervals of 5 mm near the bed, 10 mm in the middle half of the flow depth and 20 mm closer to the water surface. During the experiments, it was observed that the 105º cross section showed the greatest amount of sediment movement and the steepest cross stream bed slope. Therefore, the highest density of data for both runs was collected at 105º.

The focus of this paper will be describing the spatial distribution of bathymetry, velocity and turbulence throughout the entire bend (Run 1 data) and the difference in results between experiments by comparing bathymetry and the four matching cross sections (30, 45, 60, and 105º) that were measured during each run.

ADV data collection began approximately 43 and 70 hours after the start of Runs 1 and 2 respectively. Bed conditions were sufficiently constant during ADV data collection to be able to assume stationarity within each run. The total time to complete all ADV measurements in a given cross section varied depending on the number of data points measured. The average time to complete one cross section was 1.9 and 4.7 hours for Runs 1 and 2 respectively. Figure 5.1.2 illustrates the timing of ADV data collection for each of the four matching cross sections compared between Runs 1 and 2 (30, 45, 60, and 105º) in relation to the development of maximum scour depth at the outside wall at 135º. The difference in elapsed time between each cross section pair was 43, 57, 58 and 59 hours for the 30, 45, 60, and 105º cross sections respectively.

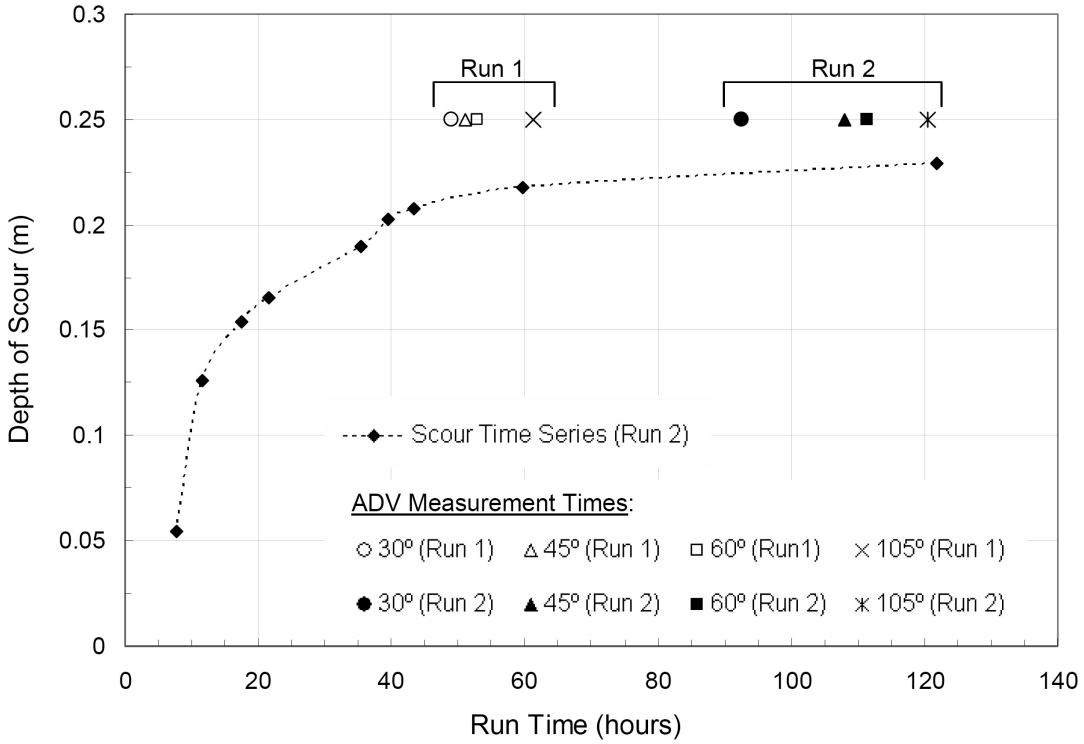

Figure 5.1.2. Development of maximum scour depth at the outside wall at 135º for Run 2. Symbols above the curve represent the elapsed run time for the completion of ADV measurements at each cross section.

At each measurement location, two minutes of ADV time series data were collected. The raw time series data were processed using Matlab code to calculate mean statistics and turbulence parameters. The four beam ADVs provide two simultaneous measurements of vertical velocity for identifying errors. Raw data were filtered based on the difference between the two simultaneous vertical measurements – if this difference was greater than 0.1 m/s each component of velocity was replaced with a value interpolated from the measurement before and after the erroneous value, after a technique introduced by Nikora and Goring (1998).

Any large spikes in the data were removed based on thresholds for both acceleration and standard deviation. Acceleration was calculated by dividing the difference between subsequent velocity measurements by the time step between. The threshold for acceleration was specified as $1.5g$, where g is the acceleration due to gravity (9.81 m/s^2). In the second threshold, new values were interpolated for any velocity measurement beyond four standard deviations from the mean. The ADV measurements were also corrected for manufacturing error – it was noticed during preliminary testing that the probe tips were each slightly rotated clockwise with respect to the electronics housing. Therefore, ADV measurements were also corrected for each instrument specific rotation angle, which varied between 2-3º.

The noise in each measurement was calculated based on a -5/3 slope fit to the power spectrum of each time series (Rennie and Hay in press). Noise is calculated by integrating over the entire spectrum by $N = \sqrt{n * f_{Nyquist}}$ where n is the measured spectral energy above the fitted -5/3 slope and $f_{Nyquist}$ is the Nyquist frequency, which is equal to one half of the sampling frequency, f in Hz ($f_{Nyquist} = f / 2$). A noise ratio (NR) was used as a relative measure, which is determined as the noise (N) divided by the mean absolute fluctuation in the velocity component ($\overline{|u'|}$). If the calculated noise ratio is greater than 0.75, then high frequency fluctuations are dominated by noise and a low pass filter should be applied (Rennie and Hay in press). However, of the total 1,191 ADV point measurements collected and presented in this study, only 7 measurements (spread over four different cross sections) were flagged with $NR > 0.75$. Therefore, the data were not considered to be biased by noise. Average ADV signal-to-noise ratio and correlation values were 23.2 and 91.3% for Run 1 and 20.0 and 90.6% for Run 2 respectively, where recommended lower limits are 15 and 70% respectively (Nortek, 1997).

There is also the added complication (or limitation) of accurate measurements over a rough or moving bed. It is possible that the presence of large roughness elements or entrained particles above the bed introduce ADV sampling error if they enter the sample volume, potentially altering the ADV's acoustic signal. High concentrations of particles in the sampling volume are likely to cause multiple scattering effects and increased signal attenuation (Hay, 1993) and thus less reliable velocity measurements. However, data collected nearest the bed (at 5 mm from the bed) had correlation and signal-to-noise values similar to data from locations higher in the water column, which indicates that measurements near the bed were not corrupted by sediment transport.

The despiked and rotated ADV point measurements of streamwise, cross stream and vertical velocity (u, v and w) were used to calculate mean velocities ($\overline{U}$, $\overline{V}$ and $\overline{W}$), from which fluctuating turbulent velocities (u', v' and w') were determined. Fluctuating velocities are combined to evaluate the three Reynolds shear stress components (τ_{uw}, τ_{uv} and τ_{vw}) and average turbulent kinetic energy (tke) such that

$$\tau_{uw} = -\rho\overline{u'w'}; \quad \tau_{uv} = -\rho\overline{u'v'}; \quad \tau_{vw} = -\rho\overline{v'w'} \tag{5.1.1}$$

$$tke = \frac{1}{2}\left(\overline{u'^2} + \overline{v'^2} + \overline{w'^2}\right) \tag{5.1.2}$$

where ρ is the density of water and $\overline{u'w'}$, $\overline{u'v'}$ and $\overline{v'w'}$, and $\overline{u'^2}$, $\overline{v'^2}$ and $\overline{w'^2}$ represent the mean of the product or square of the fluctuating turbulent velocities respectively.

After each run, the flume was drained and the elevation of the sand bed profile measured using a Leica systems Disto pro4a laser altimeter, which provides a precision of ± 1 mm. Bed level measurements were taken every 10 mm in the cross sectional direction and at 7.5º (Run 1) and 5º (Run 2) intervals through the bend and every 0.30 m in the straight section.

Kriging, with a spherical model variogram fit to the experimental variogram, was used to interpolate the bed level measurements into a three-dimensional contoured surface (Figure 5.1.3 A and B).

5.1.4 Results and Analysis

Bathymetry

Overall, the final bathymetry of Runs 1 and 2 are in good agreement and represent the expected morphology of a channel bend (Figure 5.1.3 A and B). In both cases there is erosion along the outside bank and deposition along the inside of the bend, extending beyond the exit of the bend (135º). The magnitude and location of maximum scour are near identical for both runs: the maximum scour was 0.249 m and 0.244 m for Runs 1 and 2 respectively and in both cases occurred approximately 0.05 m from the outside wall at the 135º cross section.

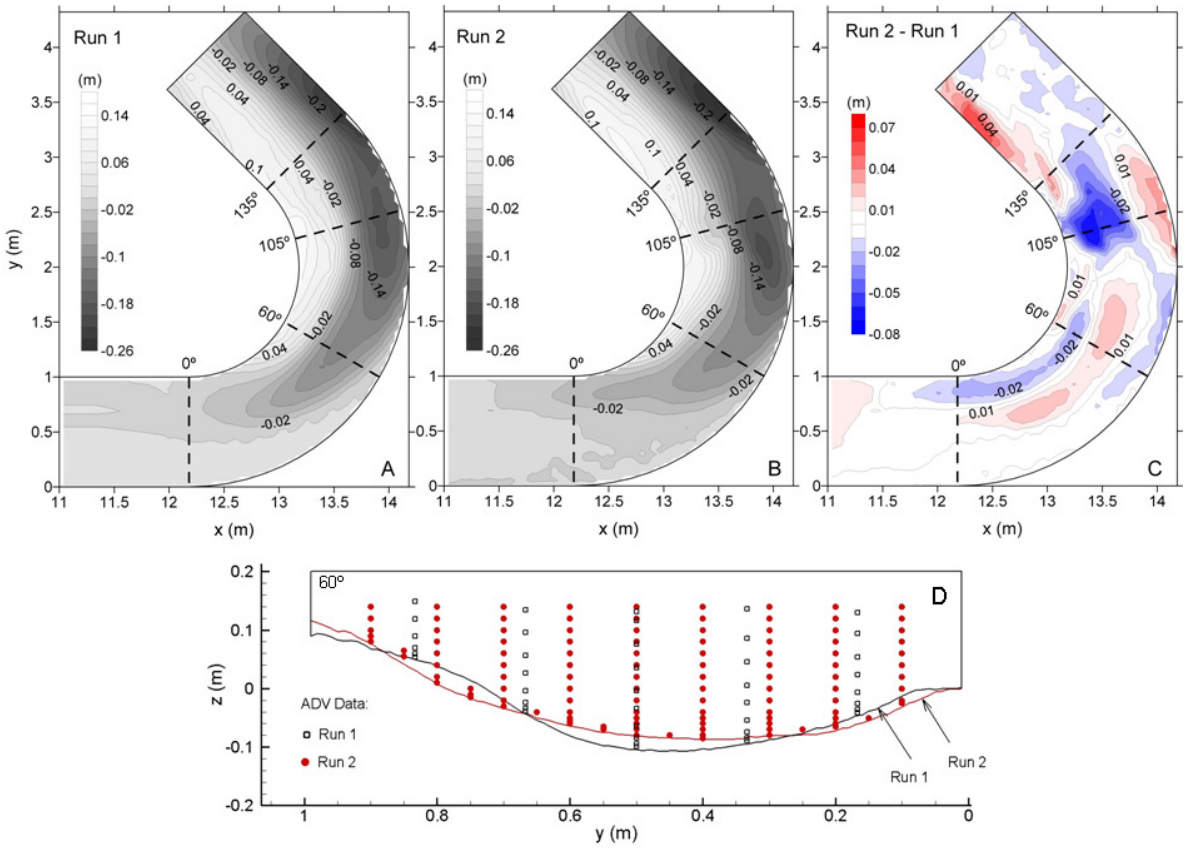

Figure 5.1.3. Bathymetric contours for Run 1 (A); Run 2 (B); and the difference map between Run 1 and 2 bathymetries (C). Initial bed level is 0 m in (A) and (B), where positive and negative values indicate deposition and erosion respectively. (D) Comparison of final bathymetry and location of ADV data for each run at the 60º cross section.

The uncertainty associated with bed topography measurements is estimated as 0.0016 and 0.0015 m for Run 1 and 2 respectively, which is calculated by $\sqrt{\sigma_m^{\,2} + \sigma_i^{\,2}}$ where $\sigma_m^{\,2}$ and $\sigma_i^{\,2}$ represent the variance due to measurement technique (Disto Laser) and interpolation (Kriging) respectively. (The value for Run 2 is slightly lower since data were more spatially dense (i.e. cross sectional data every 5º in the bend verses 7.5º in Run 1), which will reduce

the interpolation error). The total measurement uncertainty (0.0016 and 0.0015 m) is much less than the observed differences in bathymetry, which are on the order of 0.01 m.

The differences in the final bathymetry between the two runs are best illustrated in a difference map (Figure 5.1.3 C). By quantifying the difference, two locations of maximum change are noted: near the inner bank at the 105º cross section there is approximately 0.08 m more deposition in Run 1 than Run 2; and, the point bar along the inner bend downstream of the bend exit is 0.04-0.06 m higher in Run 2. However, despite these two localized differences, the overall changes in bed levels vary throughout the bend by no more than ±0.02 m (Figure 5.1.3 C). The overall similarity of the two final bathymetries provides a confidence in the general morphology for this channel geometry and flow condition, presenting suitable results for interpreting the large scale patterns of deposition and erosion and corresponding flow field.

Two explanations for the differences in bathymetry are: (1) sediment transport is an inherently stochastic process, with the formation of bed forms such as dunes adding complexity (i.e. no particular spatial and temporal dependency) as they establish unique local flow features that influence the local patterns of deposition and scour; and (2) the two runs represent two different stages of reaching equilibrium scour, since the first run was terminated 52 hours before the second. Observations made through each experiment indicate that the differences are likely due to a combination of these two reasons.

The first reason could explain the more localized differences in smaller scale features, such as the pattern of deposition and dune formation along the inner bend, which explains the two most pronounced differences at the 105º cross section and at the inner bend downstream of the bend exit (Figure 5.1.3 C). The second reason could explain the overall differences in morphology (i.e. large scale features), such as the position and length of the

thalweg through the channel bend. If the stochastic nature of sediment entrainment and transport can not be controlled or necessarily repeated between runs, then an explanation for the bathymetric differences should be focused on the overall differences in general morphology, while keeping in mind that smaller scale features will affect local turbulence.

Bathymetric changes in the flume began with deposition along the inside of the bend and scour along the outside wall at the bend exit. As sediment transport continued, the inner bank region became shallower (with large bed forms such as dunes being most pronounced, Figure 5.1.4 a) and the position of maximum scour migrated upstream along the outside wall. The thalweg then progressed upstream, beginning from the outside of the bend near the exit and bending towards the inner bank as the experiment continued, moving closer to the inside of the channel at the bend entrance.

Observation of the thalweg developing in an upstream direction indicates that this feature is time dependent; the depth and extent of the thalweg will depend on how long the experiment has been running, until it reaches equilibrium. If this is true then it would help to explain the differences in thalweg (and possibly other large scale morphological features) between the two runs. Run 1 was terminated after 70 hours (52 hours earlier than Run 2), and therefore at an earlier stage of development towards establishing an equilibrium bed under clear water scour conditions. This time difference could explain why the start of the thalweg in Run 2 is further upstream than Run 1 (Figure 5.1.3). Furthermore, the net volumetric change in each run is calculated to be -0.171 and -0.178 m^3 for Runs 1 and 2 respectively, where a negative volumetric change indicates a net loss of sediment. These results indicate Run 2 scoured approximately 0.007 m^3 more sediment then Run 1, which would support the hypothesis that at 50 hours, Run 1 had not finished scouring and therefore final equilibrium was not reached. These differences in general morphological features present an interesting

opportunity to study the time dependent nature of flow conditions (velocity and turbulence) on sediment transport. Is the distribution of velocity and turbulence in the channel bend changing as a result of reaching (or not reaching) equilibrium conditions?

Photographs of the final bed topography for Runs 1 and 2 are provided in Figure 5.1.5 and Figure 5.1.4 respectively. These figures demonstrate the unique bed form development associated with the strong secondary flow present in a relatively sharp (135º) bend. In both experiments, large dunes (height ≈ 10–15 cm) developed along the inner bank with crests orientated perpendicular to the general streamwise flow direction along the inner bank wall. Near the inner bank numerous ripples (or small scale dunes) were observed to travel up the inner bank slope, with crests perpendicular to the cross stream flow direction, indicating net transport of bed load from outside to inside of the bend (Figure 5.1.4 and Figure 5.1.5). At the completion of each run the water was drained slowly to maintain the integrity of all large and small bed forms. The density of bathymetry measurement points were not sufficient to resolve the small scale bed features (Figure 5.1.3), but photographs of the developed sand bed illustrate that there were noticeably more ripples on the inner bank slope in Run 1 (Figure 5.1.5 a-d) compared to Run 2, where the cross stream bed slope was nearly void of all ripples (Figure 5.1.4 b).

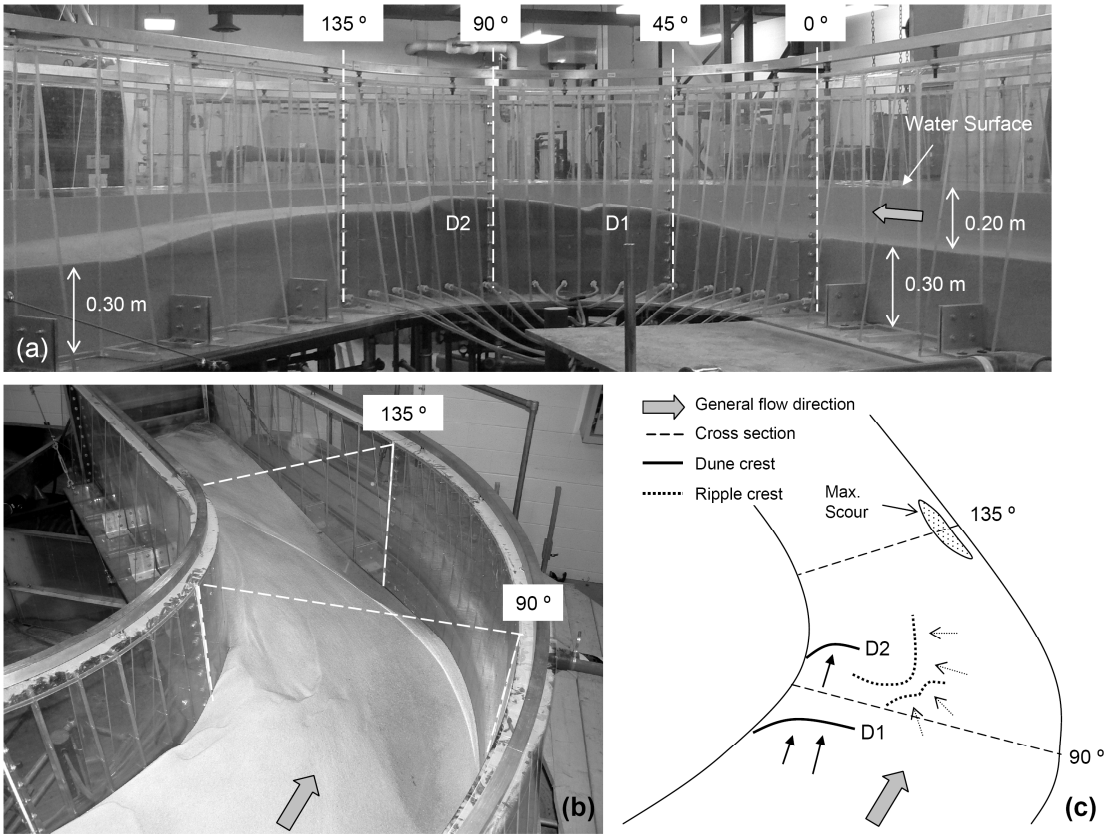

Figure 5.1.4. Bathymetric features from Run 2: (a) large dunes along inner bank; (b) oblique view of final bathymetry; (c) schematic of bed form features from (b), illustrating streamwise and cross-stream orientated bed forms. D1 and D2 refer to the first and second dune in the downstream direction respectively.

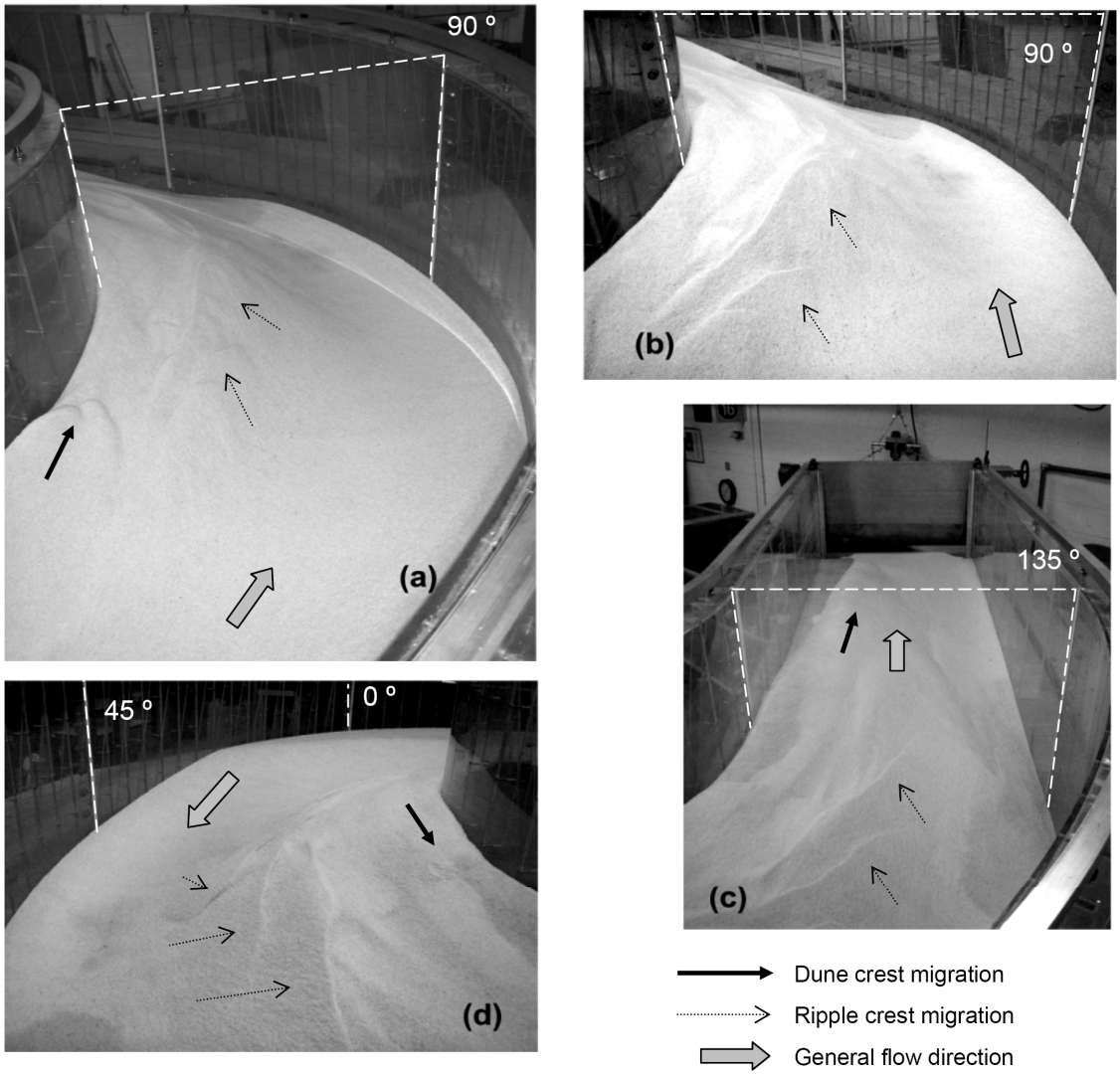

Figure 5.1.5. Bathymetric features from Run 1: (a) to (d) show ripples (or small scale dunes) which travelled up the face of the inner bank bar in a cross stream direction. (a), (c) and (d) show that the larger dunes along inner bank travel in the general streamwise direction along the inner bank wall.

Mean Velocity and Bed Shear Stress

The most identifiable characteristic of the mean velocity field for flow in a bend is the presence of secondary flow, which alters the distribution of maximum streamwise velocity. Secondary flow is best demonstrated by the cross stream (secondary) velocity; mean cross stream ($\overline{V}$) and vertical ($\overline{W}$) velocity, with magnitude $\sqrt{\overline{V}^2 + \overline{W}^2}$. Figure 5.1.6 shows contour plots of mean velocity ($\overline{U}$, $\overline{V}$ and $\overline{W}$) and mean secondary velocity vectors for each corresponding cross section between Run 1 and 2.

Overall, there was little difference in the mean velocity field between the two runs. As flow travels through the first half of the bend (30 and 45º) the maximum streamwise velocity is concentrated closer to the inside of the channel bend and near the water surface. As the flow nears the exit of the bend (105º) maximum streamwise velocity has moved away from the water surface, closer to the bed and further into and over the scour hole. The greatest difference in mean flow field is found in the mean streamwise velocity contours at 105º, where the local differences in bathymetry have resulted in much lower streamwise velocity near the inner bank for Run 2.

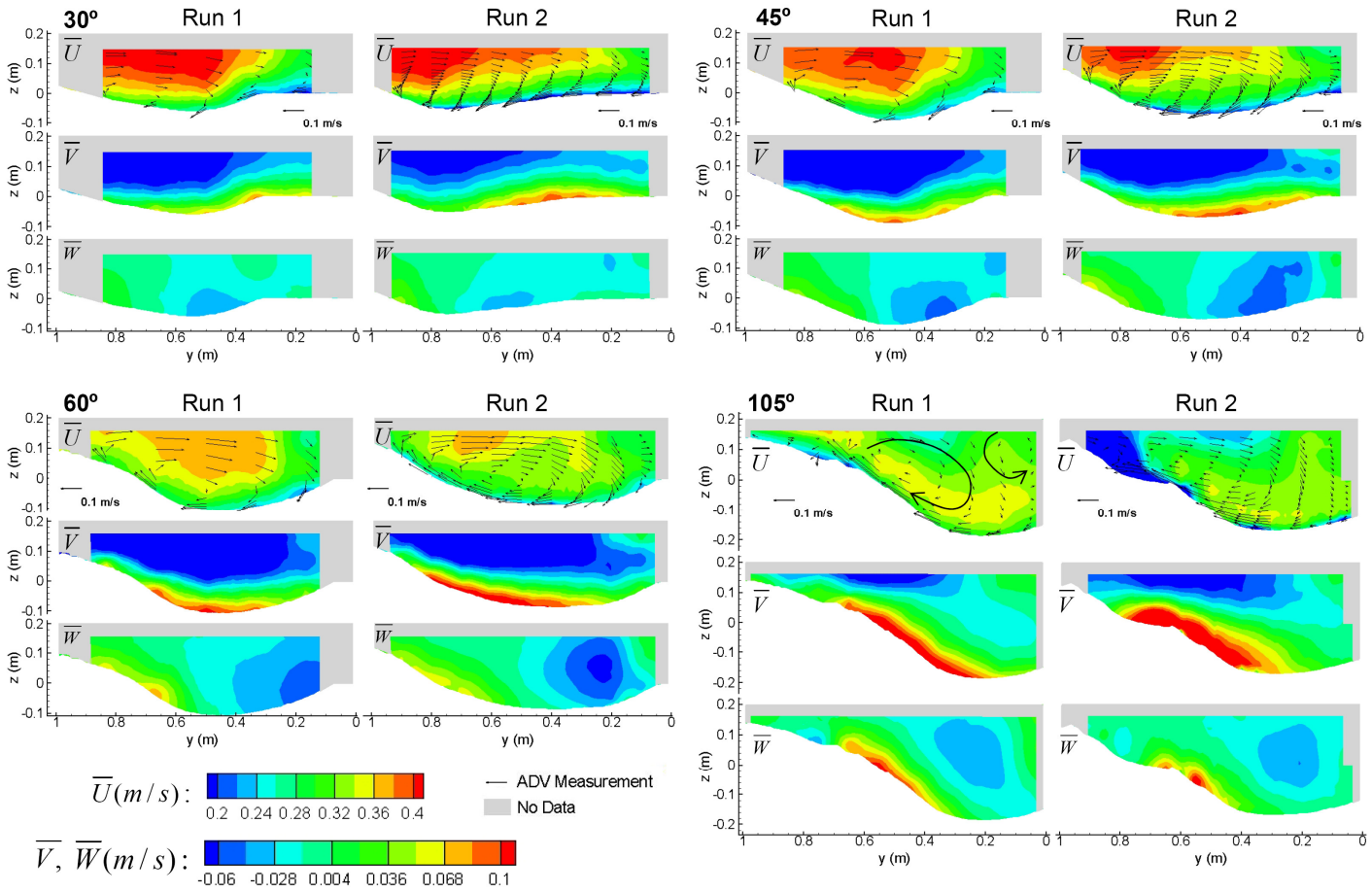

Figure 5.1.6. Contour plots of mean streamwise ($\overline{U}$), cross stream ($\overline{V}$) and vertical velocity ($\overline{W}$) for all corresponding cross sections for Runs 1 and 2. Mean cross sectional velocity vectors are plotted with $\overline{U}$ contours, where vectors represent measured ADV data. Note the development of the secondary circulation cell in the upper outside region of the flow. Grey areas indicate where no data was collected.

The velocity vectors in Figure 5.1.6 also show the development of the secondary flow through the bend. Between 30 and 45º both the magnitude of the secondary velocity vectors and the size of the primary secondary flow cell have increased. These velocity vectors also show the development of a second circulation cell in the upper half of the flow, near the outer bank (referred to now as the outer bank circulation cell), which has an opposite sense of rotation from the primary secondary flow cell. Velocity vectors for Run 2 (which had measurements at a higher density than Run 1) show how the outer bank circulation cell is not yet present at 30º but begins to take shape at 45º, one third of the way through the bend. By 105º, the outer circulation cell appears fully developed (indicated by large arrow). The relative size of the outer bank circulation cell also changes through the bend, with its maximum at 105º (the last measured cross section with a high density of data). It should be noted that, if present, the outer bank circulation cell will only be resolved with a sufficient number of measurements close to the wall. For example, the greater number of near wall measurements close to the water surface in Run 1 at 105º explains why the outer circulation cell is more pronounced in this cross section than in Run 2 (Figure 5.1.6).

In their experimental study of a 120º bend, Blanckaert and Graf (2001) noted that the most important feature observed was the existence of an outer bank cell of secondary circulation half way along the bend, at 60º. This observation agrees well with the outer bank circulation cell found in the outer region of the 105º cross section. However, Blanckaert and Graf (2001) collected data at only the outer half of a single cross section. Therefore, it is not possible to comment on the presence or growth of the outer bank circulation cell in other regions of the bend and compare with the present results. Blanckaert and Graf (2001) also reported that the core of maximum velocity in the outside of the bend was found in the lower half of the flow, closer to the bed, which is consistent with the results of the present study.

The flume was designed with a sufficiently long straight approach section to ensure a fully developed boundary layer was established before the bend. At 12 m from the flume entrance (0.19 m before the bend), Reynolds stress profiles tend to zero at the water surface (Figure 5.1.7 A) and fully developed flow is assumed. A reach averaged shear velocity ($\overline{U_*}$) in the straight section can be simply calculated by $\overline{U_*} = \sqrt{gRS}$, where g is gravitational acceleration (9.81 m/s^2), R is hydraulic radius and S is water surface slope. In both Runs 1 and 2, $\overline{U_*}$ was equal to 0.025 m/s (Table 5.1.1).

Estimates of bed shear stress and shear velocity in the main channel approach section were also made from linear regressions of the measured velocity and turbulence profiles. These two regression methods are considered superior to the reach averaged calculation since these values are based on local flow conditions and incorporate considerably more data. In the first method, the log-law (law of the wall) velocity profile for fully rough turbulent uniform flow is calculated as

$$\overline{U} = \frac{U_*}{\kappa}\ln(z) + \frac{U_*}{\kappa}\ln\left(\frac{30}{k_s}\right) \qquad (5.1.3)$$

where $\overline{U}$ is the mean streamwise velocity at a distance z from the bed, U_* is shear velocity, κ is the von Kármán constant (0.41), and k_s is the roughness parameter (equivalent to the sand grain roughness). From this equation U_* and k_s are determined from a linear regression of $\overline{U}$ versus ln(z). With each value of U_* an estimate of bed shear stress (τ_o) can be made from $\tau_o = \rho U_*^2$, where ρ is the density of water. In each experiment, profile measurements in the center third of the channel at the bend entrance (at 12 m for Run 1 and 12.19 m for Run 2) were used to plot the linear regression of $\overline{U}$ versus ln(z). By combining multiple vertical

profiles for each cross section, average values (U_{*A}, k_s and τ_{oA}, where the subscript letter refers to the estimation method) for each run were calculated and are summarized in Table 5.1.2. Similarly, using the same ADV profile data, τ_o was estimated by extrapolating the vertical distribution of Principle Reynolds stress ($-\rho\overline{u'w'}$) to the bed (Nikora and Goring, 2000), from which an estimate of U_* can be made from $U_* = \sqrt{\tau_o / \rho}$. Again, profiles in each cross section are combined to calculate the average values for this regression method (U_{*B} and τ_{oB}) (Table 5.1.2).

Table 5.1.2. Summary of calculated shear velocity (U_*) and bed shear stress (τ_o) in the approach channel just upstream of the bend entrance.

Estimation Method:			A: $\overline{U}$ vs. ln z		B: z vs. $-\rho\overline{u'w'}$		*Mean*	
Run	*Cross Section (m)*	*No. of Profiles*†	U_{*A} *(m/s)*	τ_{oA} *(N/m²)*	U_{*B} *(m/s)*	τ_{oB} *(N/m²)*	U_* *(m/s)*	τ_o *(N/m²)*
1	12	4	0.016	0.28	0.020	0.42	0.018	0.35
2	12.19	5	0.020	0.40	0.021	0.45	0.020	0.43

† No. of vertical velocity profiles within middle third of channel used in regression analysis.

Average values of shear velocity and bed shear stress at the bend entrance for each linear regression method (Table 5.1.2) follow the same trend, where shear velocity and bed shear stress are slightly higher in Run 2 for both methods (Table 5.1.2). Where turbulence measurements are available Biron *et al.* (2004) recommend that the Reynolds stress extrapolation method be used for estimates of shear stress. Given the relative agreement of these two methods, final average values of U_* and τ_o are calculated by combining the results of the two regression methods. Average U_* and τ_o values are 0.018 and 0.020 m/s,

and 0.33 and 0.43 N/m^2 for Runs 1 and 2 respectively (Table 5.1.2). It is worth noting that estimates of U_* by the same method were similar further upstream of the bend entrance (U_* was 0.019 m/s at the 10 m section in Run 1 and U_* was 0.021 m/s at the 11 m section in Run 2).

Reynolds Shear Stress and Turbulent Kinetic Energy

The calculation of Reynolds shear stress provides an indication of the stress on the fluid due to shear from turbulent fluctuations. In most straight open channel flow scenarios, the principal (streamwise-vertical) Reynolds stress (τ_{uw}) is largest and therefore most significant. However, in the case of secondary (helical) flow in a bend, where the direction of the bulk flow is not necessarily in the streamwise direction, each of the three components of Reynolds shear stress terms become important.

Figure 5.1.7 shows profile plots of mean streamwise velocity and the three Reynolds stresses at two different locations for Run 1: (A) in the straight approach section 12 m from the flume entrance (before the bend) in the center of the channel (y = 0.50 m); and (B) near the deepest region of the 105º cross section (y = 0.25 m). There are noticeable differences between each corresponding profile: (i) maximum streamwise velocity is closer to the water surface at 12 m and closer to the bed at 105º (as seen in the interpolated contours in Figure 5.1.6, Run 1); (ii) in the straight section (12 m) principal Reynolds stress near the bed is close to double and four times the values of streamwise-cross stream (τ_{uv}) and cross stream-vertical (τ_{vw}) components, while at 105º τ_{uv} and τ_{vw} components are now greater than the principal Reynolds stress components (in absolute terms); (iii) the location of maximum τ_{uv}

and τ_{vw} Reynolds stress is no longer closest to the bed, unlike the 12 m profile. It is worth noting that the streamwise velocity profile and the principal Reynolds stress profile at the 105º section have shapes typical of accelerating flow (cf. Afzalimehr and Rennie, 2009), as expected for flow rising out of the scour hole.

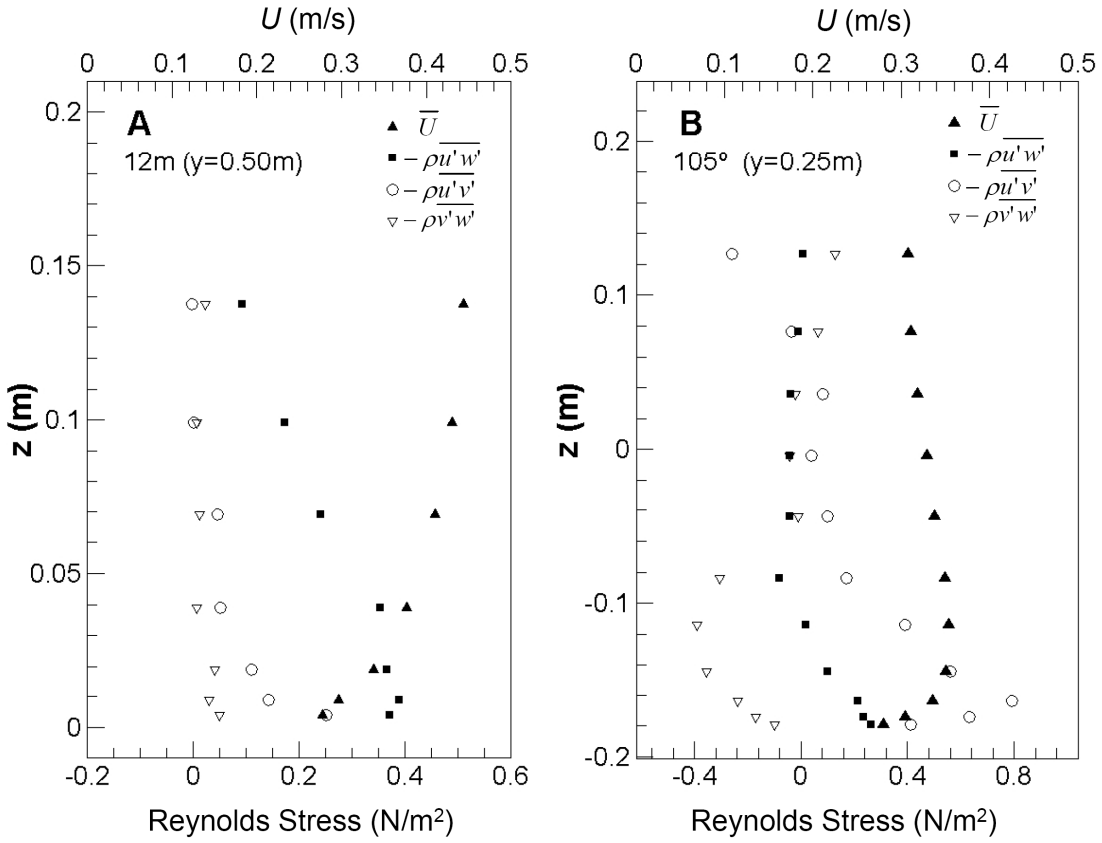

Figure 5.1.7. Profile plots of mean streamwise velocity ($\overline{U}$) and all three components of Reynolds stress ($-\rho\overline{u'w'}$, $-\rho\overline{u'v'}$ and $-\rho\overline{v'w'}$) for Run 1 at: (A) 12 m from the flume entrance at the center of the channel (y = 0.50 m); and, (B) the deepest section at 105º (in the scour hole, where y = 0.25 m). Symbols represent measured ADV data.

Secondary flow, which is the combination of cross stream and vertical velocity components, is the dominant pattern for flow in a bend, and so it is understandable that the streamwise-cross stream and cross stream-vertical Reynolds stress components, which are

each a function of cross stream turbulent velocity fluctuations and associated momentum flux, could be greatest through the bend. Figure 5.1.8 shows eight different contour plots of the distribution of near bed (5 mm from the bed surface) dimensionless Reynolds stress components and turbulent kinetic energy (*tke*) through the bend for Run 1. The contour plots on the right (A2, B2, C2 and D2) provide a two-dimensional view of contour values, while the plots on the left (A1, B1, C1 and D1) show the same two-dimensional contour plots overlain on a three-dimensional surface plot of bathymetry to show the distribution of near bed Reynolds stress and *tke* in relation to bed topography. Contour values are calculated by interpolating 67 point measurements, which were taken at 5 mm from the bed, at 12 different cross sections through the bend (Figure 5.1.8 D2 shows the spacing and density of ADV data points). Interpolation was made using Kriging and a model variogram fit to the experimental variogram for each interpolated variable. Overall, Reynolds stress through the bend varies between approximately -0.6 and 0.6 N/m^2. Reynolds stress values in Figure 5.1.8 have been non-dimensionalized by ρU_*^2 while *tke* has been non-dimensionalized by U_*^2 (Figure 5.1.8 D1 and D2). The U_* value used for non-dimensionalizing is the average value in the straight approach section (based on the two regression methods) reported in Table 5.1.2. A similar interpolation for Reynolds stress components and *tke* was not completed for Run 2 due to the lack of spatial coverage of ADV data through the bend.

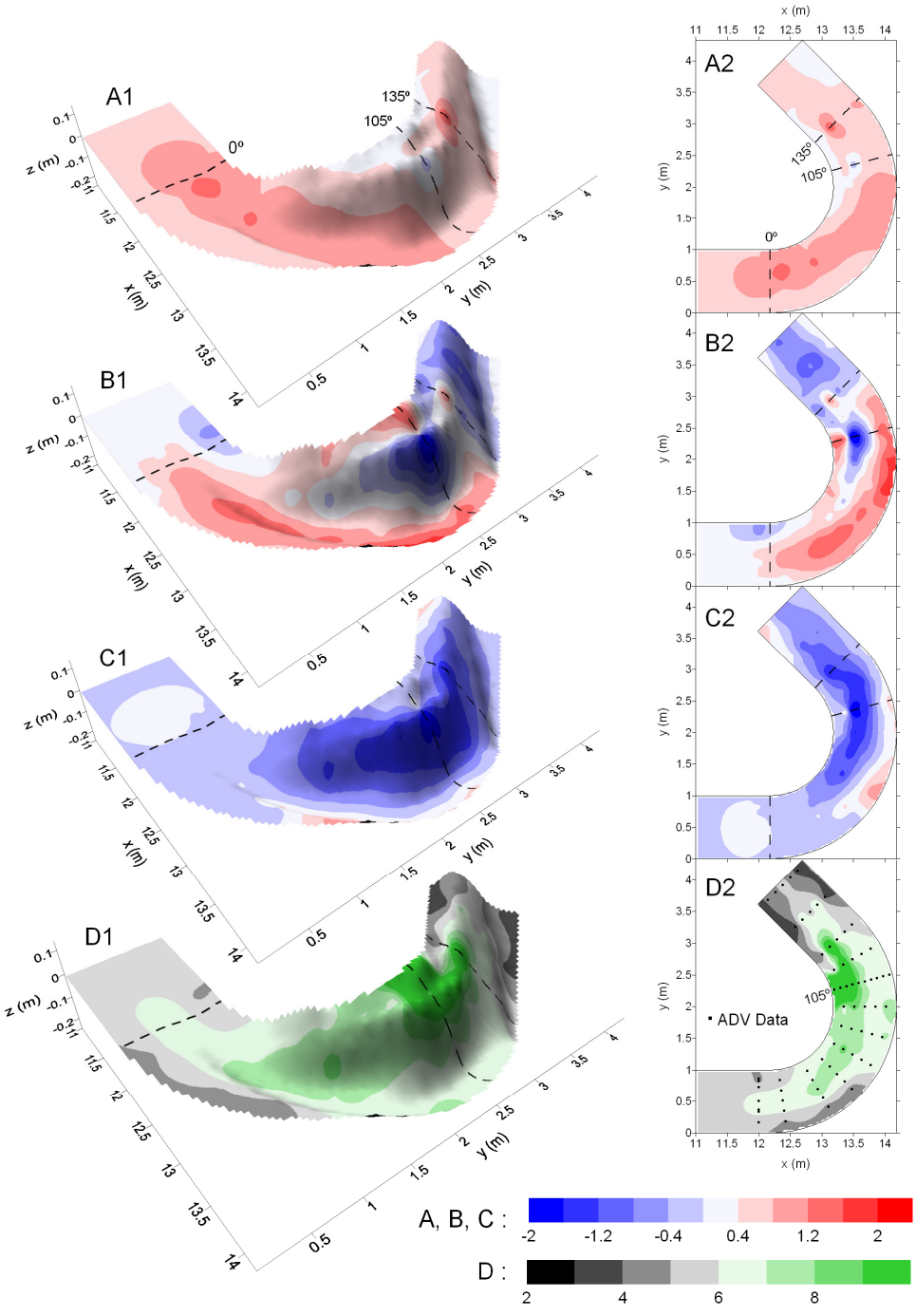

Figure 5.1.8. Distribution of dimensionless Reynolds stress components (A, B, C) and *tke* (D) measured 5 mm from the bed for Run 1. Contours represent $-\rho\overline{u'w'}/\rho U_*^2$ (A1 and A2); $-\rho\overline{u'v'}/\rho U_*^2$ (B1 and B2); $-\rho\overline{v'w'}/\rho U_*^2$ (C1 and C2); tke/U_*^2 (D1 and D2). ADV measurement locations for all plots are indicated in D2. Contour plots A1, B1, C1 and D1 have been overlaid on a three-dimensional surface plot of bathymetry.

Figure 5.1.8 provides a useful and unique overall description of how the magnitude and distribution of near bed three-dimensional turbulent stresses are changing through the bend and how they relate to bathymetry. The highest principal Reynolds stress is found near the entrance of the bend and along the inner bank, and corresponds with the beginning of the thalweg. However, progressing through the bend, principal Reynolds stress decreases and both streamwise-cross stream and cross stream-vertical Reynolds stress increase and begin to dominate. Both these "secondary" components of Reynolds stress reach maximum (absolute) values that are greater than the maximum principal Reynolds stress, which was found at the bend entrance. Through the bend, the outer bank region is dominated by high positive streamwise-cross stream Reynolds stress, while the inner bank region is dominated by high negative cross stream-vertical Reynolds stress. Figure 5.1.8 B1 clearly shows maximum positive streamwise-cross stream Reynolds stress corresponds with the outside (leading) edge of the thalweg (or scour hole). A similar pattern is observed for the distribution of *tke* through the bend: high *tke* at the bend entrance corresponds with the location of the start of the thalweg; and the inner bank slope is dominated by high *tke*, with maximum values located near the exit of the bend, between cross sections 105 and 135º.

The local peaks (positive and negative) in streamwise-cross stream Reynolds shear stress near the inner bank region at 105º could be in part due to local bed features. This region is dominated by a shallow point bar and the presence of dunes (Figure 5.1.3 A) as well as having the most active bed level differences (Figure 5.1.3 C). Flow separation at the dune crests would result in higher turbulence. As well, cross stream bank slope is steepest at 105º and therefore likely to induce the largest velocity gradient in the vertical direction, which would result in higher values of v' and w'.

The cross sectional distribution of dimensionless Reynolds stress in all four corresponding cross sections from Runs 1 and 2 are presented in Figure 5.1.9. In both experiments the maximum positive (and absolute) Reynolds stress component through the first half of the bend (30, 45 and 60º) is the streamwise-cross stream Reynolds stress component (τ_{uv}). At 105º overall Reynolds shear stress has reduced, but with high (negative) values of cross stream-vertical Reynolds stress along the inner slope of the scour hole. (Negative cross stream-vertical Reynolds stress corresponds with the product of turbulent velocity fluctuations v' and w' of equal sign, which are positive towards the inner bank and water surface respectively, indicating that fluctuations are directed parallel to the slope). Negative cross stream-vertical Reynolds stress increases though the bend with maximum values at 105º where cross stream side slope is greatest.

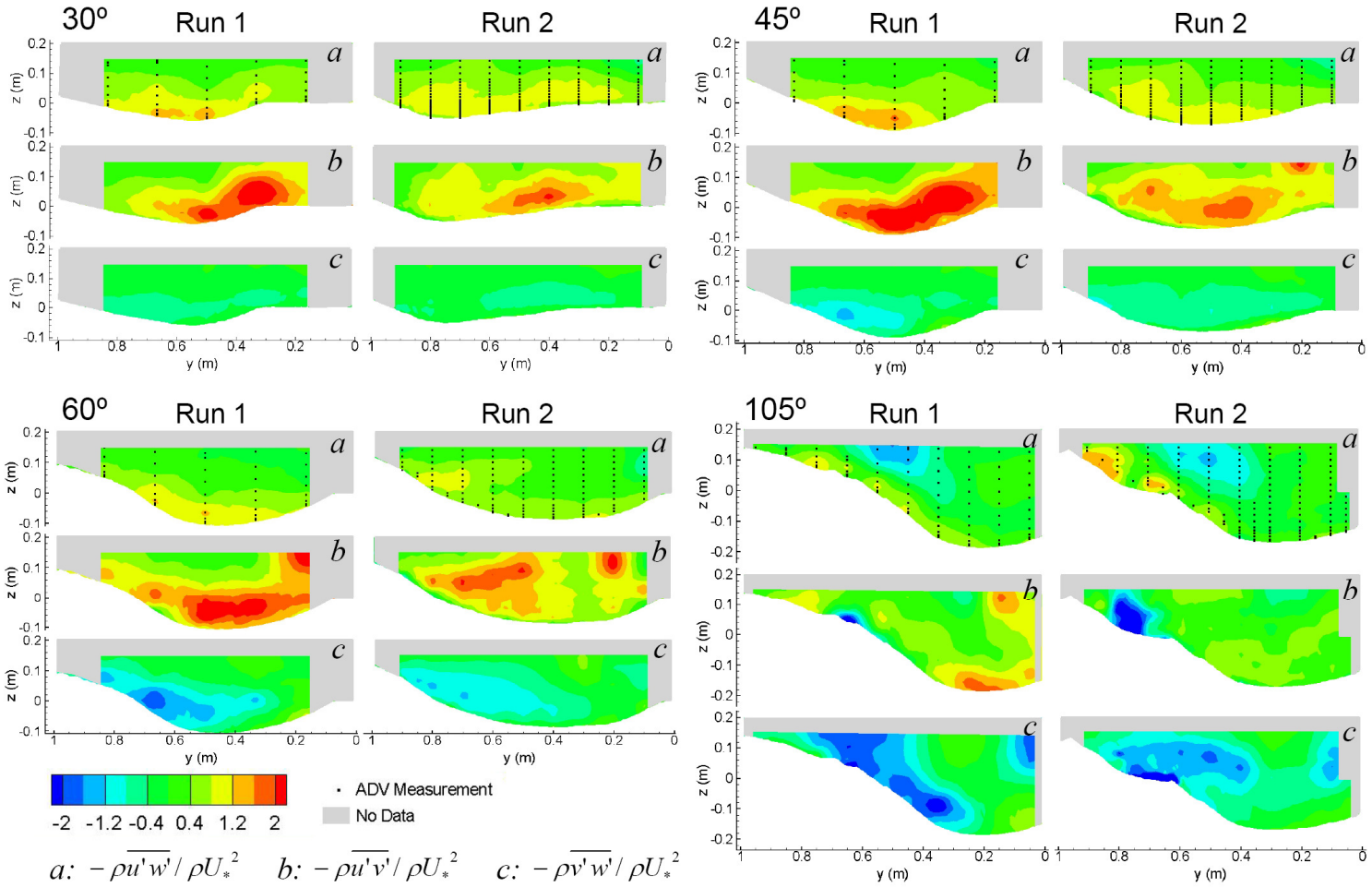

Figure 5.1.9. Distribution of dimensionless Reynolds stress components: (a) $-\rho\overline{u'w'}/\rho U_*^2$ (b) $-\rho\overline{u'v'}/\rho U_*^2$ and (c) $-\rho\overline{v'w'}/\rho U_*^2$ at four different cross sections (30, 45, 60 and 105°) for both Runs 1 and 2. Square symbols represent ADV measurement locations. Grey areas indicate where no data was collected.

The 105º results in Figure 5.1.9 also show the distinct difference in bed levels between the two runs. Run 1 shows a slowly decreasing side slope towards the inner bank, while Run 2 shows a more abrupt change with almost two distinct scour holes. This variation is also shown in Figure 5.1.3 C and has already been discussed in the bathymetry section. The variation of principal Reynolds stress between the two runs at 105º is minimal, compared to the differences in the other two components: (i) there is a region of high positive streamwise-cross stream Reynolds stress in the outer bank scour hole of Run 1, but not Run 2; and (ii) the spatial extent of high negative cross stream-vertical Reynolds stress along the inner side slope is much greater in Run 1 compared to Run 2. Considering all four cross sections, the streamwise-cross stream Reynolds stress is greater and more concentrated over the thalweg (i.e. scour hole) in Run 1 then Run 2 for all four cross sections.

The same trend in Reynolds stress distribution between Runs 1 and 2 can be seen in average *tke*. Contours of non-dimensionalized *tke* for the four corresponding cross sections in Run 1 and 2 are shown in Figure 5.1.10. In all four cross sections, average turbulent kinetic energy in Run 1 is approximately 1.5 to 2 times greater near the bed and more localized over the scour hole than Run 2. Of these four cross sections, turbulent kinetic energy is maximum (>0.0035 m^2/s^2) near the inner wall at 105º. This region represents the area behind an inner bend point bar (Figure 5.1.3 A and B) and the location of maximum elevation difference between the two runs (Figure 5.1.3 C).

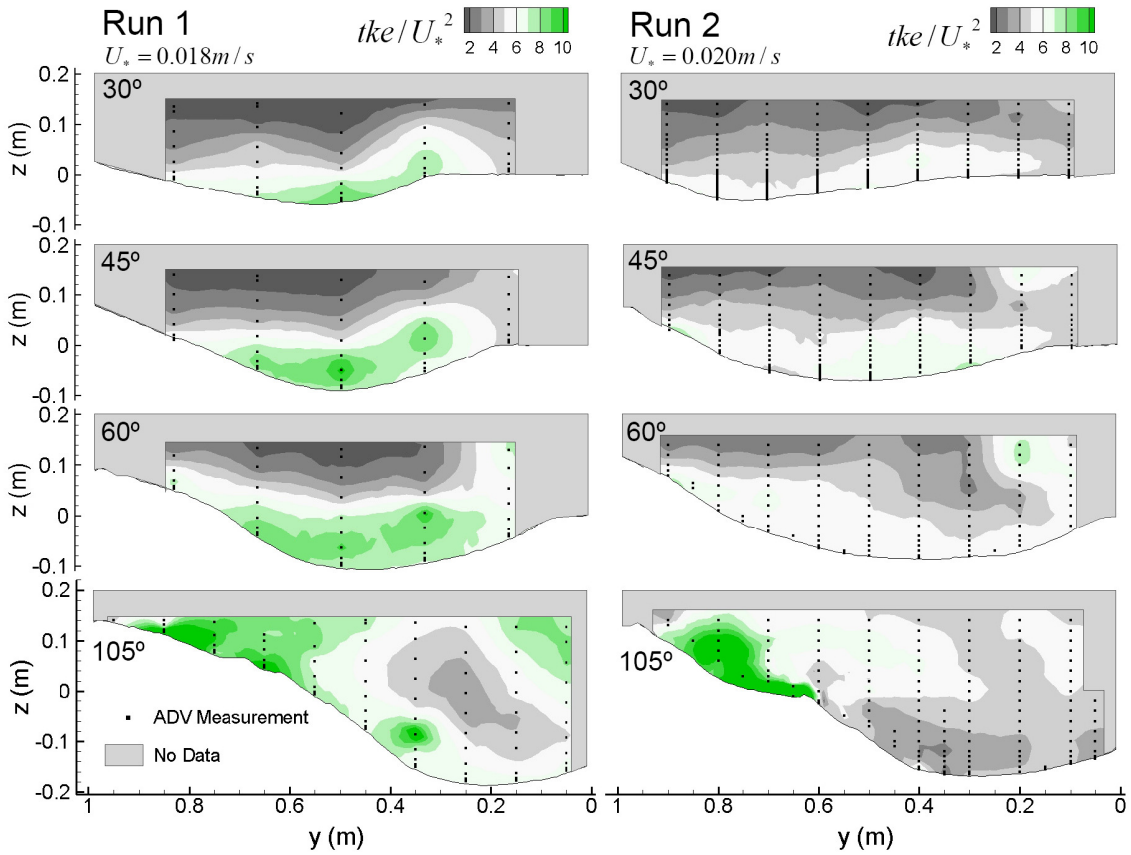

Figure 5.1.10. Distribution of dimensionless total turbulent kinetic energy (tke/U_*^2) at each cross section (30, 45, 60 and 105º) for both Run 1 (left) and 2 (right). Gray boxed areas indicate regions where ADV data was not collected.

Minimum *tke* in the 105º section is over the scour hole, near the outer bank for both runs. However, in Run 1 minimum *tke* is at approximately one-half of the local depth, compared with being directly above the bed in Run 2. The 105º result for Run 1 corresponds closely with the data presented by Blanckaert and de Vriend (2005).

The variation in Reynolds stress and turbulent kinetic energy between cross sections highlights the influence that the bend geometry has on the distribution and magnitude of these turbulent stresses. Extending the comparison between runs indicates that the nature of

these stresses may be further influenced by sediment transport activity near the bed. Equilibrium geometry had not yet been reached in Run 1, i.e., excess shear stress was still available to transport sediment. The three-dimensional nature of this excess stress is evident in Figure 5.1.8 and Figure 5.1.9.

5.1.5 Discussion

The location of the thalweg near the outer bank is of particular importance, since it promotes bank erosion through undermining of the toe of the slope along the outside bank. In previous laboratory experiments (Matsuura and Townsend, 2004) and corresponding numerical analysis (Minor *et al.*, 2007a and 2007b) for flow in a 135º channel bend, the thalweg was found to move far enough to the outside bank that it was directly in contact with the outside channel wall. Unlike these studies, the present results show that the thalweg never directly encroached on the outside wall (until the bend exit), but rather migrated toward the outside wall through the bend. The difference in location of the thalweg could be the result of the additional outer bank circulation cell: the presence of a an outer bank circulation cell, which has the opposite sense of rotation to the principal secondary flow cell, prevents the increase in flow outward from impinging onto the outer bank. As Blanckaert and Graf (2004) suggested, the cell stabilizes the region between the outer bank and the center region cell thereby keeping the core of high velocity at some distance from the outer bank. However, in the case of Blanckaert and Graf (2001) where the outer bank circulation cell was identified, maximum scour appeared to impinge along the outer bank wall.

Without detailed measurements of the velocity field, Matsuura and Townsend (2004) could not confirm directly whether or not the outer circulation cell was present in their

experiment. The numerical results of Minor (2006) and Minor *et al.* (2007b) [who modeled the same bend flume as Matsuura and Townsend (2004) and calibrated according to bathymetry], show no signs of a second outer bank circulation cell. However, it is likely that the numerical simulation simply failed to model the outer region correctly, in which case it could have been present in the experiment, but without velocity data it cannot be verified. In a recent laboratory and numerical study for a sharp (193º) channel bend with two different bathymetries (flat and equilibrium), Zeng *et al.* (2008) were only able to capture the counter rotating outer bank cell for the experimental flat bed case; both numerical simulations failed to predict this pattern, and it was not measured in the equilibrium case. Given the inconclusive results (see also Blanckaert and de Vriend, 2004), further research is clearly needed to understand the basis for an outer bank, counter-rotating cell of cross stream circulation, how it effects the distribution of shear stress at the outer bank and therefore, the consequences to outer bank erosion.

The three Reynolds stress terms (τ_{uw}, τ_{uv} and τ_{vw}) fully resolve the three-dimensional turbulent stresses due to shear from turbulent fluctuations in all directions. Even at low mean velocities, maximum instantaneous values in all directions can be very high (and vice versa), which in the context of sediment transport can be important. Velocity fluctuations in the streamwise and vertical directions (u' and w' respectively) are typically responsible for most of the contribution to the Reynolds shear stress (Lu and Willmarth, 1973), and are understood to play an important role in sediment transport dynamics (Leeder, 1983; Best, 1993). However, this association between velocity fluctuations (Reynolds stresses) and sediment transport assumes that the frame of reference is parallel to the plane of the bed and that the mean vertical velocity, which is normal to the bed, is equal to zero. In the present

study it was not possible to align the ADV perpendicular to the plane of the bed at each measurement, due to the highly variable bed topography and the need to maintain a consistent frame of reference for assessing spatial variability. Therefore, it should be emphasized that in this study, the Reynolds stress components are defined relative to the chosen frame of reference, instead of a true absolute measure at each local point based on streamlines (local flow vectors) and bed topography. Despite this, the spatial distribution of *tke*, which is not sensitive to instrument alignment or orientation in relation to local streamlines and the plane of the bed, confirms that the location of maximum turbulent stresses are along the inner bank slope, near the 105º cross section, where cross stream side slope is greatest and cross stream transport was most apparent. In this region, the relative contribution of principal Reynolds stress is negligible in comparison to the other two components.

The variation in magnitude and spatial extent of all three components of Reynolds stresses (and corresponding *tke*) for flow in a bend demonstrates that the role of turbulent stresses on sediment transport cannot be restricted (or simplified) to a two dimensional description of velocity fluctuations (i.e. principal Reynolds stresses, τ_{uw}). Although mean secondary velocity remains lower than streamwise velocity throughout the bend (Figure 5.1.6), the influence of the cross stream motion remains important as it redistributes velocity and turbulent stresses, thereby influencing the magnitude and direction of boundary shear stress. Cross stream stresses establish cross stream transport, resulting in the characteristic formation of an inner bank point bar and an outer bank pool (Dietrich and Smith, 1983). Consequently, the shallowness of the point bar and the depth of the pool will vary through

the bend as the magnitude of cross stream stresses vary in part as a function of the cross stream-vertical (secondary) flow strength and the vertical distribution of streamwise velocity.

Evidence of this relationship between turbulent cross stream stress and bar-pool morphology is found in Figure 5.1.8: (1) maximum positive streamwise-cross stream Reynolds stress (corresponding to opposite signs of u' and v') coincides with the leading edge of the outer bank thalweg (pool), until the exit of the bend, where cross stream velocity diminishes and pool depth decreases; (2) maximum cross stream-vertical Reynolds stress (in combination with high negative streamwise-cross stream Reynolds stress near the bend apex) coincide with the leading edge of the inner bank bar; (3) regions of cross stream bed load transport, which is directed from the outer bank pool to the inner bank bar (based on ripple crest orientations and observed ripple migration patterns), correspond with the regions of maximum τ_{uv}, τ_{vw} and *tke*.

Cross stream (or transverse) bed load transport in a meander bend is a function of the transverse gravitational force, which is directed down-slope towards the outer bank pool, versus the transverse fluid forcing, which (near the bed) is directed up-slope towards the inner bank. In both runs a stable bed topography was established under clearwater scour conditions when it was observed that sediment transport had ceased. However, it is proposed that Run 2 was at or closer to equilibrium than Run 1 since the experiment was run longer. This hypothesis is supported by the fact that there were more ripples present along the inner bank slope at the end of Run 1 compared to Run 2. Moreover, the region of active bed load transport (i.e. the region of cross-stream orientated ripples, which extends between 50-135º through the bend) corresponds closely with the location of maximum τ_{uv}, τ_{vw} and *tke* (Figure 5.1.8). These turbulent stresses were measurably greater in Run 1 than Run 2 for the

same regions (see 60 and 105º results in Figure 5.1.9 and Figure 5.1.10) where the presence of ripples at the end of Run 1 provides evidence of transport still in progress, which reinforces our hypothesis that at a certain magnitude and direction, all three components of turbulent stresses play a role in initiating and maintaining bed load transport.

While Blanckaert and Graf (2001) also found that the magnitude of the principal Reynolds stress was low in the outer bank region compared with the straight approach flow, principal Reynolds stress near the bed at the bend apex remained an order of magnitude larger than both τ_{uv} and τ_{vw}. The measurements of Blankaert and Graf (2001) were limited to extrapolation (by up to 40 mm above the bed) in order to resolve the near bed flow field in the outer bank region and it is possible that by imposing physical boundary conditions such as the no-slip condition at the bed and side wall, the authors may have incorrectly estimated turbulent stresses near the bed.

Considering the entire depth of the flow, the concentration of higher Reynolds stresses (and in particular τ_{uv} and τ_{vw}) and turbulent kinetic energy over the scour hole in the developing channel (Run 1) appears important (Figure 5.1.9 and Figure 5.1.10). Maximum non-dimensional turbulent stresses and kinetic energy at the leading (outside) edge of the scour hole in the developing bed case not only confirms the observations (and discussion above) of maximum near-bed Reynolds stress (Figure 5.1.8), but provides further evidence that the three-dimensional instantaneous turbulent stresses play a role in mobilizing and transporting sediment towards equilibrium scour. At the stage of final equilibrium (Run 2), non-dimensional Reynolds shear stress and turbulent kinetic energy are lower and have become slightly less concentrated over the scour hole.

The structure of turbulence can be modified by the presence of particles in natural flows and has been known to both dampen and enhance turbulence in the presence of suspended sediment depending on the distance from the bed (Best *et al.*, 1997; Nezu and Azuma, 2004) and particle size (Nino and Garcia, 1998; Cao *et al.*, 2003). In this study, sediment transport is due to bed load alone, with an active layer less than 5 mm. The presence of moving particles in the active layer could affect the growth and presence of turbulence near the bed, but it is not considered to alter the measurements of turbulent fluctuations significantly further into the flow field away from the bed. To determine the effects (if any) of a mobile bed on the distribution of velocity and turbulence in the non-equilibrium bed, the Run 1 experiment should be repeated with the same, but fixed bathymetry. Future experimental work is also planned that will involve fixing the bed at a number of different stages before equilibrium in order to describe changes in the turbulent flow field as it develops towards equilibrium conditions.

5.1.6 Conclusions

Experimental results of the mean flow field and turbulent stresses for flow in a mobile bed channel bend have been presented. Three-dimensional velocities and turbulence (Reynolds stresses and turbulent kinetic energy) were measured and described for multiple cross sections throughout the bend for two separate experiments at different stages of clear water scour.

The results present five intriguing observations. (1) The presence of a second, counter rotating outer bank circulation cell is established one-third of the way through the bend, which appears to reduce principal Reynolds stress near the outer bank, and possibly

influence the location of the thalweg. However, the basis for this feature and its importance to sediment transport and scour in the outer bank region is not fully understood as current research remains inconclusive. (2) The distribution of maximum three-dimensional Reynolds stresses and turbulent kinetic energy tend to concentrate over the thalweg and increase in magnitude through the first half of the bend. (3) The magnitude and distribution of streamwise-cross stream and cross stream-vertical Reynolds stresses increase through the bend, with maximum values exceeding the principal Reynolds stress component. (4) Maximum positive streamwise-cross stream Reynolds stress coincides with the leading edge of the outer bank scour hole, while maximum cross stream-vertical Reynolds stress (in combination with high negative streamwise-cross stream Reynolds stress near the bend apex) coincide with the leading edge of the inner bank bar. (5) Maximum dimensionless Reynolds stress and average turbulent kinetic energy near the bed and over the scour hole (thalweg) are greater and more localized before final equilibrium bathymetry is reached. This last observation suggests that the turbulent energy in the flow is higher while the channel bathymetry is developing and that as well as lower energy, an even distribution of turbulent stresses is required before equilibrium is reached and the flow is no longer able to mobilize and transport particles along the bed.

The next step in this research will be to test further the hypothesis that the mean turbulent flow field is time and space dependent, varying as a result of non-equilibrium bathymetry and bed load transport, and the added complexity of three-dimensional flow. A better understanding of the role of three-dimensional turbulent stresses in a channel bend and the consequences for sediment transport has important implications for predicting flow and morphological changes in natural rivers and river engineering applications.

5.2 Flow and sediment dynamics in a laboratory channel bend with and without stream barbs (submerged groynes) 1: Mean flow field

Jamieson, E.C., Rennie, C.D. and Townsend, R.D. (*Submitted - a*). Flow and sediment dynamics in a laboratory channel bend with and without stream barbs (submerged groynes) 1: Mean flow field. Submitted to *Journal of Hydraulic Engineering*, December, 2010; revision submitted September 2011.

5.2.1 Abstract

A series of laboratory flume experiments have been carried out to study the effect of stream barbs on flow field dynamics and sediment erosion in a 135º mobile-bed channel bend. Stream barbs (also known as spur dikes or submerged groynes) are low profile linear rock features that redirect high velocity flow away from the outer bank of channel bends. Unlike traditional (emergent) groynes, the submerged nature of these structures creates a unique combination of horizontal shear (plunging type flow) and vertical shear (at the groyne tip). Spatially dense, high frequency velocity data have been collected and analysed to describe the pattern and magnitude of three-dimensional velocity throughout the bend and in the vicinity of the stream barbs. The companion paper presents details of the spatial distribution of turbulent kinetic energy, Reynolds shear stresses and vorticity through the bend. This paper demonstrates that the outer bank region (particularly between barbs) may still be at risk of erosion (or even increased erosion greater than the same case without barbs) if stream barbs generate excessive secondary velocities (due to their size and layout) that are opposing the primary secondary flow naturally occurring in channel bends. Characterizing the role of flow field dynamics on the pattern of deposition and erosion through experimental measurements provide valuable data on how such flow features contribute to local scour, and on the performance of these structures.

5.2.2 Introduction

Many different in-stream engineering measures exist for protecting stream banks and preventing unwanted erosion. Excessive stream bank erosion can damage infrastructure and degrade aquatic habitats by increasing fine sediments in the channel substrate and widening streams (Espinosa *et al.,* 1997; Sekely *et al.,* 2003). A relatively new approach to sustainable stream bank protection is the stream barb, a submerged variation of a groyne, similar to spur dikes and bendway weirs. Stream barbs (or barbs) are low-profile linear rock structures, typically anchored, in series, to the outside bank in stream bends and extend in an upstream direction away from the bank into the flow (USDA, 2005). This configuration redirects flow away from the outer stream bank and disrupts the velocity gradient close to the outer bank, encouraging sediment deposition adjacent to the barb, near the bank. Moreover, with time, barbs cause the thalweg in a channel bend to relocate away from the outside bank region (an undesirable and unstable location) to a new more stable location closer to the channel centreline.

Unlike traditional measures of stream bank protection such as riprap, concrete paving or gabion walls, which impede the establishment of vegetated stream banks, hydraulic structures such as stream barbs that redirect the flow are a more environmentally sustainable means of maintaining stream bank stability. As well as providing bank protection, these structures promote vegetated stream banks (Piper *et al.,* 2001), create resting pools and scour holes for fish habitat (Shields *et al.*, 1998) and increase bio-diversity of aquatic species (Shields *et al.*, 2000). Research is therefore needed to investigate the suitability and optimal design of stream barbs in channel bends. The most recent studies of fluid and sediment dynamics around spur dikes and barbs have considered straight laboratory channels (Fox *et al.,* 2005a and 2005b; Kuhnle *et al.,* 2008) and non-simultaneous measurements of flow field

and bed morphology (Bhuiyan *et al.,* 2009). The one exception is the recent study of thin bank-attached vanes by Bhuiyan *et al.* (2010). We are not aware of any laboratory or field studies that have investigated the spatial variation in three-dimensional (3-D) turbulent flow structure and associated patterns of scour and deposition around a series of upstream-angled rock stream barbs in a channel bend, where in practice these structures are most typically deployed. The systematic study of the effects of in-stream structures on local flow and sediment transport processes under controlled conditions in a large-scale laboratory flume are rare. Such investigations are critical if we are to understand these complex processes and provide the necessary data for validating numerical models. This is especially true for mobile bed conditions, where data are most lacking, despite being vital for linking the influence of flow patterns and turbulence to sediment transport processes.

Flow in a channel bend can be characterized by the secondary (or helical) flow that develops as a result of centrifugal forces imposed on the flow due to the bend geometry and superelevation of the water surface. Secondary flow introduces a transverse shear that alters the distribution of bed shear stress (e.g. Dietrich and Whiting 1989, Blanckaert *et al.* 2008) and near-bed turbulent stresses (Jamieson *et al.*, 2010; Chapter 5.1; Termini and Piraino 2010) across a channel section and consequently influences the distribution of sediment. As the secondary flow interacts with the primary streamwise flow the result is maximum shear stress on the outside of the bank downstream of the channel bend, leading to increased erosion in the outer bank region (Dietrich and Whiting, 1989). In a sharp meander bend, superelevation is greatest where the primary flow collides with the outer bank, resulting in pronounced downwelling velocities that impinge on the bed and are likely the main cause of bed scour (Blanckaert, 2010). The purpose of placing stream barbs in a channel bend is to disrupt the secondary flow, thereby reducing outer bank shear stress and transport. One

mechanism for disrupting secondary velocities is the plunging (or downwelling) flow that develops immediately downstream of submerged barbs during overtopping conditions. The plunging flow leads to some substantial differences in the geometry of scour holes for in-stream structures without overtopping flow (Kuhnle *et al.,* 1999 and 2002). These observations need to be investigated further. It is not known what impact the plunging flow has on maximum scour depth and on the disruption to secondary flow, and hence the function and reliability of different barb shapes, sizes and arrangements in channel bends. Understanding the flow in detail should provide a better means of predicting the resulting bed level changes for various barb geometries and orientations.

A number of different laboratory experiments on bank-attached submerged structures (stream barbs, submerged groynes, spur dikes, bendway weirs, vanes, etc.) in open channel flows have been performed: Kuhnle *et al.,* (1999); Johnson *et al.* (2001); Kuhnle *et al.* (2002); Matsuura and Townsend (2004); Fox *et al.* (2005a and 2005b); Jia *et al.* (2005); Uijttewaal (2005); Kuhnle *et al.* (2008); and Bhuiyan *et al.* (2009 and 2010). A review of these studies highlights a few of the gaps in the current literature: (1) the limited number of studies that consider a meandering or channel bend planform, where the use of these structures is most relevant; (2) the lack of detailed velocity and turbulence measurements; (3) the lack of coupled mobile-bed studies with comprehensive velocity and turbulence measurements. Other (less relevant) experimental studies include non-submerged (or emergent) groyne studies (Uijttewaal *et al.,* 2001; Weitbrecht *et al.,* 2002; Sukhodolov *et al.,* 2002); scour depth studies at abutments (Melville, 1992; Lim, 1997) and spur dikes (Garde *et al.*, 1961; Gill, 1972; Kuhnle *et al.*, 1999); those with a focus on numerical simulations (Minor *et al.*, 2007a and 2007b; McCoy *et al.* 2008; Koken and Constantinescu, 2008a and 2008b) and finally those with a habitat objective (Biron *et al.*, 2004), where the prevention of

stream bank erosion was not a principal objective and therefore was not investigated in detail.

Flume experiments by Kuhnle *et al.* (1999, 2002 and 2008) involved a single spur dike orientated perpendicular (Kuhnle *et al.,* 1999 and 2008) and angled (Kuhnle *et al.,* 2002) along a straight laboratory sand-bed channel. The earlier studies (1999 and 2002) characterized the volume of the scour hole at the tip of the spur dike, while the 2008 study investigated the flow field in detail over a fixed, flat bed. Kuhnle *et al.* (2008) found that the 3-D flow separation at the spur dike yielded forces on the bed that were significantly different from non-submerged vertical obstructions that have been measured in other studies. The maximum bed shear stress adjacent to the dike was found to be approximately 2.7 times the approach flow value, which is substantially less than that found for emergent flat plates mounted perpendicular to the flow. Koken and Constantinescu (2008a) also found the largest bed shear stress values to be near the tip of the spur dike. Fox *et al.* (2005a and 2005b) considered a single submerged groyne (angled 50º with the upstream bank) along a straight laboratory channel, but separated their measurements of velocity and scour. In both studies, velocity measurements were carried out for immobile, flat bed conditions; while scour tests were performed by Fox et al. (2005a), but for which no velocity measurements were made. Most recently, Bhuiyan *et al.* (2010) presented velocity and turbulence measurements in a meandering channel with and without a series of "bank-attached" vanes, constructed using 2 cm-wide plywood, which sloped from bankfull height at the outer bank down to the bed. Unlike previous laboratory studies, live bed scour conditions were simulated, which allowed testing of the functionality of installing the vanes after equilibrium scour in the meander bend was reached. Under live bed conditions, the performance of vanes to reduce scour along the outer bank through deposition in the vicinity of the vanes could be studied.

Matsuura (2004) tested the effectiveness of different barb arrangements in series (barb groups), in both 90º and 135º channel bends with a mobile sand bed. However, due to a lack of velocity data, these experiments were unable to characterize the flow field. As well, the experimental barbs were constructed out of a fine metal mesh (approximate width < 2mm), essentially creating a two-dimensional, permeable structure. Preliminary tests showed that any increase in width, or the use of a more trapezoidal cross section, would result in severe local scouring beyond the available depth of sand in the channel (just as Kuhnle *et al.* (2008) predicted with their measurements of bed shear stress, and as we have found in our current experiments). This is also a limitation of Bhuiyan *et al.'s* 2009 and 2010 studies of vanes. The extent of local scour (depth and volume) adjacent to a submerged structure will depend on the geometry and size of the structure (in addition to local flow features) and every effort should be made to reproduce realistic scales of structure geometry in the laboratory. The barbs built for the current laboratory study were constructed of loose stone (i.e. solid and slightly permeable material) with a roughly trapezoidal cross-sectional shape, representing a realistic model of field-scale barbs.

With the exception of Bhuiyan *et al.* (2010), who presented results at select cross-sections through the meander bend, to date the most detailed flow measurements have been for a single structure only and one that was installed along a straight section (Fox *et al.,* 2005b and Kuhnle *et al.,* 2008). Given that the primary objective of stream barbs is to reduce bank erosion, which is usually most severe along the outside banks of river bends, it is critical that future studies focus on channel bends. The helical (secondary) flow generated in a channel bend will alter the magnitude and direction of velocity as the flow approaches the barb and as a result the flow over and past the structure. This will in turn play a role in local

flow field characteristics and ultimately how the structure functions to disrupt velocity and shift the thalweg to the center of the channel, away from the outer bank.

Matsuura (2004) found that, although scouring in a 135º bend without barbs was significantly greater than in a 90º bend (tighter bends are known to increase water surface superelevation and secondary flow strength (Knighton, 1998)), barb groups in the 135º bend performed better. For all tested flow conditions and barb group arrangements, maximum scour reduction in the 135º bend was greater than in the 90º bend. However, it should be noted that it is assumed here that "maximum scour reduction" refers to total scour in the channel, since with rigid, vertical plexiglass walls it is not possible to evaluate the reduction in scour of the outer bank. This suggests that in this case, the percent reduction may not be a useful metric since some scour at the barb tip is desirable. In fact, of the relevant laboratory-scale mobile bed studies that have been performed, none have studied bank erosion – the initial conditions of all past mobile bed experiments was a horizontal (flat) bed with rigid vertical side walls. In our study, a sand bed with a trapezoidal-shaped cross-section was installed inside a flume having a rectangular cross-section. With this arrangement, both the bed and banks of the channel, in which the model barbs were installed, were subject to scour.

This paper presents the first experimental results to describe the spatial variability of the complex flow field and changes in channel bathymetry for a series of barbs in a channel bend. These experiments were designed to address the weaknesses of previous studies and incorporate such novel features as (1) spatially dense 3-D flow data; (2) the use of a mobile bed and bank trapezoidal channel; and (3) the use of barbs made of scaled rock riprap. The results of this study provide suggestions on optimizing barb structure design for stream bank protection or other requirements (i.e. scour holes for aquatic habitat), while, at the same time, advancing our understanding of the role of these coupled processes in general. These results

have implications for employing other similarly submerged in-stream structures and for understanding natural fluvial features where similar plunging flow conditions (or horizontal flow separation) are found; such as, forced riffle-pools and dune fields.

5.2.3 Experimental Methods

Data Collection and Processing

Six different laboratory experiments were carried out using the large bend flume located in the Civil Engineering Hydraulics Laboratory at the University of Ottawa (Figure 5.2.1 and Table 5.2.1). The flume has a centerline length of 18.5 m, with a 12.19 m long approach section, followed by a 135º bend section with a constant radius of curvature of 1.5 m (at the channel centerline) and a straight 2.4 m long exit section (Figure 5.2.1 A). The flume is 1.0 m wide with 0.9 m high vertical plexiglass walls, which contained a trapezoid cross-sectional channel formed entirely of sand (Figure 5.2.1 B). The sand had a mean diameter (d_{50}) of 1.1 mm, with 98 % of particles falling within a range of particle diameters between 0.6 and 1.8 mm. The trapezoid channel had a depth of 0.15 m, side slopes of 29º (approximately equal to the angle of repose), a bottom width of 0.26 m, top width of 0.80 m and floodplain width of 0.15 m (right, outside bank) and 0.05 m (left, inside bank) (Figure 5.2.1 B). Cohesive floodplain sediments have not been modelled, thereby providing a conservative design approach where non-cohesive sediment (sand) with the same erodibility as the bed has been used.

A summary of the experimental conditions and parameters for each run is provided in Table 5.2.1. The six runs are labelled TR1, TR3, TR5, TR6, TR7 and TR10 (where TR stands for Trapezoid Run). Each experiment began with a constant bed slope (S = 0.0007), a

uniform flow condition and a horizontal cross-stream bed (along the base of the trapezoid section). Experiments were conducted under clear water scour conditions, wherein flow in the approach section was near the threshold of particle motion and negligible movement of sand grains was observed. Therefore, scour and deposition in the bend was due to the presence of the bend alone (TR1 and TR3) or a combination of the bend and the presence of barb structures (TR5, TR6, TR7 and TR10).

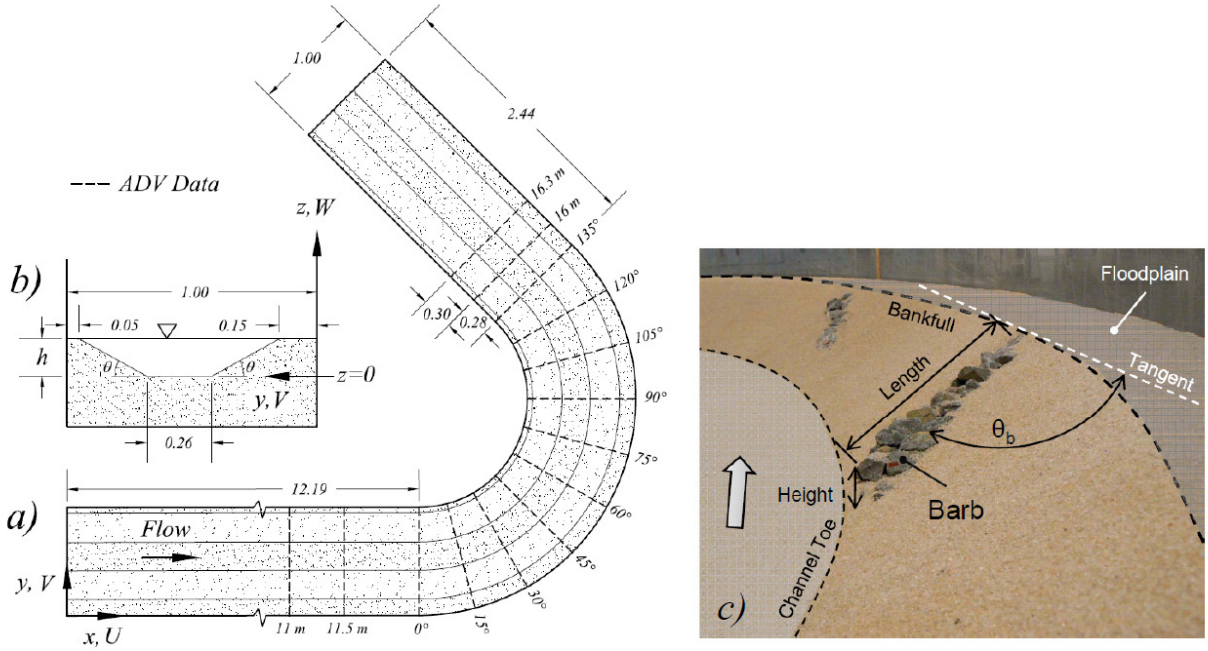

Figure 5.2.1. Experimental set up. (A) Plan view of channel geometry and location of ADV measurement cross-sections. (B) Cross-sectional view (looking downstream) of trapezoid dimensions. Water depth (h) is equal to 0.15 m at bankfull flow, i.e. when water level is equal to the height of the floodplains. θ is the side slope angle (θ = 29º) and all dimensions are in meters. Streamwise velocity component (U) is parallel to the flume wall throughout the domain. (C) Illustration of barb geometry parameters (see Table 5.2.2 for variable explanation and values)..

Table 5.2.1. Summary of experimental runs. In all runs, original bed slope was 0.0007 and mean sediment size (d_{50}) 1.1 mm. *Q* is flow rate, *H* is flume-averaged flow depth in the center of the channel, *W/H* is the width-to-depth ratio assuming width (*W*) is 0.80 m (Figure 5.2.1), *U* (=*Q*/*A*) is flume-averaged velocity (where cross-sectional area = A), $\overline{U_*}$ is mean shear velocity in the approach section. Barb layouts are shown in Figure 5.2.2.

Run Title	Barbs?	Q (m^3/s)	H (m)	W/H	U (m/s)	$\overline{U_*}$ (m/s)	τ_o (N/m^2)	Duration (hours)	ADV Measurements (Cross-Section)
TR1	No	0.017	0.142	5.6	0.231	0.011	0.123	213	• 11m, 11.5m, 0º, 15º, 30º, 45º, 60º, 75º, 90º, 105º, 120º, 135º, 16m
TR3	No	0.021	0.148	5.4	0.267	0.020	0.424	391	• 11.5m, 0º, 15º, 30º, 45º, 60º, 75º, 90º, 105º, 120º, 135º, 16m, 16.3m
TR5	Yes (4)	0.021	0.157	5.1	0.264	0.021	0.440	380	• 11.5m, 0º, 15º, 30º, 45º, 60º, 75º, 90º, 105º, 120º, 135º, 16m, 16.3m
TR6	Yes (4)	0.022	0.156	5.1	0.276	0.017	0.299	362	• 11.5m, 45º, 95º, 120º
TR7	Yes (1)	0.021	0.151	5.3	0.264	0.019	0.342	310	• 11.5m, 15º, 45º
TR10	Yes (2)	0.020	0.153	5.2	0.255	0.021	0.420	386	• 11.5m, 0º, 15º, 30º, 45º, 60º, 75º, 90º, 105º, 120º, 135º, 16m, 16.3m

The first two experiments (TR1 and TR3) represent the base case conditions (i.e. no barbs) for two different flow rates ("*low flow*", Q = 0.017 m^3/s and "*high flow*", Q = 0.021 m^3/s). The other four experiments represent various barb arrangements for the same flow conditions as TR3 (Table 5.2.1). For all experimental runs, acoustic Doppler velocimeter (ADV) data were collected over a series of consecutive days once the bed conditions had reached equilibrium and stationarity (i.e. static bathymetry) within each run could be assumed. Water flowed permanently for the duration of each run, which included the time to reach equilibrium bathymetry and to obtain ADV data. Equilibrium bathymetry was determined by regularly monitoring the extent of floodplain erosion along the outer bank.

When this erosion showed no sign of change over a 24 hour period then it was assumed that equilibrium scour was achieved. All *high flow* experiments were run for between 300-400 hours (Table 5.2.1), while the *low flow* run (TR1) required only 213 hours to reach equilibrium bathymetry and subsequently to obtain ADV data. Run time among the *high flow* runs varied based on the number of cross-sections measured with the ADVs (Table 5.2.1). TR6 and TR7 had the lowest *high flow* run times (362 and 310 hours, respectively) since they had the fewest measured cross-sections, compared to the 13 cross-sections obtained in other *high flow* runs TR3, TR5 and TR10. ADV measurement locations for each run are listed in Table 5.2.1.

Instantaneous velocity measurements in the streamwise (u), cross-stream (v) and vertical (w) direction were made using three Nortek Vectrino (four-beam) ADVs (two down-facing probes and one side-facing). However, to reduce the background acoustic noise, no more than two ADVs were ever in operation at the same time. The ADVs were mounted on a movable carriage, with each mount providing adjustment of the instruments in the lateral (cross-stream) and vertical directions. The ADVs were orientated vertically and orthogonal to the flume walls in the straight approach section and through the channel bend. This arrangement provided a consistent frame of reference from which the spatial patterns of the mean flow field through the entire bend could be assessed. Figure 5.2.1 A shows the ADV measurement locations in plan view. The ADV transducers must be fully submerged in the flow, and since the sample volume is approximately 50 mm from the central (emitting) transducer, it is not possible to collect data in the top 60 mm of the water depth (for the down-facing probes). Therefore, at select cross-sections (for example where flow overtopped a barb), the side-facing probe was used to obtain velocity data at up to 20 mm below the water surface.

The ADV configuration parameters were identical for each run: sampling time = 120 s; sampling frequency = 100 Hz; nominal velocity range = 0.30 m/s; transmit length = 1.8 mm, sampling volume diameter = 6.0 mm, and sampling volume height = 5.5 mm. The spatial coverage of measurement points in each experiment varied based on a compromise between overall coverage of the channel bend, the density of measurement points in each cross-section and the performance of the barbs to reduce scour at the outer bank (i.e. less successful runs, such as TR6 and TR7 have ADV data at only 4 and 3 cross-sections respectively (Table 5.2.1)). The locations of individual ADV measurements are indicated by the velocity vectors in Figure 5.2.5, Figure 5.2.8 and Figure 5.2.9. [Note: The vector colour in Figure 5.2.5 depends on the depth of the measurement (i.e. above or below 0.70*h*); measurements above the contoured slice will appear darker, while those below will appear lighter]. Typically, each cross-section consisted of 10 – 12 evenly spaced vertical profiles, with measurements in the vertical direction at intervals of 5 mm near the bed, 10 or 20 mm in the middle half of the flow depth and 30 or 40 mm closer to the water surface (unless side-facing ADV data were obtained, then data were typically 10 or 20 mm apart near the water surface).

The raw times series data were processed using Matlab code to calculate mean statistics. Raw data were filtered based on a vertical velocity error of 0.1 m/s and despiked based on thresholds for both acceleration (local acceleration > 1.5g, where g = 9.81 m/s^2) and standard deviation, σ (for velocity > 4σ from the mean) (Nikora and Goring, 1998). Further details regarding ADV data processing, filtering and despiking are provided in Jamieson *et al.* (2010), where the same processing techniques were applied. The processed ADV point measurements of u, v and w were used to calculate time-averaged velocities ($\overline{U}$, $\overline{V}$ and $\overline{W}$).

Estimates of shear velocity (U_*) in the main channel approach section were made from a linear regression of the measured velocity profiles, while bed shear stress (τ_o) was calculated as $\tau_o = \rho U_*^2$ (Table 5.2.1). Average U_* and τ_o for each run were calculated as the averages of values determined from three measured vertical velocity profiles taken near the center of the 11.5 m cross-section. This regression method is considered superior to the reach-averaged calculation since these values are based on local flow conditions and incorporate considerably more data. The 11.5 m section was utilized for this analysis because it was sufficiently downstream of the flume entrance to ensure that flow was fully developed, yet sufficiently upstream of the bend to ensure that flow was not influenced by the bend.

After each run, the flume was drained and the elevation of the sand bed profile was measured using a Leica systems Disto pro4a laser altimeter, which provides a precision of ± 1 mm. Bed level measurements were taken every 0.01 m in the cross-sectional direction and at 2.5º intervals through the bend and every 0.10 m in the straight section, with the exception of TR10, when the cross-sectional interval in the vicinity of the barbs (i.e. scour holes) was 1º. Kriging, with an anisotropic spherical model variogram fit to the experimental variogram, was used to interpolate the bed level measurements into a 2-D contoured surface. Grid spacing of the interpolated surface was 0.05 m x 0.05 m and consistent between experiments to facilitate comparison between runs.

Spatial Interpolation

To assess the spatial variability of all measured components, the individual ADV point measurements from each run were combined to generate a continuous 3-D volume of the flow field. The interpolated (2-D) bathymetry data were used to generate a structured 3-D

volume grid of the entire flow field for each of the runs with complete coverage of ADV data (TR1, TR3, TR5 and TR10). The 3-D grid spacing in the streamwise direction included sections every 0.10 m in the straight and exit sections and 5º through the bend; while 11 cells were specified in the cross-stream direction and 10 vertical cells from the bed to the water surface.

The processed ADV data were then interpolated into each 3-D grid using kriging. The kriging parameters included an eight-point octant search, a range of 0.3, no-drift and a zero value of 0. The range is the distance beyond which source points become insignificant and is equal to the fraction of the length of the diagonal of the 3-D volume that contains the data points. A range of zero means that any point not coincident with the destination point is statistically insignificant; while a range of one means that every point in the dataset is statistically significant for each point. The zero value is a non-dimensional measure of variance (from 0-1) of the certainty of the value at a data point. A value of 0 will specify an exact fit with the source points, while any value above zero will allow some variance and essentially a smoothing of the data.

Barbs

Barbs were constructed by hand using small, angular stone. From the approximately 750 stones selected for barb construction, the average A-axis (longest stone dimension, length) was 0.043 m and the average C-axis (shortest stone dimension, thickness) was 0.025 m. Following standard riprap design criteria (NCHRP, 2006), only rocks with an A/C ratio less than 3.0 were used, where the average A/C ratio of all selected stones was 2.2. This ratio criterion eliminates flat and/or needle-like rocks which would compromise stability and be

more likely to be captured by the flow and moved. A sliding and overturning analysis was also performed to check the stone size was suitable for the maximum streamwise velocity in the bend.

Barb dimensions (Figure 5.2.1c) and layout varied for each run and a summary of these is provided in Table 5.2.2. In general, all barbs had: (1) a bank key connecting the rock structure to the outer bank wall at bankfull height, i.e, the bank key was perpendicular to the channel side wall and its length was equal to the outer bank floodplain extent (0.15 m); (2) a bed key, where the barb base was submerged at least 5 cm below the bed surface along its length; and (3) an approximately trapezoidal cross-sectional shape, where the base of the barb was wider than the crest for increased stability of the structure. Given the rock sizes, the barb crest widths varied from approximately 8 cm (2 rock widths, TR5 and TR6) to 4 cm (1 rock width, TR7 and TR10). The overall barb layout (barb length, angle and spacing) was initially specified based on the USDA (2005) design guidelines for stream barbs (i.e. TR5 and TR6). Barb dimensions and layout were revised following each run to optimize barb performance, where performance was based on (1) the reduction of scour along the outer bank floodplain; and (2) the development of scour holes at barb tips. Overall, performance was improved as barbs were made smaller (length and width reduced) and fewer in number (i.e. 2 barbs vs. 4 barbs), but not less than two.

Barb layout was determined by placing the first barb in the location of maximum erosion (or predicated location of maximum erosion), which is typically near the bend exit. Each subsequent barb in series was then added one by one in the upstream direction with a spacing determined by the length and angle of the preceding downstream barb (see USDA, 2005 for further details). It is for this reason that all barb runs had at least one barb located at cross section 16.3 m (0.58 m downstream of the bend exit) because bathymetry results in TR1 and

TR3 indicated this to be the location of maximum erosion of the outer bank floodplain (Figure 5.2.2). A plan view of each barb layout is provided in Figure 5.2.2, where for simplicity only the barb crests have been delineated with a black line to show barb location and geometry.

Table 5.2.2. Summary of barb dimensions for each run with barbs. Barbs are numbered in the downstream direction (see Figure 5.2.2 for general barb layouts). Measurements represent as built dimensions. Barb angle (θ_b) is measured with respect to the upstream bank.

Run Title	Barb No.	Location of Barb Key (Cross-Section)	Barb Length (m)	Barb Angle, θ_b (º)	Average Height* (cm)
TR5	B1	45 º	0.55	35	4.8
	B2	75 º	0.55	35	4.6
	B3	105 º	0.61	35	5.5
	B4	16.3 m	0.61	30	5.7
TR6	B1	64 º	0.41	30	1.7
	B2	90 º	0.41	30	2.4
	B3	116 º	0.41	30	2.4
	B4	16.3 m	0.41	30	2.1
TR7	B1	16.3 m	0.40	30	~ at surface**
TR10	B1	116 º	0.40	30	~ at surface
	B2	16.3 m	0.40	30	~ at surface

*Average height represents the average height of the stones exposed above the channel bed, measured near the tip and middle of each barb.
**A height measurement at the surface indicates the barb elements are at the surface of the bed along the side slope, not yet exposed.

Finally, with this form of barb construction, each barb stone was free to move with respect to the others, thereby modeling the same conditions for riprap stone behaviour in the field. While undermining of the structure may cause instability and lead to failure, the

freedom of movement provided by the loose stone provides a protective measure from excessive undermining or scour. For example, as the local scour depth at the barb tip increases, rocks at the tip may fall into the scour hole thereby armouring the scour hole from further erosion.

5.2.4 Results and Analysis

Bathymetry

Interpolated contour plots of the equilibrium bed levels (Z) for all six runs are shown in Figure 5.2.2. Contour levels were chosen to highlight erosion of the outer bank floodplain (where the floodplain is described by $Z > 0.14$ m, orange) and local scour in the vicinity of each barb ($Z < 0$ m, red), where $Z < 0$ m indicates bed levels below the elevation of the original trapezoidal base ($Z = 0$). Figure 5.2.3 and Figure 5.2.4 show difference maps of the change in bathymetry (ΔZ) from the original bed levels (Figure 5.2.3) and from the base case scenario at equilibrium (TR3) (Figure 5.2.4). Both experiments without barbs (TR1 and TR3) show maximum erosion to be located downstream of the bend exit, near cross-section 16.3 m. This is slightly different from previous mobile-bed experiments in a 135º bend, where maximum scour occurred at (Jamieson *et al.*, 2010; Chapter 5.1) or just upstream of (Matsuura and Townsend, 2004) the bend exit. It is possible that the trapezoidal cross-section, which incorporates a sloping side wall, produces a less pronounced helical pattern (compared to experiments with vertical immobile side walls), thereby allowing a smoother transition from curved to straight exit section.

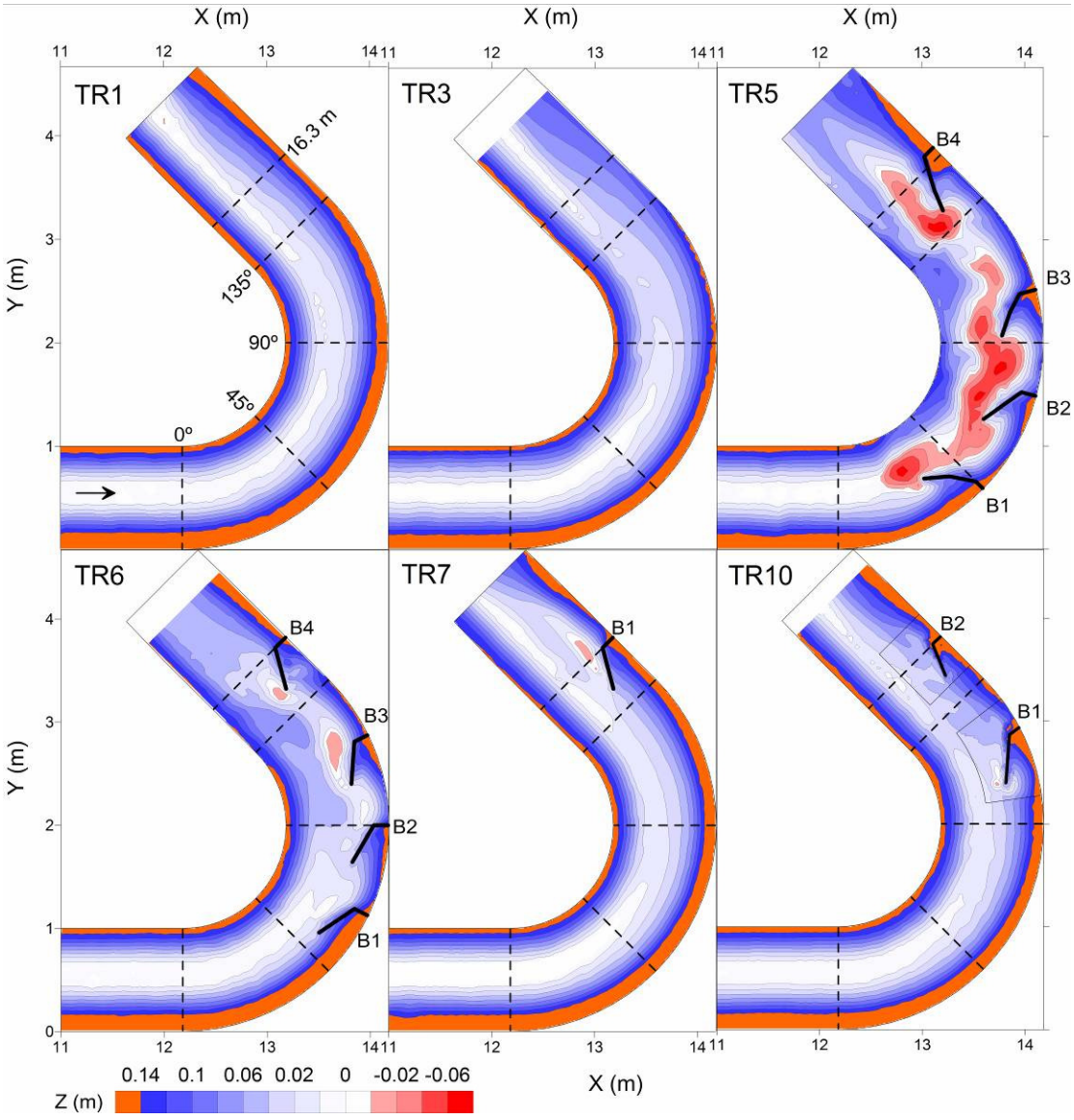

Figure 5.2.2. Contour plots of equilibrium bathymetry for each run. Select cross-sections are indicated by the dashed line and labelled in TR1. Barb crests are identified by the solid black lines and numbered in the downstream direction (see Table 5.2.2 for barb details).

In all barb experiments (TR5, TR6, TR7 and TR10), the maximum depth was consistently found in the vicinity of the barbs, either at the barb tip or along the downstream side of the barb (Figure 5.2.2). Local scour in the vicinity of each barb can be described to fall within two general types: Type I, representing scour at the barb tip; versus Type II,

representing scour of the sloping bank, along the leeside (or downstream) edge of the barb. Type II erosion is more likely to lead to erosion of the floodplain behind the barb given it's proximity to the side wall and floodplain, while Type I is concentrated more in the center of the channel. The exception, however, is in the case of excessive barb tip scour, for example B3 in TR5 (Figure 5.2.2) where the scour hole at the barb tip was so large and deep that it caused erosion into the sidewall and then floodplain upstream. However, in this case, Type II scour downstream of the upstream barb (B2) is likely to have contributed to floodplain loss as well. Matsuura (2004) found that for a series of barbs, local scour depth at barb tips increased in the downstream direction. However, in both TR5 and TR10, scour at B1 (the upstream-most barb) exhibited predominantly Type I scour (Figure 5.2.2). In both TR5 and TR6, maximum scour at the downstream-most barb (B4, near cross-section 16.3 m) was concentrated at the barb tip (Type I), while in TR7 and TR10 maximum scour at the downstream-most barb (again near cross-section 16.3 m) was concentrated along the leeside of the barb (Type II). It is possible that having three upstream barbs promotes the concentration of scour at the downstream-most barb tip, thereby reducing floodplain erosion immediately downstream of the last barb.

In all barb experiments, maximum erosion of the floodplain was consistently located immediately downstream of each barb, with two exceptions: the downstream-most barbs in TR5 and TR6, which are the only two runs to incorporate 4 barbs (Figure 5.2.2 and Table 5.2.2). As scour behind the barb becomes deeper, erosion of the floodplain behind the barb increases, since the sand side walls erode to reach a stable side slope. It is likely that in the case of TR5 and TR6, the three upstream barbs provided enough flow deflection and energy dissipation before the flow reached the bend exit to prevent excessive scour in this region.

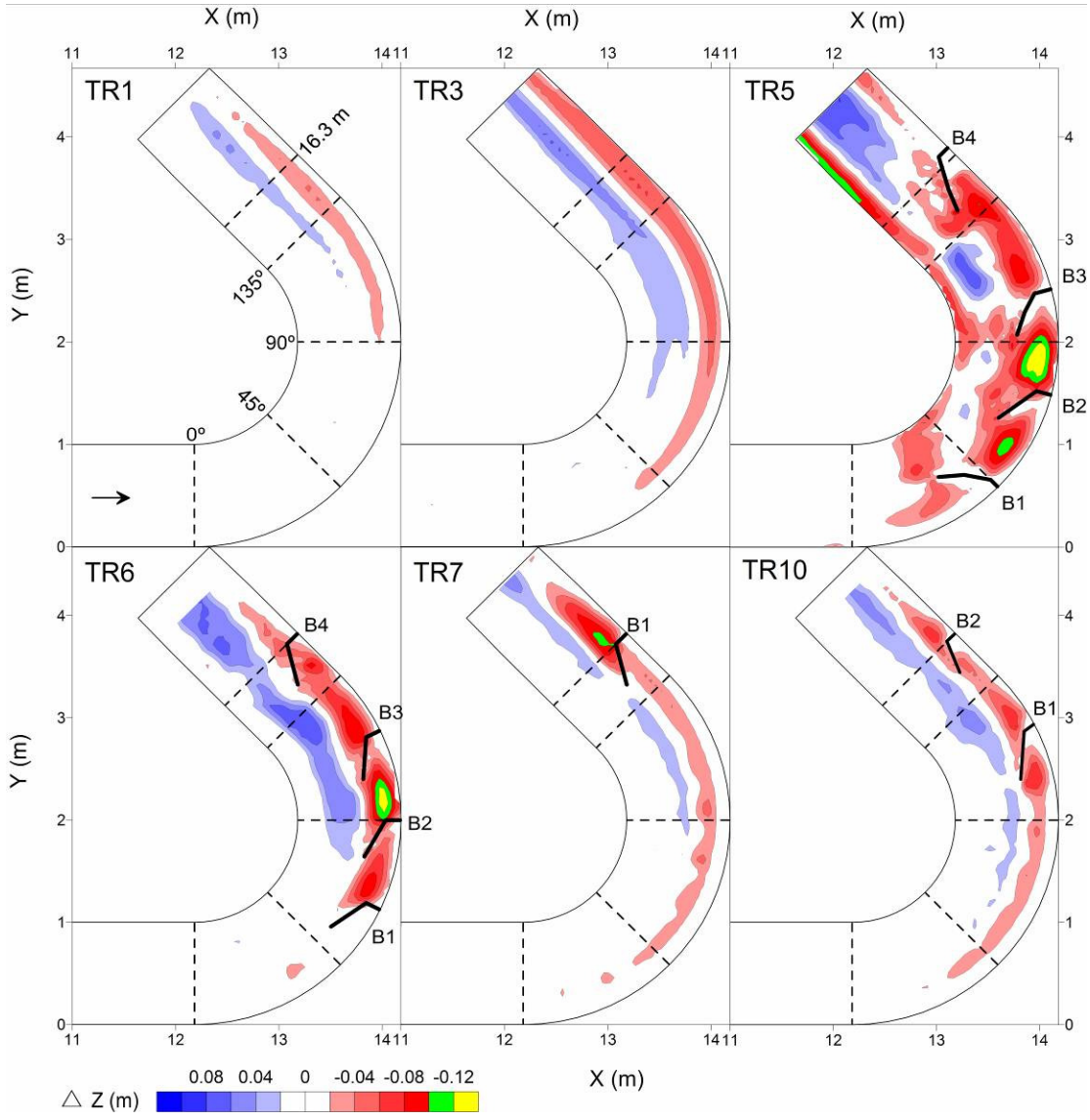

Figure 5.2.3. Contour plots of bed level changes (ΔZ) from original bed to final equilibrium. Red contours indicate sediment loss (erosion) while blue contours represent sediment gain (deposition). Green and yellow contours represent severe scour (ΔZ < -0.10 m).

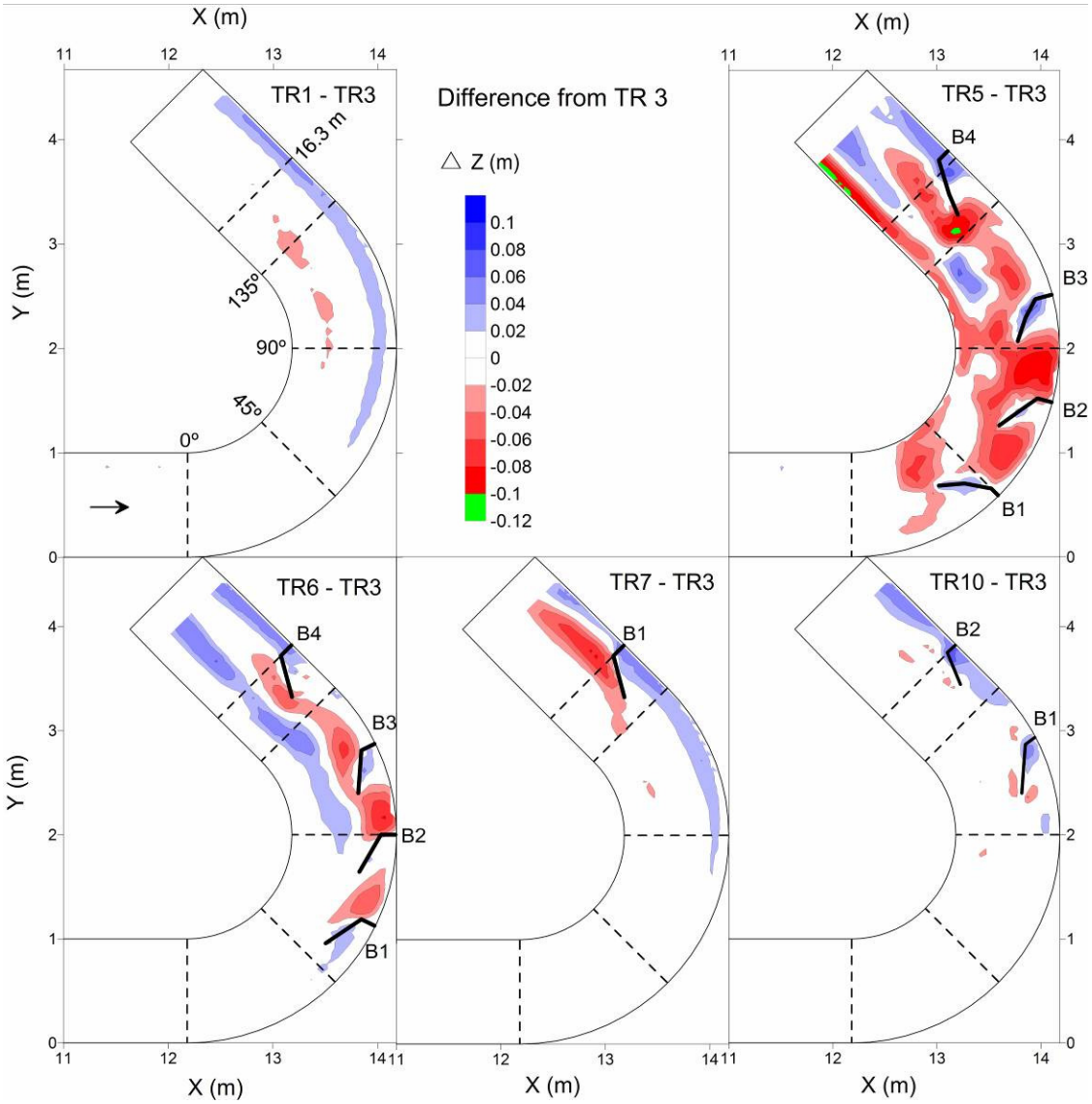

Figure 5.2.4. Contour plots of bed level differences from TR3 (base case run with no barbs).

All runs (TR1, TR3, TR5, TR6, TR7 and TR10) show scour along the outer bank (red contours) and deposition through the center of the channel (blue contours) (Figure 5.2.3). This was expected, as eroded material from the outer bank is transported downstream and cross-stream towards the inner bank. The greatest scour (for example, up to more than 0.10 m below the original bed elevation) is found in the runs with the greatest number of barbs

(TR5 and TR6, 4 barbs). The barbs in these runs were also larger than in the other two runs with barbs (TR7 and TR10, Table 5.2.2). As well, despite having the same number of barbs, TR5 has noticeably more erosion than TR6 due to the sue of larger barbs (see Table 5.2.2 for barb dimensions) Overall, Figure 5.2.2, Figure 5.2.3 and Figure 5.2.4 all show that the larger the barbs (in height and length, see Table 5.2.2), the deeper the scour in the vicinity of the barbs (for both Type I and II scour).

In all four cases with barbs (TR5, TR6, TR7 and TR10) the outer bank near the bend exit, which corresponds with the location of maximum erosion in the base case run (TR3), was successfully protected ($\Delta Z > 0$, Figure 5.2.4). Furthermore, erosion was reduced along the entire outer bank in the most successful run (TR10). However, for TR5, TR6 and TR7, it would appear that protection of the outer bank floodplain at the bend exit was at the cost of additional erosion, either upstream (TR5 and TR6) and typically between barbs, or immediately downstream of the barb crest for the least protected floodplain (TR7) where only one barb was used. As well, in the case of the run with the greatest change in bed levels (TR5), erosion of the inner bank was also observed.

Mean 3-D Flow Field

Contours of time averaged streamwise velocity ($\overline{U}$) near the water surface (at 70% of the flow depth, or 0.70*h*) for TR1, TR3, TR5 and TR10 are shown in Figure 5.2.5. Without barbs, both TR1 and TR3 exhibit a similar pattern of streamwise velocity distribution, where the high velocity core is closer to the inner bank at the entrance of the bend and then shifts outward through the bend with maximum velocity located near the outer bank at the bend exit. This pattern is consistent with experimental observations in other channel bends (e.g. Dietrich and Whiting 1989; Termini, 2009). In both cases with barbs (TR5 and TR10) overall streamwise velocity is lower than the base case conditions (TR3), with TR5 exhibiting the most significant reduction. This is likely due to the larger scour holes (Figure 5.2.2) generated by the larger barbs (Table 5.2.2), establishing an overall greater depth and width throughout the bend and therefore lower streamwise velocity for the same discharge. Figure 5.2.5 also demonstrates the reduction in streamwise velocity along the outer bank, due to the redirection of high velocity flow provided by the barbs in both TR5 and TR10. The larger barbs in TR5 provide the greatest redirection of flow and therefore show a greater reduction in near-bank streamwise velocities between the barbs (Figure 5.1.5).

It is the presence of secondary flow in a bend that alters the distribution of maximum streamwise velocity. Secondary flow is best described by the cross-stream ($\overline{V}$) and vertical ($\overline{W}$) velocities (or secondary velocities), and these are shown by contour plots in Figure 5.2.6 and Figure 5.2.7 respectively. These plots clearly illustrate the development of the secondary flow through the bend at two different depths: near the bed at 0.05*h*, the cross-stream flow is directed towards the inner bank ($\overline{V} > 0$), while closer to the water surface at 0.70*h*, the flow is directed towards the outer bank ($\overline{V} < 0$). Together with the vertical velocity, which shows

high negative vertical velocity along the outer bank and high positive vertical velocity along the inner bank (at both depths), the pattern of secondary velocities is consistent with the expected pattern of secondary, helical flow in bends. When barbs are present (TR5 and TR10), cross-stream velocities opposite the barbs are concentrated closer to the center of the channel, away from the outer bank. In TR5, this modification also leads to higher cross-stream velocities through the bend, as a greater amount of the flow is altered by the larger and more numerous barbs.

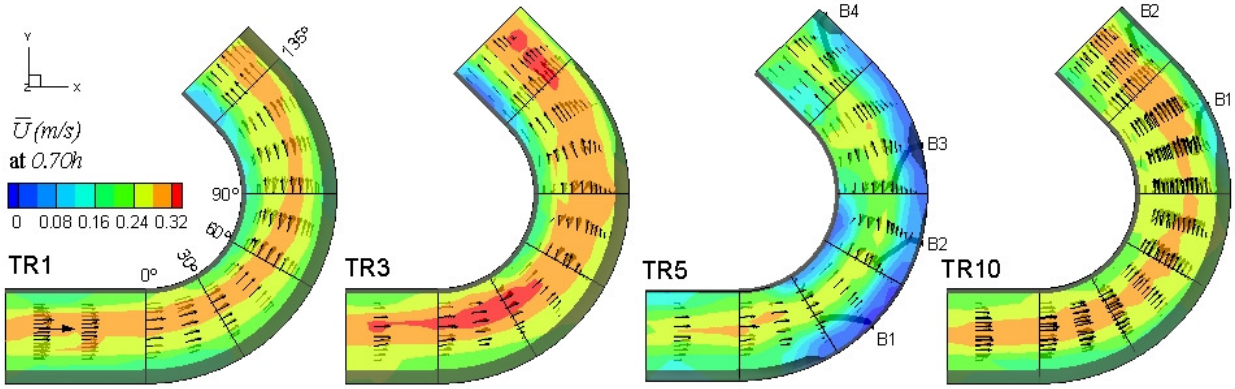

Figure 5.2.5. Contours of streamwise velocity ($\overline{U}$) at 70% of the flow depth (0.70h) for four runs with complete ADV coverage (Table 5.2.2): TR1, TR3 (without barbs) and TR5, TR10 (with barbs). Velocity vectors are shown in black and represent the location of each ADV measurement. Dark hatched areas represent regions where no ADV data were collected.

In the vicinity of individual barbs, three-dimensional mixing is generated, causing a reverse direction in cross-stream and vertical velocities, i.e. negative cross-stream velocities near the bed in the outer bank region (Figure 5.2.6); and highly positive vertical velocities between barbs near the outer bank (Figure 5.2.7). The plunging action of the flow over the barbs is demonstrated in the $\overline{W}$ contour plots for both runs with barbs (TR5 and TR10), where vertical velocity immediately upstream and downstream of each barb shows highly

positive and negative velocity respectively. The near bed (0.05*h*) cross-stream velocity towards the outer bank in TR5 would suggest horizontal mixing, where separation or shear at the barbs causes flow to be directed towards the outer bank and opposite to the typical secondary flow pattern. Interestingly, the contour plots of secondary velocity also show that the presence of the four large barbs in series in TR5 may actually have the effect of pushing the helical flow upstream beyond the start of the bend; note the significantly higher vertical velocities upstream of the bend entrance (0º) in TR5 compared to any of the other three runs (TR1, TR3 or TR10).

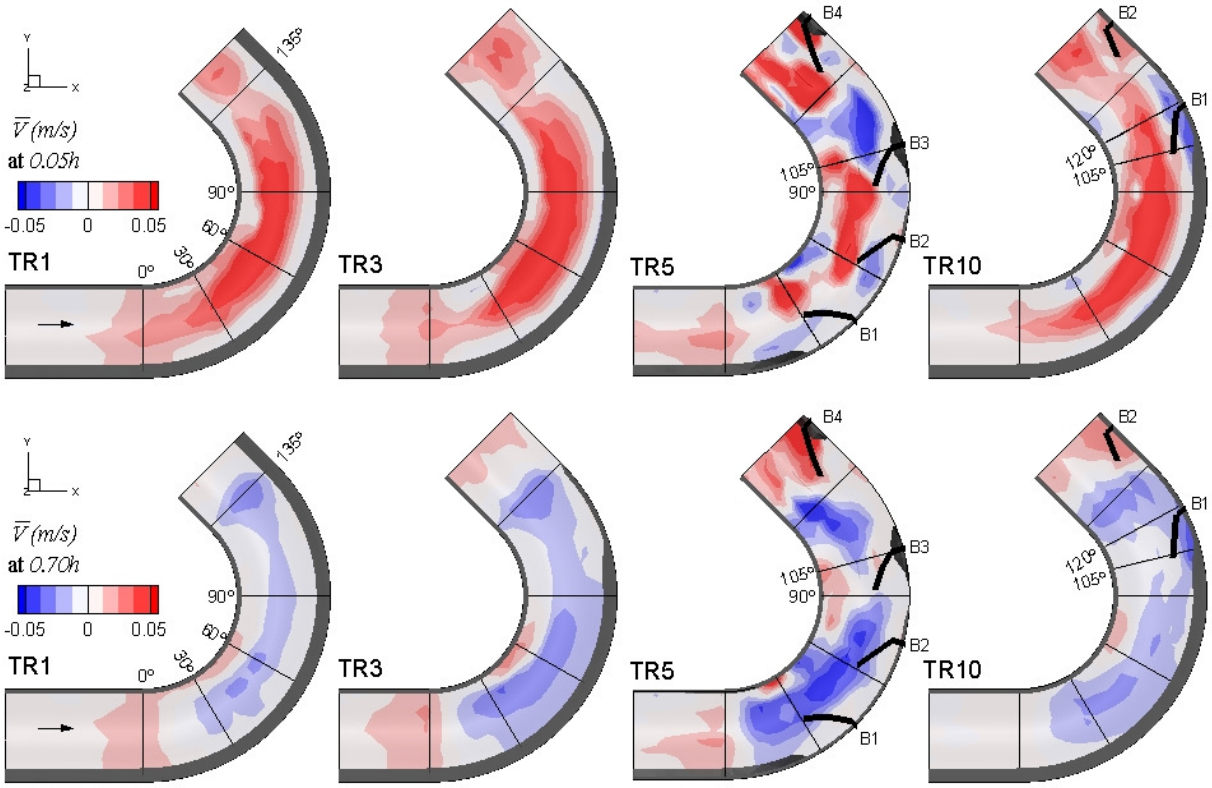

Figure 5.2.6. Contours of cross-stream velocity ($\overline{V}$) at a depth of 0.05*h* (top) and 0.70*h* (bottom). Positive cross-stream velocity is towards the left, inner bank.

All four runs with complete ADV coverage (TR1, TR3, TR5 and TR10) show a local increase in cross-stream velocity towards the outer bank near the water surface at the 135º cross-section or bend exit (Figure 5.2.6, 0.70*h*). This trend could be explained by the local amplification of the helical flow at the bend exit as it transitions from a curved channel planform to a straight one, which could help to explain why the maximum erosion in the bend is typically located near the bend exit. This local increase also appears to have been shifted away from the outer bank in the case of runs with barbs (TR5 and TR10), where the higher negative cross-stream velocity is closer to the inner bank compared to the non-barb runs (TR1 and TR3). This pattern could be contributing to reducing the erosion at this location for the barb runs.

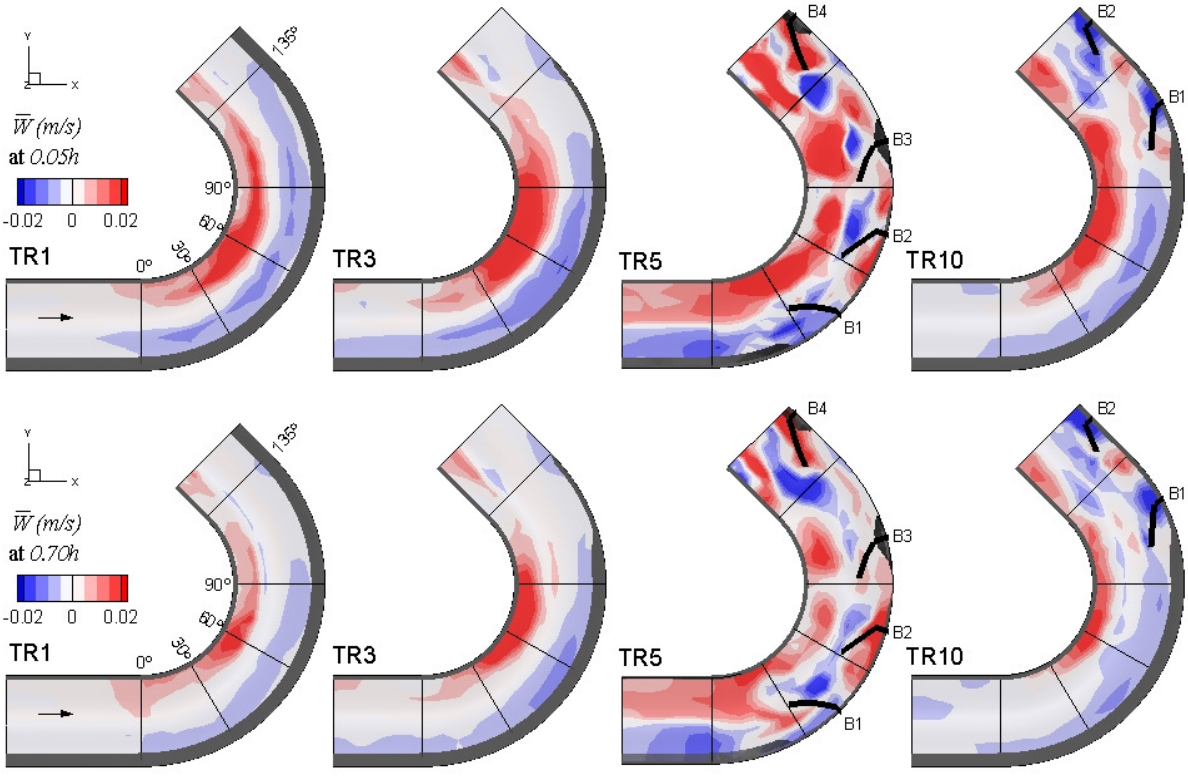

Figure 5.2.7. Contours of vertical velocity ($\overline{W}$) at a depth of 0.05*h* (top) and 0.70*h* (bottom). Vertical velocity is positive in the positive z-direction (up).

The effect of barbs on secondary velocities is also presented for cross-sections immediately upstream and downstream of individual barbs in TR5 and TR10, with data from TR3 included as a reference (Figure 5.2.8 and Figure 5.2.9). These plots clearly show the traditional helical flow pattern through the bend (TR3) and the development of a counter-rotating secondary flow cell along the outer bank, downstream of the barb at 105º for TR5 (but not at 120º for TR10). Bhuiyan *et al.* (2010) also found that the plunging flow over the crest of their vanes generated a secondary flow cell that counteracted the main secondary flow cell that is created by centrifugal forces in the bend. They suggested this was responsible for shifting the higher velocity away from the outer bank. However, TR10 results suggest that a counter-rotating cell may not be necessary: for shift of the high velocity core in a barb field: both barb runs (TR5 and TR10) show a reduction and shift in the streamwise velocity core.

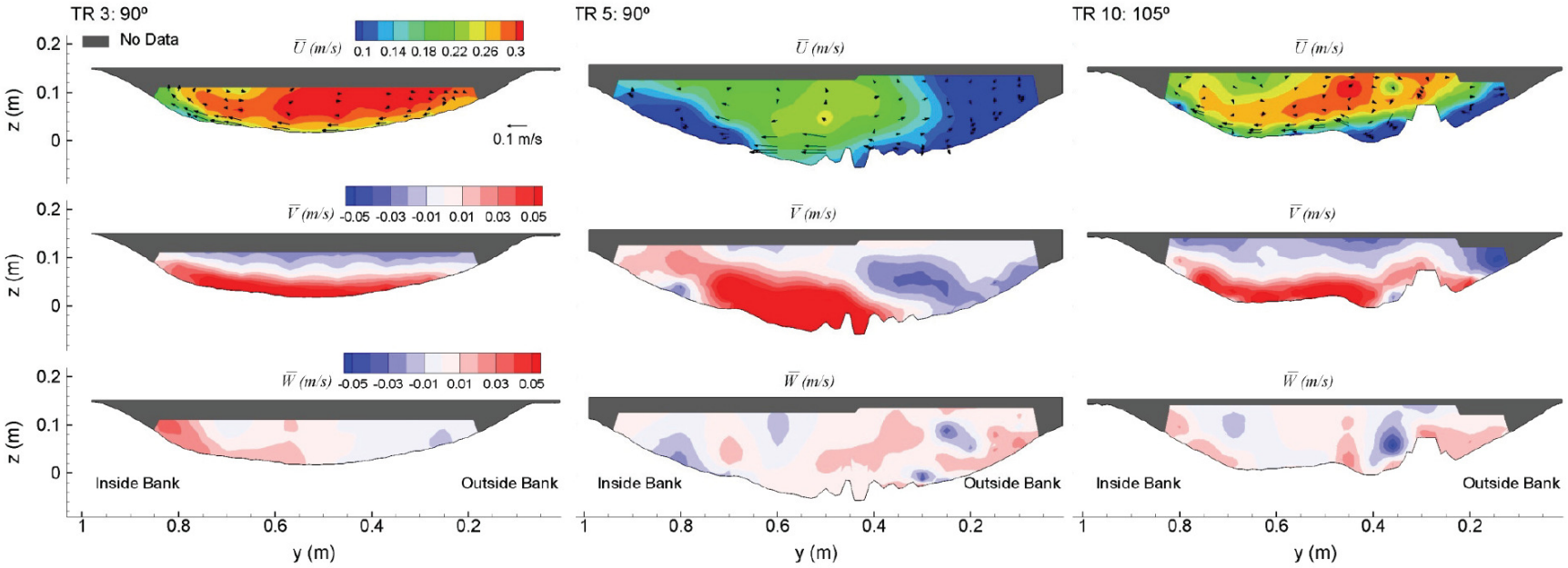

Figure 5.2.8. Contours of mean velocity ($\overline{U}$, $\overline{V}$ and $\overline{W}$) at cross-sections immediately upstream (90º, TR3 and TR5; 105º, TR10) of individual barbs (see Figure 5.2.6). Contours for TR3 represent base case (no barb) conditions. Vectors represent ADV measurement locations.

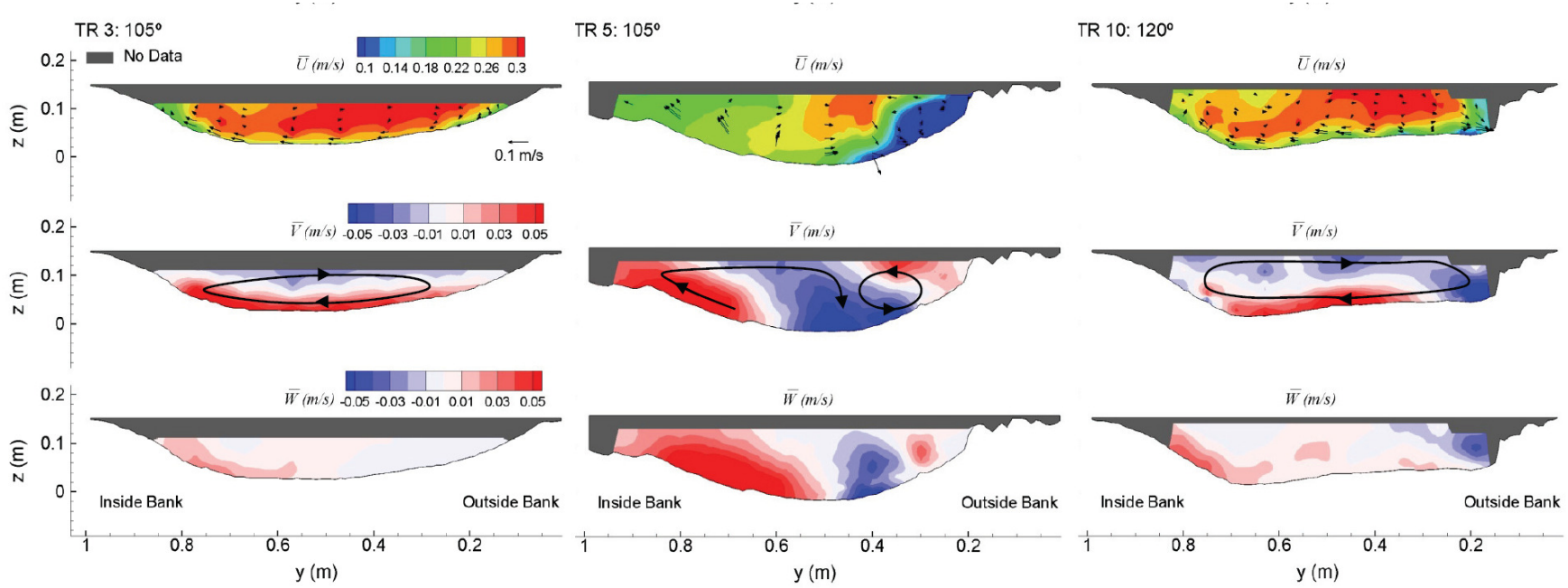

Figure 5.2.9. Contours of mean velocity ($\overline{U}$, $\overline{V}$ and $\overline{W}$) at cross-sections immediately downstream (105°, TR3 and TR5; 120°, TR10) of individual barbs (see Figure 5.2.6). Contours for TR3 represent base case (no barb) conditions. Vectors represent ADV measurement locations.

5.2.5 Discussion

Barb and Channel Geometry

As previous research has suggested (Matsuura, 2004 and Kuhnle *et al.,* 2008) the geometry or size of the structure will have an effect on the pattern and magnitude of the local scour depth. In the present study, the magnitude of scour (extent and depth) was greatly reduced when the size (height, width and length) and number of barb structures were reduced. However, it is important to differentiate between desirable scour at the barb tip (Type I) and scour of the floodplain or bank (Type II). To compare our results to previous studies is difficult, since the pattern of scour in the vicinity of the barbs is a function in part of the original trapezoidal channel geometry. Unlike previous experiments with rectangular cross-sections, incorporating erodible channel side slopes composed of the same material as the bed complicates the analysis. For one, for non-cohesive materials, the critical shear stress for side slopes is less than for the bed, due to the contribution of gravitational force in aiding sediment particle motion. Therefore, the side walls are already more susceptible to erosion, which would likely explain the dominance of Type II scour in the vicinity of the barbs. Physical modeling with cohesive floodplain sediments and relatively erodible non-cohesive bed sediments may have resulted in greater Type I scour at barb tips. Previous studies with rectangular geometries and fixed side walls (Kuhnle *et al.,* 1999; Kuhnle *et al.*, 2002; Matsuura and Townsend, 2004; Fox. *et al.*, 2005a and 2005b; Jia *et al.*, 2005; Kuhnle *et al.*, 2008; and Bhuiyan *et al.*, 2009 and 2010) failed to demonstrate the impact of barbs on actual bank erosion. The focus was typically on studying local scour of the bed at the barb tip only. Our results suggest the barb structures greatly influence the flow field and sediment dynamics along the side slope, and this interaction should not be ignored; particularly when

the objective is to protect the near-bank, side slope region. As well, the pattern of near-bank secondary currents depends on the inclination and roughness of the bank, and, at least in the case of straight channels, an inclined side wall will generate an additional vortex (or circulation cell) near the water surface and corner of the channel, while increased roughness will strengthen the secondary currents and the corner surface vortex (Blanckaert *et al.*, 2010)

Our results indicate that two barbs placed near the bend exit are most effective in reducing outer bank scour. When four barbs were used, the bend exit remained protected, but at the cost of additional erosion to the outer bank side slope, particularly in the regions between each barb. It is likely that flow blockage plays a role, where excessive blockage of the cross-sectional area due to large barb geometries will increase scour beyond desirable amounts as the channel adjusts its cross-sectional area to convey the same flow. When only one barb was used (TR7), only the floodplain upstream of the barb was adequately protected (indeed, more protected than the four-barb cases, TR5 and TR6); but excessive scour downstream of the barb caused undesirable outer bank erosion. Barbs should not be placed too far upstream of the bend exit (or location of maximum potential erosion) as flow upstream of the bend will be affected (Figure 5.2.7, TR5), which could compromise overall channel equilibrium and stability. This is another reason for favouring shorter barb lengths as, according to existing design guidelines (USDA, 2005), longer barbs require greater spacing and therefore a greater upstream presence. It is difficult to comment on optimum barb spacing as none of the runs with barbs used barbs with the same dimensions. Therefore, it is possible that while spacing was a factor in altering flow and sediment patterns, the influence of barb size can not be discounted. As well, it is worth noting that the degree of curvature in a channel bend will also impact optimum barb design (Matsuura and Townsend, 2004). Since bank erosion rates vary with the ratio of the radius of curvature to width

(Nanson and Hickin, 1986), optimum design for a sharp bend (present study), may be different than for a milder bend, where the secondary flow is weaker. Furthermore, even in sharp bends, locations of scour differ. For example, Roca et al. (2007) showed that in their 183º bend flume, which had the same constant radius of curvature of 1.5 m and flume width of 1.0 m as the present experiments, an outer bank maximum scour hole occurred upstream of the bend apex (between 60º and 80º) as well as at the bend exit. Accordingly, it is likely that optimum barb geometry would differ for their 183º bend.

In summary, the following suggestions are made regarding optimum barb geometry and layout:

1. Barbs should be placed only in the vicinity of expected maximum erosion. Too many barbs in series, which extend beyond the region selected for protection (particularly in the upstream direction), may cause additional, unwanted erosion by (i) altering and increasing secondary velocities throughout the bend; and (ii) reducing the available cross-sectional flow area. We emphasize that optimum barb geometry will vary between bends.
2. Barb height, width and length should be scaled to (i) minimize any blockage of original cross-sectional flow area, (ii) reduce plunging flow and reduce reverse secondary velocities near the outer bank, and (iii) prevent excessive local scour at the barb tip causing erosion of the channel side slope; while maintaining proportions still capable of deflecting primary streamwise velocity away from the outer bank. It is worth emphasizing that in both TR7 and TR10, the barb top was at the elevation of the initial bed surface, thus the barbs did not obstruct flow in the initial trapezoidal channel. Once outer bank erosion began to occur, the barbs began to deflect flow toward the centre of the channel.

3. The barb bank key width should be wider than the barb itself and should be extended along the channel bank in the downstream direction, as the floodplain directly downstream of the barb is particularly susceptible to erosion.

Secondary Velocity

How the secondary flow in the bend is disrupted or altered due to the presence of barbs appears to play a role in the distribution of sediment and the pattern of scour. In TR5, plunging flow was strongest, coupled with cross-stream flow near the bed in the direction of the outer bank and highly positive vertical velocity along the outer bank between barbs – both of which are contrary to the typical secondary flow pattern in a channel bend. It is possible that the complete disruption of secondary flow and the generation of a counter-rotating cell behind (or between) the barbs is responsible for increased erosion in these locations. Bhuiyan *et al.* (2010) also found that the plunging flow over the crest of their vanes generated a counter-rotating secondary flow cell, but they did not observe erosion downstream of the vanes; in fact, there was evidence of deposition. Such contrasting results may be due to the difference in the slope of the channel side walls. In Bhuiyan *et al.* (2010) the side wall was vertical and fixed, establishing a larger embayment or lee zone downstream of the structure, where velocities may be more reduced and consequently deposition more likely. Typical emergent groynes will induce recirculating flow downstream of the structure, often leading to deposition in the center of this gyre (dead zone) where velocities are close to zero (Uijttewaal *et al.*, 2001). However, with a smaller lee zone (due to both the lower profile of submerged and sloping groynes and the addition of a sloping bank), reverse flow is not generated and the reduction in velocity is less significant.

Our results indicate that barbs should not disrupt the secondary (helical) flow in the bend entirely (TR5), but rather weaken it (TR10), particularly near the downstream bend exit, where erosion (without added protection) is typically greatest. The greatest outer bank scour reduction occurred in TR10, in which an outer bank counter-rotating cell was not generated. However, the development of a second counter-rotating cell near the outer bank may be found in bends even without the addition of structures (Bathurst *et al.*, 1977; Blanckaert and Graf, 2001; Zeng *et al.*, 2008, Termini and Piraino, 2010; and Jamieson *et al.*, 2010; Chapter 5.1). It is thought that this cell stabilizes the region between the outer bank and the center region cell, thereby keeping the core of high velocity at some distance from the outer bank. However, results remain inconclusive (Blanckaert and de Vriend, 2004; Zeng *et al.*, 2008; Blanckeart, 2010), and there is likely more to the role of the counter-rotating cell than we understand. Our results suggest that, beyond the simple presence or absence of a counter-rotating cell, its magnitude, size, proximity to the bed and persistence may all be important in determining whether the counter-rotating cell will diminish or exacerbate outer bank erosion. More research is required to elucidate the importance of these parameters in determing the influence of the outer bank cell on bank erosion.

5.2.6 Conclusions

Experimental results of the bathymetry and mean flow field through a mobile channel bend, with and without submerged barbs, have been presented. Contour plots of the 3-D flow field, secondary velocities and bed level changes describe the spatial variability of these variables through the bend and in the vicinity of the submerged barbs. Results indicate that the addition of upstream-angled submerged barbs in a channel bend can successfully redirect the high velocity core away from the outer bank region and prevent erosion of the floodplain at

the bend exit. However, the size and number of barbs will affect the overall amount of erosion incurred along the outer bank throughout the bend. In this particular experimental set-up and bend geometry, the use of two barbs (versus 1 and 4) was found to be most successful in protecting the outer bank floodplain while preventing unwanted bank erosion upstream of the bend exit. Maximum erosion of the outer bank occurred between barbs and in particular corresponded with regions of counter-rotating secondary velocities. The highest secondary velocities were associated with the largest barbs, and were located between the barbs. The increased plunging action of the flow associated with the larger barbs, and the generation of a counter-rotating secondary flow cell, increased erosion downstream of each barb. Lastly, barbs (or any similar type of in-stream structure) work to prevent erosion of the outer bank and future laboratory research should not ignore the importance of both a sloping side wall and an erodible bank. These features impact the development and strength of secondary velocities in a bend as well as the interaction between the altered flow field around the barb and adjacent bed levels. By reproducing bank erosion, it was evident that scour of the side slope immediately downstream of the structure could be severe and could compromise the stability of both the side wall (leading to erosion of the floodplain) and the structure itself. This is a problem not seen in previous experiments that have used channels with fixed vertical side walls.

5.3 Flow and sediment dynamics in a laboratory channel bend with and without stream barbs (submerged groynes) 2: Turbulence and vorticity

Jamieson, E.C., Rennie, C.D. and Townsend, R.D. (*Submitted - b*). Flow and sediment dynamics in a laboratory channel bend with and without stream barbs (submerged groynes) 2: Turbulence and vorticity. Submitted to *Journal of Hydraulic Engineering*, December, 2010; revision submitted September 2011.

5.3.1 Abstract

Laboratory flume experiments have been conducted to study the flow field and sediment dynamics in a mobile-bed channel bend with and without the presence of stream barbs (upstream-angled submerged groynes). The companion paper describes the experimental conditions in detail and presents the spatial distributions of equilibrium bathymetry, erosion and deposition, and three-dimensional velocity through the bend and in the vicinity of the barbs. Unlike traditional (emergent) groynes, barbs are submerged structures which slope away from the bank in an upstream direction, creating plunging type flow and slightly less significant vertical shear at the barb tip. Understanding the flow in detail, at the scale and structure of the vortical and turbulent motions generated by the barbs and the channel bend itself, should provide a better means of predicting the impact of barbs on flow and sediment dynamics. The study goals were to (1) optimize barb design for reducing erosion along the outer bank regions of channel bends, and (2) advance our general understanding of the role that certain turbulence parameters, especially vorticity, play in the erosion process. Results indicate that (1) z-vorticity and streamwise-cross-stream Reynolds stress play more of a role than other components of Reynolds stress, turbulent kinetic energy, or vorticity magnitude in the development of local scour in the vicinity of the barbs; and (2) the outer bank region (particularly between adjacent barbs) may still be susceptible to erosion (possibly beyond

those levels observed for the corresponding case without barbs) if stream barbs generate excessive turbulence and secondary velocities (due to their size and layout).

5.3.2 Introduction

Stream barbs (or barbs) are a relatively new form of bank protection that are primarily used to prevent the erosion of stream banks in channel bends. Barbs are low-profile linear rock structures that extend in an upstream direction away from the bank into the flow and are typically anchored, in series, to the outside bank in bends (USDA, 2005). This configuration redirects flow away from the outer bank and disrupts the velocity gradient close to the outer bank. With time, the barbs cause the thalweg in a channel bend to migrate from the outside bank region (its usual, undesirable and unstable location) to a more stable location closer to the channel centreline. Barbs are a variation of a groyne, similar to spur dikes and bendway weirs, but their low-profile in the flow field allows continuous overtopping of flow at bankfull (or greater) water levels. Unlike traditional bank protection measures such as riprap, concrete paving or gabion walls, barbs require less material, promote vegetated stream banks, create resting pools and scour holes for fish habitat, and increase bio-diversity for aquatic species (Shields *et al.*, 1998; Shields *et al.*, 2000; Piper *et al.,* 2001). Despite these benefits, barbs are not a common means of stream bank protection due to a lack of suitable design guidelines and an incomplete understanding of their effect on flow and sediment dynamics in channel bends.

A number of different laboratory experiments on submerged structures (barbs, submergeed groynes, spur dikes, bendway weirs, vanes, etc.) in open channel flows have been performed and are summarized in the companion paper Jamieson *et al.* (*Submitted* - a) (Chapter 5.2). For the most part, many of these studies; (1) were not performed in channel

bends (Kuhnle *et al.*, 1999; Johnson *et al.*, 2001; Kuhnle *et al.*, 2002; Fox *et al.*, 2005a and 2005b; Uijttewaal, 2005; Kuhnle *et al.*, 2008), where the use of these structures is most relevant; (2) did not provide detailed turbulence measurements (Kuhnle *et al.*, 1999; Johnson *et al.*, 2001; Kuhnle *et al.*, 2002; Matsuura and Townsend, 2004; Jia *et al.*, 2005); (3) lacked coupled mobile-bed studies with comprehensive velocity and turbulence measurements (Fox *et al.*, 2005a and 2005b; Uijttewaal, 2005). Recent numerical studies have provided new insight into the patterns of turbulence around submerged structures (Minor *et al.*, 2007a and 2007b; McCoy *et al.* 2008; Koken and Constantinescu, 2008a and 2008b), but experimental data remain lacking.

Fox *et al.* (2005b), Kuhnle *et al.* (2008) and Bhuiyan *et al.* (2010) present the most rigorous investigations to date of flow field dynamics around a submerged structure, with Fox *et al.* (2005b) developing an eddy taxonomy methodology, in which small- and large-scale eddies are separately decomposed from velocity time series, to identify small- and large- scale eddies in the vicinity of an upstream-orientated barb along a straight channel. However, Fox *et al.* (2005b) found that, while this method provided conclusive spatial and temporal scales of small- and large-scale eddies at locations where the barb had less impact on eddy generation (i.e. the approach flow and outer extent of the shear layer), the results were “more ambiguous” within the overtopping shear layer and downstream stagnant flow regions, where the barb presence dominates eddy generation. The combination of multiple eddy scales and strong secondary currents (generated in this case by the overtopping, plunging action) complicated the analysis of the spatial and temporal eddy scales downstream of the barb obstacle, thereby increasing the uncertainty of the results.

Minor *et al.*, 2007b used a 3-D numerical model (SSIIM) to examine the turbulent flow field and associated sediment transport for the same barb group arrangements as Matsuura

(2004). Maximum bed shear stresses were calculated in the same regions as the maximum scour and velocity, while velocity vectors over and around the submerged structures illustrated the plunging action of the flow over the structure and flow separation at the barb tip, which was observed in previous studies using dye (Fox *et al.,* 2005a). Select results were further analysed to provide a comprehensive view of the 3-D characteristics of the flow for a series of barbs in a channel bend (Minor *et al.,* 2007a). This analysis demonstrated that the pattern and magnitude of erosion and deposition were dependent on the characteristics of the flow field, and perhaps most significantly, vorticity: the location of maximum vorticity (and in particular z-vorticity), which was found at the barb tips, corresponded with the locations of maximum scour (Minor *et al.,* 2007a).

By definition, barbs are submerged structures that slope away from the bank along the channel bed, with their highest crest elevation nearest to the bank typically corresponding to the bankfull water level. With this arrangement, at high (channel forming) flows the structure is continuously overtopped, resulting in plunging type flow over the structure. Bhuiyan *et al.* (2010) found that vanes sloping to the channel bed from bankfull level at the bank showed better performance than low level vanes (not at bankfull). Unlike other groyne structures that are emergent and perpendicular to the flow, the vertical separation of the flow is less significant for barbs because they are submerged and orientated in a more streamlined direction (i.e. not perpendicular to the main streamwise flow direction). If a structure (or object) obstructs a high Reynolds number flow, due to the significant velocity gradient created and the corresponding low pressure, the boundary layer developed against the object will separate from the wall. The separated flow will generate a downstream shear layer with the main flow and vertically-orientated vortical structures may develop (i.e. rotation about the vertical axis or z-vorticity). Conversely, the plunging of the flow causes regions of high

velocity above the barbs and low velocity between the barbs. This velocity gradient can induce cross-stream (transverse) mixing which will interact with the primary secondary flow cell (developed as a result of bend geometry), potentially deflecting the secondary flow (along with the maximum velocity core) towards the center of the channel, away from the outer bank. Both Bhuiyan *et al.* (2010) and (Jamieson *et al.*, *Submitted* – a; Chapter 5.2) found that plunging action generated a counter-rotating secondary flow cell, but it's impact on reducing outer bank erosion was inconsistent.

By comparing the patterns and magnitude of scour and deposition around the barbs with detailed contours of turbulence and vorticity it may be possible to estimate the relative magnitude of these flow properties required to generate a scour hole or initiate deposition. Discerning the relative contributions of these to local scour will lead to better understanding and prediction of the changes in bed level for different flow fields associated with different barb geometries and arrangements in series. While Minor *et al.* (2007a) discussed the relationship between local scour and vorticity, the simulated (numerical) results were never validated with measured velocity data. Validation of both the flow field and bathymetry is crucial before any significant relationships between flow field dynamics and sediment transport are revealed through numerical simulation.

This paper presents the first experimental results to describe the spatial variability of the complex turbulent flow field associated with a series of submerged barbs installed in a channel bend. With the exception of Bhuiyan *et al.* (2010), who present results at select cross-sections through a meander bend, the most detailed flow measurements to date have been for only a single structure installed in a straight section (Fox *et al.,* 2005b and Kuhnle *et al.,* 2008). Given that the primary objective of stream barbs is to reduce bank erosion, a problem principally found along the outside banks of river bends, it is critical that future

studies consider channel bends. The helical (secondary) flow generated in a channel bend will alter the magnitude and direction of velocity as the flow approaches the barb and as a result the flow over and past the structure. This will in turn play a role in local flow field characteristics and ultimately how the structure functions: how effectively it disrupts velocity and shifts the thalweg away from the outside bank to the center of the channel. As well, all previous mobile-bed studies considered rigid, vertical walls, where the reduction in scour of the outer bank could not be evaluated. In the current study, a uniform trapezoidal cross-section formed within the rectangular cross-sectional flume has been used, where both the bed and banks were composed of sand and subject to scour.

The goal of this study is to confirm the numerical modelling results of Minor *et al.* (2007a and 2007b) and demonstrate the role of turbulence and vorticity on the development of local scour. Understanding the flow in detail (i.e. at the scale and structure of the vortical and turbulent motions) should provide a better means of predicting the resulting bed level changes for various barb geometries and orientations. It is expected that these results will lead to improved design of barb structures, provide necessary data for better validation of numerical simulations of turbulent flow and sediment transport for submerged in-stream structures, while advancing our general understanding of the role of these coupled processes.

5.3.3 Data Collection and Processing

Laboratory flume experiments were performed in the large 135º bend flume at the University of Ottawa (Figure 5.3.1). A complete description of the experimental conditions for each of the six different experiments (TR1, TR3, TR5, TR6, TR7 and TR10) is provided in the companion paper (Jamieson *et al.*, *Submitted* – a; Chapter 5.2). The six experiments represent two base case conditions (experiments without barbs, TR1 and TR3) and four different

barb sizes and arrangements (TR5, TR6, TR7, TR10). In this paper, data are presented for only TR1, TR3, TR5 and TR10, where acoustic Doppler velocimeter (ADV) data were collected at 13 cross-sections through the bend (Figure 5.3.1 and Table 5.3.1), which provided sufficient coverage for the spatial assessment of turbulence and vorticity through the bend. The experimental conditions for these four experiments are summarized in Table 5.3.1.

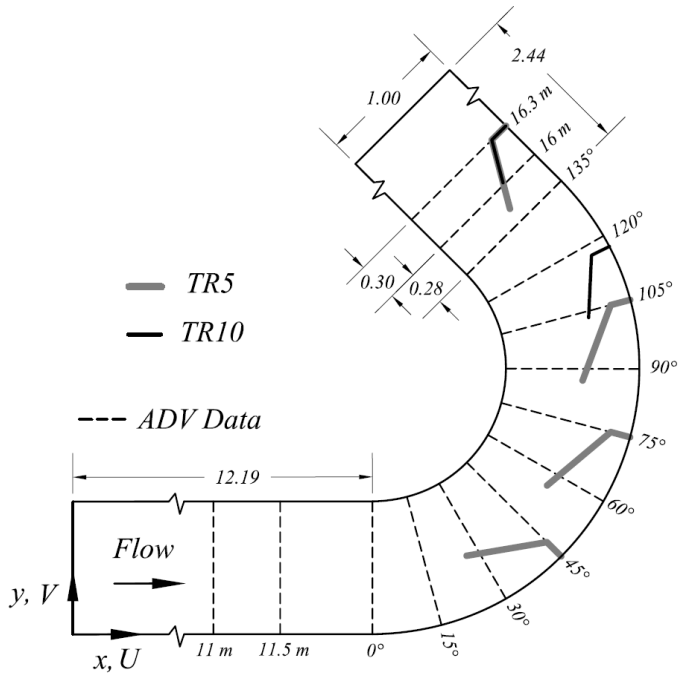

Figure 5.3.1. Plan view of channel geometry, barb layout and location of ADV measurement cross-sections. Streamwise velocity component (U) is parallel to the flume wall throughout the domain. All dimensions are in meters.

A 0.15 m deep trapezoid cross-sectional channel (with a top and bottom width of 0.80 and 0.26 m respectively), built entirely of sand (d_{50} = 1.1 mm), was constructed within the channel bend, allowing erosion of the bed and banks to be assessed. Experiments were performed under clear water scour conditions, wherein flow in the channel's approach section to the bend was near the threshold of particle motion and negligible movement of sand grains was observed. Under these conditions, scour and deposition in the bend were due

to the bend geometry alone (TR1 and TR3) or a combination of the bend and the presence of barb structures (TR5 and TR10). Barbs were constructed by hand using small, angular stone, with average sizes of 0.043 m in length and 0.025 m in thickness. Four barbs were used in TR5 compared to two barbs in TR10 (Figure 5.3.1). Barbs in TR5 were both larger (height and width) and longer than the barbs used in TR10 (Table 5.2.2, Jamieson *et al.*, *Submitted* – a; Chapter 5.2). A plan view of each barb layout is provided in Figure 5.3.1 and in plots of the entire flume (Figure 5.3.2 - Figure 5.3.6), where for simplicity only the barb crests have been delineated with a black line to show barb location and geometry. Bathymetry results presented in Jamieson *et al.* (*Submitted* - a) (Chapter 5.2) indicated that the barb arrangement in TR10 was most successful in reducing erosion along the outer bank. Among all runs, the largest scour holes and greatest amount of outer bank erosion were generated in TR5, which predominantly occurred between barbs.

Table 5.3.1. Summary of experimental runs. In all runs, original bed slope was 0.0007 and mean sediment size (d_{50}) 1.1 mm. Q is flow rate, H is flume-averaged flow depth in the center of the channel, W/H is the width-to-depth ratio assuming width (W) is 0.80 m, U (=Q/A) is flume-averaged velocity (where cross-sectional area = A), $\overline{U_*}$ is mean shear velocity in the approach section. Barb layouts are shown in Figure 5.3.1.

Run Title	Barbs?	Q (m^3/s)	H (m)	W/H	U (m/s)	$\overline{U_*}$ (m/s)	τ_o (N/m^2)	Duration (hours)	ADV Measurements (Cross-Section)
TR1	No	0.017	0.142	5.6	0.231	0.011	0.123	213	• 11m, 11.5m, 0º, 15º, 30º, 45º, 60º, 75º, 90º, 105º, 120º, 135º, 16m
TR3	No	0.021	0.148	5.4	0.267	0.020	0.424	391	• 11.5m, 0º, 15º, 30º, 45º, 60º, 75º, 90º, 105º, 120º, 135º, 16m, 16.3m
TR5	Yes (4)	0.021	0.157	5.1	0.264	0.021	0.440	380	• 11.5m, 0º, 15º, 30º, 45º, 60º, 75º, 90º, 105º, 120º, 135º, 16m, 16.3m
TR10	Yes (2)	0.020	0.153	5.2	0.255	0.021	0.420	386	• 11.5m, 0º, 15º, 30º, 45º, 60º, 75º, 90º, 105º, 120º, 135º, 16m, 16.3m

ADV point measurements (typically 40-60 points per cross-section) of streamwise, cross-stream and vertical velocity (u, v and w) were used to calculate time averaged velocities ($\overline{U}$, $\overline{V}$ and $\overline{W}$) and fluctuating turbulent velocities (u', v' and w'). Fluctuating velocities were combined to evaluate the three Reynolds shear stress components (τ_{uw}, τ_{uv} and τ_{vw}) and average turbulent kinetic energy (*tke*) such that

$$\tau_{uw} = -\rho\overline{u'w'};\ \tau_{uv} = -\rho\overline{u'v'};\ \ \tau_{vw} = -\rho\overline{v'w'} \tag{5.3.1}$$

$$tke = \frac{1}{2}\left(\overline{u'^2} + \overline{v'^2} + \overline{w'^2}\right) \tag{5.3.2}$$

where ρ is the density of water and $\overline{u'w'}$, $\overline{u'v'}$ and $\overline{v'w'}$, and $\overline{u'^2}$, $\overline{v'^2}$ and $\overline{w'^2}$ represent the mean of the product and square of the fluctuating turbulent velocities, respectively.

Reynolds stresses and turbulent kinetic energy are useful for quantifying the magnitude of turbulence, however they do not provide any information on the size or scale of the flow oscillations or eddies, which can be important for quantifying mixing lengths of the transport of sediment. Turbulence scales were calculated from the correlation function. For each time series measurement of velocity, the integral time scale (T_E) was calculated in the streamwise direction (x) by integrating the correlation coefficient, $R_x(\tau)$ such that

$$T_E = \int_0^L R_x(\tau)dr \qquad \text{for} \qquad R_x(\tau) = \frac{\overline{u'(t)\cdot u'(t+\tau)}}{\overline{u'^2}} \tag{5.3.3 and 5.3.4}$$

where τ is the time lag between two measurements of streamwise velocity fluctation $u'(t)$ and $u'(t+\tau)$, and L is the time lag at which R_x is no longer greater than zero. For measurements with a relative turbulent intensity ($\left|\hat{u}\right| = \left|\sqrt{\overline{u'^2}}\,/\,\overline{U}\right|$) << 1 (we have used $\left|\hat{u}\right| < 0.25$), Taylor's frozen field hypothesis is assumed valid (Hinze, 1959; Lumley, 1965) and the integral length scale (L_x) for the macroscale turbulence or energy containing eddies is calculated as

$L_x = \overline{U} T_E$. The integral length scale measures the largest separation distance over which components of the eddy velocities at two distinct points are correlated, and thus is an indication of the largest eddy sizes in the flow.

To assess the spatial variability of all measured components and calculate additional flow features such as vorticity, the individual ADV point measurements from each run were combined to generate a continuous 3-D volume of the flow field. The interpolated bathymetry data were used to generate a structured 3-D grid of the entire flow field for each run and the processed ADV data were then interpolated into each 3-D grid using kriging. The kriging parameters and grid spacing for the 3-D volume are discussed in the companion paper (Jamieson *et al.*, *Submitted* - a) (Chapter 5.2). The grid spacing varied through the domain depending on local depth and location in the inner versus outer portion of the bend, but was of order 0.1 m in the horizontal and 0.015 m in the vertical.

Vorticity magnitude (ω) is defined as the vector sum of the three components of rotation (ω_x, ω_y and ω_z) about the *x*, *y* and *z*-axis respectively. The rotation about each axis is defined as the average of the angular velocities perpendicular to the axis of rotation such that

$$\omega_x = \frac{1}{2}\left(\frac{\partial w}{\partial y} - \frac{\partial v}{\partial z}\right); \quad \omega_y = \frac{1}{2}\left(\frac{\partial u}{\partial z} - \frac{\partial w}{\partial x}\right); \quad \omega_z = \frac{1}{2}\left(\frac{\partial v}{\partial x} - \frac{\partial u}{\partial y}\right) \tag{5.3.5}$$

where $\partial v / \partial x$ and $\partial w / \partial x$ are angular velocities along the x-axis, $\partial u / \partial y$ and $\partial w / \partial y$ are angular velocities along the y-axis, and $\partial u / \partial z$ and $\partial v / \partial z$ are angular velocities along the z-axis (assuming the right hand rule for positive rotation about each axis). For a mean (or time-averaged) flow field, we assume that the velocity at a given point in space does not vary with time. Therefore, the calculated vorticity for a time-averaged flow field must also be constant. Furthermore, we emphasise that vorticity is based on spatial velocity gradients about a given axis, and the resolution of the volume grid dictates the scale of velocity gradients that are

included in the calculation. We note that vertical resolution was relatively fine in the volume grid, thus vertical gradients, which are typically steepest, were relatively well represented. Furthermore, as discussed below, the calculated vorticity was insensitive to the grid resolution.

5.3.4 Results and Analysis

Reynolds Shear Stress and Turbulent Kinetic Energy

The magnitude of Reynolds shear stress (RS) in open channel flows provides an indication of the stress within the fluid due to shear from turbulent fluctuations (e.g. Blanckaert and Graf, 2001; Termini and Piraino, 2010). In typical straight channels, the principal RS (τ_{uw}) is largest and therefore most important in the role of sediment transport. However, when helical flow develops in a bend, secondary velocities increase and the other two components of RS terms (τ_{uv} and τ_{vw}) become important, possibly exceeding τ_{uw} (Jamieson *et al.*, 2010; Chapter 5.1). Contours of τ_{uw}, τ_{uv} and τ_{vw} near the bed (Figure 5.3.2) confirm that without barbs, τ_{uw} remains highest in the straight approach section, but less than τ_{uv} through the bend. The patterns of RS in TR1 and TR3 match well with results in the same bend (Jamieson *et al.*, 2010; Chapter 5.1); where slight differences are likely due to the difference in cross-sectional geometry and flow rate. With barbs present, all components of RS are highest in the vicinity of each barb, with the larger barbs in TR5 generating the highest values.

On the other hand, the introduction of barbs appears to slightly reduce τ_{uw} and τ_{uv} upstream of the bend, where no change in bed elevation was measured in any of the experimental runs (cf. Figure 5.2.3, Jamieson et al., *Submitted - a*). The greatest reduction is

found in TR5, where the presence of four large barbs has most influenced the patterns of mean flow upstream of the bend. It is possible that in both cases, τ_{uw} and τ_{uv} are slightly reduced in the upstream section of TR5 (four barbs) and TR10 (2 barbs) compared to TR3 (non barbs), due to the presence of barbs downstream. It appears the barbs result in a small backwater effect (cf. Azinfar and Kells, 2011), which upstream of the bend: (1) reduces the local water surface slope, (2) reduces the streamwise velocity, and (3) alters the helical bend flow pattern. Consequently, upstream near-bed Reynolds stresses are reduced. Contour plots of streamwise and secondary velocities (Figure 5.2.5, Figure 5.2.6 and Figure 5.2.7, Jamieson et al., *Submitted - a*) confirm this observation.

The distribution of *tke* through the bend is presented in Figure 5.3.3. As expected, the flow in the vicinity of the barbs (TR5 and TR10) shows the highest values of *tke*. Compared to the base case (TR3), maximum *tke* was more than 10 times greater in TR5 and more than 2-4 times in TR10. In the vicinity of the barbs, *tke* increased with depth as more of the flow is overtopping at greater water depths. When compared to the results of TR10, the noticeably higher RS and *tke* in TR5 are likely due to the larger and more numerous barbs in TR5, which caused greater flow separation, overtopping and mixing, and therefore higher turbulence. While the barbs act to redirect high streamwise velocity away from the outer bank, the more varied bathymetry in TR5 and TR10 associated with scour holes, eroded floodplain (i.e. steeper side slopes) and the abrupt change in elevation due to the presence of barbs themselves, results in higher values of *v* and *w* (Figure 5.2.6 –Figure 5.2.9, Jamieson *et al.*, *Submitted* – a; Chapter 5.2). This increase is likely to lead to higher values of v' and w', which would explain the higher observed RS and *tke*. However, although turbulence is

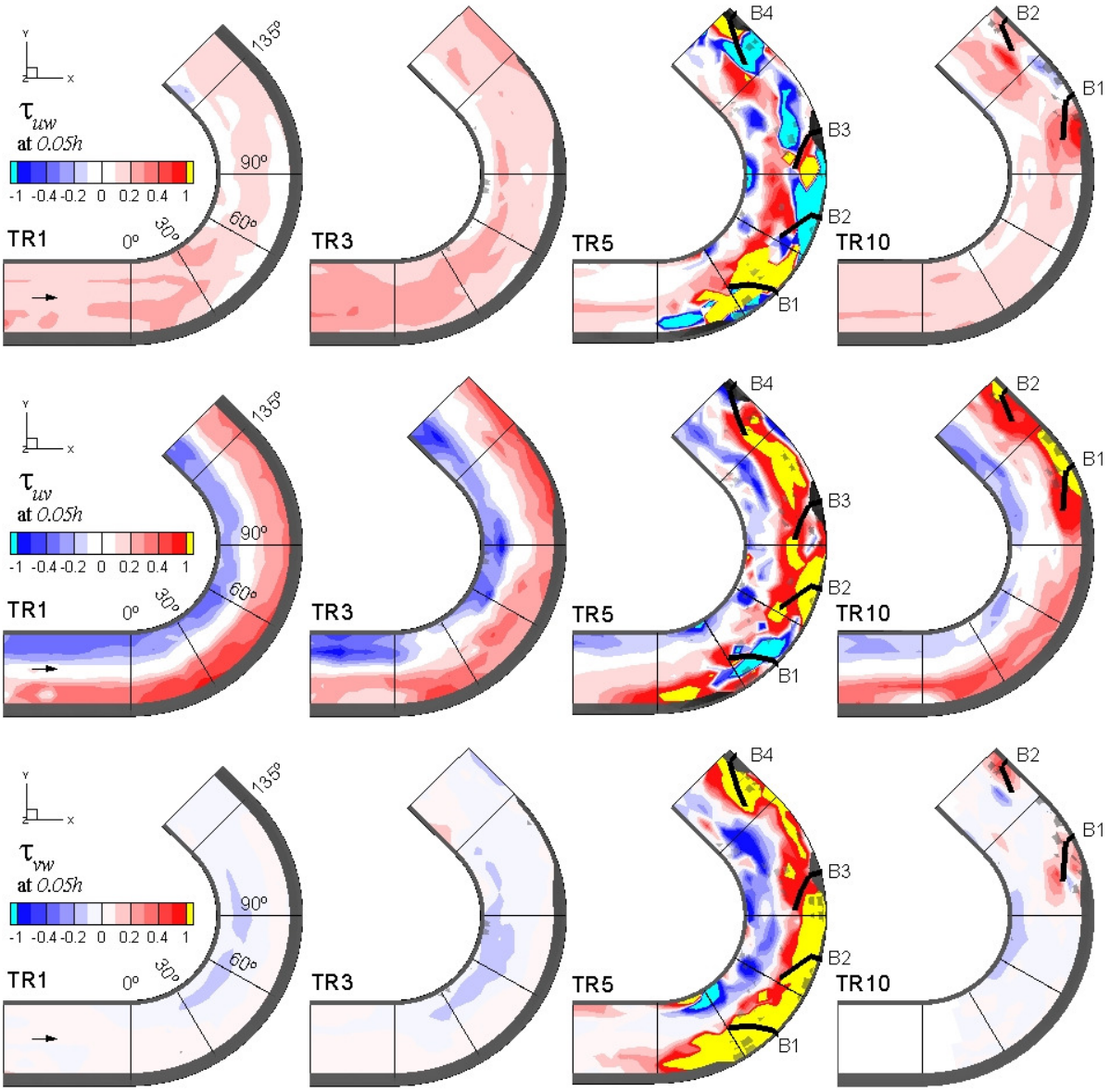

Figure 5.3.2. Contours of the three components of Reynolds shear stress: $\tau_{uw} = -\rho\overline{u'w'}$ (top); $\tau_{uv} = -\rho\overline{u'v'}$ (middle); and $\tau_{vw} = -\rho\overline{v'w'}$ (bottom) at 0.05h. Note the non-linear colour scale. Dark grey regions indicate where no data were collected.

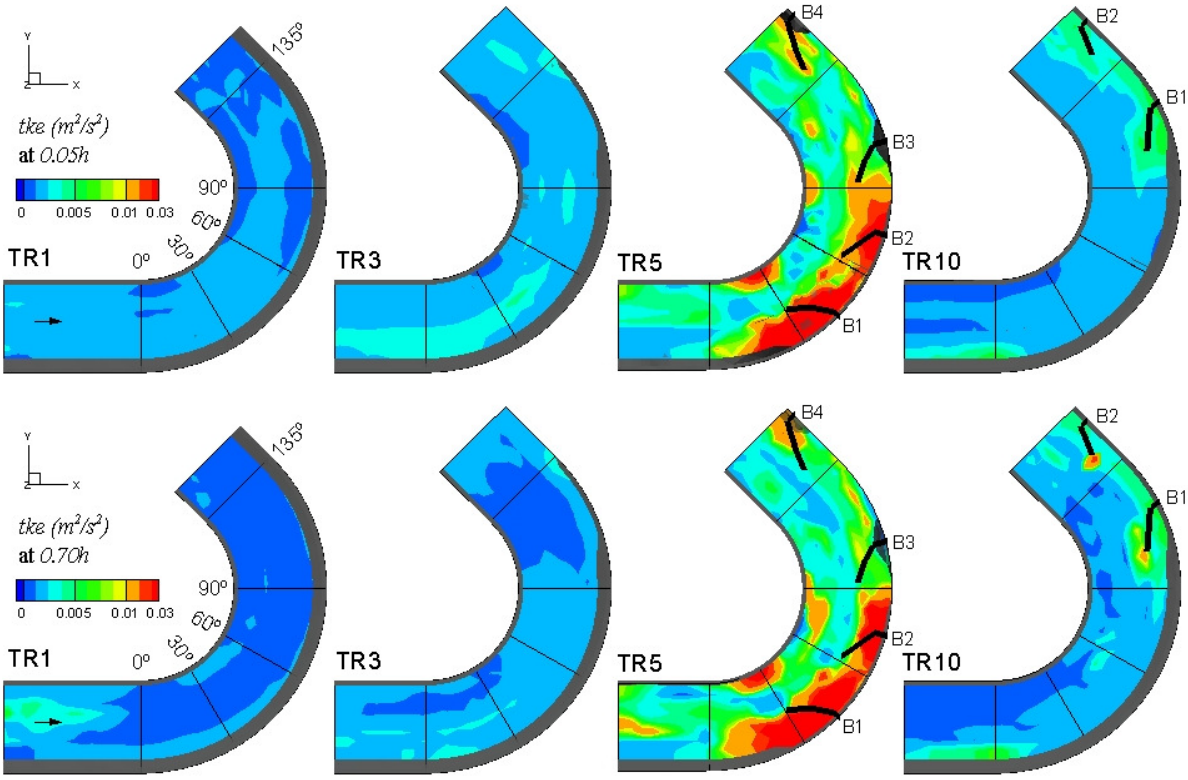

Figure 5.3.3. Contours of turbulent kinetic energy (*tke*) at 0.05*h* (top) and 0.70*h* (bottom). Note the non-linear colour scale.

highest in the vicinity of the barbs in both TR5 and TR10, the pattern of turbulence is different. In TR10, the highest RS and *tke* appear to be concentrated over and near the barb tips, while in addition to high RS and *tke* over the barbs in TR5, it is also highest along the outer bank near B1 and B2 (the two upstream most barbs). Comparing contours plots of RS and *tke* with bathymetry (Figure 5.2.2, Jamieson *et al.*, *Submitted* – a; Chapter 5.2) shows that high turbulence is not necessarily concentrated over the scour holes. However, highest RS and *tke* do correspond to the greatest bed level changes (ΔZ, Figure 5.2.3, Jamieson *et al.*, *Submitted* – a; Chapter 5.2). One such example is the outer bank regions between B1 and B2 and between B2 and B3 in TR5, where $\Delta Z < -0.10$ m and *tke* > 0.03 m^2/s^2, or more than 10 times the value at the same location for the case without barbs (TR3). As well, the

calculated local bed slope (not shown) shows that while slope is > 30º in the vicinity of barbs and the side walls downstream of the barbs, the magnitude of slope associated with the scour holes is much less, typically slope < 20º. Therefore, it is possible that at lower side slopes (i.e. slope < 20º) the scour holes do not noticeably increase v' and w' (or *tke*), while steeper slopes do. Indeed, side slope is greatest in TR5 compared to TR10 and corresponds closely with the regions of highest RS and *tke*.

Reducing the height and length of the barbs (TR10 results) appears to prevent high RS and *tke* from dominating the near outer bank region between barbs, which possibly reduces erosion in these regions. These results would suggest that higher RS and *tke* are contributing to greater sediment transport along the outer bank side slope (leading to erosion of the floodplain and an increase in side slope), but not necessarily on the development of the scour holes closer to the barb tips. However, what is less certain is whether the increased RS and *tke* are a result of the steeper side slopes or the cause of the steeper side slopes. Most likely there is a positive feedback, in which the increased turbulence results in increased transport and hence increased side slope, which ultimately leads to increased turbulent fluctuations (v' and w') and so on. With vanes installed in series, Bhuiyan *et al.* (2010) found that maximum turbulent intensities ($\sqrt{\overline{u'^2}}$, $\sqrt{\overline{v'^2}}$ and $\sqrt{\overline{w'^2}}$) occurred near the vane crest in the zones of downwelling downstream of the structures, at the interface of the two counter-rotating secondary circulating cells.

Turbulence Time and Length Scales

The integral time scale (T_E) is a measure of the time scale for the largest period oscillations in the flow, or the time scale over which there is some organization in the flow. Contours of

T_E are shown in Figure 5.3.4 and show subtle differences between runs without barbs (TR1 and TR3) and runs with barbs (TR5 and TR10). In all cases, high values of T_E are found near the bend entrance and along the outer bank, and in TR3 and TR10 the highest values are at the bend exit (TR3) and over the first barb (TR10). In TR5, high T_E is concentrated between barbs, but remains lower than values in TR3 and TR10. A similar overall pattern is found for the integral length scale (L_x) in Figure 5.3.4: high L_x is found near the bend entrance and along the outer bank, while highest values remain in TR3 and TR10 in the same locations as high T_E. While L_x appears lower in TR5, much of the contour plot has been blanked due to the prevalence of high relative turbulence intensity ($|\hat{u}| > 0.25$). The results in Figure 5.3.4 indicate that the barbs (and in particular the larger barbs in TR5) disrupt the integral time and length scales, suggesting that the turbulence (or vortices) generated by the barbs are smaller (and get smaller as barbs get bigger), and therefore are less developed than in a regular meander bend.

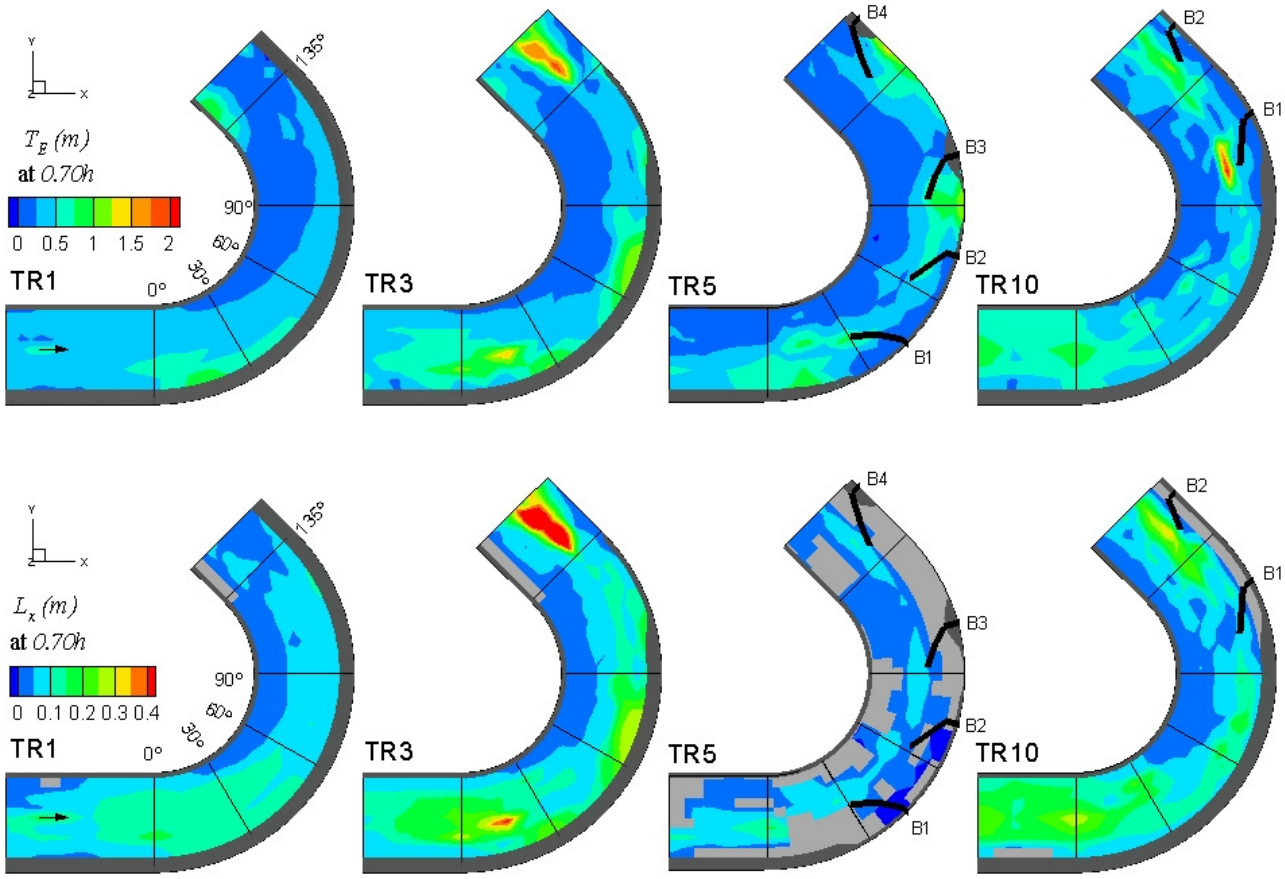

Figure 5.3.4. Contours of integral time scale (T_E) (top) and integral length scale (L_x) (bottom) at 0.70h. Data with a relative turbulence intensity ($|\hat{u}|$) greater than 0.25 have been blanked from the L_x contours, where blanked regions are indicated by light grey.

Vorticity

Vorticity magnitude was calculated throughout the flow field of each run and is presented in Figure 5.3.5. In all runs, vorticity magnitude was higher closer to the bed (at 0.05h). The highest magnitudes (> 5 s^{-1}) were calculated in runs T3 and TR10 and occurred along the outer bank at the bend exit (TR3 and TR10) and in the case of barbs (TR10), near the tip of both barbs (B1 and B2). Closer to the water surface (at 0.70h, not shown), vorticity magnitude decreases considerably, to near zero throughout the bend for all runs. The one

exception is TR5, where maximum vorticity was also found at the bend exit, but near the inner bank. This location again corresponds with maximum change in elevation (Figure 5.2.3, Jamieson *et al.*, *Submitted* – a; Chapter 5.2), and may be located along the inner bank because the barbs in this case were large enough to deflect enough of the high vorticity (and secondary currents) away from the outer bank and into the inner bank.

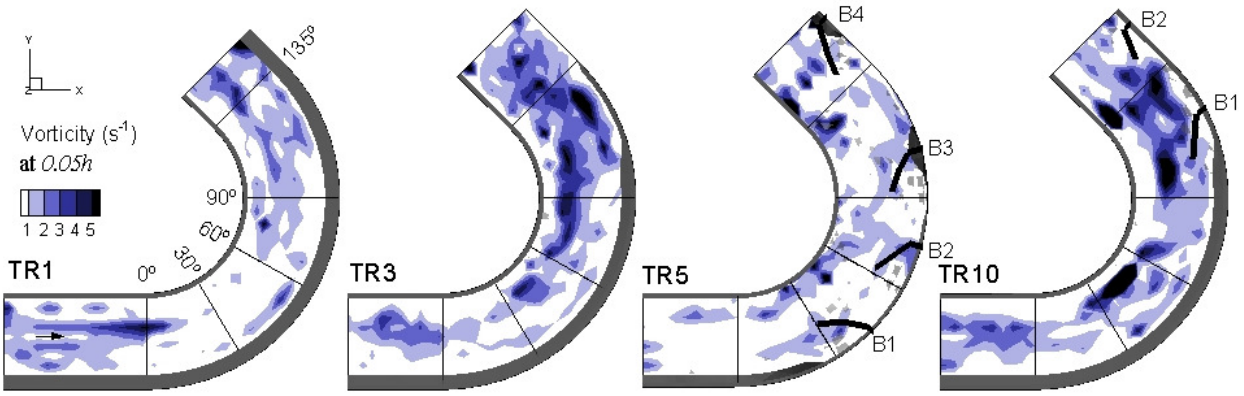

Figure 5.3.5. Contours of vorticity magnitude at 0.05*h*.

Contours of z-vorticity near the bed and water surface (0.05*h* and 0.70*h* respectively) are shown in Figure 5.3.6. In all runs and at both depths, maximum positive z-vorticity was along the inner bank through the bend, which is consistent with helical flow through the bend and contours of vertical velocity. On the other hand, highly negative z-vorticity was present along the outer bank, but only along the straight approach section and near the bend exit (all runs) and in the vicinity of barbs (TR5 and TR10). Interestingly, while TR3 and TR10 had the highest values of vorticity magnitude, TR5 exhibited the highest values of negative z-vorticity, where flow in the vicinity of all barbs was dominated by high negative z-vorticity. This was also present in TR10; however, the pattern is slightly different. Just like the contours of RS and *tke*, high negative z-vorticity was located near the barb tips in TR10 (see B2,

Figure 5.3.6), while the distribution in TR5 appeared to be more spread out between barbs and particularly high over and downstream of each barb, rather than concentrated at the tip. It should be noted here that the sign of z-vorticity (positive or negative) is a function of the designated velocity vector direction, and provided the same right-hand-rule is applied, it will vary depending on the orientation of the shear layer (or boundary layer) with respect to positive streamwise direction. Therefore, we necessarily have negative z-vorticity along the right (outer) bank and positive z-vorticity along the inner bank due to sign convention.

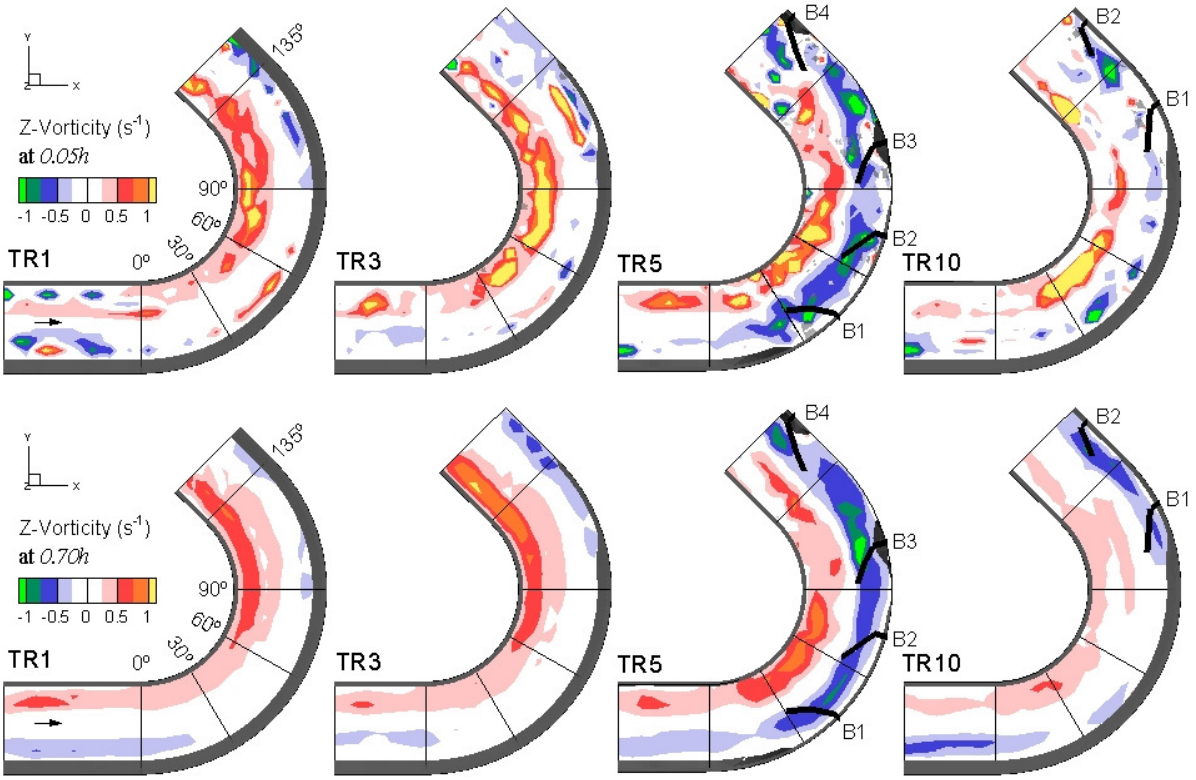

Figure 5.3.6. Contours of z-vorticity at 0.*05h* (top) and 0.70*h* (bottom).

Comparing TR5 and TR10 results indicates that if barbs are constructed too large (i.e. TR5) they generate higher turbulence between the barbs which has negative effects on protecting the outer bank. Barbs must redirect the flow while, at the same time, either

minimizing any increase in turbulence generation or concentrating any turbulent flow near the barb tips (away from the outer bank). Bhuiyan *et al.*'s (2010) vane design did not generate large-scale vortices behind the structures, and did establish deposition downstream of the structure, near the toe of the bank.

5.3.5 Discussion

Velocity data were collected at equilibrium bed conditions. Therefore, the impact of the flow properties (mean flow field, turbulence and vorticity) on the development of scour can not be stated for certain, because these were evolving simultaneously during the run and equilibrium is only reached when the bed shear stress and turbulent fluctuations are no longer able to entrain sediment. However, in their numerical investigations, Koken and Constantinescu (2008a and 2008b) found that the horseshoe vortex system forming around the upstream base of a single emergent spur dike (which they describe as the main driving mechanism behind the growth of a scour hole at the structure's tip) was present during both the initial and final stages of the scouring process. The authors found that, compared to the initial stage when the bed was flat, the presence of the scour hole stabilized the horseshoe vortex system. In the following it is assumed that turbulent flow variables measured during equilibrium bed conditions can be related to sediment transport dynamics based on their association with measured changes in bed elevation due to scour and/or deposition.

Turbulence versus Vorticity

To quantify the relative contributions of turbulence and vorticity to the development of scour, bivariate intensity plots are presented in Figure 5.3.7 to compare the joint probability

densities for τ_{uv}, *tke*, vorticity magnitude and z-vorticity with change in bed elevation (ΔZ) for TR3, TR5 and TR10. These joint probability distributions demonstrate the frequency of occurrence for combinations of these four variables with ΔZ, thus the plots demonstrate the frequency of occurrence of each variable as a function of locations of sediment transport or scour (represented by ΔZ). The marginal (single variable) probability densities of each variable and ΔZ can also be interpreted from these plots based on the frequency of occurrence across a single axis. All three RS components were analysed, but it was τ_{uv} that established the most dominant and consistent pattern in the joint probably plots. To create the plots, data were extracted from the interpolated flow field and bathymetry near the bed at 5% of the flow depth (0.05*h*) and paired according to horizontal (x, y) spatial location. The locations of extracted data correspond with mesh nodes from the interpolated flow field. In order to increase the population of paired points for the bivariate analysis, a mesh twice as dense as the one used for Figure 5.3.2 – Figure 5.3.6 was used. Contour values were near identical between the two meshes, with the denser mesh having slightly more jagged contour lines. To focus the analysis on the most dynamic region of the channel, data were extracted from the outer bank region, labelled Zone C (Figure 5.3.7). This zone extends in the downstream direction from 0º (or 90º in the case of TR10) to cross section 16.5 m (0.78 m downstream of the bend exit), and in the cross-stream direction from the outer bank wall to the toe of the left (inner) bank side slope. For better comparison between runs (and zones, Figure 5.3.8), the joint probability frequencies were normalized by the total population of compared points for each run (or zone), such that the cumulative joint distribution of each joint probability density plot equals 1. Regression coefficients (R^2) are provided in each joint distribution plot (Figure 5.3.7 and Figure 5.3.8) based on the fit of a linear model to scatter

plots of each paired data set. Despite generally low R^2 values, large sample sizes gave sufficient statistical power such that all but one of the joint distributions had linear trends that were statistically different from zero at the 95% confidence level, the exception being vorticity magnitude in TR5 Zone A (Figure 5.3.8). As well, using a t-test it was possible to determine whether any two R^2 values were statistically different from each other. For example, despite these low R^2 values, all regression coefficient combination pairs (e.g. τ_{uv} and *tke;* τ_{uv} and z-vorticity; etc.) for Zone C in all runs (Figure 5.3.7) were found to be significantly different. (at >95% confidence level). This test provides statistical justification for the comparison of variables for understanding their relative significance with respect to scour (i.e. ΔZ).

The TR5 intensity plots show a greater spread of magnitudes compared to TR3 and TR10 (Figure 5.3.7) due to the higher and more frequent occurrence of bed level changes coupled with higher turbulence and z-vorticity. The highest frequencies in TR5 were found in the τ_{uv} and *tke* joint distributions (which is not the case for the other two runs). However, these frequencies were spread horizontally along the lowest magnitudes of both τ_{uv} and *tke* ($\tau_{uv} \approx 0$ and $tke < 0.01$) and across a large range of bed level changes ($-0.1 < \Delta Z < 0$). This suggests there was not a strong relationship between scour and either τ_{uv} or *tke* in TR5.

Comparing between the three runs, z-vorticity shows the most consistent pattern, and unlike τ_{uv}, *tke* and vorticity magnitude, there are fewer outliers and a continuous linear trend is apparent. This trend is a positive slope, with greater negative z-vorticity being associated with increased scour ($\Delta Z < 0$). The greatest pairing of negative z-vorticity and scour occurred in TR5, which had the largest barbs. For TR3 and TR10 in particular, this trend

extends to describe deposition ($\Delta Z > 0$), with increased positive z-vorticity associated with increased deposition.

The streamwise-cross-stream Reynolds stress (τ_{uv}) had the highest regression coefficients of any variable (in both TR3 and TR10, R^2 = 0.318 and 0.338, respectively). This suggests that positive near-bed τ_{uv} was associated with scour while small positive and negative near-bed τ_{uv} were associated with deposition. Furthermore, the relatively small barbs in TR10 did not substantially alter this trend. It was evident from Figure 5.3.2 that positive τ_{uv} occurred on the outer channel bank while negative τ_{uv} occurred on the inner bank. This pattern occurred even in the straight inlet reach, but was amplified in the bend. This must have been related to near-bed momentum transfer away from the side slope of the trapezoidal channel, which continued throughout the channel bend in the cases without barbs (TR3) and with small barbs (TR10). Consequently, positive τ_{uv} was correlated with outer bank scour while small positive and negative τ_{uv} were associated with deposition in the middle of the channel (compare τ_{uv} in Figure 5.3.2 and ΔZ in Figure 5.2.3 of Jamieson *et al.*, *Submitted* – a; Chapter 5.2). In TR5, the trend was disrupted by the large barbs (see Figure 5.3.2), with the consequence that less trend is evident in Figure 5.3.7. While R^2 for τ_{uv} (R^2 = 0.019) is higher than for *tke* or vorticity magnitude in TR5, it remains lower than for z-vorticity (R^2 = 0.061), with the regressions being significantly different with a 99% confidence interval. This suggests that the scour due to the large barbs in TR5 is more related to z-vorticity than τ_{uv}.

Much weaker trends were observed in vorticity magnitude than z-vorticity, which suggests that vertically oriented vortices dominated the scouring process. Interestingly,

vorticity magnitude had a slight positive trend in all runs, wherein scour decreased (or deposition increased) with increased magnitude, and was strongest in TR5. Possibly, vorticity magnitude is more indicative of the large scale secondary circulation through the bend, which is typically associated with deposition along the inner bank. This would explain why it is higher in TR3 and TR10 in the center of the channel and near the toe of the inner bank side slope (Figure 5.3.5), because the pattern of secondary circulation through the bend was least disrupted in these two runs compared to TR5 (see Figure 5.2.6, Figure 5.2.7, Figure 5.2.8 and Figure 5.2.9 in Jamieson *et al.*, *Submitted* – a; Chapter 5.2). However, it is worth emphasizing that the vorticity magnitude trends are weak.

Lastly, a relatively strong trend between increased *tke* and increased scour was observed in TR10 but not in TR3 or TR5. The values of *tke* in TR10 were of similar magnitude to those of TR3, but a few higher values were observed in TR10 and these tended to be associated with scour. Possibly, the relatively small barbs in TR10 had vortices that produced scour that were less consistent such that consistent spatial accelerations (measured by z-vorticity) were weaker but overall turbulence levels were increased.

To assess any spatial correspondence in the joint probability frequencies, plots were generated for two sub-zones of Zone C, namely Zone A (outer bank region) and Zone B (channel center), and results are presented for TR5 (Figure 5.3.8). Zone A, which extends from y = 0 to 0.28 m (close to 1/3 of the channel width) represents the outer bank region, including any eroded floodplain (0 < y < 0.15 m) and side slope. Zone B extends from y = 0.28 m to the toe of the side slope along the inner bank (y = 0.68 m).

In Zone A, the highest τ_{uv} and *tke* frequencies remain clustered near zero values of τ_{uv} and *tke* for a range of bed level changes, and little trend with scour is apparent. These results

are inconsistent with the apparent correspondence between contour plots of τ_{uv} and *tke* (Figure 5.3.2 and Figure 5.3.3) and ΔZ (Figure 5.2.3, Jamieson *et al.*, *Submitted* – a; Chapter 5.2). On the other hand, despite the presence of outliers, a negative linear trend is apparent for both τ_{uv} and *tke* in Zone B (with these R^2 values being significantly different). Further away from the barb influence, the patterns of joint probability for τ_{uv} and *tke* begin to resemble TR3 and TR10.

A positive linear trend for vorticity magnitude is apparent for both Zones A and B, although the R^2 value is insignificant in Zone A. Frequency magnitudes are less concentrated near ΔZ = 0 in Zone B than Zone A, suggesting a slightly stronger relationship between decreased vorticity magnitude and scour in the mid-channel region, which contains the barb tips. In Zone B, negative z-vorticity (R^2 = 0.059) and τ_{uv} (R^2 = 0.134) were more correlated to scour than *tke* (R^2 = 0.037) and vorticity magnitude (R^2 = 0.019), with all these R^2 value pairs being significantly different, with the one exception of vorticity magnitude and z-vorticity). Scour in Zone B is assumed to be indicative of the local scour generated at the barb tips and would most likely be associated with horseshoe vortices generated at the tip. A similar trend (of high R^2 for z-vorticity) is also present in Zone A, although, compared to Zone B, R^2 is less, the joint distribution is slightly less continuous, and the trend line is less steep. Still, R^2 is higher for z-vorticity (R^2 = 0.049) than all other variables (including τ_{uv}) in Zone A. Indeed, in Zone A, only the regression coefficient for z-vorticity was significantly different from all other variables (e.g. all other pair combinations without z-vorticity were not significantly different). This suggests that z-vorticity is the primary indicator of barb scour, even in the region between the barbs where overtopping flow would contribute to horizontal vorticity.

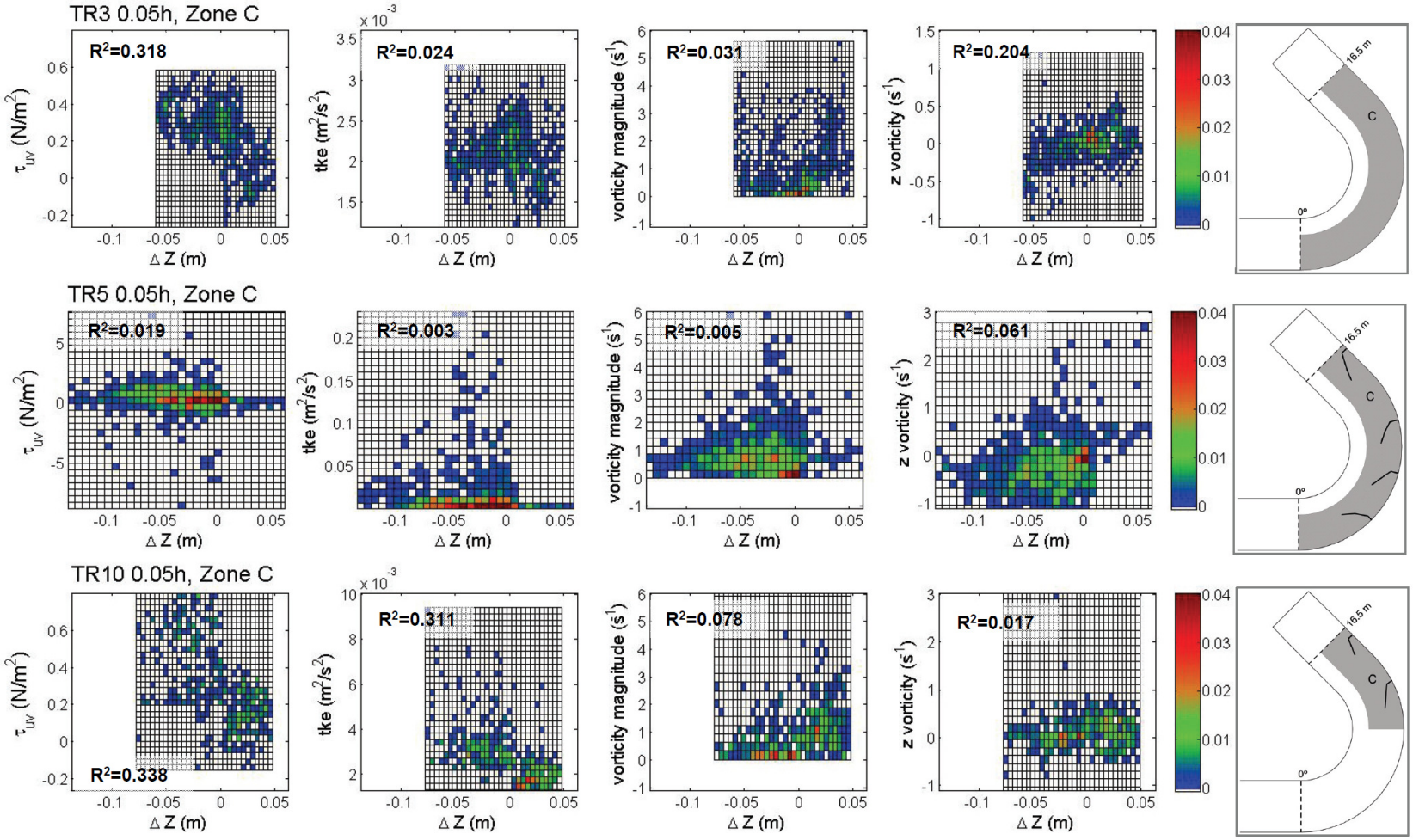

Figure 5.3.7. Bivariate intensity plots of the joint probability density for τ_{uv}, *tke*, vorticity magnitude and z-vorticity with ΔZ, for TR3 (top), TR5 (middle) and TR10 (bottom) at 0.05*h* for Zone C. Note the different scale along the y-axis for τ_{uv}, *tke* and z-vorticity. Frequencies have been normalized by the total population of each zone, such that the-cumulative joint distribution equals 1 for each plot.

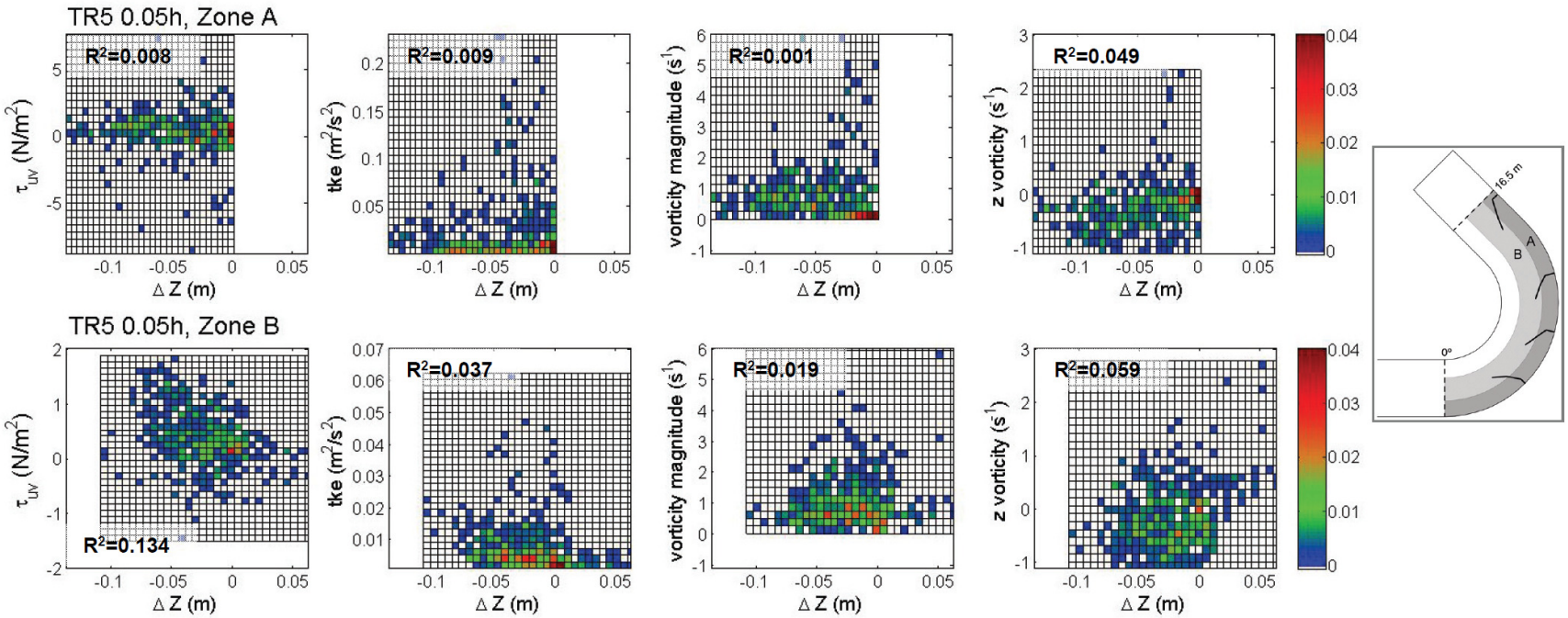

Figure 5.3.8. Bivariate intensity plots of the joint probability density for τ_{uv}, *tke*, vorticity magnitude and z-vorticity with ΔZ, for TR5 Zone A (top) and Zone B (bottom) at 0.05*h*. Note the different scale along the y-axis for τ_{uv} and *tke*. Frequencies have been normalized by the total population of each Zone.

The near-bed streamwise-cross-stream Reynolds stress (τ_{uv}) was found to be most associated with scour in bend flows without barbs and with small barbs. This is consistent with previous findings in bend flows (Jamieson *et al.* 2010), and is reasonable given that near-bed τ_{uv} represents the cross-stream stress of the fluid on the bed. In bend flows with developed secondary circulation, the cross-stream stress causes transfer of sediment from the outer bend toward the inner bend, which scours the pool and builds the point bar (Dietrich and Whiting 1989).

However, it appears that in the case of large barbs (experiment TR5), z-vorticity also contributes to scour. Vorticity in this case was calculated from the mean flow field, thus vorticity is indicative of spatial velocity gradients in the mean flow. The gradients for z-vorticity are for angular velocities around a vertical axis, i.e., cross-stream velocity in the streamwise direction ($\frac{\partial v}{\partial x}$) and streamwise velocity in the cross-stream direction ($\frac{\partial u}{\partial y}$). As flow convectively accelerates around the tip of large barbs, these gradients are large (compare run TR5 to the other runs in Figure 5.2.6 and Figure 5.2.8 of Jamieson *et al. Submitted - a*), resulting in large negative values of z-vorticity at and between the barb tips (Figure 5.3.6). Large negative z-vorticity values are consistent with clockwise fluid rotation (looking towards the bed), as flow accelerated around the right-bank barbs. Large velocity gradients that contribute to vorticity result in rotation of the fluid, as opposed to Reynolds stresses which represent strain of the fluid. The fluid rotation represented by vorticity results in near-bed velocity gradients that induce high local bed stresses, and we suggest that these bed stresses were important for scour. While Reynolds stresses also increased in the vicinity of the barbs in TR5 (Figure 5.3.2) including in locations of deep scour (cf Figure 5.2.3 of Jamieson *et al. Submitted - a*), negative z-vorticity was more uniformly increased at and

between barb tips where scour was observed (Figure 5.3.6). It is worth noting that τ_{uv} is generated both due to helical bend flow and acceleration around barbs, whereas the rotational flow represented by z-vorticity is mostly generated due to the presence of the barbs (compare run TR5 (run with barbs) with runs TR1 and TR3 (runs without barbs) in Figure 5.3.6). For these reasons, z-vorticity appears to serve as a useful indicator of scour due to the barbs.

5.3.6 Conclusions

Experimental results of the spatial variability of turbulence and vorticity through a mobile channel bend with and without submerged barbs have been presented. Contour plots of the 3-D Reynolds stresses, turbulent kinetic energy, turbulent time and length scales and vorticity described how these variables develop through a meander bend and how they are altered (both amplified and reduced) by the presence of submerged barbs. Further analysis using joint probability density plots quantified the frequency of correspondence (if any) between some of these flow variables and changes in bed levels, while differentiating between erosion of the floodplain and local scour at the barb tips.

Secondary velocities in the bend increase due to the addition of barbs, most notably through changes in vertical velocity due to plunging flow (Jamieson *et al.*, *Submitted* – a; Chapter 5.2), and likely play a role in distributing and magnifying turbulence near the outer bank. While the role of stream barbs is to redirect high streamwise velocity away from the bank, excessive redirection of the flow may actually have a negative impact on bank protection. Therefore, the size and number of barbs is important: barbs should not completely disrupt the general patterns of turbulence (and secondary velocities) naturally occurring due to the bend geometry, as this will cause higher RS, *tke* and z-vorticity along the outer bank

between barbs, leading to increased erosion of the bank. Turbulence generation between barbs may be reduced by reducing barb size, while barbs should be made large enough to weaken the helical flow near the outer bank and concentrate the barb-generated turbulence and vorticity near the barb tips and away from the outer bank. While the addition of barbs in a meander bend will increase turbulence magnitude, turbulence length and time scales are reduced and smaller turbulent and vortical motions are concentrated in the vicinity of the barbs.

Correlations between turbulent flow properties and bed level changes were generally weak, which limits the predictive capability of the observed relations. However, correlations were significant and calculated regressions for the various variables were significantly different from each other, thus the observed correlations provide a useful means to assess the relative importance of various turbulent flow properties for scour and deposition. Negative z-vorticity is the best indicator for bed level change compared to RS, *tke* and vorticity magnitude when large barbs are present. However, for small or no barbs, secondary RS, τ_{uv}, showed the greatest correspondence with bed level change over other variables. High positive τ_{uv} was observed on the right bank of the straight channel, and this was amplified in the channel bend where outer bank scour was observed (with or without barbs) and in the vicinity of the barbs, when these were present. High negative z-vorticity was also observed near the toe of the right bank slope in the straight channel, but this was diminished in the bend and magnified in vicinity of the barbs (Figure 5.3.6). It appears then that scour was most likely due to the combined effect of positive τ_{uv} and negative z-vorticity, with bend scour dominated by high positive τ_{uv} and barb scour dominated by high negative z-vorticity.

5.4 Vorticity, turbulence and scour: Measurements from a laboratory channel bend with stream barbs (submerged groynes)

Jamieson, E.C., Rennie, C.D. and Townsend, R.D. (2011b). Vorticity, turbulence and scour: Measurements from a laboratory channel bend with stream barbs (submerged groynes). *Proceedings of the 34th Congress of IAHR*, Brisbane, Australia, June 2011.

5.4.1 Abstract

Detailed measurements of the unique 3-D patterns of velocity, turbulence and bed morphology associated with flow in a channel bend with a series of stream barbs (upstream-pointing submerged groynes) have been carried out in a mobile-bed laboratory channel. The submerged nature of these structures creates a unique combination of flow separation at the barb tips and overtopping (plunging) flow conditions, causing 3-D eddies of various scales to form. Quantifying the influence of this highly 3-D and complex flow field on a mobile sand bed provides new and valuable data for understanding the impact and performance of these structures. Densely-spaced velocity data collected in the vicinity of the barbs indicate a correspondence between the calculated vorticity field, turbulent stresses and the location of coherent structures with the scour holes at the barb tip. These results provide new insight into possible connections between vorticity, coherent structures, turbulence and local scour phenomena.

5.4.2 Introduction

A relatively new approach to sustainable stream bank protection is the stream barb, a submerged variation of a groyne, similar to spur dikes and bendway weirs. Barbs are low-profile linear rock structures, typically anchored, in series, to the outside bank in stream

bends and extend in an upstream direction away from the bank into the flow (USDA, 2005). This configuration redirects high streamwise velocity away from the outer stream bank, thereby reducing outer bank erosion and promoting the development of local scour at barb tips. Moreover, with time, barbs cause the thalweg in a channel bend to relocate away from the outside bank region (an undesirable and unstable location) to a new more stable location closer to the channel centerline.

By definition, stream barbs slope away from the bank along the bed, with their highest elevation nearest to the bank at bankfull water level. This type of arrangement means that at high flows (at or near bankfull) the structure is continuously overtopped, resulting in plunging weir-type flow over the structure. Unlike typical groyne structures, which are traditionally emergent (i.e. no regular overtopping) and perpendicular to the flow, the vertical separation of the flow is less significant for barbs because they are submerged and orientated in a more streamline direction (i.e. not perpendicular to the main streamwise flow direction). If a structure (or object) obstructs a high Reynolds number flow, due to the significant velocity gradient created and the corresponding low pressure, the boundary layer developed against the object will separate from the wall. The separated flow will generate a downstream shear layer with the main flow and vertically-orientated vortical structures may develop (i.e. rotation about the vertical axis or z-vorticity). Conversely, the plunging of the flow causes regions of high velocity above the barbs and low velocity between the barbs. This velocity gradient can induce a cross-stream (transverse) vortex (i.e. rotation about the horizontal axis or y-vorticity). The numerical results of Minor *et al.* (2007a) revealed that the location of maximum vorticity magnitude (and in particular z-vorticity) corresponded with the location of maximum scour, which was found at the barb tips installed in series in a channel bend. However, the simulated results were never validated with velocity data.

The most recent and relevant experimental studies lack the density of data (Bhuiyan *et al.*, 2010) or barb arrangement (Fox *et al.*, 2005; Kuhnle *et al.*, 2008) to adequately describe the spatial variability of the complex turbulent flow field for a series of submerged structures in a channel bend, where the use of these structures is most common. As well, previous studies on submerged structures have all been performed in flumes having rigid, vertical walls, where the influence of a sloping, erodible outer bank could not be evaluated. Previous experiments (Jamieson *et al.*, *Submitted – a*; Chapter 5.2) found that the side slope region immediately downstream of the barb was particularly susceptible to scour, sometimes leading to structure failure. This is a problem not seen in previous experiments. In our study, a trapezoidal-shaped channel formed entirely of sand at the bottom of a standard rectangular-shaped flume was used, where both the bed and banks of the trapezoid channel were subject to scour.

The goal of this study is confirm the numerical modeling results of Minor *et al.* (2007a) and investigate the role of the unique three-dimensional flow field, turbulence and vorticity on the development of local scour. This research provides comprehensive quantitative measurements of the 3-D flow field in the vicinity of a submerged barb in a channel bend. Understanding the flow in detail (i.e. the scale and structure of the vortical and turbulent motions) should advance our understanding of the role of these coupled processes. These results have implications for improving our understanding and prediction of local scour associated with barbs and other similarly submerged in-stream structures and for understanding natural fluvial features where similar plunging flow conditions (or horizontal flow separation) are found; such as, forced riffle-pools and dune fields.

5.4.3 Experimental Methods

Laboratory experiments were carried out using a large 135º bend flume, which has a constant radius of curvature of 1.5 m (at the channel centerline) (Figure 5.4.1 A). The flume is 1.0 m wide with 0.9 m high vertical plexiglass walls, which contain a trapezoid cross-sectional channel built entirely of sand (Figure 5.4.1 B). The sand has a mean diameter (d_{50}) of 1.1 mm with a range of particle diameters between 0.6 and 1.8 mm. The dimensions of the trapezoid channel are provided in Figure 5.1.1 B.

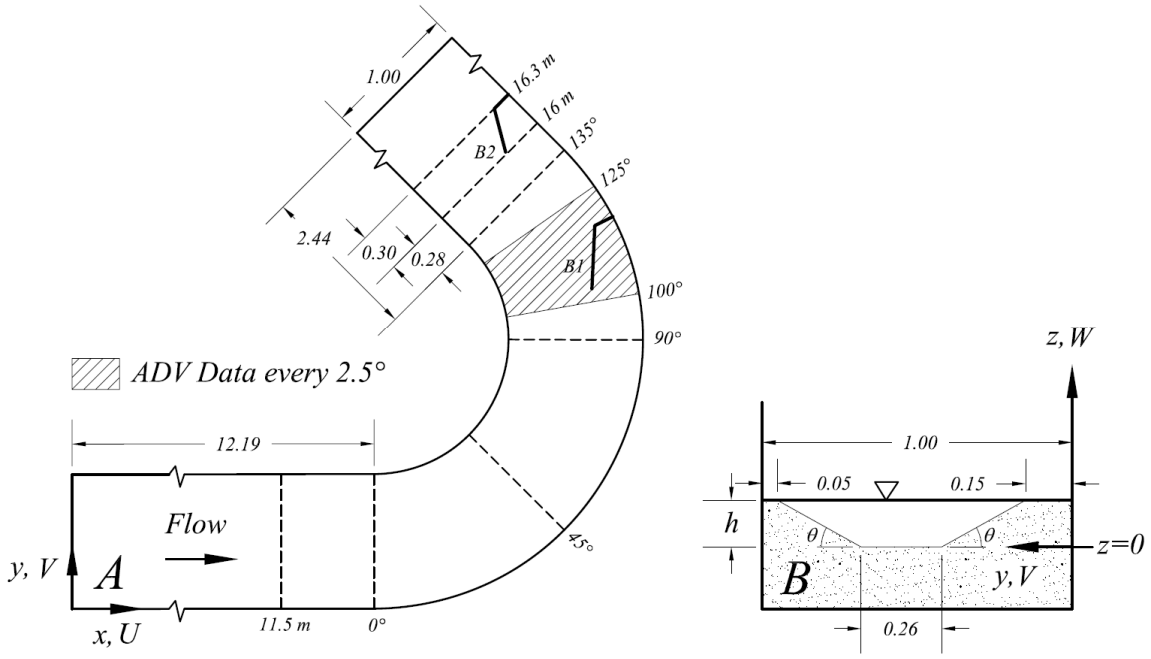

Figure 5.4.1. (A) Plan view of channel bend, barb layout and ADV measurement region for TR10. (B) Cross-sectional view of trapezoid dimensions looking downstream. $\Theta = 29º$ is the side slope angle, and all other dimensions are in meters.

A summary of the experimental conditions and parameters for each run is provided in Table 1. The experimental runs are labeled TR3 and TR10, where TR3 represents the base case conditions (i.e. no barbs) and TR10 the optimum barb arrangement from previous experiments (Jamieson *et al.*, *Submitted – a*; Chapter 5.2) Each experiment began with a

constant bed slope (S = 0.0007), uniform flow and a horizontal cross-stream bed slope (along the base of the trapezoid section), and conducted under clear water scour conditions, near the threshold of particle motion in the straight approach section. Therefore, scour and deposition in the bend was due to the presence of the bend alone (TR3) or a combination of the bend and the presence of barb structures (TR10).

Table 5.4.1. Summary of experimental runs. Q is flow rate, H is flume-averaged flow depth, U ($=Q/A$) is flume-averaged velocity (where cross-sectional area = A), $\overline{U_*}$ and τ_o are mean shear velocity and bed shear stress in the approach section (data from cross-section 11.5 m).

Run Title	Barbs?	Q (m^3/s)	H (m)	U (m/s)	$\overline{U_*}$ (m/s)	τ_o (N/m^2)	Duration (hours)
TR3	No	0.021	0.148	0.267	0.020	0.424	391
TR10	Yes (2)	0.020	0.153	0.255	0.021	0.420	386

Instantaneous velocity measurements in the streamwise (u), cross-stream (v) and vertical (w) direction were made using three Nortek Vectrino (four-beam) ADVs (two down-facing probes and one side-facing) at 13 different cross-sections through the bend (11.5m, 0º, 15º, 30º, 45º, 60º, 75º, 90º, 105º, 120º, 135º, 16m, 16.3m) in both TR3 and TR10. Data were also collected in the vicinity of Barb 1 (B1, Figure 5.4.1) in TR10, including 9 additional cross-sections every 2.5º from 100º to 125º inclusive (Figure 5.4.2 D). Typically, each cross-section consisted of 10 – 12 evenly spaced vertical profiles, with measurements in the vertical direction at intervals of 5 mm near the bed, 10 or 20 mm in the middle half of the flow depth and 30 or 40 mm closer to the water surface (unless side-facing ADV data were obtained, then data were typically 10 or 20 mm apart near the water surface). The raw times series data were processed and filtered using Matlab code (following the same procedure

outlined in Jamieson *et al.*, 2010 (Chapter 5.1)) and then used to calculate time-averaged velocities ($\overline{U}$, $\overline{V}$ and $\overline{W}$) and fluctuating turbulent velocities (*u*', *v*' and *w*'). Fluctuating velocities were combined to evaluate the three Reynolds shear stress components (τ_{uw}, τ_{uv} and τ_{vw}) and average turbulent kinetic energy (*tke*) such that

$$\tau_{uw} = -\rho\overline{u'w'};\ \tau_{uv} = -\rho\overline{u'v'};\ \ \tau_{vw} = -\rho\overline{v'w'} \tag{5.4.1}$$

$$tke = \frac{1}{2}\left(\overline{u'^2} + \overline{v'^2} + \overline{w'^2}\right) \tag{5.4.2}$$

where ρ is the density of water and $\overline{u'w'}$, $\overline{u'v'}$ and $\overline{v'w'}$, and $\overline{u'^2}$, $\overline{v'^2}$ and $\overline{w'^2}$ represent the mean of the product and square of the fluctuating turbulent velocities respectively.

The elevation of the sand bed was measured at the end of each run using a Leica systems Disto pro4a laser altimeter, which provides a precision of ± 1 mm. Bed level measurements were taken every 0.01 m in the cross-sectional direction and at 2.5º intervals through the bend and every 0.10 m in the straight sections, with the exception of TR10, where the cross-sectional interval in the vicinity of the barbs was 1º (Figure 5.4.2 B). Kriging was used to interpolate the bed level measurements into a 2-D contoured surface (Figure 5.4.2). Grid spacing of the interpolated surface was 0.05 x 0.05 m for the entire bend (TR3 and TR10) and 0.01 x 0.01 m in the vicinity of B1 and B2 (TR10) (Figure 5.4.2 B).

To assess the spatial variation of mean velocities, a 3-D volume grid was generated from each 2-D surface grid. However, due to space limitations, only select velocity data from TR10 (ADV data near B1, see Figure 5.4.2 D) are presented here. In this grid, nodes were every 1º in the streamwise direction, every 0.025 m in the cross-stream direction, and included 10 cells in the vertical between the bottom elevation and the water surface. ADV data were interpolated into the 3-D volume using a kriging technique that has been successfully applied in other 3-D flow analyses (Jamieson *et al.*, 2011a; Chapter 4.2).

Coherent structures may be identified by the presence of vortices, which exhibit correlated velocity components in both space and time. The interpolated volume of 3-D velocities may be combined to extract vortex cores by determining spatial correlations (if any) in velocity gradients. Two criteria were used for identifying the presence of vortices:

- λ_2*-criterion* (Jeong and Hussain, 1995): $\lambda_2\left(\boldsymbol{S}^2+\boldsymbol{\Omega}^2\right)<0$ (5.4.3)
- $|\omega|$*–criterion*: the region of absolute vorticity magnitude ($|\omega|$) is greater than a certain threshold

where $\boldsymbol{S}=\frac{1}{2}\left[\nabla \upsilon+(\nabla \upsilon)^T\right]$ is the rate-of-strain tensor, $\boldsymbol{\Omega}=\frac{1}{2}\left[\nabla \upsilon-(\nabla \upsilon)^T\right]$ is the vorticity tensor, $\nabla \upsilon$ is the velocity gradient, and $\lambda_2(\mathrm{A})$ denotes the intermediate eigenvalue of a symmetric tensor (A). Vorticity magnitude (ω) is defined as the vector sum of the three components of rotation (ω_x, ω_y and ω_z) about the *x*, *y* and *z*-axis respectively. The rotation about each axis is defined as the average of the angular velocities perpendicular to the axis of rotation, such that

$$\omega_x=\frac{1}{2}\left(\frac{\partial w}{\partial y}-\frac{\partial v}{\partial z}\right);\quad \omega_y=\frac{1}{2}\left(\frac{\partial u}{\partial z}-\frac{\partial w}{\partial x}\right);\quad \omega_z=\frac{1}{2}\left(\frac{\partial v}{\partial x}-\frac{\partial u}{\partial y}\right) \tag{5.4.4}$$

where $\partial v/\partial x$ and $\partial w/\partial x$ are angular velocities along the x-axis, $\partial u/\partial y$ and $\partial w/\partial y$ are angular velocities along the y-axis, and $\partial u/\partial z$ and $\partial v/\partial z$ are angular velocities along the z-axis (assuming counter-clockwise rotation is positive).

Barbs were constructed by hand using small, angular stone, with average sizes of 0.043 m in length and 0.025 m in thickness. Barbs in TR10 were 0.40 m long, positioned at an angle of 30º (with respect to the upstream bank) and built flush in height with the original trapezoid side slope. The barb crest width was approximately 4 cm (or 1 rock width). Barb layout was determined by placing the first barb in the location of maximum erosion from

TR3, which was near the bend exit, at cross-section 16.3 m. The second barb was then added in the upstream direction with a spacing determined by the length and angle of the preceding, downstream barb. A plan view of the barb layout in TR10 is provided in Figure 5.4.1, where for simplicity only the barb crests have been delineated with a black line to show barb location and geometry. The true barb extents for B1 are shown in Figure 5.4.2 C.

5.4.4 Results and Discussion

The addition of barbs in TR10 successfully protected the outer bank floodplain (orange contours, Figure 5.4.2) compared to the base case (no barbs) run (TR3). Local scouring in the vicinity of each barb (Figure 5.4.2 B and C) did cause some floodplain loss, with the severest erosion occurring immediately downstream of the first barb (B1, Figure 5.4.2 C). Previous experiments with various barb layouts (Jamieson *et al.*, *Submitted – a*; Chapter 5.2) all found that the floodplain was particularly susceptible to erosion immediately downstream of the barbs. The detailed contours near B1 (Figure 5.4.2 C) also show the development of a scour hole at the barb tip, with the zone of maximum depth (Z = -0.02) immediately downstream of the tip.

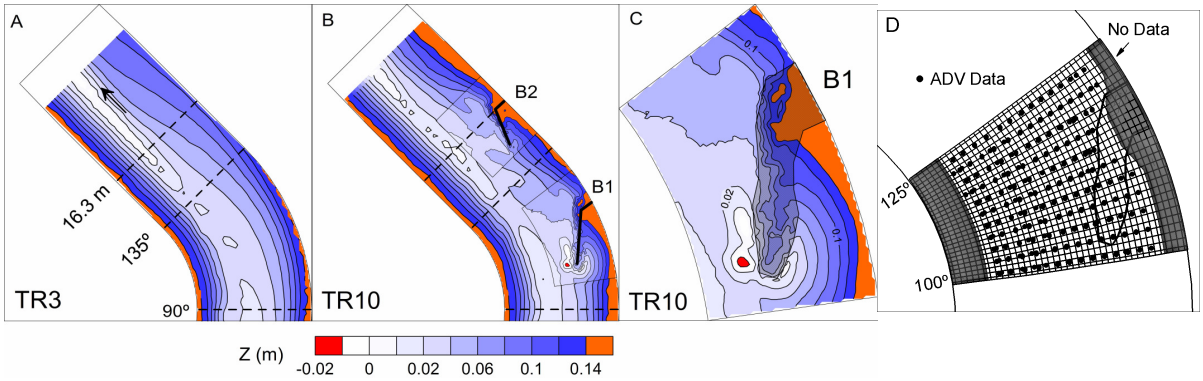

Figure 5.4.2. Contour plots of equilibrium bathymetry for each run (A and B), with a close up of TR10 at B1 (C). Barb crests are identified by the solid black lines (B), while the true barb extent for B1 is shown in C and D. The B1 flow domain and location of dense ADV data is shown in D.

Contours of the interpolated time-averaged velocities ($\overline{U}$, $\overline{V}$ and $\overline{W}$) for individual cross-sectional slices (numbered 1-3) through the B1 flow domain (Figure 5.4.2 D) are presented in Figure 5.4.3. These plots clearly illustrate: (1) the redirection of the $\overline{U}$ velocity core away from the outer bank as it passes the barb; (2) the concentration of helical flow in the center of the channel, away from the outer bank; (3) the extreme magnitude and opposite direction (to typical helical flow) of secondary velocities downstream of the barb, along the outer bank (slice 3, Figure 5.4.3). The strong plunging flow ($\overline{W} < 0$) along the downstream face of the barb is clearly illustrated in slice 2 (Figure 5.4.3). Upstream of the barb (slice 1), streamwise velocity was lowest, particularly near the outer bank and over the barb tip scour hole. Downstream (slice 3), the velocity increases, but remains lowest near the outer bank.

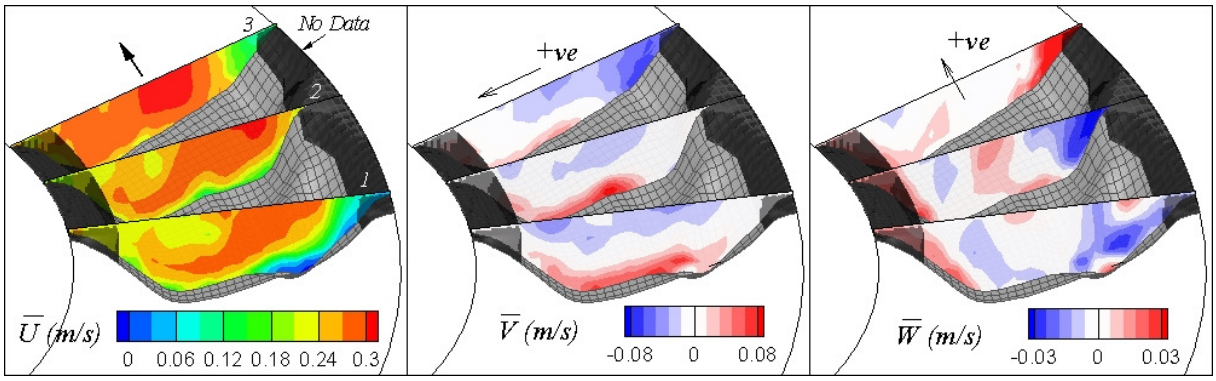

Figure 5.4.3. Contour slices of time-averaged velocities $\overline{U}$, $\overline{V}$ and $\overline{W}$ in the vicinity of B1 in TR10. See Figure 5.4.4 - 2a for location of slices. Positive $\overline{V}$ is towards the inner (left) bank and positive $\overline{W}$ towards the water surface. Vertical dimension is scaled 2:1 with the horizontal.

Contours of vorticity magnitude, z-vorticity and y-vorticity are provided in Figure 5.4.4, for both cross-sectional and plan view slices. Near the bed (Figure 5.4.4 - 1), and at 10% of the flow depth (or 0.10*h*) (Figure 5.4.4 - 2), all components of vorticity peaked at the barb tip, and downstream of the barb towards the center of the channel. As well, near bed y-vorticity was more than double z-vorticity. The similarity in contour patterns (in particular the shapes and location of maximum contour values) between vorticity magnitude and y-vorticity (Figure 5.4.4 - 2a and Figure 5.4.4 - 2c respectively), suggests the latter contributes most to vorticity magnitude (compared to z-vorticity).

Maximum negative z-vorticity was closely associated with the pattern of local scour at the barb tip and along the downstream barb edge (Figure 5.4.2 C), while scour immediately upstream of the barb tip corresponds with highly positive y-vorticity. Positive y-vorticity indicates rotation about the horizontal y-axis (which is positive towards the inner bank and

positive rotation assigned following the right hand rule) and likely illustrates the pattern of downflow upstream of the barb tip (Figure 5.4.4 - 2c), similar to the downflow common to bridge piers and abutments. The line of neighbouring negative and positive z-vorticity regions leading downstream from the barb tip (Figure 5.4.4 - 2b) likely illustrates the cast-off vorticies (also associated with flow past a pier or abutment). These two y- and z-vorticity patterns were not seen higher in the flow depth (Figure 5.4.4 - 3b and 3c) because the crest of the barb was submerged and close to the bed. All components of vorticity weaken away from the bed (Figure 5.4.4 - 1 and 3), yet remain highest along the outer bank, where side slope was steepest and flow was still influenced by the barb, since the barb height was sloping up to meet the bank. This pattern likely contributes to greater side slope erosion, particularly immediately downstream of the barb, where vorticity peaks (Figure 5.4.4 - 3) and floodplain loss was greatest (Figure 5.4.2 C).

Both the region of maximum vorticity magnitude and positive y-vorticity downstream of the barb were shaped in a pattern similar to the shape of the barb (linear, with an angle ~ 30º with respect to the outer bank). Positive y-vorticity here likely describes the plunging action of the flow immediately downstream of the structure, which was weakest near the tip and strongest along the center of the barb. Interestingly, this pattern of maximum y-vorticity (and vorticity magnitude), was not associated with the scour hole (Figure 5.4.2 C). Indeed, there has been erosion of the outer bank side wall here, but the local scour hole dominating the barb tip area does not extend into this region, where plunging flow ($\overline{W}$, y-vorticity and vorticity magnitude) was greatest.

The two methods used to identify vortex cores both indicate the presence of coherent structures immediately upstream (and towards the outer bank) of the barb tip (Figure 5.4.4 and Figure 5.4.5). These cores were near the bed and orientated in the horizontal y-axis

direction (see dotted circle in Figure 5.4.4 - 1 and legend in Figure 5.4.4 - 2b). [Note that the λ_2 – criterion vortex cores can not be seen in Figure 5.4.4 - 1 based on the slice locations (Figure 5.4.4 - 2)]. The location of these cores corresponds to the local scour hole, but not the maximum depth (Figure 5.4.2 C). The orientation of these cores was also consistent with the dominant magnitude of y-vorticity in the same location. The lack of vertically orientated vortex cores was likely due to the low profile design of the barb tip, which would produce less vertical separation and therefore lower z-vorticity (Figure 5.4.4 - 2). Clearly, rotation of the flow about the horizontal axis (in the positive direction) was dominating the flow field.

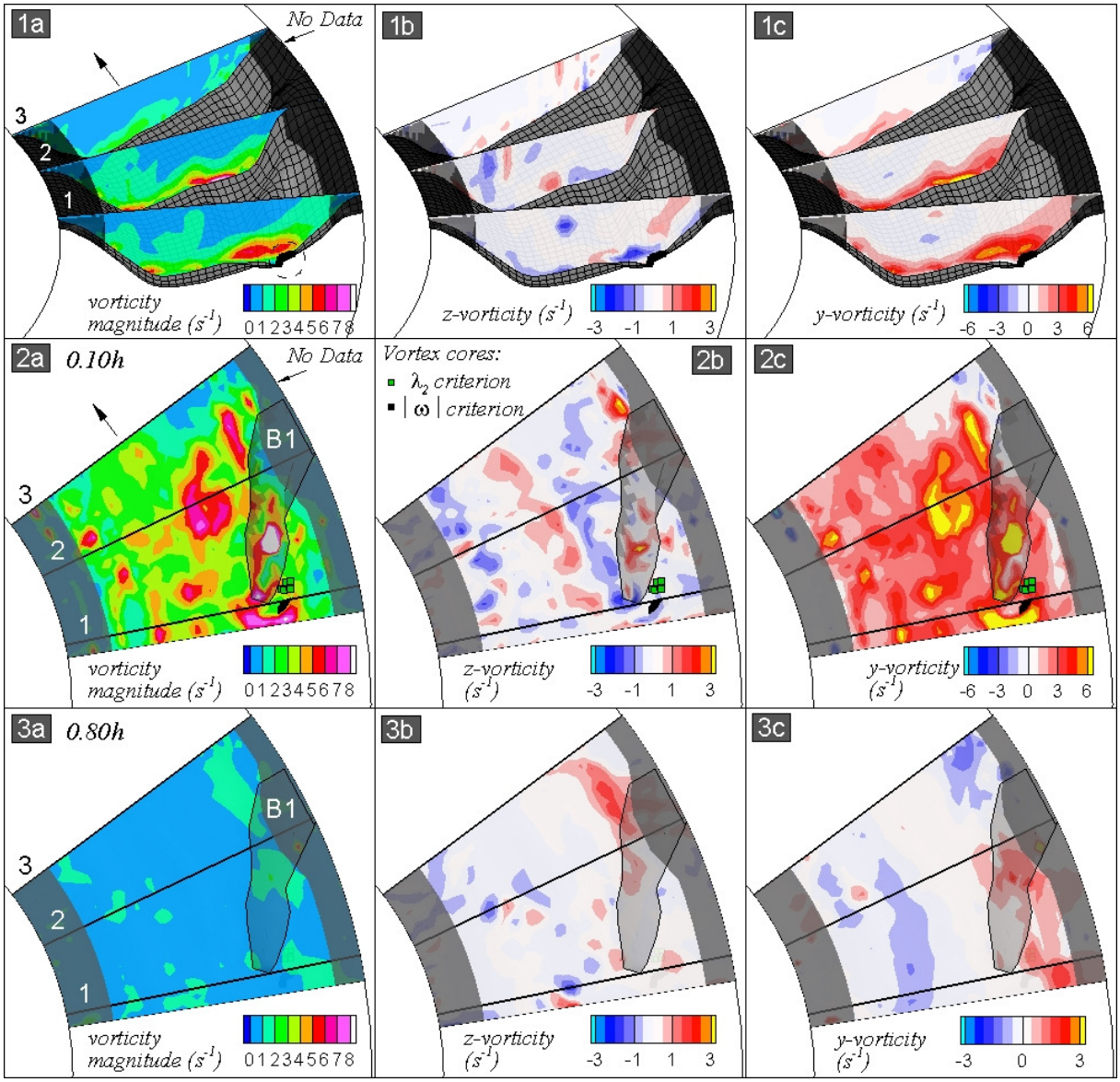

Figure 5.4.4. Contour slices of vorticity in the vicinity of B1 in TR10: Cross-sectional slices (1a-1c) and plan slices at a depth of 0.10h (2a-2c) and 0.80h (3a-3c) of vorticity magnitude (a), z-vorticity (b) and y-vorticity (c). Vertical dimension in (1) is scaled 2:1 with the horizontal. The locations of vortex cores are shown in (1) ($|\omega|$ criterion only due to slice positions) and (2).

Contours of turbulence (*tke* and the three components of Reynolds stresses) near the bed (at 0.10h) are shown in Figure 5.4.5. While principal Reynolds stress (τ_{uw}) typically

dominates in turbulent open channel flows, in this case, either due to the helical flow in the bend or the complex flow around the barb (or likely a combination of both), the magnitude of a secondary Reynolds stress, τ_{uv}, dominates (Figure 5.4.5 c). Maximum turbulence (and in particular *tke* and τ_{uv}) was found upstream of the barb and near the outer bank, corresponding with erosion of the side slope and subsequent loss of floodplain (Figure 5.4.2 C). Turbulent fluctuations were likely highest in this location because of the neighbouring steep side slopes associated with the outer bank on one side and the barb side wall or edge on the other.

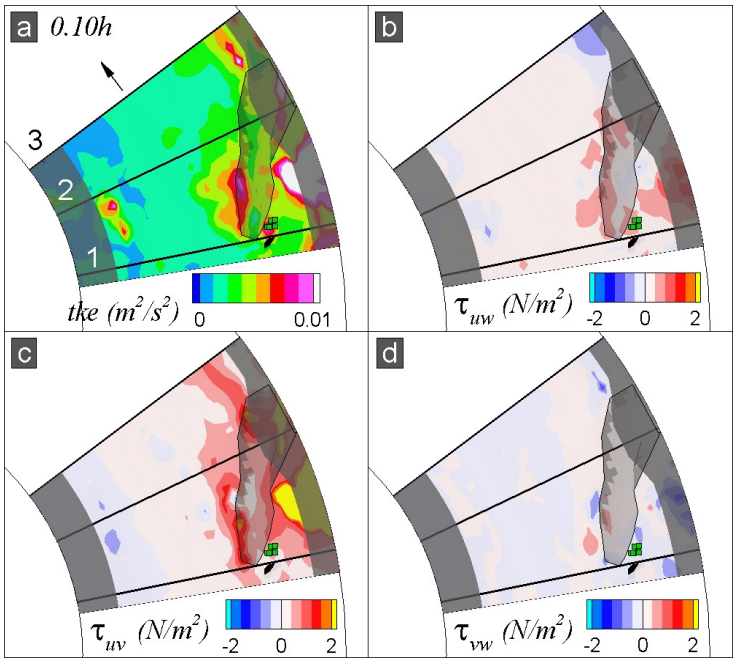

Figure 5.4.5. Contour slices of *tke* (a) and Reynolds stresses: τ_{uw} (b), τ_{uv} (c) and τ_{vw} (d) in the vicinity of B1 at a depth of 0.10h. The location of vortex cores is also shown (see Figure 5.4.4 - 2b for vortex core legend).

High turbulence (for all components) was also located along the downstream edge of the barb and near the outer bank, immediately downstream of the barb. *tke* and τ_{uv} were most

pronounced in these regions and show remarkable proximity with respect to the barb's downstream edge and slightly less with the location of the scour hole. Another region of high *tke* and this time τ_{uw} was also found at the barb tip location corresponding to the position of vortex cores. Overall, the results indicate that both consistent vortical motion and turbulent fluctuations dominate and contribute to local scour.

5.4.5 Conclusions

Densely-spaced ADV data were capable of resolving the complex, turbulent and three-dimensional nature of the time-averaged flow field around a submerged and sloping barb in a channel bend. Further analysis, including spatial interpolation and the calculation of vorticity and the presence of vortex cores, provided unique observations concerning the magnitude and direction of these features in relation to the barb and the pattern of scour. Relating these variables to the pronounced scour hole at the barb tip and erosion of the outer bank region, reveals that it is likely not one single component of the flow that is responsible. However, some specific observations are made:

- Negative z-vorticity corresponds most closely with the deepest region of the scour hole.
- Positive y-vorticity corresponds most closely with the scour hole upstream of the barb tip and with erosion of the side slope downstream of the barb.
- Maximum turbulence (*tke* and Reynolds stresses) correspond most closely with erosion of the outer bank floodplain – both upstream and downstream of the barb.
- Vortex cores, which are orientated along the horizontal axis and positioned over the upstream region of the scour hole, correspond most closely with positive y-vorticity and high *tke* and τ_{uw}.

6 Additional Results and Discussion

Additional results and analysis that were not included in Chapters 3, 4 or 5 are presented below. The additional data are primarily taken from other sources (with the exception of Sawmill Creek topography) and are still considered preliminary. For this reason, these results were not included in earlier chapters (i.e. as published or submitted manuscripts). The additional results presented here include the stream barb impact on aquatic habitat (Chapter 6.1) and the unique characteristics of a semi-alluvial, urban channel (Chapter 6.2). A discussion of the key findings from each of the studies in Chapters 4 and 5, regarding the relative importance of turbulence versus vorticity, and the experimental approach taken, is also presented (Chapter 6.3). It should be noted that the Sawmill Creek habitat data collection and anlaysis were primarly completed by City of Ottawa staff and not the author. However, the author was involved in planning the data collection protocol and communicated closely with City staff at all stages of the project.

6.1 Stream barb impact on aquatic habitat

To assess any changes to aquatic wildlife and habitat in Sawmill Creek in the vicinity of the stream barbs, a fish and fish habitat monitoring program was established by the City of Ottawa Water Environment Protection Program (WEPP) in cooperation with the Rideau Valley Conservation Authority (RVCA) and the University of Ottawa. WEPP has conducted monitoring to assess temporal and spatial fish and fish habitat conditions throughout the study area over a three-year period (2008-2010) in order to determine pre- and post-barb construction conditions of the aquatic ecosystem at the site. The purpose of the 2008 and 2009 data (prior to stream barb construction), was to provide baseline data with which to

compare post construction sampling results (2010 data and beyond). [Monitoring activities comply with regulatory requirements under the *Fisheries Act*, and these were reviewed and approved by regulatory and participating agencies and were completed following approved provincial and federal protocols and procedures (City of Ottawa, 2009a)].

The area under investigation includes the Sawmill Creek corridor between Heron Road (upstream limit) and Bank Street (downstream limit), including the road crossings, which are both culverts. This area is divided into two zones of assessment: a zone of general assessment and two zones of detailed assessment, CK18-Y and CK18-X (Figure 6.1.1). The CK18-Y zone is 97.8 metres in length and includes the barb locations within bends 1 and 2 (Figure 6.1.1). The second zone of detailed assessment (CK18-X) is 96.3 m in length and located approximately 200m downstream of the first zone (CK18-Y) and acts as a control site for assessing any post-barb construction changes in the CK18-Y zone (Figure 6.1.1). Zone boundaries were defined according to geomorphic criteria, specifically the meander sequence of the creek (City of Ottawa, 2009a). The zone of general assessment includes all areas of the Sawmill Creek corridor between Bank Street and Heron Drive that are not covered under the zone of detailed assessment.

WEPP has collected information on physical habitat, the fish community, the benthos community, water chemistry, hydrology and temperature. The results from the first two years of assessment (2008 and 2009) are now available (City of Ottawa, 2009a and 2009b).

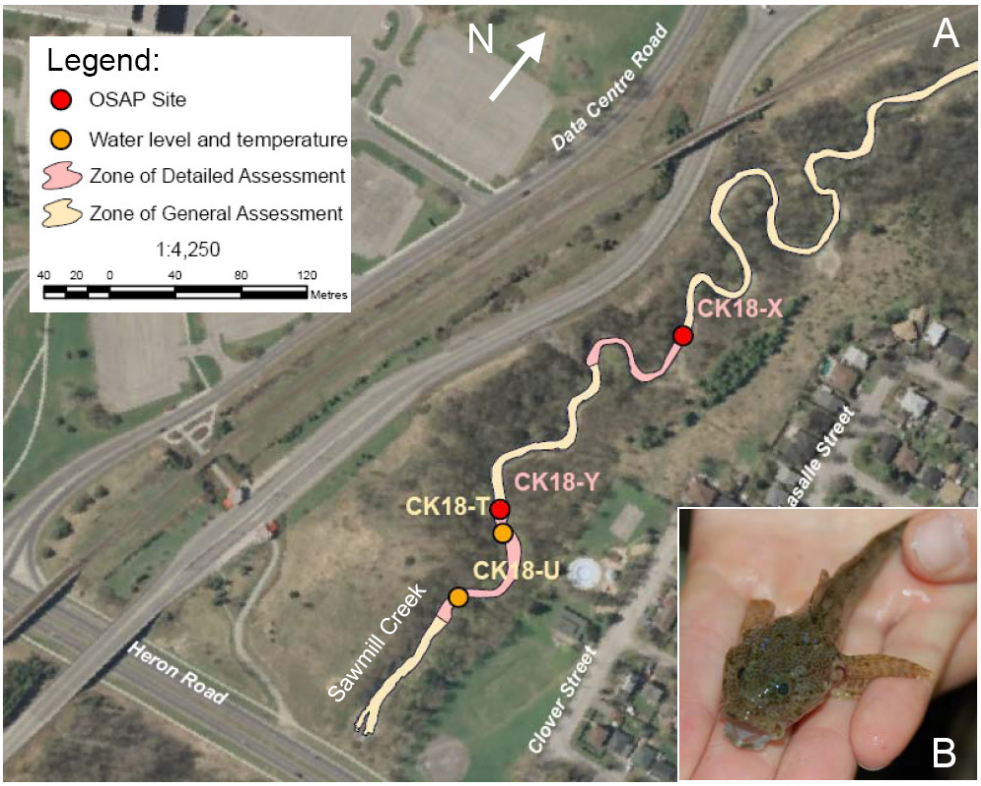

Figure 6.1.1. (A) Area of fish habitat assessment (adapted from City of Ottawa, 2009a). The area of general assessment (not shown in full) continues north to Bank Street. The area of detailed assessment for the stream barb project is CK18-Y. CK18-X is the detailed assessment control site. (B) Photo of mottled sculpin captured within CK18-Y during electrofishing in the 2009 survey season.

The 2008 sampling season was considered by WEPP to be a wet one. This made habitat and fish community assessments challenging, since the creek experienced fluctuating flows and water levels, and high turbidity for much of the sampling period. The 2009 report (2008 sampling data) concluded that another year of sampling pre-construction conditions would be beneficial, as it would account for sampling error associated with the high water and turbid conditions that were encountered in 2008. This was satisfied since the barbs were constructed during the last two weeks of September 2009, shortly following the last day of

fish and fish habitat monitoring for the 2009 season. However, data were not collected at the control site in 2009.

To assess the impact of stream barbs on the biological communities and habitat conditions, WEPP recommended that the sampling include: surface water temperature monitoring; OSAP channel morphology module for fish habitat; OSAP fish community module; OBBN benthos; surface water elevation monitoring; and water chemistry (where OSAP and OBBN stand for Ontario Stream Assessment Protocol (Stanfield, 2005) and Ontario Benthos Biomonitoring Network (Jones *et al.,* 2005), respectively). WEPP continued its assessment in the spring and summer of 2010 to monitor post-construction conditions. However, these results are not yet available.

6.1.1 Pre-barb Results (2008 and 2009 Data)

Fish captures for 2008 and 2009 are documented in Table 6.1.1. Capture rates increased for all species in 2009, which can likely be attributed to the less turbid conditions encountered on the day of sampling compared with conditions in 2008 (City of Ottawa, 2009b). Unfortunately, sampling at the control site (CK18-X) was not repeated in 2009. Species abundance and diversity indices (not shown) were higher in 2009 at the barb site (CK18-Y), reflecting the increased capture rates in 2009.

Fish captures were made using electrofishing (a common fish collection technique used in wadeable streams), which involves sending an electric current into the water from a backpack electrofishing unit, against which fish involuntarily swim. As the fish swim towards the source of the current, someone nearby collects the fish with a net. Once collected, fish are identified, counted and weighed and then returned to the creek. According to the City of Ottawa (2009a), a wet field season in 2008 made habitat and fish community

assessments challenging throughout the summer. The creek experienced fluctuating flows and water levels, and the water was very turbid for much of the sampling period. Electrofishing surveys were completed when conditions were safe, however the turbidity of the water hindered the netters ability to see fish, specifically small individuals and benthic species such as sculpin. This is of particular concern for the results at site CK18-Y, where the presence of deeper pools and cover were more prominent than at CK18-X (Table 6.1.2), and would likely explain the much lower total of fish species collected at the barb site (21) compared to the control site (71) (Table 6.1.1). In the following year (2009), species abundance at the barb site (70) was comparable with the control site data from 2008.

Table 6.1.1. Species and abundance (#/100m^2) for CK18-X and Y sampled (using electrofishing) in 2008 and 2009 following the OSAP protocol (Data from City of Ottawa, 2009a and 2009b).

Species	CK18-X (Control) 2008	CK18-Y (Barbs) 2008	CK18-Y (Barbs) 2009
White Sucker	3	1	5
Longnose Dace	57	17	39
Creek Chub	9	1	20
Brook Stickleback	-	-	2
Mottled Scuplin	2	2	4
Total	**71**	**21**	**70**

Note: Dates of sampling were July 10, 2008 (CK18-X); July 11, 2008 (CK18-Y, 2008) and September 9, 2009 (CK18-Y, 2009).

Daily mean discharge on the three sampling dates, July 10 and 11, 2008 and September 9, 2009, were taken at the stream gauging station 1.2 km downstream from the barb site, and were 0.147, 0.177 and 0.102 m^3/s respectively. These are all considered low, base flow

conditions ($Q \leq 0.2$ m^3/s). Therefore, it is unlikely that flow rate was responsible for the differences found in total species captured.

Existing fish habitat was assessed using two protocols for (1) visual assessment and habitat mapping, and (2) point transect sampling (City of Ottawa, 2009a). Only point transect sampling is discussed here as it was completed for the two zones of detailed assessment (CK18-X and CK18-Y). The point transect sampling was completed following the channel morphology module of the Ontario Stream Assessment Protocol and involves establishing transects perpendicular to the flow throughout the site and taking measurements at points along these transects. Measurements include information on depth, water velocity, cover, substrate composition and diversity, and degree of undercutting. For a complete description of the methodology that was followed, see Section 4, Module 2 – Point-Transect Sampling for Channel Structure, Substrate and Bank Conditions – of the Ontario Stream Assessment Protocol (Stanfield, 2005).

The results of the point transect habitat assessment in the zone of detailed assessment for the stream barb project in 2008 (2009) reveal a total habitat area of 563 m^2 (590 m^2) consisting of 63% (72%) pool habitat type, 22% (13%) glide habitat type, 13% (13%) riffle habitat type, and 2% (2%) islands. Cover is available for fish in approximately 26% (36%) of the stream barb site, consisting of wood, flat rock, round rock, and macrophytes. There was a slight increase in cover of 10% between the two years.

The results of the point transect habitat assessment in the zone of detailed assessment for the control site reveal a total habitat area of 322 m^2, consisting of 40% pool habitat type, 25% glide habitat type, 33% riffle habitat type, and 2% islands. Cover is available for fish in approximately 11% of the control site, consisting of flat rock, round rock, and macrophytes. Results in Table 6.1.2 indicate that even before the addition of barbs, there was more overall

habitat (and in particular pool habitat) and more total cover at the barb site over the control site.

Table 6.1.2. Point transect habitat assessment results for CK18-X and Y. (Select data from City of Ottawa, 2009a and 2009b).

Site	CK18-X (Control) 2008	CK18-Y (Barbs) 2008	CK18-Y (Barbs) 2009
Total Habitat Area (m^2)	**322**	**563**	**590**
Total Habitat Type (%)			
Pools	40	63	72
Glides	25	22	13
Slow Riffles	13	8	8
Fast Riffles	20	5	5
Islands	2	2	2
Cover Type Distribution (%)			
Wood	0	5	7
Flat Rock	3	10	19
Round Rock	3	8	10
Macrophyte	5	3	0
Bank	0	0	0
Total Cover (%)	**11**	**26**	**36**

The results of the fish community sampling (Table 6.1.1) show that a high variability in species abundance may be expected from year to year (or from day to day). A more complete picture would be provided if sampling were carried out on multiple days throughout the summer, to capture the variability within a season (and possibly from day to day). This would provide a better estimate of the average abundance for each year, for comparison with

the next, and take into account any seasonal (or daily) variations due to weather (e.g. increased rainfall, changes in turbidity). Therefore, even with similar data (i.e. 1 sample day at comparable low flow conditions) from the 2010 (post-barb construction) season, it would be difficult to estimate the significance of these results, given the possibility for variability from day to day and season to season. On the other hand, the habitat assessment may provide a better means of assessing aquatic improvement at the site due to the addition of barbs. Provided the sites are always assessed during the same time each season (i.e. mid to late summer), then it is expected that any change in available habitat due to the barb construction could be measured and adequately compared each year.

6.2 Semi-alluvial channels

The three years of topographic surveying at Sawmill Creek (which spanned over 4 years; i.e. 2007, 2009 and 2010), found little to no change in bed and bank topography at the study site. This was despite near-record water levels in 2009 (the July 24, 2009 rain event was considered a 1:100 year rainfall in some parts of the city, Ottawa Citizen, July 30, 2009; and July 2009 the wettest month on record at the Ottawa International Airport, Environment Canada news release), the removal of large woody (and other) debris, and the construction of seven stream barbs. The lack of recorded change may be for two reasons. First, Ottawa's surficial geology is dominated by glaciomarine clays that derive from the fine material that settled in the Champlain Sea after being eroded by glaciers. These sediments are consolidated and relatively difficult to entrain given their cohesive, consolidated nature. Second, annual topographic surveys are not adequate for representing change (or morphological response) in a semi-alluvial and/or urban stream.

6.2.1 Consolidated Cohesive Soils

Deposited cohesive beds are composed of flocs and/or higher order aggregates whose properties have been moulded by the flow-induced stresses. Therefore, their erosional resistance and mechanical properties are expected to also be functions of the flow conditions (Partheniades, 2009). Conversely, consolidated cohesive soils (such as those found at Sawmill Creek) are compacted sediments, whose properties and erosional behaviour are more complex and less likely to be a function of the flow conditions.

Using samples collected from our field site and other nearby semi-alluvial streams in South Eastern Ontario, researchers at the University of Saskatchewan have conducted a

series of tests to estimate the critical boundary shear stress for these sites. The critical shear stress for natural semi-alluvial channels is still not adequately defined in the current literature and yet it is critical for sediment transport and scour predictions.

Critical shear stress values at the Sawmill Creek study site were calculated as 3.4, 24.9 and 16.0 Pa. These values are based on two sample averages using three different methods; Hanson and Cook (2004), a visual method and the Thomas method, respectively (Cossette and Mazurek, *submitted*). A summary of critical shear stress values and grain size distributions from Sawmill Creek and the other water courses tested are provided in Table 6.2.1. Compared to the other semi-alluvial streams in South Eastern Ontario, Sawmill Creek appears to have the highest critical shear stress values of all calculation methods, and therefore, demonstrates the lowest relative erobability. Between methods, there appears to be some variability in the estimate of critical shear stress, particularly in the Sawmill Creek data, where values are the highest. The Hanson and Cook (2004) procedure is considered the most widely accepted methodology at this time (Dr. Kerry Mazurek, personal communication). Therefore, it is possible that the other methods are over estimates of the critical shear stress, since the other two methods typically had higher values for all sites (Table 6.2.1).

Table 6.2.1. Summary of grain size distributions and critical shear stress (τ_c) for samples collected in South Eastern Ontario. Values represent the average result from two samples taken at each location. Data from Cossette and Mazurek (submitted).

Sample Origin	Grain Size Distribution (%)				Critical Shear Stress (Pa) [1]		
	Medium Sand (0.425 – 2 mm)	Fine Sand (75 μ – 0.425 mm)	Silt (5 μ – 75 μ)	Clay (< 5 μ)	τ_c Hanson (Pa)	τ_c visual (Pa)	τ_c Thomas (Pa)
South Nation	13	30	40	4	2.20	2.23	7.55
Wilton Creek	1	31	58	9	0.77	1.03	2.19
Little Cataraqui Creek	10	7	67	16	0.31	1.08	1.15
Sawmill Creek	7	41	39	14	3.37	24.85	15.95
Bear Brook	1	33	57	10	0.58	4.16	1.83
Jock River	5	31	63	2	3.19	2.93	6.70

[1] where $\tau_{c\ Hanson}$ is calculated following the theory outlined in Hanson and Cook (2004); $\tau_{c\ visual}$ is calculated from visual observations of the stress required for the first movement of particles on the surface; and $\tau_{c\ Thomas}$ is calculated by plotting the erosion rate vs. the shear stress on the bed and estimating from this plot where this shear stress goes to zero (more information on methods in Cossette and Mazurek (*submitted*)).

Of the samples collected, Sawmill Creek had the second highest clay content (14%), with Little Cataraqui Creek having the highest (16%) (Table 6.2.1). For consolidated cohesive soils, erodibility decreases with increasing clay content for all soil mixtures (Grissinger, 1966). However, plotting the critical shear stress with clay content for our samples (Figure 6.2.1) reveals that with the exception of the Sawmill Creek results (which appear as extreme outliers), critical shear stress decreases with increasing clay content, according to both the Hanson and Thomas methods. This suggests that the erodiability is in fact increasing with increasing clay content for these samples. The data for the visual method are more scattered and a trend is less apparent.

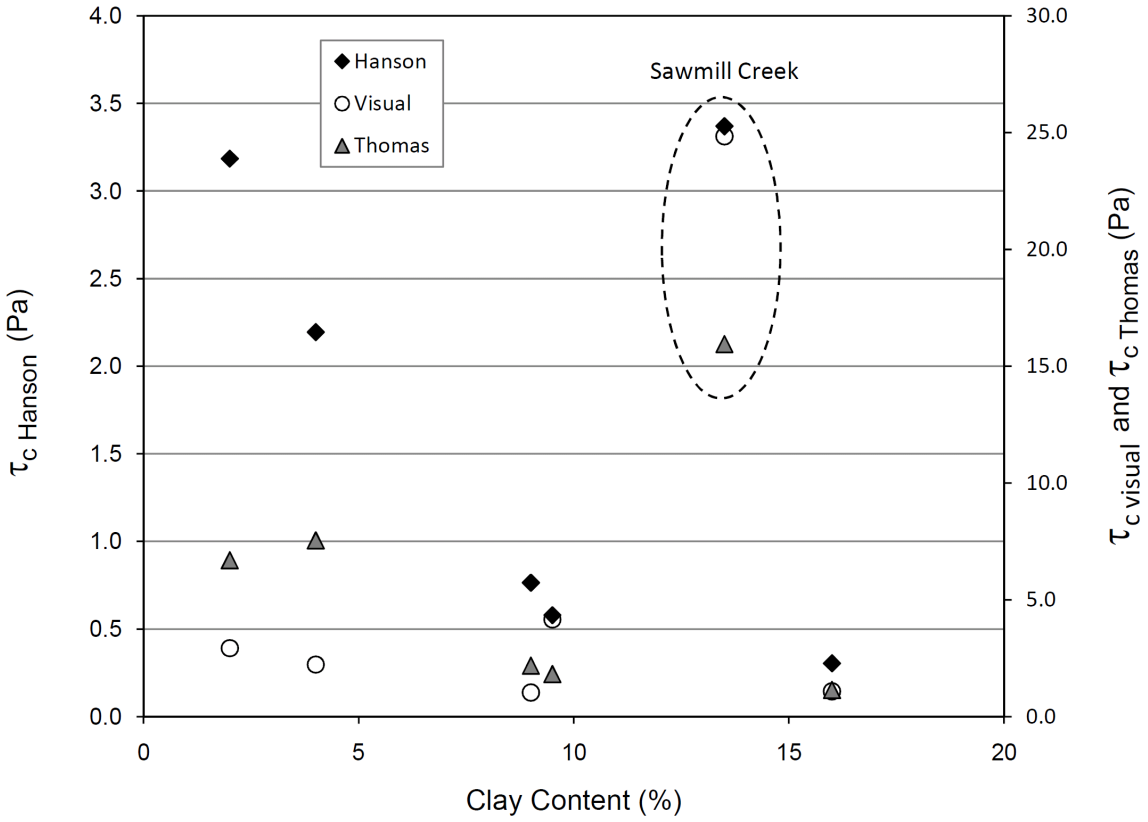

Figure 6.2.1. Comparison of critical shear stress values with clay content for samples in South Eastern Ontario (Table 6.2.1). (Note the difference in scale for the primary and secondary y-axis).

Typically, soil is not considered to behave as cohesive until it has at least approximately 10 % clay content (Raudkivi, 1998). It may be that some of our samples are not cohesive due to their relatively low clay content. For example, four of the six samples had ≤ 10 % clay content. As well, some samples contained vegetation, which may affect the results. These samples may appear to behave as cohesive due to the presence of vegetation (Dr. Mazurek, personal communication).

In the Sawmill Creek SSIIM model (Chapter 3.1), a Shield's coefficient (τ^*) is specified in the model and is used for defining the critical shear stress for particle transport. This value

was set at 0.055 on the basis of establishing minimal sediment transport in the reference run (i.e. no barbs). Therefore, when barbs were added, any change in flow and morphology were considered due to the barb layout, geometry and orientation alone. This approach was taken for establishing the optimum barb design since no estimate of the actual critical shear stress at the site was available at the time of modelling. Based on a critical Shields coefficient of 0.055 and values used in the numerical model for water and sediment properties, an estimate of the critical shear stress (τ_c) used in the modelling can be made using the equation for the critical Shield's coefficient (τ_c^*)

$$\tau_c^* = \frac{\tau_c}{g(\rho_s - \rho)D} \tag{6.2.1}$$

where g is acceleration due to gravity (9.81 m/s^2), ρ_s is sediment density (2,650 kg/m^3), ρ is water density (1,000 kg/m^3) and D is sediment size (0.01 m). Therefore, according to equation 6.2.1, the critical shear stress used in the Sawmill Creek modelling was 8.9 N/m^2 (or 8.9 Pa). This value is greater than the estimate based on soil samples using the Hanson method, but less than the other two methods (Table 6.2.1). Therefore, the critical shear stress used in the modelling falls within the estimated values based on soil samples taken from the site and was likely an over estimate, assuming the Hanson method provides the most reliable estimate.

6.2.2 Capturing Meaningful Topographic Change

Despite the little to no change in annual topographic surveys at most transects, in some cases, noticeable bed level changes were measured within a single year. For example, bed levels measured at T21 before (July 9, 2009) and after (July 28, 2009) the extreme flow event on July 24, 2009, showed significant erosion – up to 40 cm bed level drop – between the two

survey dates (Figure 6.2.2 B). However, by the time of the annual survey in November 2009, bed levels had returned to the pre-event values and appeared to remain unchanged by the time of the 2010 annual survey (Figure 6.2.2 B). Note that the slight misalignment of measured points along the transect line, which is more pronounced near the left bank (Figure 6.2.2 A), could explain the variation in bed levels along the left bank slope between the two July 2009 surveys and the two annual (November 2009 and 2010) surveys. While initial results indicated that the channel was somewhat unresponsive to annual morphological change (Chapter 3.2), the July 2009 measurements indicate that substantial change may result from a single extreme event, but that such a change may not be permanent. In an urban stream, extreme rainfall events lead to substantial flows that may exceed the spring freshet (for example, Figure 3.2.2). Therefore, while less sustained, the occurrence of these extreme flows may play the most important role in urban stream morphology and it is important that the impact of these events be captured by regular, event-based topographic measurement, rather than only the use of annual topographic surveys.

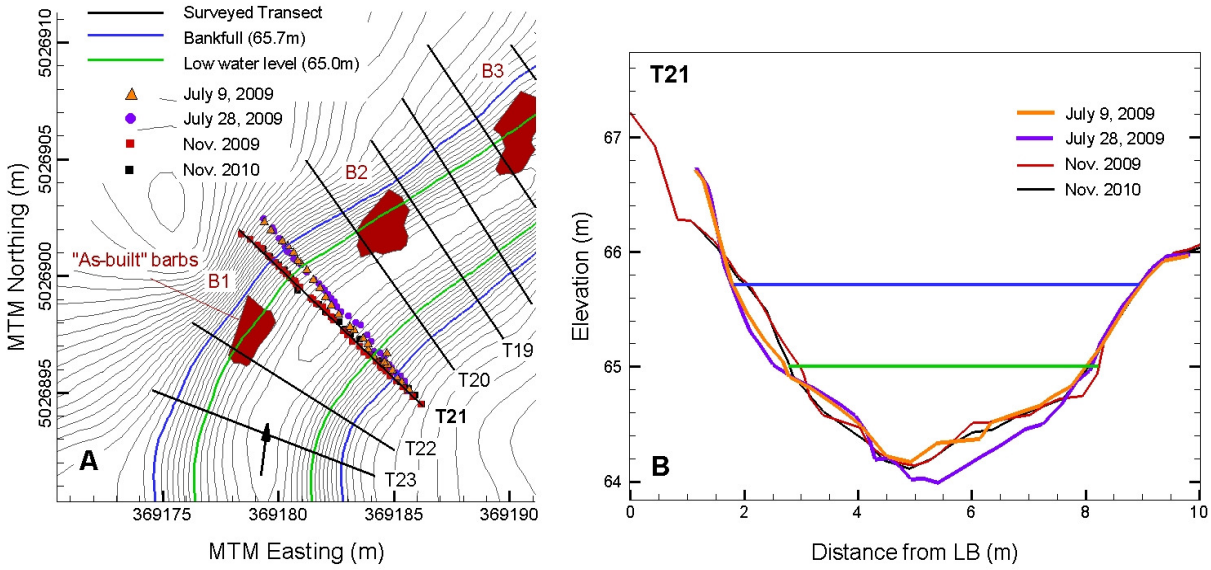

Figure 6.2.2. Comparison of topographic survey data at Transect T21, before and after extreme July 24, 2009 rain event. (A) Close up plan view of first bend and survey points at T21. (B) Cross-sectional view of survey data. Contour lines in (A) are at 0.1 m intervals and black arrow represents flow direction. Barbs are labelled B1, B2 and B3. [A full plot of surveyed transects in provided in Figure 3.2.5].

6.3 Turbulence versus vorticity

The central hypothesis of this thesis was that vortical motion dominates the development of local scour. Results from both the Missouri River flow field study (Chapter 4.2) and the laboratory study of barbs in a channel bend (Chapters 5.2 – 5.4) suggests that there is a close connection between vorticity and the location of vortex cores with local scour. However, results from the laboratory studies reveal that in some instances, the contribution of turbulence, and in particular, streamwise-cross-stream Reynolds stress (τ_{uv}) may be more significant to scour development than vortical motion. In Chapter 5.3 we found that in TR3 (no barbs) and TR10 (small barbs), τ_{uv} had the highest regression coefficients of any variable (τ_{uw}, τ_{vw}, *tke*, vorticity magnitude and z-vorticity) when compared with scour (Figure 5.3.7). The trend suggested that positive near-bed τ_{uv} was associated with scour while small positive and negative near-bed τ_{uv} was associated with deposition. Indeed, in all trapezoid channel bend runs (Chapter 5.3), with the exception of TR5 (where large barbs were used), highly positive τ_{uv} was observed along the right (outer) bank of the channel bend where outer bank scour was observed, while highly negative τ_{uv} was observed along the inner bank (Figure 5.3.2). This is consistent with results in the rectangular channel bend runs (Chapter 5.1), where maximum positive τ_{uv} coincided with the leading edge of the outer bank thalweg, and highly negative τ_{uv} near the bend apex coincided with the leading edge of the inner bank bar (Figure 5.1.8).

This trend was disrupted by the large barbs in TR5, where the distribution of near bed Reynolds stresses no longer matched the other trapezoid or rectangular runs (Figure 5.3.2). In particular, while the regression coefficient for τ_{uv} with scour was higher than for *tke* or

vorticity magnitude, it remained lower than for z-vorticity. This suggests that the scour due to the large barbs in TR5 was more related to z-vorticity than to τ_{uv}. Overall, it appears that scour was most likely due to the combined effect of positive τ_{uv} and negative z-vorticity, with bend scour dominated by high positive τ_{uv} and barb (local) scour dominated by high negative z-vorticity. This is consistent with the local scour occurring at wing dike tips, where the most concentrated contours of high positive z-vorticity were found (Chapter 4.2), and with previous numerical results that indicate a correspondence between high positive z-vorticity and local scour at submerged groyne tips (Minor *et al.*, 2007a). (Recall that turbulence measurements on the Missouri River were not possible). The sign of z-vorticity (positive or negative) is a function of the designated velocity vector direction, and, provided the same right-hand-rule is applied, it will vary depending on the location of the structures disrupting the flow field in relation to the positive streamwise direction (i.e. whether they are on the left or right bank). The z-vorticity sign varies between studies because the laboratory channel had barbs placed along the right bank (positive y-velocity towards the left bank and negative z-vorticity was dominant at the barb tips), while the Missouri River wing dikes and barbs in Minor *et al.* (2007a and 2007b) were along the left bank (positive y-velocity towards the left bank and positive z-vorticity was dominant).

One uncertainty remains. By using effectively time-averaged velocity data and stationary (or equilibrium) bed conditions, it is difficult to assess what came first: the vortical motion leading to local scour, or increased vorticity as a result of the morphology and development of the scour hole. Most likely, the two processes (local scour and vortex/vorticity magnitude) are developing simultaneously, exhibiting positive feedback. For the Missouri wing dikes, the most active region of bed mobility – the upstream scour hole crest at one wing dike tip

(Figure 4.2.8 and Figure 4.2.13) – corresponded with the most concentrated contours of high positive z-vorticity and the presence of vortex cores (Figure 4.2.13 and Figure 4.2.14). However, these vortex cores also change their location to remain at the upstream scour hole crest, as this moves downstream (Figure 4.2.13), suggesting their presence could be a function of bed morphology. On the other hand, numerical investigations (Koken and Constantinescu, 2008a and 2008b) have found that the horseshoe vortex system forming around the upstream base of a single emergent spur dike (which they describe as the main driving mechanism behind the growth of a scour hole at the structure's tip) was present during both the initial and final stages of the scouring process. The authors found that, compared to the initial stage when the bed was flat, the presence of the scour hole stabilized the horseshoe vortex system. Additional measurements of the flow field at various stages of bed development before equilibrium are required to confirm this phenomena, and verify that it is principally the vorticity that is driving the scour hole growth and not the other way round.

6.3.1 3-D Interpolation of Experimental Data

A new method for interpolating and processing discrete experimental (measured) data into continuous 3-D volumes was presented, and was successful in generating realistic continuous velocity fields. At both the scales of a large natural river and a laboratory channel, densely spaced velocity data were capable of resolving the 3-D flow patterns around a submerged structure. Further, by generating a volume of continuous velocity information, it was possible to calculate additional flow features, such as vorticity and the presence of vortex cores, which showed remarkable consistency between these two scales: the dominance of high z-vorticity and the presence of vortex cores was identified at both the wing dike tip (Missouri

River) and barb tip (laboratory channel), which both corresponded to scour holes at these locations. However, the orientation of the vortex cores (vertical vs. horizontal) and their specific location (i.e. upstream or downstream of the tip) did vary slightly.

These results also show that the density of velocity data will affect whether or not (or how many) vortex cores are resolved. For example, transects at 1% of the channel width (5 m transect data on the Missouri River), identified more vortex cores than transects spaced at 5% of the channel width (Chapter 4.2). As well, it was not until ADV data were collected every 2.5º in the channel bend (or ~ 6.5% of the channel width) that vortex cores were resolved in the vicinity of the barb tip (Chapter 5.4). Vortex cores were not resolved when data were collected every 15º. However, the identification of vortex cores remains a function of the flow field – data must be dense enough to capture the velocity gradients across the scale of coherent structures that are present.

The 3-D interpolation also provided spatially-continuous data, which offered a unique perspective for understanding the spatial variability of velocity and turbulence. This was particularly relevant for understanding the distribution of Reynolds stresses and turbulent kinetic energy in a channel bend, and how this pattern related to sediment transport and in particular scour.

7 Conclusions and Recommendations

Extensive laboratory and field investigations have been performed to study the role of vorticity, turbulence and three-dimensional flow structure on the development of scour. These experimental results provide new and valuable data on how each of these complex flow features impact sediment transport and scour in meander bends, with and with submerged structures, and at a range of scales. As well, field and laboratory testing of stream barb performance has provided a new understanding of their optimum design and use in channel bends.

The installation of seven stream barbs at Sawmill Creek has and will continue to serve as a demonstration project for the use of these structures for reducing stream bank erosion and improving aquatic habitat in semi-alluvial channels. However, monitoring results remain preliminary and it is too early to confirm their suitability and longer term impacts. More monitoring and data collection at the site is recommended.

In our laboratory study of stream barb performance, it was found that, contrary to the findings expressed in the latest design guidelines (USDA, 2005), if structures are too large or numerous, additional unwanted erosion may result. Barbs should only be placed in those regions of anticipated severe erosion; otherwise local scour generated at barbs outside those regions may result in excessive outer bank erosion. By incorporating a mobile-sand bed and banks channel into these laboratory tests, it was revealed that the floodplain directly downstream of a barb was particularly susceptible to erosion, an observation not seen in any previous experiments. This erosion is associated with the use of larger barbs, which generate greater plunging and recirculating flow downstream of the structures. To prevent this

erosion, the barb bank key width should be wider than the barb itself and should be extended along the channel bank in the downstream direction.

The work on the Missouri River presents improvements on existing methodologies and techniques related to ADCP and eco-sounder measurements for observing and quantifying 3-D flow field and sediment transport patterns in large rivers. This work presents new methodologies and original field observations of complex flow and sediment transport around a wing dike in a large sand-bed river. These results have implications for measuring and understanding large-scale complex flow fields and their role in scour hole dynamics. As well, the novel data collection scheme and analysis techniques dispel previously published work suggesting that only time-averaged spatial data are appropriate for flow characterization and use in model validation.

Using similar techniques for collecting and analyzing densely-spaced velocity and bathymetry data in the laboratory revealed key relationships between turbulence and vorticity with sediment transport and scour dynamics. While it was not possible to quantify turbulence phenomena in the Missouri River (due to instrument limitations and the method of spatial mapping using moving-boat transects), it was possible to describe the pattern of turbulence in a laboratory channel bend, with and without stream barbs, and compare these with the patterns of vortical motion and changes in bed levels. Results indicated that when large barbs are present, z-vorticity is the best indicator for bed level change compared to Reynolds stress, *tke* and vorticity magnitude. However, for small or no barbs, secondary Reynolds stress, τ_{uv}, showed the greatest correspondence with bed level change over other variables. The correspondence between high z-vorticity and local scour was also found in the vicinity of the wing dike tips on the Missouri River.

7.1 Recommendations and future research

To build on this research, the following recommendations are made for future work:

1. Live Bed Experiments

With the exception of Bhuiyan *et al.* (2010), all previous mobile bed studies involving stream barbs (or spur dikes, etc.) considered only clear water scour conditions. Clear water scour refers to the case when scour occurs and there is no additional sediment supply from upstream. Clear water scour conditions are not typical of flood flows in alluvial channels, where sediment is transported through the reach at high flows. Due to the constant influx of upstream sediment that is supplied in the live bed case, the pattern and magnitude of local scour will vary for live bed versus clear water scour conditions. To model fully the performance of stream barbs, future research should focus on testing live bend conditions for a channel with erodible side walls.

The bend flume at the University of Ottawa's hydraulic laboratory is capable of reproducing both clear water and live bed conditions. A slurry pump is used for the live bed case, which recirculates the sediment (sand) that has been transported out the channel back to the inlet. Preliminary testing for live bed conditions in the bend (without barbs) has been successful (Jamieson, unpublished) and showed noticeable differences in scour development compared to earlier clear water experiments for the same water depth and sediment size (Figure 7.1.1 A). In preliminary testing, it was found that clear water scour in the bend approaches equilibrium asymptotically, over a period of days or a week, while the live bed scour developed rapidly, but reached a dynamic equilibrium as depth fluctuated in response

to passing bed forms. This observation is consistent with extensive literature relating to local scour at bridge piers (Raudkivi, 1998) (Figure 7.1.1 B).

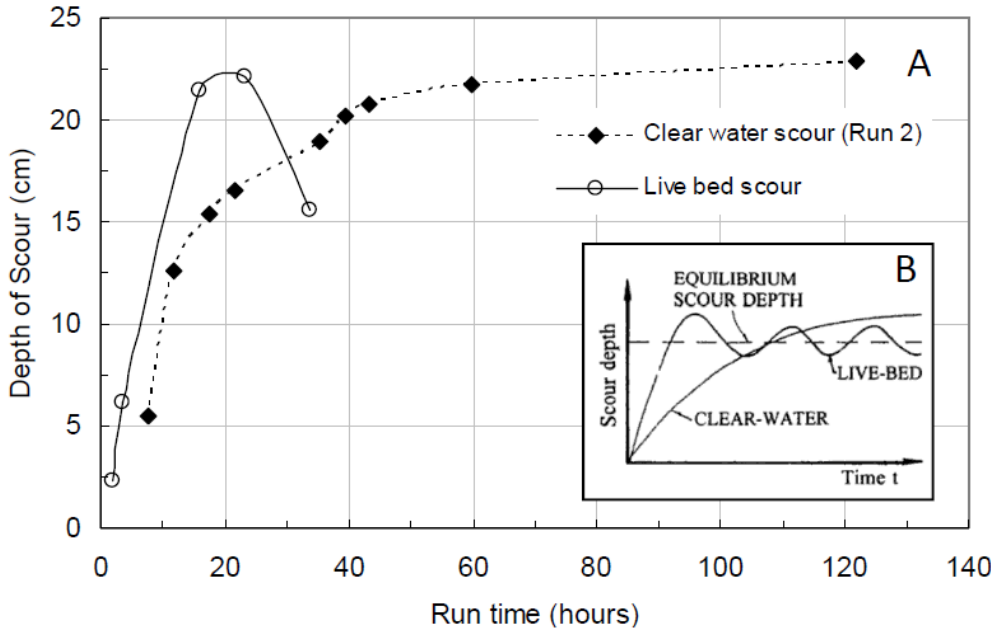

Figure 7.1.1. (A) Development of maximum scour depth at the outside wall at the exit of a 135º channel bend for clear water and live bed scour conditions. Live bed data terminated after 30 hours due to unexpected failure of the slurry pump. (B) Scour depth at a pier as a function of time (Raudkivi, 1998). [Run 2 is the same as Run 2 in Chapter 5.1, Figure 5.1.2].

Incorporating live bed conditions for a trapezoidal-shaped sand channel with barbs installed will be challenging, as a greater bed slope will be required to initiate live bed conditions. This would likely lead to excessive local scour at the barb tips and along the outer bank through the bend, possibly exceeding the 0.15 m floodplain and thereby reaching the fixed plexiglass wall.

2. Numerical Analysis for Stream Barb Design Guidelines

Given our experience and success with SSIIM, work is underway to develop a more complete and validated 3-D numerical model of Sawmill Creek. The field measurements at the site, both before and after the barb construction phase, will be used to calibrate the new model and develop a finer mesh (made possible by the M9 ADP bathymetry data) to provide more detailed modelling of the local flow field. Modelling complex geometries, such as those found in nature are difficult (and time consuming) and the numerical results can be sensitive to the definitions of the model boundaries and size of the computational mesh. The use of the ADP bathymetry data will help to overcome some of these limitations. As well, detailed ADV measurements collected at T21 and T22 on five different days during the Summer of 2009 (Jamieson, unpublished) will provide useful velocity and turbulence data for validation of the new model.

Another important parameter that must be considered closely in future modelling, and in assessing barb performance at Sawmill Creek, is bankfull discharge. Recall that discharge data at the stream gauging station for Sawmill Creek at Riverside (CK18-Q1), approximately 1.2 km downstream of the study site, is available from 2002-2010 (excluding 2003) (Chapter 3). However, two different stage-discharge curves (or equations) have been used to estimate discharge over this period. The stage-discharge curve used to calculate discharge values from 2002-2007 was developed by Environment Canada in the 1980's (Wayne Jackson, WEPP, personal communication) and was not revised until the City of Ottawa (2010) Report. It was this data (2002-2007) that lead to the initial estimate of bankfull discharge of 9 m^3/s at the barb site (Chapter 3.1), which was the value used in the numerical modelling and design of stream barbs at the site. However, the revised stage-discharge rating curve developed by the

City of Ottawa (City of Ottawa, 2010) suggests that the above value was possibly a gross over-estimate.

The more recent stage-discharge curve (Figure 7.1.2 A) is based on data collected in 2008 and 2009. This revised rating curve represents a medium degree of confidence, where a medium degree of confidence has been assigned for a rating curve with at least ten stage-discharge points, at least two years of data, and all but the extreme range of stages (water surface elevations) are reflected (City of Ottawa, 2010). Due to the heavily armoured banks (bedrock and large boulders) at the gauging site, this rating curve is considered to be reliable. However, additional points are required to ensure the highest degree of confidence in this curve. There is a particular need to include additional points beyond 2.1 m^3/s (Figure 7.1.2 A). The upper limit of the curve is 4.3 m^3/s (stage = 59.5 m), according to hydrological principles for extrapolation (Rantz *et al.*, 1982, reported in City of Ottawa, 2010), and it is not currently possibly to estimate discharge beyond this point. The rating curve was exceeded during several high flow events in 2009 (Figure 7.1.2 B). The highest recorded stage was 60.04 m (on July 24, 2009), which is 0.54 m higher than the upper limit of the curve.

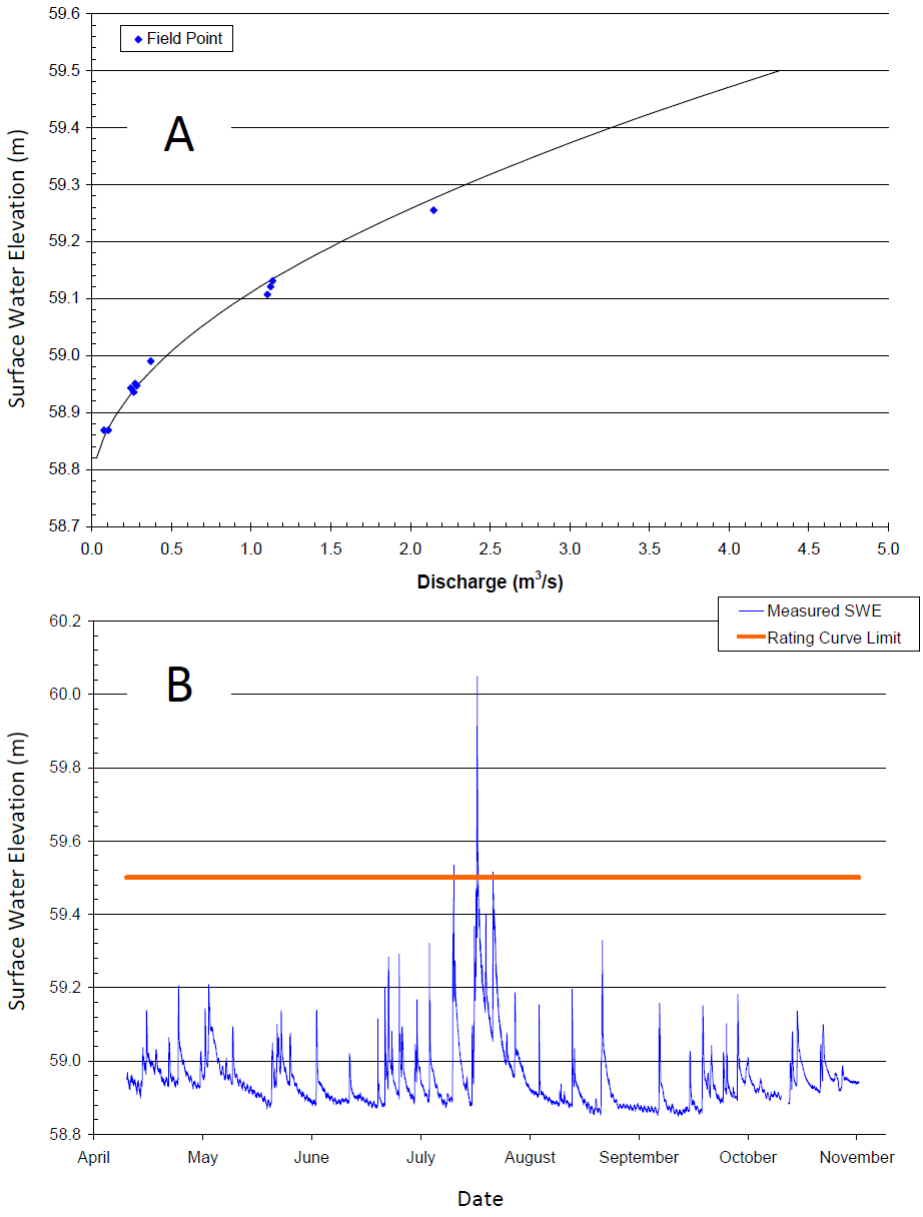

Figure 7.1.2. (A) Stage-discharge rating curve for Sawmill Creek at Riverside, based on data collected in 2008 and 2009. (B) Measured surface water elevation (stage) from 2009 displayed against upper limit of rating curve for Sawmill Creek at Riverside. (Adapted from City of Ottawa (2010)).

Comparing the two different stage-discharge relations, it was found that the earlier curve may have overestimated peak discharge, leading to an overestimate of bankfull discharge for

the stream barb design. The maximum recorded stage at the gauging station in 2007 was 59.5 m (on July 20, 2007) and corresponds to a calculated discharge of 8.86 m^3/s (according to the old stage-discharge curve), which was the discharge used in Chapter 3.1 for estimated bankfull discharge at the study site (i.e. 9 m^3/s). A stage of 59.5 m on the current rating curve (Figure 7.1.2 A) would yield an estimated discharge of approximately 4.3 m^3/s, approximately half of the value estimated with the previous stage-discharge relationship. The correspondence between discharge measurements at the study site made from ADP surveys in 2009 (Chapter 3.2) with mean daily flow data from the gauging station, suggests that the more recent stage-discharge relationship is reliable (at least at low to moderate flows) and that this curve, as well as a new bankfull discharge estimate, should be used in future analyses. It is worth noting that a stormwater management pond (the Sawmill Creek Constructed Wetland) was built upstream of the site by the City of Ottawa over a period of three years, ending in 2007. This wetland may be one factor contributing to a discrepancy in the rating curves. However, in personal communication, the City of Ottawa staff have maintained that the pond is primarly designed for water quality control (i.e. to treat stormwater runoff), rather than controlling water levels downstream during heavy rain events.

It is also recommended that SSIIM (or other equivalent 3-D numerical model with sediment transport capabilities) be used to assess various design alternatives for barb geometry and layout in the laboratory flume. The detailed measurements of flow and bathymetry collected in the laboratory phase of this research (Chapters 5.2, 5.3 and 5.4) will enable complete calibration of a numerical model of the laboratory flume flow and sediment transportation processes. Recall that detailed velocity measurements by Matsuura (2004) were lacking in Minor's (2006) thesis, preventing complete validation of the simulated

results. With this new model, it will be possible to simulate different barb arrangements and orientations, thereby providing a more comprehensive set of results and therefore a more complete assessment of the structures' optimum arrangement for use in future design guidelines. Once established and calibrated, manipulation and running of the model will take significantly less time than the same physical set-up in the laboratory, where typical runs take on the order of 10-12 days to reach bathymetric equilibrium and 2-3 weeks when velocity measurements are also desired (not to mention the time required to set up and prepare subsequent runs).

3. Continued Monitoring at Sawmill Creek

It is recommended that regular monitoring of bed and bank topography, flow rates, water levels and velocity patterns at Sawmill Creek continue for at least another 3 years. Little to no change in topography was recorded over the four years of previous monitoring (i.e. 2007, 2009 and 2010 topographic surveys). This suggests that semi-alluvial channels are resistant to change, that a longer monitoring period is required to record meaningful changes in semi-alluvial or clay-type channels, and/or that shorter time scales should be considered (i.e. select transects be measured multiple times throughout the season, before and after extreme events, if possible). As well, hydrology at Sawmill Creek appears to be inconsistent, due to its urban location (and therefore sensitivity to rainfall and runoff) and seasonal climatic variations. This made it difficult to determine a reliable bankfull discharge and water level, and perhaps most importantly, to obtain detailed velocity data at moderate to high flow events.

It is also recommended that the fish habitat monitoring and assessment continue. The data required for a complete before-after-control-impact (BACI) statistical analysis is

incomplete. Future data must be collected at both the study site and the control site, and careful attention paid to the influence of natural variations (i.e. changes due to external factors such as weather, and not the introduction of stream barbs). Fish and habitat data collected throughout each season could prevent the possible bias of seasonal variations when comparing single-sample data from year to year.

References

Abad, J.D., Rhoads, B.L., Guneralp, I., Garcia, M.H. (2008). Flow structure at different stages in a meander-bend with bendway weirs. *Journal of Hydraulic Engineering*, 134(8), pp. 1052-1063.

Afzalimehr, H., Rennie, C.D. (2009). Determination of bed shear stress using boundary layer parameters in a gravel-bed river. *Hydrological Sciences Journal,* 54(1), pp. 147-159.

Allen, R.J. (1986). The role of the particulate matter in the fate of contaminants in aquatic ecosystems. *Scientific Series 142, Inland Waters Directorate*, Environment Canada, Burlington, ON.

Azinfar, H., Kells, J.A. (2011). Drag force and associated backwater effect due to an open channel spur dike field. *Journal of Hydraulic Research*, 49(2), pp. 248-256.

Bagnold, R.A. (1956). The flow of cohesionless grains in fluids. *Philosophical Transactions of the Royal Society of London A,* 265, pp. 315-319.

Bathurst, J.C., Thorne, C.R., Hey, R.D. (1977). Direct measurements of secondary currents in river bends. *Nature,* 269, pp. 504-506.

Bathurst, J.C., Thorne, C.R., Hey, R.D. (1979). Secondary flow and shear stress at river bends. *J. Hydraul. Div. Am. Soc. Civ. Eng.,* 105, pp. 1277-1295.

Best, J.L. (1993). On the interactions between turbulent flow structure, sediment transport and bedform development: some considerations from recent experimental research. In *Turbulence: Perspectives on Flow and Sediment Transport,* John Wiley & Sons, Chichester, Clifford NJ, French JR and Hardisty J(eds), pp. 61-92.

Best, J., Bennett, S., Bridge, J., Leeder, M. (1997). Turbulence modulation and particle velocities over flat sand beds at low transport rates. *Journal of Hydraulic Engineering*, 123(12), pp. 1118-1129.

Bhuiyan, F., Hey, R.D., Wormleaton, P.R. (2009). Effects of vanes and w-weir on sediment transport in meandering channels. *Journal of Hydraulic Engineering*, 135(5), pp. 339-349.

Bhuiyan, F., Hey, R.D., Wormleaton, P.R. (2010). Bank-attached vanes for bank erosion control and restoration of river meanders. *Journal of Hydraulic Engineering*, 136(9), pp. 583-596.

Biron, P.M., Robson, C., Lapointe, M.F., Gaskin, S.J. (2004). Comparing different methods of bed shear stress estimates in simple and complex flow fields. *Earth Surface Processes and Landforms*, 29, pp. 1403-1415.

Blanckaert, K. (2009). Saturation of curvature-induced secondary flow, energy losses, and turbulence in sharp open-channel bends: Laboratory experiments, analysis, and modelling. *Journal of Geophysical Research*, 114, F03015, doi:10.1029/2008JF001137.

Blanckaert, K. (2010). Topographic steering, flow recirculation, velocity redistribution, and bed topography in sharp meander bends. *Water Resources Research*, 46, W09506, doi:10.1029/2009WR008303.

Blanckaert, K. (2011). Hydrodynamic processes in sharp meander bends and their morphological implications. *Journal of Geophysical Research*, 116, F01003, doi:10.1029/2010JF001806.

Blanckaert, K., Buschman, F.A., Schielen, R., Wijbenga, J.H.A. (2008). Redistribution of velocity and bed-shear stress in straight and curved open channels by means of bubble screen: Laboratory experiments. *Journal of Hydraulic Engineering*, 134(2), pp. 184-195.

Blanckaert, K., de Vriend, H.J. (2004). Secondary flow in sharp one-channel bends. *Journal of Fluid Mechanics*, 498, pp. 353-380.

Blanckaert, K., de Vriend, H.J. (2005). Turbulence characteristics in sharp open-channel bends. *Physics of Fluids*, 17, 055102.

Blanckaert, K., Duarte, A., Schleiss, A.J. (2010). Influence of shallowness, bank inclination and bank roughtness on the variability of flow patterns and boundary shear stress due to secondary currents in straight open-channels. *Advances in Water Resources*, 33, pp. 1062-1074.

Blanckaert, K., Graf, W.H. (2001). Mean flow and turbulence in open-channel bend. *Journal of Hydraulic Engineering*, 127(10), pp. 835-847.

Blanckaert, K., Graf, W.H. (2004). Momentum transport in sharp open-channel bends. *Journal of Hydraulic Engineering*, 130(3), pp. 186-198.

Bridge, J.S. (1977). Flow, bed topography, grain size and sedimentary structure in open channel bends: a three-dimensional model. *Earth Surface Processes and Landforms,* 2, pp. 401-416.

Bridge, J.S., Jarvis, J. (1977). Velocity profiles and bed shear stress over various bed configurations in a river bend. *Earth Surface Process and Landforms,* 1, pp. 303-336.

Brodkey, R.S., Wallace, J.M., Eckelmann, H. (1974). Some properties of truncated turbulence signals in bounded shear flows. *Journal of Fluid Mechanics*, 63(2), pp. 209-224.

Buffin-Bélanger, T., Roy, G.A. (2005). 1 min in the life of a river: selecting the optimal record length for the measurement of turbulence in fluvial boundary layers. *Geomorphology*, 68, pp. 77-94.

Buijse, A.D., Coops, H., Staras, M., Jans, L.H., Van Geest, G.J., Grift, R.E., Ibelings, B.W., Oosterberg, W., Roozen, F.C.J.M. (2002). Restoration strategies for river floodplains along large lowland rivers in Europe. *Freshwater Biology*, 47(4), pp. 889-907.

Cao, Z., Egashira, S., Carling, P.A. (2003). Role of suspended-sediment particle size in modifying velocity profiles in open channel flows. *Water Resources Research*, 39(2), WR000934.

Carré, D.M., Biron, P.M., Gaskin, S.J. (2007). Flow dynamics and bedload sediment transport around paired deflectors for fish habitat enhancement: a field study in the Nicolet River. *Can. J. Civ. Eng*., 34, pp. 761-769.

Chong, M.S., Perry, A.E., Cantwell, B.J. (1990). A general classification of three-dimensional flow fields. *Phys. Fluids A*, 2, pp. 765-777.

City of Ottawa (2009a). *Sawmill Creek Fish & Fish Habitat Assessment Report – 2008*. Prepared by the Water Environment Protection Program, Strategic and Environmental Services, Environmental Services, Infrastructure Services & Community Sustainability, City of Ottawa.

City of Ottawa (2009b). *Sawmill Creek Fish & Fish Habitat Assessment Report Addendum – 2009*. Prepared by the Water Environment Protection Program, Strategic and Environmental Services, Environmental Services, Infrastructure Services & Community Sustainability, City of Ottawa.

City of Ottawa (2010). *Flow Monitoring Program, City of Ottawa – 2008 & 2009*, Prepared by the Water Environment Protection Program, Strategic and Environmental Services, Environmental Services, Infrastructure Services & Community Sustainability, City of Ottawa.

Clifford, N.J., French, J.R. (1993). Monitoring and modelling turbulent flow: Historical and contemporary perspectives. *Turbulence: Perspectives on Flow and Sediment Transport*. Ed. N.J. Clifford, J.R. French and J. Hardisty. John Wiley & Sons Ltd.

Corney, R.K.T., Peakall, J., Parsons, D.R., Elliott, L., Amos, K.J., Best, J.L., Keevil, M., Ingham, D.B. (2006). The orientation of helical flow in curved channels. *Sedimentology*, 53(2), pp. 249-257.

Cossette, D., Mazurek, K.A. (*submitted*). Scour by a submerged vertical circular turbulent impinging jet in natural cohesive soils. *Proceedings of the 20th Canadian Hydrotechnical Conference,* Ottawa, Canada, June 2011.

Crowder, D.W., Diplas, P. (2000). Evaluating spatially explicit metrics of stream energy gradients using hydrodynamic model simulations. *Canadian Journal of Fisheries and Aquatic Sciences*, 57, pp. 1497-1507.

Crowder, D.W., Diplas, P. (2002). Vorticity and circulation: spatial metrics for evaluating flow complexity in stream habitats. *Canadian Journal of Fisheries and Aquatic Sciences*, 59, pp. 633-645.

Debnath, K., Aberle, J., Nikora, V., Westrich, B., Muste, M. (2007). Erosion of cohesive sediments: re-suspension, bed load, and erosion patterns from field experiments, *Journal of Hydraulic Engineering*, 133 (5), pp. 508–520.

De Boer, D.H., Hassan, M.A., MacVicar, B., Stone, M. (2005). Recent (1999-2003) Canadian research on contemporary processes of river erosion and sedimentation, and river mechanics. *Hydrological Processes*, 19(1), pp. 265-283.

Derrick, D.L. (1997). Harland Creek BendwayWeir/Willow Post Bank Stabilization Demonstration Project. Proceedings of the Conference on *Management of Landscapes Disturbed by Channel Incision,* pp. 351–356.

Dietrich, W.E., Smith, J.D. (1983). Influence of the point bar on flow through curved channels. *Water Resources Research*, 19(5), pp. 1173-1192.

Dietrich, W.E., Smith, J.D. (1984). Bed load transport in a river meander. *Water Resources Research*, 20(10), pp. 1355-1380.

Dietrich, W.E., Whiting, P.J. (1989). Boundary shear stress and sediment transport in river meanders of sand and gravel. In *River Meandering, Water Resources Monograph Series* vol. 12, American Geophysical Union, Washington D.C., Ikeda S, Parker G (eds); pp. 1-50.

Dinehart, R.L., Burau, J.R. (2005). Averaged indicators of secondary flow in repeated acoustic Doppler current profiler crossings of bends. *Water. Resour. Res.*, 41, W09405, doi:10.1029/2005WR004050.

Diplas, P., Dancey, C.L., Celik, A.O., Valyrakis, M., Greer, K., Akar, T. (2008). The role of impulse on the initiation of particle movement under turbulent flow conditions. *Science*, 322, pp. 717-720.

Drake, T.G., Shreve, R.L., Dietrich, W.E., Whiting, P.J., Leopold, L.B. (1988). Bedload transport of fine gravel observed by motion-picture photography. *Journal of Fluid Mechanics*, 192, pp. 193-217.

Droppo, I.G. (2001). Rethinking what constitutes suspended sediment. *Hydrological Processes*, 15, pp. 1551–1564.

Droppo, I.G., Ongley, E.D. (1994). Flocculation of suspended sediment in rivers of southwestern Canada. *Water Research,* 28, pp. 1799–1809.

Elliott, C.M., Jacobson, R.B., Delonay, A.J. (2004), Physical aquatic habitat assessment, Fort Randall segment of the Missouri river, Nebraska and South Dakota: *U.S. Geological Survey Open-File Report 2004-1060*, 80 p.

Elliott, C. M., Reuter, J. M., Jacobson, R. B. (2009). Channel morphodynamics in four reaches of the Lower Missouri River, 2006-07. *U.S. Geological Survey Scientific Investigations Report 2009-5074*, 258 p. http://pubs.usgs.gov/sir/2009/5074/

Engelhardtm, C., Kruger, A., Sukhodolov, A.A. (2004). A study of phytoplankton spatial distributions, flow structure and characteristics of mixing in a river reach with groynes. *Journal of Plankton Research*, 26(11), pp. 1351-1366.

Engelund, F. (1974). Flow and bed topography in channel bends. *J. Hydraul. Div. Am. Soc. Civ. Eng.*, 100, pp. 1631-1648.

Espinosa, F.A., Rhodes, J.J., McCullough, D.A. (1997). The failure of existing plans to protect salmon habitat in the Clearwater National Forest in Idaho. *Journal of Environmental Management*, 49, pp. 205–230.

Everest, F.H., Chapman, D.W. (1972). Habitat selection and spatial interaction of juvenile Chinook salmon and steelhead trout in two Idaho streams. *Journal of the Fisheries Research Board of Canada*, 29, pp. 91-100.

Fausch, K.D. (1993). Experimental analysis of microhabitat selection by juvenile steelhead (*Oncorhynchus mykiss*) and coho salmon (*O. kisutch*) in a British Columbia stream. *Canadian Journal of Fisheries and Aquatic Sciences*, 50, pp. 1198-1207.

Field, W.G. (1971). Flood protection at highway bridge openings. *University of Newcastle*, N.S.W., Engng. Bulletin, CE3.

Fox, J.F., Papanicolaou, A.N., Hobbs, B., Kramer, C., Kjos, L. (2005a). Fluid-sediment dynamics around a barb: an experimental case study of a hydraulic structure for the Pacific Northwest. *Canadian Journal of Civil Engineering,* 32, pp. 853–867.

Fox, J.F., Papanicolaou, A.N., Kjos, L. (2005b). Eddy taxonomy methodology around submerged barb obstacle within a fixed rough bed. *Journal of Engineering Mechanics*, 131(10), pp. 1082-1100.

Gaeuman, D., Jacobson, R.B. (2005). Aquatic habitat mapping with an Acoustic Doppler Current Profiler: Considerations for Data Quality. *U.S. Geological Survey Open-File Report 2005-1163*, 20 p. http://www.cerc.usgs.gov/pubs/center/pdfDocs/

Gaeuman, D., Jacobson, R.B. (2006). Acoustic bed velocity and bed load dynamics in a large sand be river. *J. Geophys. Res*. 11, F02005, doi:10.1029/2005JF000411.

Gaeuman, D., Jacobson, R.B. (2007a). Field assessment of alternative bed-load transport equations. *Journal of Hydraulic Engineering*, 133(12), pp. 1319-1328.

Gaeuman, D., Jacobson, R.B. (2007b). Quantifying fluid and bed dynamics for characterizing benthic physical habitat in large rivers. *J. Appl. Ichthyol*, 23, pp. 359-364.

Galat, D.L., Berry, C.R., Jr., Peters, E.J., White, R.G. (2005). Missouri River basin, *in* Benke, A.C., and Cushing, C.E., eds., *Rivers of North America*: Oxford, Elsevier Academic Press, pp. 427–480.

Garde, R.J., Subramanya, K., Nambudaripad, K.D. (1961). Study of scour around spur dikes, *Journal of the Hydraulics Division,* ASCE (6), pp. 23-27.

Gaskin, S.J., Pieterse, J., Al Shafie, A., Lepage, S. (2003). Erosion of undisturbed clay samples from the banks of the St. Lawrence River. *Canadian Journal of Civil Engineering*, 30, pp. 585-595.

Gill, M.A. (1972). Erosion of sand beds around spur dikes. *Journal of the Hydraulics Division, ASCE*, 98(9), pp. 1587-1602.

Gomez, B., Church, M. (1989). An assessment of bed load sediment transport formulae for gravel bed rivers. *Water Resources Research*, 25(6), pp. 1161-1186.

Gordon, R.L. (1989). Acoustic measurement of river discharge. *Journal of Hydraulic Engineering*, 115(7), pp. 925-936.

Gorman, O.T., Karr, J.R. (1978). Habitat structure and stream fish communities. *Ecology*, 59, pp. 507-515.

Grass, A.J. (1971). Structural features of turbulent flow over smooth and rough boundaries. *Journal of Fluid Mechanics*, 50, pp. 233-255.

Grass, A.J. (1983). The influence of boundary layer turbulence on the mechanics of sediment transport. *Proc. Euromech 156; Mechanics of Sediment Transport*, Balkema, Rotterdam, The Netherlands, pp. 3–17.

Grissinger, E.H. (1966). Resistance of selective clay systems to erosion by water, *Water Resources Research*, 2(1), First Quarter, pp. 131-138.

Gross, T.F., Nowell, A.R.M. (1985). Spectral scaling in a tidal boundary layer. *Journal of Physical Oceanography*, 15, pp. 496-508.

Habersack, H.M., Laronne, J.B. (2002). Evaluation and improvement of bed load discharge formulas based on Helley-Smith sampling in an alpine gravel bed river. *Journal of Hydraulic Engineering*, 128(5), pp. 484-499.

Haller, G. (2005). An objective definition of a vortex. *Journal of Fluid Mechanics*, 525, pp. 1-26.

Hanratty, T.J., Theofanous, T., Delhaye, J-M., Eaton, J., McLaughlin, J., Prosperetti, A., Sundaresan, S., Tryggvason, G. (2003). Workshop findings. *International Journal of Multiphase Flow*, 29, pp. 1047-1059.

Hanson, G.J., Cook, K.R. (2004). Apparatus, test procedures, and analytical methods to measure soil eroidbility *in situ*. *Applied Engineering in Agriculture*, 20(4), pp. 455-462.

Harper, D., Everard, M. (1998). Why should the habitat level approach underpin holistic river survey and management? *Aquatic Conservation: Marine and Freshwater Ecosystems*, 8, pp. 395-413.

Hay, A.E. (1993). Sound scattering from a particle-laden, turbulent jet. *Journal of the Acoustical Society of America*, 90(4), pp. 2055-2074.

Hinze, J.O. (1959). *Turbulence*, McGraw-Hill Book Co., New York, 586 p.

Hunt, J.C.R., Wray, A.A., Morin, P. (1988). Eddies, stream and convergence zones in turbulent flows. Technical Report CTR – S88, Centre for Turbulence Research.

Hussain, A.K., Reynolds, W. (1972). The mechanics of an organized wave in turbulent shear flow. *Journal of Fluid Mechanics*, 54, pp. 241-261.

Ikeda, S., Parker, G. (eds). (1989). *River Meandering, Water Resources Monograph Series* vol. 12, American Geophysical Union, Washington D.C.

Jackson, R.G. (1976). Sedimentological and fluid-dynamic implications of the turbulent bursting phenomenon in geophysical flows. *Journal of Fluid Mechanics*, 77(3), pp. 531-560.

Jamieson, E.C., Post, G., Rennie, C.D. (2010). Spatial variability of three-dimensional Reynolds stresses in a developing channel bend. *Earth Surface Processes and Landforms*, 35, pp. 1029-1043.

Jamieson, E.C., Rennie, C.D., Jacobson, R.B., Townsend, R.D. (*in press*). Evaluation of ADCP bed velocity in a large sand-bed river: Moving versus stationary boat conditions. *Journal of Hydraulic Engineering*, Accepted December 2010.

Jamieson, E., Rennie, C.D., Ramooz, R. (2008). Validation of aDcp bedload transport measurements. *Proceedings of the 2008 River Flow Conference*, Cesme, Turkey, Sept. 2008, pp. 2343-2351.

Jamieson, E.C., Rennie, C.D., Townsend, R.D. (2009). Design of stream barbs for field scale application at Sawmill Creek, Ottawa. *WIT Transactions on Ecology and the Environment* (*Proceedings of River Basin Management V*, Malta, September 2009), 124, pp. 281-292.

Jamieson, E.C., Rennie, C.D., Townsend, R.D. (2011a). 3-D flow and scour near a submerged wing dike: ADCP measurements on the Missouri River. *Water Resources Research*. 47, W07544, doi: 10.1029/2010WR010043.

Jamieson, E.C., Rennie, C.D., Townsend, R.D. (*submitted – a*). Flow and sediment dynamics in a laboratory channel bend with and without stream barbs (submerged groynes) 1: Mean flow field. *Journal of Hydraulic Engineering*, submitted December 2010.

Jamieson, E.C., Rennie, C.D., Townsend, R.D. (*submitted – b*). Flow and sediment dynamics in a laboratory channel bend with and without stream barbs (submerged groynes) 2: Turbulence and vorticity. *Journal of Hydraulic Engineering*, submitted December 2010.

Jamieson, E.C., Rennie, C.D., Townsend, R.D. (2011b). Vorticity, turbulence and scour: Measurements from a laboratory channel bend with stream barbs (submerged groynes). *Proceedings of the 34th Congress of IAHR*, Brisbane, Australia, June 2011.

Jeong, J., Hussain, F. (1995). On the identification of a vortex. *Journal of Fluid Mechanics*, 285, pp. 69-94.

Jia, Y., Scott, S., Xu, Y., Huang, S., Wang, S.S.Y. (2005). Three-dimensional numerical simulation and analysis of flows around a submerged weir in a channel bendway. *Journal of Hydraulic Engineering*, 131(8), pp. 682-693.

Johnson, PA., Hey, R.D., Tessier, M., Rosgen, D.L. (2001). Use of vanes for control of scour at vertical wall abutments. *Journal of Hydraulic Engineering*, 127(9), pp. 772-778.

Jones, C., Somers, K.M., Craig, B., Reynoldson, T.B. (2005). Ontario benthos biomonitoring network protocol manual. Version 1.0. 111p.

Jones, N.E., Tonn, W.M. (2004). Enhancing productive capacity in the Canadian Arctic: Assessing the effectiveness of instream habitat structures in habitat compensation. *Transactions of the American Fisheries Society*, 133, pp. 1356-1365.

Keevil, G.M., Peakall, J., Best, J.L., Amos, K.J. (2006). Flow structure in sinuous submarine channels: Velocity and turbulence structure of an experimental submarine channel. *Marine Geology*, 229(3-4), pp. 241-257.

Kline, S.J., Reynolds, W.C, Straub, F.A., Runstadler, P.W. (1967). The structure of turbulent boundary layers. *Journal of Fluid Mechanics*, 30(4), pp. 741-773.

Knighton, D. (1998). *Fluvial Forms and Processes: A New Perspective*, Arnold, London.

Koken, M., Constantinescu, G. (2008a). An investigation of the flow and scour mechanisms around isolated spur dikes in a shallow open channel: 1. Conditions corresponding to the initiation of the erosion and deposition process, *Water Resources Research*, 44, W08406, doi:10.1029/2007WR006489

Koken, M., Constantinescu, G. (2008b), An investigation of the flow and scour mechanisms around isolated spur dikes in a shallow open channel: 2. Conditions corresponding to the final stages of the erosion and deposition process, *Water Resources Research*, 44, W08407, doi:10.1029/2007WR006491

Kostaschuk, R., Villard, P., Best, J. (2004). Measuring velocity and shear stress over dunes with acoustic Doppler profiler. *Journal of Hydraulic Engineering*, 130, pp. 932–936.

Krishnappan, B.G. (2007). Recent advances in basic and applied research in cohesive sediment transport in aquatic systems. *Canadian Journal of Civil Engineering*, 34, pp. 731-743.

Kuhnle, R.A., Alonso, C.V., Shields, F.D. Jr. (1999). Geometry of scour holes associated with 90º spur dikes. *Journal of Hydraulic Engineering*, 125(9), 972-978.

Kuhnle, R.A., Alonso, C.V., Shields, F.D. Jr. (2002). Local scour associated with angled spur dikes. *Journal of Hydraulic Engineering*, 128(12), pp. 1087-1093.

Kuhnle, R.A., Jia, K., Alonso, C.V. (2008). Measured and simulated flow near a submerged spur dike. *Journal of Hydraulic Engineering*, 134(7), pp. 916-924.

Kulick, J.D., Ressler, J.R., Eaton, J.K. (1994). Particle response and turbulence modification in fully developed channel flow. *Journal of Fluid Mechanics*, 277, pp. 109-134.

Lapointe, M. (1992). Burst-like sediment suspension events in a sand bed river. *Earth Surface Processes and Landforms*, 17, pp. 253-270.

Lau, Y.L., Krishnappan, B.G. (1997). *Measurement of size distribution of settling flocs. NWRI Publication 97-223*, National Water Research Institute, CCIW, Environment Canada, Burlington, Ont.

Laursen, E.M. (1958). Scour at bridge crossings. *Iowa Highway Res. Board*, Bulletin No. 8.

Laursen, E.M. (1960). Scour at bridge crossings. *Proc. ASCE*, Vol. 86, HY2, pp. 39-54.

Laursen, E.M. (1963). Analysis of relief bridge scour. *Proc. ASCE*, Vol. 89, HY3, pp/93-118.

Leeder, M.R. (1983). On the dynamics of sediment suspension by residual Reynolds stresses – confirmation of Bagnold's theory. *Sedimentology*, 30, pp. 485-491.

Lim, S.Y. (1997). Equilibrium clear-water scour around an abutment. *Journal of Hydraulic Engineering*, 123(3), pp. 237-243.

Liu, H.K., Chang, F.M., Skinner, M.M. (1961). Effect of bridge constriction on scour and backwater. *Colorado State University*, Engng. Res. Center Rep. CER60HKL22.

Lu S.S., Willmarth, W.W. (1973). Measurements of the structure of the Reynolds stress in a turbulent boundary layer. *Journal of Fluid Mechanics*, 60, pp. 481-511.

Lumley, J.L. (1965). Interpretation of time spectra measured in high-intensity shear flows. *The Physics of Fluids*, 8(6), pp. 1056-1062.

MacVicar, B.J., Roy, A.G. (2007). Hydrodynamics of a forced riffle pool in a gravel bed river: 2. Scale and structure of coherent turbulent events. *Water Resources Research*, 43, W12402, doi:10.1029/2006WR005274.

Matsuura, T. (2004). Stream-bank protection in narrow channel bends using 'barbs' – a laboratory study. *M.A.Sc Thesis*, University of Ottawa, Canada.

Matsuura, T., Townsend, R. (2004). Stream-barb installations for narrow channel bends – a laboratory study. *Canadian Journal of Civil Engineering*, 31, pp. 478–486.

McCoy, A., Constantinescu, G., Weber, L.J. (2008). Numerical investigation of flow hydrodynamics in a channel with a series of groynes. *Journal of Hydraulic Engineering*, 134(2), pp. 157-172.

McLean, S.R., Nelson, J.M., Wolfe, S.R. (1994). Turbulence structure over two-dimensional bed forms: Implications for sediment transport. *Journal of Geophysical Research*, 99(C6), pp. 12749-12747.

McLean, S. R., Wolfe, S. R., Nelson, J. M. (1999). Predicting boundary shear stress and sediment transport over bedforms. *Journal of Hydraulic Engineering*, 125, pp. 725–736.

McLelland, S.J., Nicholas, A.P. (2000). A new method for evaluating errors in high-frequency ADV measurements. *Hydrological Processes*, 14, pp. 351-366.

Melville, B.W. (1992). Local scour at bridge abutments. *Journal of Hydraulic Engineering*, 118(4), pp. 615-630.

Mesick, C.F. (1988). Effects of food and cover on numbers of Apache and brown trout establishing residency in artifical stream channels. *Transactions of the American Fisheries Society*, 117, pp. 421-431.

Minor, B. (2006). Barbs (submerged groynes) for river bend bank protection: Application of a three-dimensional numerical model. *M.A.Sc Thesis*, University of Ottawa, Canada.

Minor, B., Jamieson, E., Rennie, C.D., Townsend, R.D. (2007a). Three-dimensional flow in a barb field. *WIT Transactions on Ecology and the Environment*, 104, pp. 371-380.

Minor, B, Rennie, C.D., Townsend, D.R. (2007b). "Barbs" for river bend bank protection: Application of a three-dimensional numerical model. *Canadian Journal of Civil Engineering*, 34, pp. 1087- 1095.

Movafagh Kerman, S., Rennie, C.D. (2007). Mapping three-dimensional velocity in a large gravel-bed river. *Proceedings of Hydraulic Measurements and Experimental Methods 2007 (ASCE/IAHR)*, Lake Placid, NY.

Muhar, S., Jungwirth, M., Unfer, G., Wiesner, C., Poppe, M., Schmutz, S., Hohensinner, S., Habersack, H. (2007). 30 Restoring riverine landscapes at the Drau River: successes and deficits in the context of ecological integrity, *in* Helmut Habersack, H.P., and Massimo, R., eds., *Developments in Earth Surface Processes*: Elsevier, pp. 779-803.

Muste, M., Kim, D., González-Castro, J.A. (2010). Near-transducer errors in ADCP measurements: Experimental Findings. *Journal of Hydraulic Engineering*, 136(5), pp. 275-289.

Muste, M., Patel, V.C. (1997). Velocity profiles for particles and liquid in open-channel flow with suspended sediment. *Journal of Hydraulic Engineering*, 123(9), pp. 742-751.

Muste, M., Yu, K., Fujita, I., Ettema, R. (2009). Two-phase flow insights into open-channel flows with suspended particles of different densities. *Environmental Fluid Mechanics*, 9, pp. 161-186.

Muste, M., Yu, K., Pratt, T., Abraham, D. (2004b). Practical aspects of ADCP data use for quantification of mean river flow characteristics; Part II: fixed-vessel measurements. *Flow Meas. Inst.* 15, pp. 17-28.

Muste, M., Yu, K., Spasojevic, M. (2004a). Practical aspects of ADCP data use for quantification of mean river characteristics; Part I: moving-vessel measurements. *Flow Meas. Inst.* 15, pp. 1-16.

Nanson, G.C., Hickin, E.J. (1986). A statistical analysis of bank erosion and channel migration in western Canada. *Geological Society of America Bulletin*, 97(4), pp. 497-504.

National Cooperative Highway Research Program (NCHRP) Report 568: *Riprap Design Criteria, Recommended Specifications, and Quality Control*, Transportation Research Board, Washington D.C. 125p. 2006.

Nezu, I., Azuma, R. (2004). Turbulence characteristics and interaction between particles and fluid in particle-laden open channel flows. *Journal of Hydraulic Engineering*, 130(10), pp. 988-1001.

Nezu, I., Nakagawa, H. (1993). *Turbulence in Open-Channel Flows*. A.A. Balkema, Rotterdam, Brookfield.

Nikora, V.I., Goring, D.G. (1998). ADV measurements of turbulence: Can we improve their interpretation. *Journal of Hydraulic Engineering*, 124(6), pp. 630-634.

Nikora, V.I., Goring, D.G. (2000). Flow turbulence over fixed and weakly mobile gravel beds. *Journal of Hydraulic Engineering*, 126(9), pp. 679–690.

Nino, Y., Garcia, M. (1998). Engelund's analysis of turbulent energy and suspended load. *Journal of Engineering Mechanics*, 124(4), pp. 480-483.

Nortek. (1997). *ADV Operation Manual*. Nortek AS, Bruksveien 17, 1390 Vollen, Norway, 33.

Odgaard, A.J., Bergs, M.A. (1988). Flow processes in a curved alluvial channel. *Water Resources Research*, 24(1), pp. 45-56.

Olsen, N.R.B. (2003). Three-dimensional CFD modelling of self-forming meandering channel. *Journal of Hydraulic Engineering*, 129(5), pp. 366-372.

Olsen, N.R.B. (2005). *A Three-dimensional Numerical Model for Simulation of Sediment Movements in Water Intakes with Multiblock Option: User's Manual*, Department of Hydraulic and Environmental Engineering, Norwegian University of Science and Technology.

Oweis, G.F., Ceccio, S.L. (2005). Instantaneous and time-averaged flow fields of multiple vortices in the tip region of ducted propulsor. *Experiments in Fluids*, 38, pp. 615-636.

Papanicolaou, A.N., Elhakeem, M., Dermisis, D., Young, N. (*in press*). Evaluation of the Missouri River shallow water habitat using a 2D-hydrodynamic model, v. 9999, no. 9999, p. n/a 10.1002/rra.1344.

Papanicolaou, A.N.T., Kjos, L.J., Fox, J.F. (2004). *Investigations of Flow and Local Scour Characteristics around a Partially Submerged Permeable WSDOT Barb*. Washington State Department of Transportation, Report No. WA-RD 581.1, 2004.

Parish Geomorphic (2005). *Sawmill Creek Monitoring: Final Report*. January, 2005.

Partheniades, E. (2009). *Cohesive Sediments in Open Channels: Properties, Transport and Applications*. Elsevier, Oxford UK.

Parsons, D.R., Best, J.L., Lane, S.N., Orfeo, O., Hardy, R.J., Kostaschuk, R. (2007). Form roughness and the absence of secondary flow in a large confluence-diffluence, Rio Paraná, Argentina. *Earth Surface Processes and Landforms*, 32, pp. 155-162.

Parsons, D.R., Best, J.L., Orfeo, O., Hardy, R.J., Kostaschuk, R., Lane, S.N. (2005). Morphology and flow fields of three-dimensional dunes, Rio Paraná, Argentina: Results from simultaneous multibeam echo sounding and acoustic Doppler current profiling. *Journal of Geophysical Research*, 110, F04S03, doi:10.1029/2004JF000231.

Piper, K.L., Hoag, J.C., Allen, H.H., Durham, G., Fischenich, J.C., Anderson, R.O. (2001). Bioengineering as a tool for restoring ecological integrity to the Carson River, *WRAP Technical Notes Collection* ERDC TN-WRAP-01-05; *Water Quality Technical Notes Collection* (ERDC WQTN-CS-03, U.S. Army Engineer Research and Development Center, Vicksburg, MS.

Post, G.C. (2007). The measurement of Reynolds stress in a model river bend using acoustic Doppler velocimeters. *M.A.Sc Thesis*, University of Ottawa, Canada

Ramooz, R., Rennie, C.D. (2010). Laboratory measurement of bedload with an ADCP, In *Bedload-Surrogate Monitoring Technologies*, J.R Gray, J.B. Laronne and J.D.G. Marr (eds.). United States Geological Survey Scientific Investigations Report 2010-5091, available online at http://pubs.usgs.gov/sir/2010/5091/papers/Ramooz.pdf.

Rantz, E.S. *and others*. (1982). *Measurement and Computation of Streamflow : Volume 2 Computation of Discharge*. Geological Survey Water-Supply Paper 2175. United States Government Printing Office, Washington.

Raudkivi, A.J. (1998). *Loose Boundary Hydraulics*. Fourth Edition, A.A. Balkema, Rotterdam, Netherlands.

RD Instruments, Inc. (2009). *Workhorse Rio Grande ADCP User's Guide*, RD Instruments, Inc., Sand Diego, CA.

Rennie, C.D. (*accepted*). "Mapping water and sediment flux distributions in gravel-bed rivers using aDcps" Discussion of Muste *et al.* "Modern digital instruments and techniques for hydrodynamic and morphologic characterization of streams", Gravel-Bed Rivers VII, to be published by Wiley.

Rennie, C.D., Church, M. (2010). Mapping spatial distributions of uncertainty of water and sediment flux in large gravel-bed river reach using an aDcp. *Journal of Geophysical Research – Earth Surfaces*, 115, F03035, doi:10.1029/2009JF001556.

Rennie, C.D., Hay, A. (in press). Reynolds stress estimates in a tidal channel from phase-wrapped ADV data. *Journal of Coastal Research*.

Rennie, C.D., Millar, R.G. (2004). Measurement of the spatial distribution of fluvial bedload transport velocity in both sand and gravel, *Earth Surface Processes and Landforms*, 29(10), pp. 1173-1193.

Rennie, C.D., Millar, R.G., Church, M.A. (2002). Measurement of bed load velocity using an Acoustic Doppler Current Profiler. *Journal of Hydraulic Engineering,* 128(5), pp. 473-483.

Rennie, C.D., Villard, P.V. (2004). Site specificity of bed load measurement using an acoustic Doppler current profiler. *Journal of Geophysical Research*, 109, F03003.

Rennie, C.D., Rainville, F., Kashyap, S. (2007). Improved estimation of ADCP apparent bed-load velocity using a real-time Kalman filter. *Journal of Hydraulic Engineering,* 133(12), pp. 1337-1344.

Reuter, J.M., Jacobson, R.B., Elliott, C.M., DeLonay, A.J. (2009). Assessment of Lower Missouri River physical aquatic habitat and its use by adult sturgeon (genus *Scaphirhynchus*), 2005–07: U.S. Geological Survey Scientific Investigations Report 2009–5121, 81 p.

Richardson, W.R., Thorne, C.R. (1998). Secondary currents around braid bar in Brahmaputra River, Bangladesh. *Journal of Hydraulic Engineering*, 124(3), pp. 325-328.

RiverSurveyor S5/M9 System Manual (February 2010). SonTek/YSI.

Roca, M., Blanckaert, K., Martin-Vide, J.P. (2009). Reduction of bend scour by an outer bank footing: Flow field and turbulence. *Journal of Hydraulic Engineering*, 135(5), pp. 361-368.

Roca, M., Martin-Vide, J.P., Blanckaert, K. (2007). Reduction of Bend Scour by an Outer Bank Footing : Footing Design and Bed Topography. *Journal of Hydraulic Engineering*, 133(2), pp. 139-147.

Roy, A.G., Biron, P.M., Buffin-Bélanger, T., Levasseur, M. (1999). Combined visual and quantitative techniques in the study of natural turbulent flows. *Water Resources Research*, 35(3), pp. 871-877.

Roy, A.G., Biron, P., De Serres, B. (1996). On the necessity of applying a rotation to instantaneous velocity measurements in river flows. *Earth Surface Processes and Landforms*, 21, pp. 817-827.

Rozovskii, I.L. (1957). *Flow of water in bends of open channels*, Academy of Sciences of the Ukrainian SSR, Kiev, 1957; Israel Program for Scientific Translations, Jerusalem, 1961.

Ruther, N., Olsen, N.B.R. (2005). Three-dimensional modelling of sediment transport in a narrow 90º channel bend. *Journal of Hydraulic Engineering,* 131(10), pp. 917-920.

Sanjou, M., Nezu, I. (2009). Turbulence structure and coherent motion in meandering compound open-channel flows. *Journal of Hydraulic Research*, 47(5), pp. 598-610.

Schmeeckle, M.W., Nelson, J.M. (2003). Direct numerical simulation of bedload transport using local, dynamic boundary condition. *Sedimentology*, 50, pp. 279-301.

Sekely, A.C., Mulla, D.J., Bauer, D.W. (2003). Streambank slumping and its contribution to the phosphorus and suspended sediment loads of the blue earth river, Minnesota. *Journal of Soil and Water Conservation*, 57(5), pp. 243–249.

Shields, F.D. (1995). Fate of Lower Mississippi River habitats associated with river training dikes. *Aquatic Conservation: Marine and Freshwater Ecosystems*, 5(2), pp. 97-108.

Shields, F.D., Knight, S.S., Cooper, C.M. (1998). Addition of spurs to stone toe protection for warmwater fish habitat rehabilitation. *Journal of the American Water Resources Association*, 34, pp. 1427-1436.

Shields, F.D., Knight, S.S., Cooper, C.M. (2000). Warmwater stream bank protection and fish habitat: A comparative study. *Environmental Management*, 26(3), pp. 317-328.

Shields, F.D., Knight, S.S, Testa III, S., Cooper, C.M. (2003). Use of Acoustic Doppler Current Profilers to Describe Velocity Distributions at the Reach Scale. *Journal of the American Water Resources Association*, 39(6), pp. 1397-1408.

Shields, F.D., Knight, S.S., Stofleth, J.M. (2006). Large wood addition for aquatic habitat rehabilitation in an incised, sand-bed stream, Little Topashaw Creek, Mississippi. *River Research and Applications*, 22, pp. 803-817.

Shields, F.D., Rigby, J.R. (2005). River habitat quality from river velocities measured using acoustic Doppler current profiler. *Environmental Management*, 36(4), pp. 565-575.

Shiono, K., Spooner, J., Chan, T., Rameshwaran, P., Chandler, J. (2008). Flow characteristics in meandering channels with non-mobile and mobile beds for overbank flows. *Journal of Hydraulic Research*, 46(1), pp. 113-132.

Simpson, M.R. (2001). Discharge Measurements Using a Broad-Band Acoustic Doppler Current Profiler, *United States Geological Survey Open File Report* 01-1, Sacremento, CA.

Sreenivasan, K.R. (1990). Turbulence and the tube. *Nature*, 344, pp. 192-193.

Standfield, L. (Ed). (2005). *Ontario stream assessment protocol. Version7, Fish and Wildlife Branch*. Ontario Ministry of Natural Resources. Peterborough, Ontario. 256 p.

Sukhodolov, A., Uijttewaal, W.S.J., Engelhardt, C. (2002). On the correspondence between morphological and hydrodynamic patterns in groyne fields. *Earth Surface Processes and Landforms*, 27, pp. 289-305.

Sutherland, A.J. (1967). Proposed mechanism for sediment entrainment by turbulent flows. *Journal of Geophysical Research*, 72, pp. 6183-6194.

Szupiany, R.N., Amsler, M.L., Best, J.L., Parsons, D.R. (2007). Comparison of fixed- and moving-vessel flow measurements with an aDcp in a large river. *J. Hyd. Eng.* 133(12), pp. 1299-1307.

Szupiany, R.N., Amsler, M.L., Parsons, D.R., Best, J.L. (2009). Morphology, flow structure, and suspended sediment transport at two large braid-bar confluences. *Water Resources Research*, 45, W05415.

Teledyne RD Instruments (TRDI) (2008). WinRiver II User's Guide, version 2.02.

Teledyne RD Instruments (TRDI) (2009). WinRiver II User's Guide, version 2.06.

Termini, D. (2009). Experimental observations of flow and bed processes in large-amplitude meandering flume. *Journal of Hydraulic Engineering*, 135(7), pp. 575-587.

Termini, D., Piraino, M (2010). Experimental analysis of cross-sectional flow motion in a large amplitude meandering bend. *Earth Surface Processes and Landforms*. 36, pp. 244-256(2011), DOI: 10.1002/esp.2095.

Thompson, D.M. (2006). The role of vortex shedding in the scour of pools. *Advances in Water Resources*, 29, pp. 121-129.

Thompson, D.M., Wohl, E.E. (2009). The linkage between velocity patterns and sediment entrainment in a forced-pool and riffle unit. *Earth Surface Processes and Landforms*, 34, pp. 177-192.

Trump, C.L., Marmorino, G.O. (2002). Spatial processing of range-bin ADCP data to resolve small-scale frontal features. *Journal of Atmospheric and Oceanic Technology*, 19, pp. 1461-1468.

Uijttewaal, W.S.J. (2005). Effects of groyne layout on the flow in groyne fields: Laboratory experiments. *Journal of Hydraulic Engineering*, 131(9), pp. 782-791.

Uijttewaal, W.S.J., Lehmann, D., van Mazijk, A. (2001). Exchange processes between a river and its groyne fields: Model experiments. *Journal of Hydraulic Engineering*, 127(11), pp. 928-936.

USDA (2000). *Engineering Technical Note No. 23: Design of Stream Barbs (Version 1.3).* United States Department of Agriculture, Natural Resources Conservation Service, Portland, Oregon.

USDA (2005). *Engineering Technical Note No. 23: Design of Stream Barbs (Version 2.0).* United States Department of Agriculture, Natural Resources Conservation Service, Portland, Oregon.

Van Balen, W., Uijttewaal, W.S.J., Blanckaert, K. (2009). Large-eddy simulation of a mildly curved open-channel flow. *Journal of Fluid Mechanics*, 630, pp. 413-442.

Van Leussen, W. (1988). Aggregation of particles, settling velocity of mud flocs. *In Physical process in estuaries*. Ed. J. Dronkers and W. van Leussen. Springer-Verlag, New York, pp. 348-403.

Villard, P. V., R. A. Kostaschuk (1998). The relation between shear velocity and suspended sediment concentration over dunes: Fraser Estuary, Canada. *Marine Geology*, 148, pp. 71– 81.

Weitbrecht, V., Kühn, G., Jirka, G.H. (2002). Large scale PIV-measurements at the surface of shallow water flows. *Flow Measurement and Instrumentation*, 13, pp. 237-245.

Wormleaton, P.R., Ewunetu, M. (2006). Three-dimensional k-e numerical modeling of overbank flow in a mobile bed meandering channel with floodplains of different depth, roughness and planform. *J. of Hydraulic Res*., 44(1), pp. 18-32.

Yarin, L.P., Hetsroni, G. (1993). Turbulence intensity in dilute two-phase flows-3: the particles-turbulence interaction in dilute two-phase flow. *International Journal of Multiphase Flow*, 20(1), pp. 27-44.

Zeng, J., Constantinescu, G., Blanckaert, K., Weber, L. (2008). Flow and bathymetry in sharp open-channel bends: Experiments and predictions. *Water Resources Research*, 44, W09401.